Università degli Studi Roma Tre

DIPARTIMENTO DI SCIENZE

PhD School in Scienze della Materia, Nanotecnologie e Sistemi Complessi

Tuning the Photoluminescence Emission Wavelength of Ge/SiGe Quantum Wells: Leveraging on Quantum Confinement, Strain, and Doping

Candidato:
Michele Montanari

Tutor:
Prof. Giovanni Capellini

XXXI Ciclo

"*The electric light did not come from*
the continuous improvement of candles"

Oren Harari

CONTENTS

Introduction v
- 1 Moore's law . . . v
- 2 Silicon Photonics: quest for a laser . . . vii
- 3 Germanium is a candidate gaining material . . . viii
- 4 Thesis outline . . . x

1 SILICON-GERMANIUM HETEROSTRUCTURES 1
- 1.1 General properties of Silicon and Germanium . . . 1
- 1.2 Band gap Modifications . . . 5
  - 1.2.1 Band structure of semiconductor alloys . . . 6
  - 1.2.2 Band structure modifications by heterostructures . . . 7
  - 1.2.3 Band structure modifications by strain . . . 9
- 1.3 General properties of SiGe alloys . . . 18
- 1.4 Band alignment in SiGe heterostructures . . . 19
- 1.5 Heteroepitaxy . . . 21
  - 1.5.1 Lattice mismatch and elastic energy: relaxed and coherent growth . . . 22
- 1.6 Crystal growth . . . 29
  - 1.6.1 Thermodynamics of crystal growth . . . 29
  - 1.6.2 Atomistic model . . . 31
  - 1.6.3 Heterostructures growth techniques . . . 34

2 INTER-BAND TRANSITIONS IN QUANTUM WELLS 39
- 2.1 Quantum Wells Properties . . . 39
  - 2.1.1 Infinite potential well . . . 40
  - 2.1.2 Finite potential well . . . 41
  - 2.1.3 Energy levels of holes . . . 43
  - 2.1.4 Asymmetric Coupled Quantum Wells . . . 43
- 2.2 Inter-band transitions in semiconductors . . . 45
  - 2.2.1 Direct band-to-band transitions . . . 45
  - 2.2.2 Indirect band-to-band transitions . . . 47
- 2.3 Inter-band transitions in quantum wells . . . 49
- 2.4 Recombination processes in semiconductors . . . 51
  - 2.4.1 Radiative electron-hole recombination . . . 53

2.4.2 Non-radiative transitions 55
2.4.3 Rate of recombination for excess carrier density 58
2.4.4 Scaling of photoluminescence intensity as a function of excitation power 58
2.4.5 Spectral shape of direct gap emission 59
2.4.6 Self-absorption 60
2.4.7 Photoluminescence spectra: resonant and non-resonant excitation conditions 61
3 EXPERIMENTAL TECHNIQUES 65
3.1 CVD growth set-up 65
3.2 Structural characterization 69
3.2.1 X-ray photoemission spectroscopy 69
3.2.2 X-ray diffraction 72
3.2.3 Atomic force microscopy 78
3.2.4 Raman spectroscopy 84
3.3 Optical characterization 90
3.3.1 Photoluminescence Spectroscopy 90
3.3.2 Photoluminescence Set-up 91
4 GROWTH AND CHARACTERIZATION OF VIRTUAL SUBSTRATES 95
4.1 Substrate preparation 98
4.2 Ge Virtual Substrate 100
4.2.1 Optical Properties of the Ge Virtual Substrate 103
4.3 SiGe Virtual Substrate 106
4.3.1 Optical Properties of the SiGe Virtual Substrate 110
5 GROWTH AND CHARACTERIZATION OF GE/SIGE QUANTUM WELLS 113
5.1 Symmetric Quantum Wells 115
5.1.1 Structural Properties of Symmetric QWs 115
5.1.2 Optical Properties of Symmetric QWs 122
5.2 Strained Quantum Wells 130
5.2.1 Strain Analysis of Strained QWs 131
5.2.2 Optical Properties of Strained QWs 136
5.3 Doping 142
5.3.1 Structural Properties of Doped QWs 144
5.3.2 Optical Properties of Doped QWs 146
5.4 Asymmetric Quantum Wells 148
5.4.1 Structural Properties of Asymmetric QWs 149
5.4.2 Optical Properties of Asymmetric QWs 151

Summary and conclusions 155
List of Publications 158
List of Abbreviations 161
List of Figures 163
List of Tables 171
Bibliography 171

INTRODUCTION

1 MOORE'S LAW

Since the early 70's, the semiconductor industry has been working hardly to satisfy a virtuous cycle: through transistor scaling, one obtains a better performance-to-cost ratio of products, which induces an exponential growth of the semiconductor market supplying more money for further investments in new technologies that enhance scaling, and the cycle starts again [1]. This cycle has been predicted by the observation of Gordon Moore in 1965 that the number of transistors in a dense integrated circuit doubles approximately every two years, observation universally known as Moore's law. In Figure 2 it is reported a plot of transistor count for a variety of commercial microprocessor chips versus the year of introduction; we can see that Moore was indeed prescient, or, on the other side, that electronics industry has been working hardly to follow this "roadmap". Minimum feature sizes were on the order of 10 μm in the 70's, while today they are about 16 nm, giving three orders of magnitude decrease in device size and four orders of magnitude increase in device density. The downscaling of the integrate circuit (IC) minimum feature size and increased density, while feeding the continuous improvement of performance of the computer system, has also created significant challenges. Nowadays, on a system level, issues related to more-dense copper interconnects overshadow the enhancement in chip performance due to scaling [3]. This is the interconnect bottleneck that has arisen as a natural consequence of device miniaturization. In particular, interconnection through copper wires has reached several limits:

Figure 1 – The virtuous circle of the semiconductor industry.

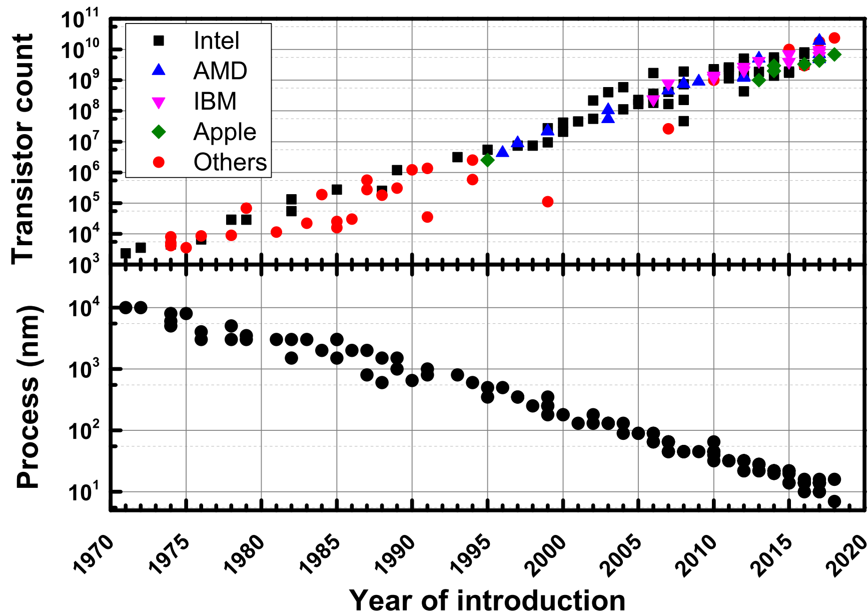

Figure 2 – Plot of CPU transistor counts against dates of introduction. Data from [2].

- No parallel signal can be transferred without any interference.
- Although the downscaling of transistor increases the speed, the same is not true for the downsizing of interconnect [4].
- A bandwidth to transmit 10 Gbps of data is very challenging [5].
- High power dissipation.

Since interconnects consume 80% of a microprocessor's power [6], and server interconnect powers exceed the total power generated from solar energy, the last point is very important because the power consumption of information technology is now so large that it is starting to be environmentally significant [7].

Moore's law is not a "physical" law but a consequence of the scaling heuristics of semiconductor manufacturing: by holding the cost per unit area of manufacturing constant, increasing transistor density gives lower cost per function [8]. But nowadays smaller transistors are more difficult to make and the engineering effort is so high that the economic benefits arising from the shrinking of transistors do not hold anymore.

To overcome this saturation, the global semiconductor industry is following a new trend called "More-than-Moore" (MtM). The goal of this trend is

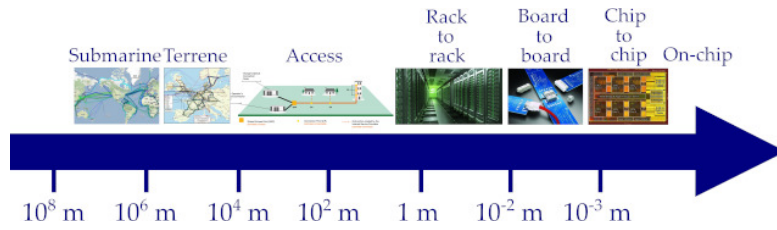

Figure 3 – Optical from submarine to on-chip. Adapted from [9].

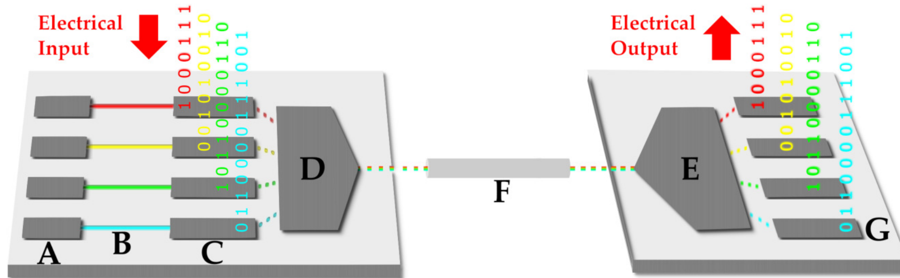

Figure 4 – Configuration of an optical circuit.

to improve the performance of devices adding functionalities that do not necessarily scale according to Moore's law. An example of a MtM technology is the Silicon Photonics which combines the merit of photons in data trasmission with the merit of electrons in data processing on a single chip.

2 SILICON PHOTONICS: QUEST FOR A LASER

Since its inception in the transatlantic telecommunications between USA, UK, and France in 1988, optical fiber has nowadays replaced all of the electronic wires for long-haul telecommunication systems. Besides long-haul trans-ocean telecommunications, at present, optics it is increasingly exploited in intermediate distance telecommunication networks like metropolitan area networks (MANs), campus networks, local-area networks (LANs), and fiber-to-the-home (FTTH) applications [10]. For server clusters and data storage center applications, Luxtera has already made commercially available silicon photonics-based 100 Gigabit optical transceiver. A fiber optic transceiver (depicted in Fig. 4) is a device that encodes electrical inputs into light pulses and uses fiber optical technology to transmit and receive data. The building blocks of a transceiver are:

- **A**: Laser source.
- **B**: Waveguide: its role is to optimize the transport of light.

- **C**: Modulator: its role is to convert the electrical signal 0 or 1 to an optical signal.
- **D/E**: Multiplexer/Demultiplexer. Multiplexing consists in the association of multiple optical signals to a single waveguide. The Demultiplexer performs the inverse function.
- **F**: Optical fiber: its role it to transport data from the transmitter to the receiver.
- **G**: Photodetector: its role is to convert an optical signal to an electrical signal.

However, to be competitive with electrical interconnects at the chip scale, optical interconnects have to meet several aggressive requirements in term of power consumption, data density, and monolithic integration of optical components in silicon. One of the main hurdles preventing the use of optics at shorter distance scales is the cost of optical components which are significantly higher than the electronic devices. As a matter of fact, commercially available photonic devices consist mainly of III-V lasers integrated on silicon that are good light emitters but are not fully integrable on the CMOS technology. To reduce costs, taking advantage of CMOS foundries, it would be convenient to find a laser source which meets the following requirements:

1. the device is electrically pumped;
2. it is directly grown on Silicon and is CMOS compatible;
3. it emits around 1550 nm.

If the third requirement is satisfied the chip can be directly connected to the fiber optic network. Usually optical fiber are made of silica glass which has an attenuation spectrum reported in Figure 5. At 1550 nm the attenuation is near 0.2 dB/km.

3 GERMANIUM IS A CANDIDATE GAINING MATERIAL

Among all the proposed approaches, Ge-based solutions are now considered the most promising ones. As a component of the column IV, germanium has

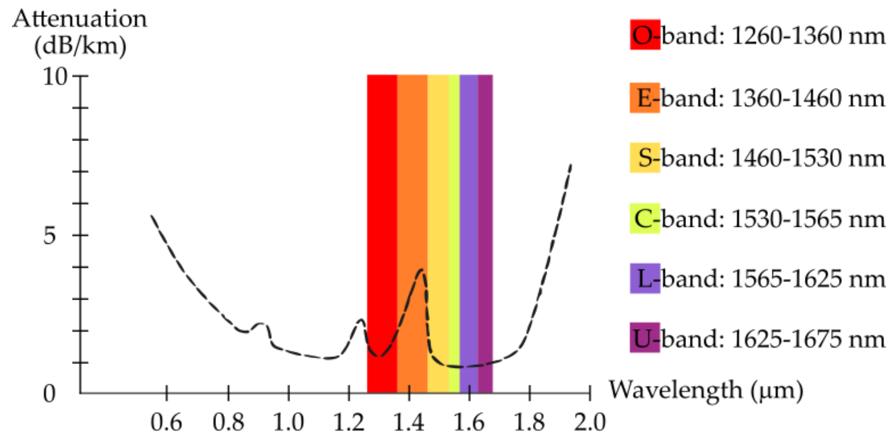

Figure 5 – Optical fiber transmission windows.

a high compatibility with silicon and fits well in the already used CMOS manufacturing process. At the same time, the direct emission energy of Ge is 800 meV, exactly matching the 1550 nm used in fiber-based telecommunications systems. Moreover, it has recently attracted a large interest, owing to the possibility of changing the nature of its band structure [11]. As a matter of fact, germanium is a priori an inefficient light emitter, because of its indirect band gap. However, it is considered a quasi-direct gap semiconductor because the distance in energy between the indirect gap in bulk Ge (located at the L-valley) and the direct gap in Γ is only 140 meV (Fig. 6). If electrons can overcome this small energy barrier and occupy the Γ valley, then the light emitting efficiency will be greatly increased, because the radiative recombination rate for direct band-to-band transitions is five orders of magnitude higher than that of the indirect ones.

Since the deformation potential in the Ge conduction band at the Γ point is larger than the L-band one, applying high tensile strain to the Ge lattice both direct and indirect gaps shrink, but the direct gap shrinks faster. Therefore, applying tensile strain, the energy difference between the Γ and the L valleys decreases. In particular, the energy difference between the two vanishes for a biaxial strain about 1.6% [12], driving the material toward a direct gap regime (Fig. 6). Thanks to the reduced energy difference, heavy n-type doping can also be effectively used to increase the radiative efficiency, since the excess electrons in the conduction band first fill the indirect L valley and then the direct Γ valley. These approaches actually led to the demonstration of optically [13] and electrically [14, 15] pumped Ge-based laser. However, none of the reported laser is of pratical use yet, due to the extremely high threshold current, or the poor overall emission efficiency. Moreover, as already

mentioned, the effect of tensile strain is to shrink the band gap energy moving away from the 1550 nm targeted for telecom applications.

An alternate way proposed to increase the radiative recombination efficiency in Ge is to take advantage from the quantum confinement effect (QCE) in Ge multiple quantum wells (MQWs) surrounded by SiGe barriers [16]. Thanks to recent successes in advanced heteroepitaxial techniques, these structures can be realized on Si wafers with appropriate SiGe virtual substrates [17]. Moreover, Ge/SiGe MQWs have attracted great interest for Si-based photonic devices since the demonstration of quantum confined Stark effect (QCSE) at room temperature (RT) [18]. Optical modulators [19, 20, 21, 22, 23], photodetectors [24, 25, 26] and spin-based opto-electronic concepts [27, 28, 29, 30] have been investigated using this promising material. Furthermore, RT direct gap emission has been observed by means of electroluminescence (EL) [31] and photoluminescence (PL) [32], indicating that Ge/SiGe MQWs are potential candidates for an efficient silicon-compatible light emitter. While Ge/SiGe MQWs meet the requirement of compatibility with the CMOS technology, they are limited by a larger direct bandgap energy than bulk Ge. As a consequence, their light emission is blueshifted in the telecommunications O-E-band wavelength range of 1260-1460 nm and hardly reach the commercially important C-band (1530-1565). Therefore there is a significant demand to shift the wavelength operation-range into the C-band for pratical applications and the employment of tensile strain results in a redshift, as discussed above. Moreover, the energy levels of confined states in QWs can be modified by changing the thickness of the layers and the lattice strain of both wells and barriers. This gives the opportunity of tuning the energy of the emitted light varying the thickness of the layers and the magnitude of the strain.

4 THESIS OUTLINE

The goal of this thesis is to investigate how the photoluminescence properties of Ge/SiGe heterostructures can be tuned by the effect of quantum confinement, doping, and strain.

In *Chapter 1* we give an introduction of the basic properties of silicon, germanium, and their alloys from structural properties to their band structure.

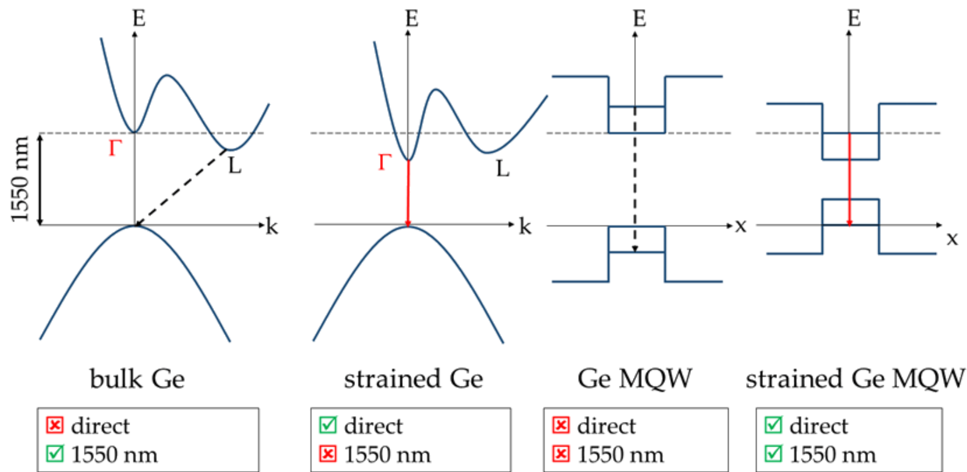

Figure 6 – Gap modification

We discuss how strain, quantum confinement and alloying affect the band structure of a semiconductor. Finally, we report how it is possible to realize SiGe heterostructures by means of chemical vapor deposition.

In *Chapter 2* we introduce the theory of optical transitions in semiconductor, distinguishing between radiative and non-radiative transitions.

In *Chapter 3* we introduce the experimental set-ups employed to characterize the samples and we discuss the properties of the material we can investigate with these techniques.

In *Chapter 4* we describe how the concentration of defects in SiGe heterostructures can be reduced with the employment of virtual substrates. Their deposition and their optical properties will be discussed in detail.

In *Chapter 5* the structural characterization and the optical properties of the Ge QWs will be discussed. Thanks to the results obtained in Chapter 4 we will be able to distinguish in the PL spectra the features related to the virtual substrate from those related to the quantum wells. As a consequence, the effect of quantum confinement, doping, and strain can be unambiguously analyzed.

1

SILICON-GERMANIUM HETEROSTRUCTURES

The present work is focused on the effect of quantum confinement and tensile strain on the optical properties of heterostructures realized in silicon-germanium (SiGe) alloys. Before analyzing any optical feature, it is important to introduce the main properties of the material they are made of. To this aim, this first chapter introduces the fundamental properties of silicon, germanium and their alloys. Particular attention is devoted to the effect of strain on the band structure. Afterwards, we introduce how heterostructures are obtained and the main challenges that need to be faced during their realization.

1.1 GENERAL PROPERTIES OF SILICON AND GERMANIUM

This work is focused on silicon (Si) and germanium (Ge), which are both semiconductors of the IV group and crystallize in the diamond structure. The Bravais lattice of the diamond structure is face centered cubic (FCC) with a basis of two atoms. A symmetric set of primitive vectors for the FCC lattice is [see Figure 1.1(a)]:

$$\boldsymbol{a_1} = \frac{a}{2}(0,1,1), \qquad \boldsymbol{a_2} = \frac{a}{2}(1,0,1), \qquad \boldsymbol{a_3} = \frac{a}{2}(1,1,0), \tag{1.1}$$

where a is the side of the conventional unit cell. The diamond structure can be described as two inter-penetrating FCC lattices displaced by $(\frac{a}{4})(1,1,1)$ along the body diagonal of the conventional cube [34]. The two vectors of the basis are

$$\boldsymbol{d_1} = 0, \qquad \boldsymbol{d_2} = \frac{a}{4}(1,1,1). \tag{1.2}$$

The corresponding primitive vectors of the FCC reciprocal lattice are

$$\boldsymbol{g_1} = \frac{2\pi}{a}(-1,1,1), \qquad \boldsymbol{g_2} = \frac{2\pi}{a}(1,-1,1), \qquad \boldsymbol{g_3} = \frac{2\pi}{a}(1,1,-1), \tag{1.3}$$

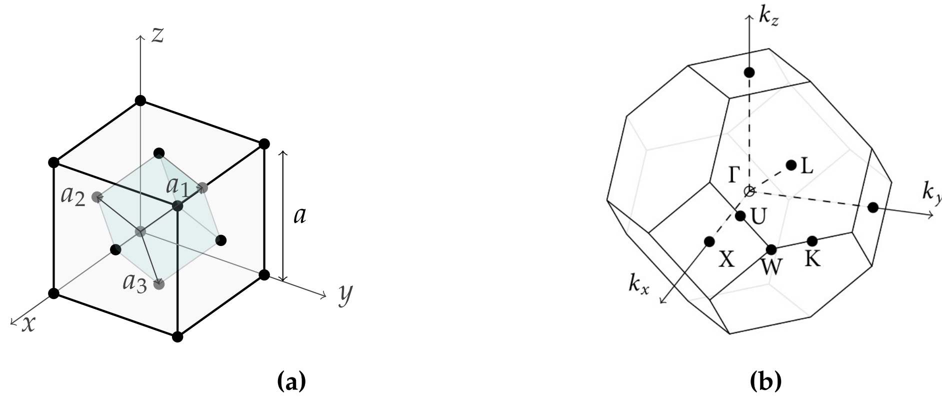

Figure 1.1 – (a) Face centered cubic lattice and primitive translation vectors a_1, a_2 and a_3 given by Eqs. 1.1 in the text; the primitive cell is reported in light blue. (b) Brillouin zone of a crystal with a FCC Bravais lattice. The points of high symmetry are shown.

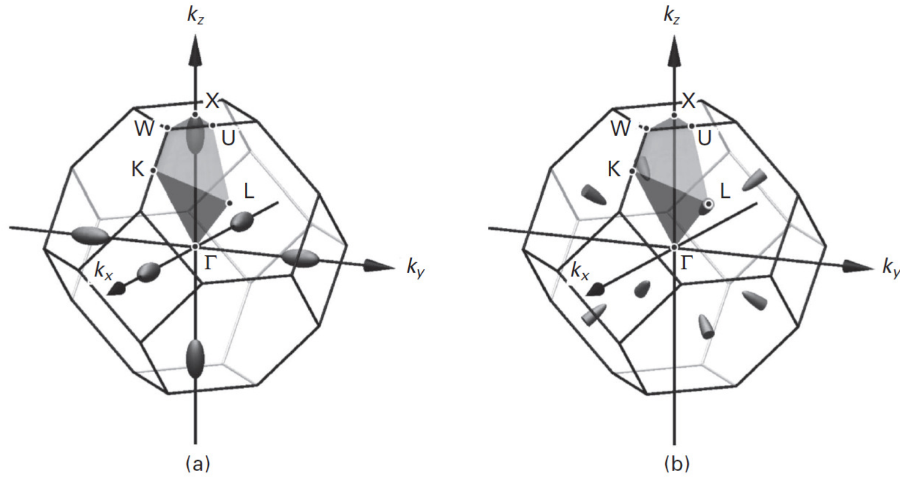

Figure 1.2 – Many-valley structure of (a) Si and (b) Ge. Taken from [33].

which form a BCC lattice. The Brillouin zone is a truncated octahedron depicted in Fig. 1.1(b). Some points of high symmetry in the Brillouin zone are denoted by conventional names:

$$\Gamma = (0,0,0), \qquad X = \frac{2\pi}{a}(1,0,0), \qquad L = \frac{2\pi}{a}(\frac{1}{2},\frac{1}{2},\frac{1}{2}),$$
$$W = \frac{2\pi}{a}(1,\frac{1}{2},0), \qquad K = \frac{2\pi}{a}(\frac{3}{4},\frac{3}{4},0), \qquad U = \frac{2\pi}{a}(1,\frac{1}{4},\frac{1}{4}).$$

The lattice parameter a is a function of lattice temperature, i.e., it increases with temperature due to thermal expansion. The change with temperature of the lattice parameter can be expressed with the linear thermal coefficient of expansion, $\alpha(T)$, that also depend on temperature, defined as

$$\alpha(T) = \frac{1}{a}\frac{\partial a}{\partial T}. \tag{1.4}$$

	$a(300\ K)$ (Å)	$\alpha(300\ K)$ $(10^{-6}\ K^{-1})$	$\alpha(600\ K)$ $(10^{-6}\ K^{-1})$
Si	5.431	2.6	3.7
Ge	5.658	5.7	6.7

Table 1.1 – Lattice constants and thermal expansion coefficients at different temperatures for silicon and germanium, taken from [35].

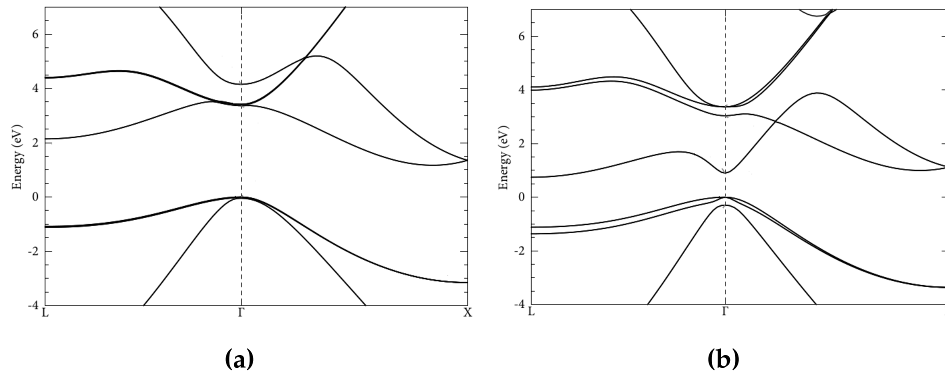

(a) **(b)**

Figure 1.3 – (a) Band diagram of Si. (b) Band diagram of Ge.

Table 1.1 provides the lattice constants and the thermal expansion coefficients for silicon and germanium.

Both silicon and germanium are indirect gap semiconductor whose conduction and valence band extremes occur at different points in the Brillouin zone. In both the semiconductors, the maximum of the uppermost filled band, called the *valence band*, occurs at the Γ point ($\boldsymbol{k} = 0$). In silicon the minimum of the lowest empty (*conduction*) band exhibits a six-fold degeneracy [see Fig. 1.2(a)] and occurs at the Δ point along the [100] crystallographic direction connecting Γ to X. The corresponding band gap is 1.12 eV [36]. The energy band separation at Γ is 3.40 eV. On the contrary, the Ge conduction band minimum exhibits a four-fold degeneracy (8 semi-ellipsoids) [see Fig. 1.2(b)] and occurs at the L point along the [111] crystallographic direction. The corresponding band gap is 0.66 eV. The next minimum of the conduction band occurs at the zone center and the direct gap is 0.8 eV, thus making the difference between L and Γ point minima about 136 meV only, as compared to the 2.3 eV $X - \Gamma$ difference in silicon. The E–$\boldsymbol{k}$ diagrams for different crystallographic directions in both materials are shown in Figure 1.3.

In silicon and germanium, the valence band is derived from p type atomic states. The spin-orbit interaction results in the splitting of the p type state into two states with total angular momentum j=3/2 and j=1/2. The state j=3/2 is 4-fold degenerate (m_j=3/2, 1/2, -1/2, -3/2) whereas the state j=1/2 is 2-fold degenerate (m_j=1/2, -1/2). This two states are separated by an energy Δ called the spin-orbit splitting energy. States corresponding to j=3/2 and m_j=±3/2 are called *heavy-holes* (HH), while *light-holes* (LH) correspond to j=3/2 and m_j=±1/2. The two band are degenerate in the Γ point, and the degeneracy is lost for finite $\boldsymbol{k}$. The split-off band is separated by an energy Δ from the heavy, light hole bands at Γ, and it corresponds to j=3/2 and m_j=±1/2 states (see Fig. 1.4). Ge has a significantly larger spin-orbit splitting (Δ=0.29 eV) compared to Si (Δ=0.044 eV), which is primarily due to the heavier atom of Ge [33]. The values of the energy band minima and maxima as well as the effective masses are listed in Table 1.2.

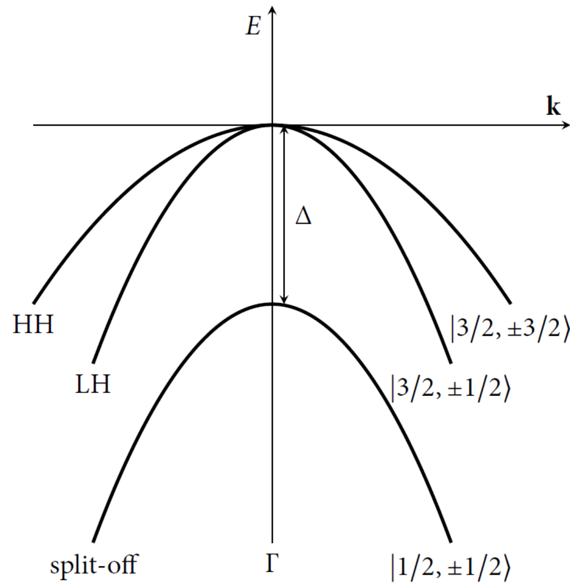

Figure 1.4 – The valence band structure in Si and Ge.

The values of the energy band gaps given up to now are valid only at room temperature (RT). As a matter of fact, in semiconductors the dependence of the band gap E_g on the temperature is given by the empirical Varshni law:

$$E_g(T) = E_g(0) - \frac{\alpha T^2}{T + \beta}, \tag{1.5}$$

where α and β are parameters typical of each semiconductor and $E_g(0)$ is the energy gap value at 0 K [37]. The values of α and β for Si and Ge are reported in Table 1.3, while for $Si_{1-x}Ge_x$ alloys a linear interpolation between

	Silicon	Germanium
Minimum energy in Γ	3.5 eV	0.8 eV
Effective mass	0.2 m_0	0.041 m_0
Minimum energy *not* in Γ	1.12 eV	0.66 eV
Longitudinal effective mass	0.92 m_0	1.64 m_0
Transverse effective mass	0.19 m_0	0.082 m_0
Heavy-hole effective mass	0.54 m_0	0.28 m_0
Light-hole effective mass	0.15 m_0	0.044 m_0
Split-off band valence band energy	-0.044 eV	-0.29 eV
Effective mass	0.24 m_0	0.084 m_0

Table 1.2 – The values of the energy band minima and maxima as well as the effective masses for silicon and germanium. $m_0 = 9.11 \times 10^{-31}$ kg is the free electron rest mass [36].

	Si	Ge
E_0 direct gap	4.34 eV	0.89 eV
α direct gap	$3.91 \cdot 10^{-4}$ eV/K	$5.82 \cdot 10^{-4}$ eV/K
β direct gap	125 K	296 K
E_0 indirect gap	1.17 eV	0.742 eV
α indirect gap	$4.73 \cdot 10^{-4}$ eV/K	$4.77 \cdot 10^{-4}$ eV/K
β indirect gap	636 K	235 K

Table 1.3 – E_0, α and β Varshni's parameters of bulk Si and Ge.

this values is usually accepted.

1.2 BAND GAP MODIFICATIONS

After discussing the structural and electronic properties of Si and Ge, we now see how the band structure of a semiconductor can be engineered following three different approaches:

1. Alloying;

2. Use of heterostructures;

3. Use of strain.

Although in most of the heterostructures the three effects occur concurrently, we start introducing their effect separately to get familiar with the main results and definitions. The joint effect of the three approaches, in the case of SiGe heterostructures, will be discussed in details in the following.

1.2.1 *Band structure of semiconductor alloys*

The easiest way to modify the electronic properties of a given material, or to produce a material with new properties, is based on making an alloy [38]. The desire to form semiconductors alloys is mainly motivated by two objectives:

1. To achieve a desired bandgap;

2. To create a material with a proper lattice constant to match with a specific substrate.

The properties of most of semiconductor alloys can be easily described in terms of simple interpolations between the properties of the compounds [39]. This is theoretically justified by the so-called "*virtual crystal approximation*" (VCA), which describes the alloy as a perfect crystal made of imaginary average "atoms" [40]. As an example, is possible to estimate the lattice parameter of an alloy using *Vegard's law*.

Vergard's law is an approximate empirical rule which says that a linear relation exists between the crystal lattice constant of an alloy and the concentrations of the constituent elements [41]. Sometimes, the linear interpolation is not accurate enough, and a non-linear term is added. In this case, the lattice parameter of an $A_{1-x}B_x$ alloy is given by

$$a_{A_{1-x}B_x} = (1-x)a_a + xa_B - b^{AB}(1-x)x, \tag{1.6}$$

where a_i are the lattice parameters of the constituents, x is the concentration of the compound B, and the curvature correction is characterized by the *bowing parameter* b^i.

Similarly, the bandgap of the alloy is given by:

$$E_g^{AB}(x) = E_g^A(1-x) + E_g^B x - b^{AB}(1-x)x. \tag{1.7}$$

In the previous expression E_g^i is the bandgap of the i compound. If the minimum of the conduction band of the two compounds occurs along different directions, the bowing parameter b^{AB} may differs. As we will see in the following, this has important consequences in SiGe alloys.

1.2.2 *Band structure modifications by heterostructures*

When two semiconductors with different energy gaps are brought together abruptly to form an interface, the discontinuity of valence band and conduction band results in a potential step. Choosing properly the energy discontinuity, it is possible to confine electron and/or holes in a spatial region, thanks to the potential barrier they encounter at the interface. Embedding a material B with a certain energy gap E_{gB} between two layers of another semiconductor with an higher energy gap E_{gA}, it is possible to realize a *quantum well* (QW) in which electrons and holes are confined in the direction perpendicular to the interfaces, while they behave as free carriers in the other two directions. But how do we know whether the conduction band edge of one semiconductor is above or below the conduction band edge of the other semiconductor? The precise determination of the band offsets is generally difficult in both experiments and theory, since it depends upon many parameters such as materials composition, interface orientation, and strain conditions. Moreover, in the neighborhood of the interface, the electron distribution will clearly differ from the bulk, setting up a dipole moment which will cause shifts in the bands, even far from the interface [42]. However, since we are interested in the specific case of band alignments in SiGe heterostructures, and a detailed description of the general case is beyond the purpose of this work, we will now introduce the main results and definitions, presenting a thorough study of the specific system of interest in the following.

Let's start considering the electron affinity χ of the materials, i.e., the energy required to take an electron from the bottom of the conduction band E_c to the vacuum level, where it can escape from the crystal. Unlike the work function, the electron affinity is nearly independent of the position of the Fermi level [36]. *Anderson's rule* states that the vacuum levels of the two materials should be

lined up. It follows that the relative position of conduction and valence band (*band alignment*) is determined by the electron affinities, as shown in Fig. 1.5. However, the theory of band alignment based on electron affinity, although very simple, does not work in many cases. Despite various models have been proposed to improve the accuracy of Anderson's rule, the heterostructure designs usually depend on experiments to provide band alignment informations.

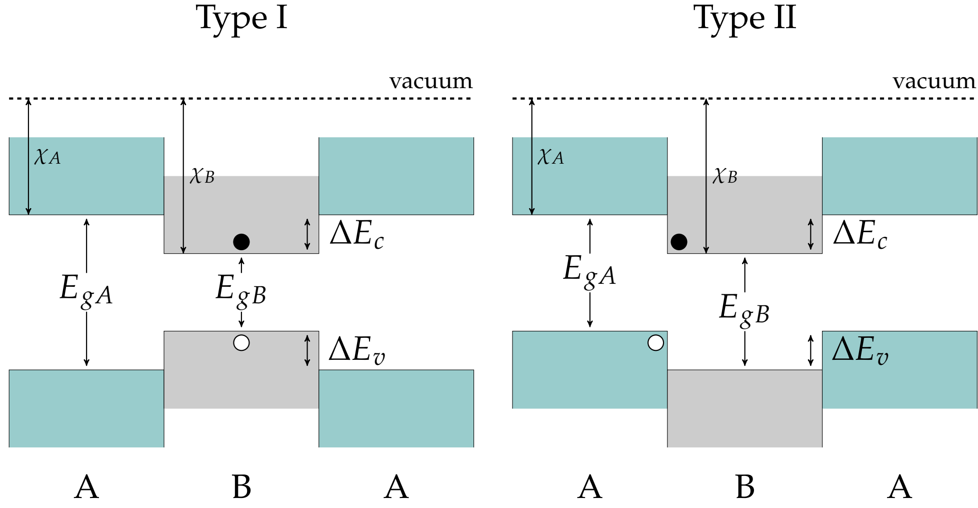

Figure 1.5 – Possible band alignments in heterostructures. Type I: QW for both electrons and holes; Type II: QW for electrons in material B and holes in material A.

As shown in Fig. 1.5 two main band lineups can arise. In the type I heterostructures (straddled band lineup) the lower conduction band edge and the higher valence band edge are both in the same layer. Thus, electrons and holes will localize there. In type II herostructures (staggered lineup), instead, while electrons are localized in one layer, holes are confined in a different layer [43].
In a type I heterostructure, the conduction and valence band discontinuities are given, respectively, by

$$\Delta E_c \equiv E_{cA} - E_{cB} = \chi_B - \chi_A \tag{1.8a}$$

$$\Delta E_v \equiv E_{vA} - E_{vB} = (\chi_B + E_{gB}) - (\chi_A + E_{gA}). \tag{1.8b}$$

In principle, heterostructures can be made from any sequence of materials. However, a mismatch in lattice constant (or a different crystal structure) leads to strains and stresses that significantly influence the band gap of the materials, and introduce crystal defects that can limit the performance of devices, as we will see in the following.

1.2.3 *Band structure modifications by strain*

The band structure of a semiconductor is related to the arrangement of atoms of the material in real space. Hence, a deformation of the crystal lattice and, consequently, the change of position of the atoms affects the energy band structure of the crystal.

We start with a short summary of the main definitions and results of the theory of elastic strains; we then focus on how the band structure is affected by strain.

We start [44] considering an orthonormal tern of vectors $(\hat{x},\ \hat{y},\ \hat{z})$ which describes the unstrained structure of the crystal: after fixing an arbitrary origin, a generic atom of the crystal structure can be identified by a vector $\boldsymbol{r}$, which can be expressed as a linear combination of the three unit vectors: $\boldsymbol{r} = x\hat{x} + y\hat{y} + z\hat{z}$. After a small uniform deformation of the solid has taken place, the axes are distorted in orientation and length. The new axes $\hat{x}',\ \hat{y}',\ \hat{z}'$ may be written in terms of the old axes:

$$\begin{aligned}
\hat{x}' &= (1+\varepsilon_{xx})\hat{x} + \varepsilon_{xy}\hat{y} + \varepsilon_{xz}\hat{z};\\
\hat{y}' &= \varepsilon_{yx}\hat{x} + (1+\varepsilon_{yy})\hat{y} + \varepsilon_{yz}\hat{z};\\
\hat{z}' &= \varepsilon_{zx}\hat{x} + \varepsilon_{zy}\hat{y} + (1+\varepsilon_{zz})\hat{z},
\end{aligned} \tag{1.9}$$

so that the atom at $\boldsymbol{r}$, is now at the position

$$\boldsymbol{r}' = x\hat{x}' + y\hat{y}' + z\hat{z}'. \tag{1.10}$$

The displacement $\boldsymbol{R}$ of the deformation is defined by

$$\boldsymbol{R} \equiv \boldsymbol{r}' - \boldsymbol{r} = x(\hat{x}' - x) + y(\hat{y}' - y) + z(\hat{z}' - z), \tag{1.11}$$

or, from 1.9,

$$\begin{aligned}
\boldsymbol{R}(\boldsymbol{r}) \equiv (x\varepsilon_{xx} + y\varepsilon_{yx} + z\varepsilon_{zx})\hat{x} + (x\varepsilon_{xy} + y\varepsilon_{yy} + z\varepsilon_{zy})\hat{y} +&\\
(x\varepsilon_{xz} + y\varepsilon_{yz} + z\varepsilon_{zz})\hat{z} = u(\boldsymbol{r})\hat{x} + v(\boldsymbol{r})\hat{y} + w(\boldsymbol{r})\hat{z}.&
\end{aligned} \tag{1.12}$$

If the deformation is non uniform we must relate $u,\ v,\ w$ to local strains. We take the origin of $\boldsymbol{r}$ close to the region of interest and we can expand the displacement $\boldsymbol{R}$ around $\boldsymbol{R}(0) = 0$, obtaining the definition for the coefficients ε_{ij} in the non uniform case:

$$\varepsilon_{xx} \simeq \frac{\partial u}{\partial x}; \qquad \varepsilon_{yx} \simeq \frac{\partial u}{\partial y}; \qquad \varepsilon_{zy} \simeq \frac{\partial v}{\partial z} \dots$$

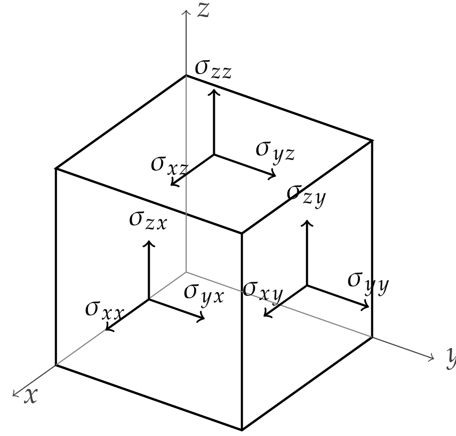

Figure 1.6 – Graphical representation of the stress components acting on the surfaces of an infinitesimal cube.

So we obtain the strain tensor ε_{ij}:

$$\varepsilon_{ij} = \begin{pmatrix} \frac{\partial u}{\partial x} & \frac{\partial v}{\partial x} & \frac{\partial w}{\partial x} \\ \frac{\partial u}{\partial y} & \frac{\partial v}{\partial y} & \frac{\partial w}{\partial y} \\ \frac{\partial u}{\partial z} & \frac{\partial v}{\partial z} & \frac{\partial w}{\partial z} \end{pmatrix}$$

Relation between strains and stresses

The force acting on a unit area in the solid is defined as the stress; these forces are responsible for the strain of the structure. Stress components have the dimensions of force for unit area or energy per unit volume. The strain components are ratio of lengths and are dimensionless. Given a surface orthogonal to an arbitrary direction, we can decompose the force acting on it in its three components along the axes. If we do the same with surfaces orthogonal to the other directions, we end up with the 3×3 stress tensor:

$$\sigma_{ij} = \begin{pmatrix} \sigma_{xx} & \sigma_{xy} & \sigma_{xz} \\ \sigma_{yx} & \sigma_{yy} & \sigma_{yz} \\ \sigma_{zx} & \sigma_{zy} & \sigma_{zz} \end{pmatrix}$$

With the notation introduced, the first letter of the subscript is the direction of the force, while the second one is the direction of the normal to the plane on which the force is acting (Figure 1.6). For an elastic material, the strain is proportional to stress:

$$\sigma_{ij} = S_{ijkl}\varepsilon_{kl}, \tag{1.13}$$

where S_{ijkl} is the *stiffness matrix*. Equation 1.13 is refered as generalized Hooke's law. In the case of cubic symmetry, if the x, y, and z axes coincide with the [100], [010], and [001] directions in the crystal, the stiffness matrix is:

$$S = \begin{pmatrix} C_{11} & C_{12} & C_{12} & 0 & 0 & 0 \\ C_{12} & C_{11} & C_{12} & 0 & 0 & 0 \\ C_{12} & C_{12} & C_{11} & 0 & 0 & 0 \\ 0 & 0 & 0 & C_{44} & 0 & 0 \\ 0 & 0 & 0 & 0 & C_{44} & 0 \\ 0 & 0 & 0 & 0 & 0 & C_{44} \end{pmatrix} \tag{1.14}$$

with only three independent parameters $C_{11},\ C_{12}$ and C_{44} , which depend on the material and are experimentally known for a large set of cubic semiconductors. These parameters for silicon and germanium are:

	$C_{11}\ [N/m^2]$	$C_{12}\ [N/m^2]$	$C_{44}\ [N/m^2]$
Si	$1.601 \cdot 10^{11}$	$0.578 \cdot 10^{11}$	$0.800 \cdot 10^{11}$
Ge	$1.240 \cdot 10^{11}$	$0.413 \cdot 10^{11}$	$0.683 \cdot 10^{11}$

Table 1.4 – Stiffness constants of silicon and germanium at 298 K, taken from [45].

From 1.13 and 1.14

$$\begin{cases} \sigma_{xx} = C_{11}\varepsilon_{xx} + C_{12}\varepsilon_{yy} + C_{12}\varepsilon_{zz} \\ \sigma_{yy} = C_{12}\varepsilon_{xx} + C_{11}\varepsilon_{yy} + C_{12}\varepsilon_{zz} \\ \sigma_{zz} = C_{12}\varepsilon_{xx} + C_{12}\varepsilon_{yy} + C_{11}\varepsilon_{zz} \\ \sigma_{ij} = C_{44}\varepsilon_{ij}, \quad i \neq j \end{cases} \tag{1.15}$$

In the hypothesis of no mixed terms $\sigma_{ij} = 0$, from 1.15 we obtain:

$$\begin{cases} \varepsilon_{xx} = \frac{C_{11}^2 - C_{12}^2}{C_{11}^3 - 3C_{11}C_{12}^2 + 2C_{12}^3}\left[\sigma_{xx} - \frac{C_{12}}{C_{11}+C_{12}}(\sigma_{yy} + \sigma_{zz})\right] \\ \varepsilon_{yy} = \frac{C_{11}^2 - C_{12}^2}{C_{11}^3 - 3C_{11}C_{12}^2 + 2C_{12}^3}\left[\sigma_{yy} - \frac{C_{12}}{C_{11}+C_{12}}(\sigma_{xx} + \sigma_{zz})\right] \\ \varepsilon_{zz} = \frac{C_{11}^2 - C_{12}^2}{C_{11}^3 - 3C_{11}C_{12}^2 + 2C_{12}^3}\left[\sigma_{zz} - \frac{C_{12}}{C_{11}+C_{12}}(\sigma_{xx} + \sigma_{yy})\right] \end{cases} \tag{1.16}$$

Introducing *Young's module*, E, and *Poisson ratio*, ν, as

$$E = \frac{C_{11}^3 - 3C_{11}C_{12}^2 + 2C_{12}^3}{C_{11}^2 - C_{12}^2}, \qquad \nu = \frac{C_{12}}{C_{11} + C_{12}} \tag{1.17}$$

Eq.s 1.16 become

$$\begin{cases} \varepsilon_{xx} = \frac{1}{E}(\sigma_{xx} - \nu(\sigma_{yy} + \sigma_{zz})) \\ \varepsilon_{yy} = \frac{1}{E}(\sigma_{yy} - \nu(\sigma_{xx} + \sigma_{zz})) \\ \varepsilon_{zz} = \frac{1}{E}(\sigma_{zz} - \nu(\sigma_{xx} + \sigma_{yy})) \end{cases} \tag{1.18}$$

We can now investigate the different cases of interest:

- In presence of an *uniaxial stress* $\sigma_{xx} \neq 0$ and $\sigma_{yy} = \sigma_{zz} = 0$

$$\begin{aligned} \varepsilon_{xx} &= +\tfrac{\sigma_{xx}}{E} \\ \varepsilon_{yy} &= -\tfrac{\nu}{E}\sigma_{xx} \\ \varepsilon_{zz} &= -\tfrac{\nu}{E}\sigma_{xx} \end{aligned} \tag{1.19}$$

from which

$$\frac{\varepsilon_{zz}}{\varepsilon_{xx}} = -\nu \tag{1.20}$$

- In presence of an *uniaxial stress* $\sigma_{zz} \neq 0$ and $\sigma_{xx} = \sigma_{yy} = 0$

$$\begin{aligned} \varepsilon_{xx} &= -\tfrac{\nu}{E}\sigma_{zz} \\ \varepsilon_{yy} &= -\tfrac{\nu}{E}\sigma_{zz} \\ \varepsilon_{zz} &= \tfrac{\sigma_{zz}}{E} \end{aligned} \tag{1.21}$$

from which

$$\frac{\varepsilon_{zz}}{\varepsilon_{xx}} = -\frac{1}{\nu} \tag{1.22}$$

- In presence of a *biaxial stress* $\sigma_{xx} = \sigma_{yy} = \sigma_{\|} \neq 0$ and $\sigma_{zz} = 0$

$$\begin{aligned} \varepsilon_{xx} &= \varepsilon_{\|} = \tfrac{1}{E}(1-\nu)\sigma_{\|} \\ \varepsilon_{yy} &= \varepsilon_{\|} = \tfrac{1}{E}(1-\nu)\sigma_{\|} \\ \varepsilon_{zz} &= -\tfrac{2\nu}{E}\sigma_{\|} \end{aligned} \tag{1.23}$$

from which

$$\frac{\varepsilon_{zz}}{\varepsilon_{xx}} = -\frac{2\nu}{1-\nu} = -\eta. \tag{1.24}$$

Effect of strain on the band structure

If a semiconductor is strained, the band structure is modified by two basic effects: the shift due to hydrostatic strain ΔE_h, and the change due to uniaxial or biaxial strain ΔE_s

$$\Delta E = \Delta E_h + \Delta E_s. \tag{1.25}$$

The effect of the hydrostatic strain, which is the strain resulting from the change in the volume of the material, results in the position of both the conduction and valence band edges to be moved in energy. Uniaxial strain, instead, will split the degeneracy of both the conduction and valence bands. For small strain, typically $\varepsilon < 0.01$ the shift of the band edges is linear with the strain, for a larger strain it becomes non-linear[46]. The overall effect is schematically illustrated in Figure 1.7.

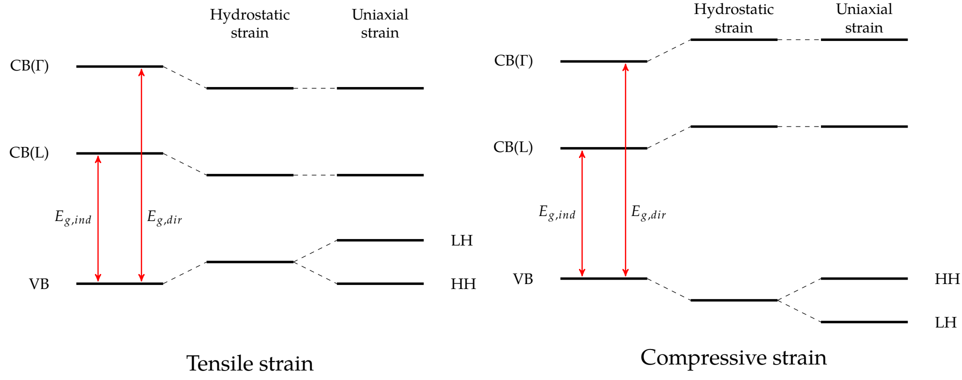

Figure 1.7 – A schematic diagram of the contributions of hydrostatic and uniaxial strain to a doubly degenerate band. Hydrostatic strain will shift the band edge to either higher or lower energy, while uniaxial strain will split the degeneracy of the bands.

The volume V of a small volume element of the deformed body is changed by the strain to

$$V + \Delta V = V \cdot (1 + \varepsilon_{xx}) \cdot (1 + \varepsilon_{yy}) \cdot (1 + \varepsilon_{zz}). \tag{1.26}$$

Thus, the fractional change in volume is

$$\frac{\Delta V}{V} \simeq \varepsilon_{xx} + \varepsilon_{yy} + \varepsilon_{zz} \tag{1.27}$$

which is the trace of the strain tensor ε_{ij}.

The relation between the change in volume and the modification in the band structure can be easily understood within the tight-binding framework, considering that bond-length alterations results in a variation of orbitals overlap [47].

In the deformation potential formalism [48], changes in the energy levels of semiconductors at the band edges, are evaluated within the first order perturbation theory. A perturbation Hamiltonian H_ε, linearly dependent on the strain tensor is assumed:

$$H_\varepsilon^{\alpha\beta} = \sum_{ij} D_{ij}^{\alpha\beta} \varepsilon_{ij}, \tag{1.28}$$

where $D_{ij}^{\alpha\beta}$ are the matrix element of the deformation potential operator D_{ij}. A detailed discussion on how the band edge energies are influenced by the strain tensor can be found in Refs. [42, 38] and the main results are here

reported.

Hydrostatic strain shifts the average position of band edges $E_{c,av}$ and $E_{v,av}$ according to the formula

$$\Delta E_{c,av} = a_c \frac{\Delta V}{V} = a_c Tr(\varepsilon), \tag{1.29a}$$

$$\Delta E_{v,av} = a_v \frac{\Delta V}{V} = a_v Tr(\varepsilon), \tag{1.29b}$$

where a_c and a_v is the hydrostatic deformation potential for the conduction and valence band, respectively. Therefore the bandgap is modified as

$$\Delta E_g = aTr(\varepsilon), \tag{1.30}$$

with $a = a_c - a_v$. It follows that, depending on the sign of the trace of the strain tensor ε_{ij}, the bandgap can be increased or reduced.
Uniaxial strain, instead, leads to a splitting of the valence band (above and beyond the splitting introduced by the spin-orbit coupling). These splittings can also be expressed in terms of deformations potentials.
For perpendicular strains along the [001] or [111] directions, the following expressions [49] describe the shift of the bands with respect to the average $E_{v,av}$

$$\Delta E_{SO} = -\frac{1}{6}\Delta + \frac{1}{4}\delta E - \frac{1}{2}[\Delta^2 + \Delta\delta E + \frac{9}{4}(\delta E)^2]^{1/2} \tag{1.31a}$$

$$\Delta E_{LH} = -\frac{1}{6}\Delta + \frac{1}{4}\delta E + \frac{1}{2}[\Delta^2 + \Delta\delta E + \frac{9}{4}(\delta E)^2]^{1/2} \tag{1.31b}$$

$$\Delta E_{HH} = \frac{1}{3}\Delta - \frac{1}{2}\delta E \tag{1.31c}$$

In these equations, δE is given by

$$\text{for [001] strain:} \quad \delta E_{001} = 2b(\varepsilon_\perp - \varepsilon_\parallel)$$

$$\text{for [111] strain:} \quad \delta E_{111} = 2\tfrac{\sqrt{3}}{3} d(\varepsilon_\perp - \varepsilon_\parallel),$$

where $\varepsilon_\parallel$ and $\varepsilon_\perp$ are the strain components parallel and perpendicular to the (001) lattice plane, respectively.
Eqs. 1.31 include the effects of uniaxial strain as well as spin-orbit coupling; in the absence of strain they reduce to the spin-orbit shifts Δ. The quantity b is the deformation potential for a strain of tetragonal symmetry; it is negative for Si and Ge. The quantity d is the deformation potential for a strain of trigonal symmetry; it is also negative.
Note that, for zero strain, the light hole band and the heavy hole band are degenerate and the two equations give the same result. Upon application of strain, the valence band degeneracy is broken and the light hole band and heavy hole band are split into separate energy levels.

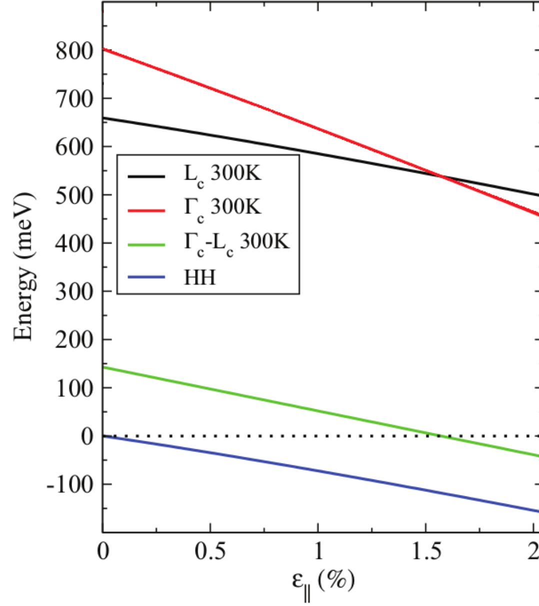

Figure 1.8 – Band-edge energies in Ge as a function of the in-plane biaxial strain $\varepsilon_{\parallel}$ calculated with the topmost LH valence band set as reference zero energy [12].

Effect of biaxial strain on the band structure of Ge

Since in this work we are specifically interested in strained Ge, we will focus on the effect of biaxial strain on the band structure of Ge.

In biaxially strained [001] Ge films [12], if we set the zero of the energy scale at the barycenter of heavy-hole, light-hole, and split-off (SO) valence bands, the Γ_c and L_c point conduction edges are located at [42]

$$E^{L_c,\Gamma_c} = \frac{1}{3}\Delta + E_g^{L,\Gamma} + \Delta E_h^{L,\Gamma}, \tag{1.32}$$

where E_g^L and E_g^Γ are, respectively, the fundamental indirect and direct gaps of unstrained bulk Ge, and Δ is the spin-orbit interaction parameter. The $\Delta E_h^{L,\Gamma}$ terms represent the modification of the Ge gaps due to the hydrostatic component of the strain field (since the uniaxial component of the strain tensor does not affect the L and Γ point conduction band edges) and are evaluated according to the expression

$$\Delta E_h^{L,\Gamma} = (a_c^{L,\Gamma} - a_v)(2\varepsilon_{\parallel} + \varepsilon_{\perp}). \tag{1.33}$$

In Eq. 1.33 $a_c^{L,\Gamma}$, and a_v are the deformation potentials for the L and Γ conduction edges and for the barycenter of the valence bands, respectively; their values are reported in Table 1.5. From Eq. 1.33 and the values reported in

Parameter	Value	Ref.
$a_c^\Gamma - a_v$	-10.06 eV	[47]
$a_c^L - a_v$	-2.78 eV	[42]

Table 1.5 – Deformation potentials for the L and Γ conduction edges.

Table 1.5 is evident that, since the conduction deformation potential for the Γ_c band is larger than the L-band one, applying biaxial *tensile* strain both direct and indirect gaps shrink, but the direct gap shrinks faster (Figure 1.8). If we assume the band edge of the LH valence energy as reference zero energy (dotted line, independent of $\varepsilon_{\|}$), starting from the unstrained value of $\Gamma_c - L_c$ = 134 meV (green curve in Fig. 1.8), the energy difference vanishes for $\varepsilon_{\|} \simeq 1.6\%$. This results in an indirect-to-direct band gap crossover with a corresponding gap energy of 540 meV at 300 K. The technological asset of the reduction of the $\Gamma_c - L_c$ energy barrier, is that, since the population of the Γ valley is facilitated, the radiative emission efficiency of the material is enhanced [12, 50], as we will see in the following. Moreover, tensile strain removes the HH-LH valence band degeneracy at the Γ point and lowers the HH band edge with respect to the LH band-edge energy. Therefore, while in relaxed Ge layers the large majority of holes populate the HH band because of its larger density of states, in tensile-strained Ge, holes thermalize into the LH band.

Up to now, we considered the case of Ge films biaxially tensile-strained in the (001) plane, but the effect of strain on the band structure depends on the direction of strain with respect to the crystal orientation. The effect of different biaxial and uniaxial tensile strain configurations on the electronic structure of Ge, obtained using density functional theory calculations, is reported in Fig. 1.9 [51]. Although the bandgap energy is reduced under tensile strain in any case, biaxial tensile strain parallel to the (001) and (110) plane, and uniaxial strain parallel to the [001] and [111] direction, can transform Ge in a direct bandgap material. Moreover, biaxial strain is more efficient in energy band transformation than uniaxial strain. In Ref. [50] the state-of-the-art of the strain approach toward the realization of a direct band gap group IV material, has been reviewed, selecting those approaches that are potentially compatible with CMOS fabrication and are suited for optical applications. In

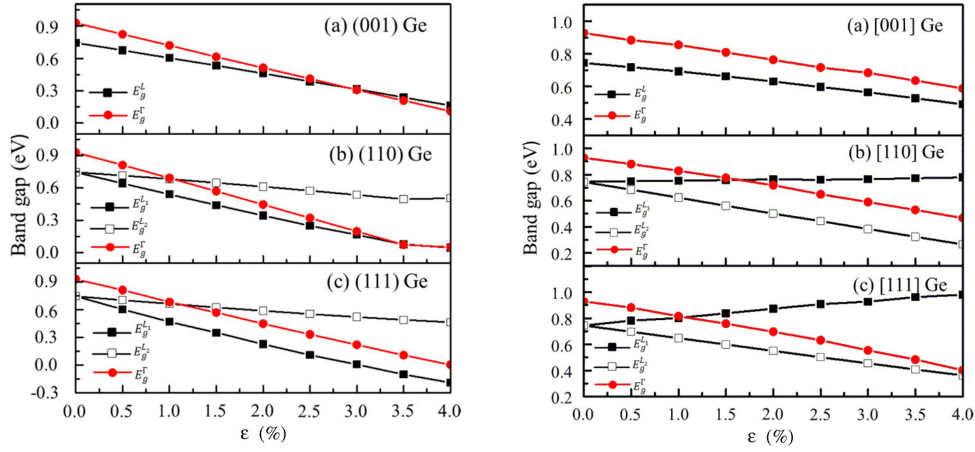

Figure 1.9 – *Left:* Changes in the bandgaps with biaxial tensile strains ε parallel to (a) the (001) plane, (b) the (110) plane, and (c) the (111) plane. *Right:* Changes in the bandgaps with uniaxial tensile strain ε parallel to (a) the [001] direction, (b) the [110] direction, and (c) the [111] direction. Figure taken from [51].

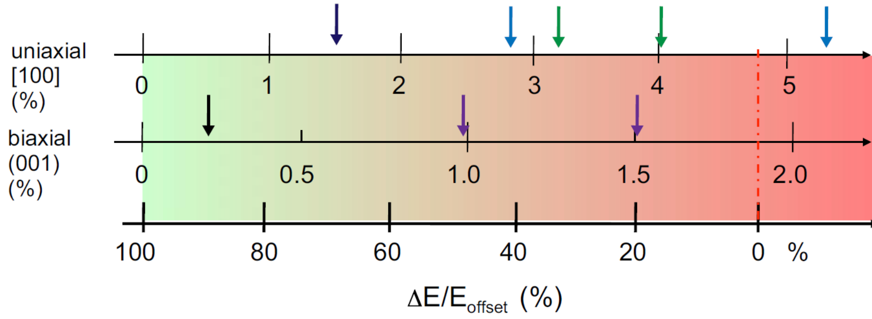

Figure 1.10 – Relative offset of the Γ and L conduction band minima realized in Ge by uniaxial tensile strain along [001] direction (dark blue: [52], light blue: [53]; [54], olive: [55]; [56]), and biaxial tensile strain on (001) oriented substrate (black: [13]; violet: [57]; [58]). The dash-dotted line marks the transition from an indirect to a direct band gap semiconductor. Figure taken from [50].

Fig. 1.10 are reported two strain loadings (uniaxial and biaxial) against the achieved relative band offset, $\Delta E/E_0$, where an offset ΔE of 100% is equal to $E_0 \sim 140$ meV for the case of unstrained Ge. An offset parameter of 0 meV (0%) corresponds, thus, to Γ and L valleys having their band edges at the same energy. Although in almost all the works reported in Fig. 1.10 Ge is still an indirect gap material, the strain-driven enhancement of the electron population in the Γ valley can lead to a significant increase of the radiative emission efficiency. For instance, when $\varepsilon_{\|}$ increases from zero to 0.25%, the carrier density in the Γ valley n^{Γ}, normalized to the total $n^{\Gamma} + n^{L}$ conduction

carrier density, is enhanced from 6×10^{-5} to 1.5×10^{-4}, leading to a boost of the PL intensity of one order of magnitude [12].

1.3 GENERAL PROPERTIES OF SIGE ALLOYS

Silicon and germanium are the only group-IV elements that are miscible in all proportions, i.e. they form a continuous series of solid substitutional solutions with gradually varying properties over the entire composition range [59]. The phase diagram of the $Si_{1-x}Ge_x$ system is reported in Fig. 1.11 and no phase changes or decomposition can be observed [60].

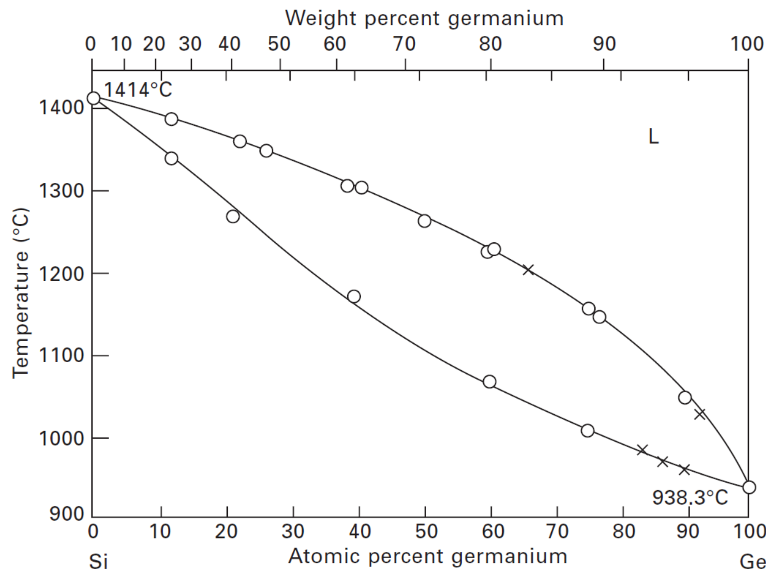

Figure 1.11 – Liquidus–solidus curve of the $Si_{1-x}Ge_x$ system. Figure taken from [60].

The relaxed lattice constant $a(x)$ of a $Si_{1-x}Ge_x$ alloy is given (in Å units) by [61] :

$$a(x) = a(Si) + 0.200326 \cdot x(1-x) + [a(Ge) - a(Si)] \cdot x, \qquad (1.34)$$

where a(Si) and a(Ge) are the bulk lattice constants of Si and Ge given in Table 1.1, and the factor 0.200326 is a quadratic correction, which is introduced in order to reproduce the experimental deviation from Vegard's law.

The band structure of the $Si_{1-x}Ge_x$ alloys has been profusely studied with many approaches and methods [62]-[61] which all report an indirect band gap for any Ge concentration x. The extension of the band gap in the Δ, L, and Γ

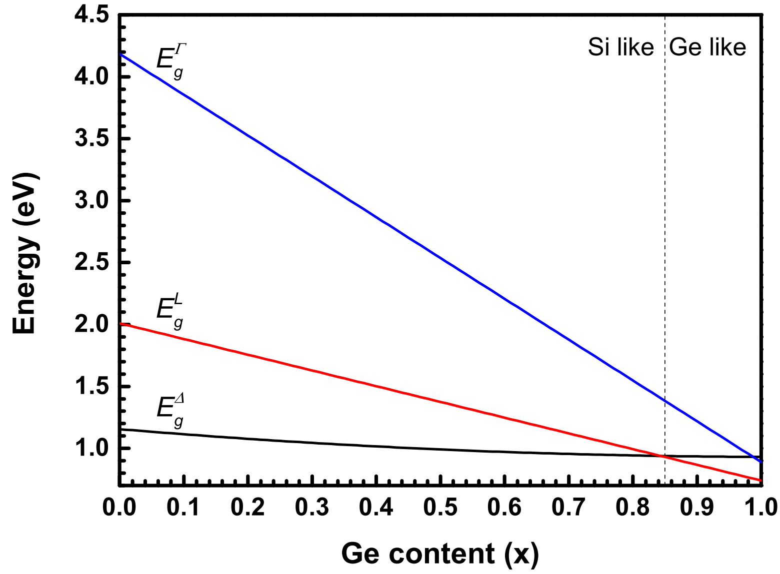

Figure 1.12 – $Si_{1-x}Ge_x$ band gap extension as a function of the Ge content x.

points is described by the following empiric relations, valid at a temperature of T = 4.2 K [63]:

$$E_g^\Delta(x) = 1.155 - 0.43 \cdot x + 0.206 \cdot x^2 \tag{1.35a}$$

$$E_g^L(x) = 2.01 - 1.27 \cdot x \tag{1.35b}$$

$$E_g^\Gamma(x) = 4.185 - 3.296 \cdot x. \tag{1.35c}$$

As we can see in Fig. 1.12, the indirect gap extension has a drastic change in its behavior around Ge concentrations of x=0.85. For lower concentrations the conduction band minimum is located at the Δ point, as happens in Si, and the alloy is therefore said to be *Si-like*. For higher concentrations, instead, the conduction band minimum is locate at L point and the alloy is *Ge-like*. The direct band gap energy, instead, presents a very steep linear dependence on the Ge content x. The detailed knowledge of the trend of the band gaps varying the Ge concentration, will be essential for the interpretation of the photoluminescence spectra reported in Chapter 4.

1.4 BAND ALIGNMENT IN SIGE HETEROSTRUCTURES

The band alignments between heterointerfaces are one of the most important parameters for both transport and optical device applications. In SiGe heterostructure, the band alignment is determined by the Ge concentrations y and x of the adjacent $Si_{1-y}Ge_y$ and $Si_{1-x}Ge_x$ layers. At the same time, the Ge concentrations define if the alloy is Ge-like or Si-like. How these properties

vary as a function of the Ge concentration of a $Si_{1-x}Ge_x$ epilayer grown on a $Si_{1-y}Ge_y$ substrate has been extensively studied in Ref. [64] for the whole composition range (0 ≤ x, y ≤ 1), whose results are reported in Fig. 1.13. In this calculation, based on the tight-binding method, it is assumed that the substrate is unstrained while the epilayer layer is strained.

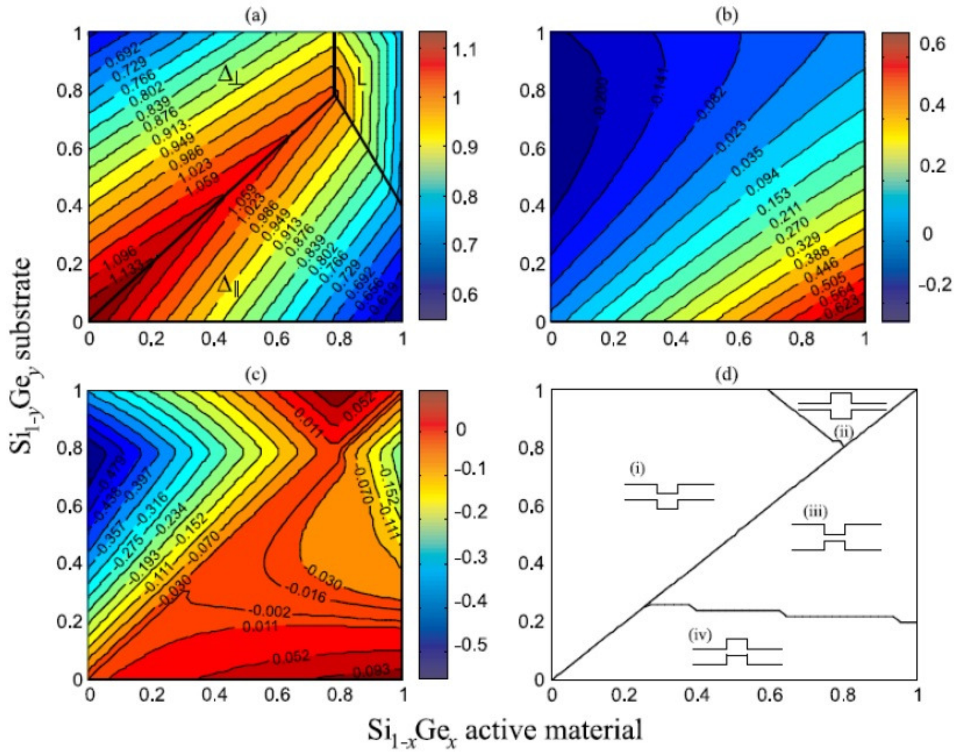

Figure 1.13 – Band alignment properties of $Si_{1-x}Ge_x/Si_{1-y}Ge_y$ heterostructures as a function of x and y. (a) band gap, band offset in (b) valence and (c) conduction band, and (d) resulting band profile [64]. Energies are in eV.

For application in working devices, it is highly desirable to have a confinement potential large enough to avoid a thermal promotion of electrons in the barrier region, thus ensuring high temperature operation. This implies the request of a conduction band offset ≥ 100 meV, which falls in the yellow-green region of the plot reported in Fig. 1.13(c). A proper QW system in SiGe alloys can be realized in two ways: the first one is employing QWs of pure Si ($x = 0$) grown on a $Si_{1-y}Ge_y$ substrate with $y > 0.1$, while the second one considers QWs of pure Ge ($x = 1$) grown on a $Si_{1-y}Ge_y$ substrate with high Ge concentration (i.e. $0.75 \leq y \leq 0.90$). The first approach is not the best option for opto-electronic devices because of the low optical transition rate between the conduction

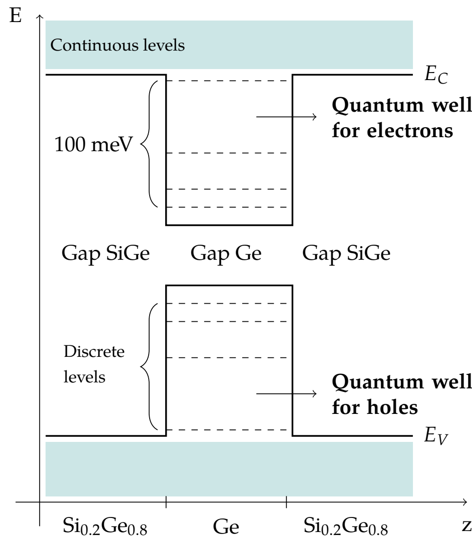

Figure 1.14 – Type I band alignment in a Ge/$Si_{0.2}Ge_{0.8}$ quantum well. E_c and E_v denote the conduction and valence band edge profile in the heterostructure along z.

and valence band in Si, as it will be discussed later. On the contrary, Ge QWs feature better performance and higher transition rate. Moreover, this kind of system results in a type-I band alignment for both the indirect [as can be seen in Fig. 1.13(d)] and the direct gap, which further increases the radiative emission probability, as we shall discuss in Chapter 2. The type I band alignment has been experimentally demonstrated in Ref. [16]. A sketch of the resulting heterostructure is depicted in Fig. 1.14, in which the bottom of the conduction band E_c and the top of the valence band E_v generate a band profile with a QW both in the conduction and valence band of Ge, confined by the larger energy gaps of the SiGe layers.

1.5 HETEROEPITAXY

In the previous sections we have investigated how the band structure of two semiconductors is affected when they are brought together to form an heterostructure. We have also seen the effect of strain on the electronic properties of a material. We will now discuss what happens when a semiconductor is deposited on another material, and how the deposition is strongly affected by the strain originating by the lattice mismatch between the two materials.

The deposition of a given material (*epilayer*) on a *substrate* is called *epitaxial* if the crystallographic orientation is conserved. If the epilayer and the substrate are of the same material the deposition is named *homoepitaxy*, on the opposite,

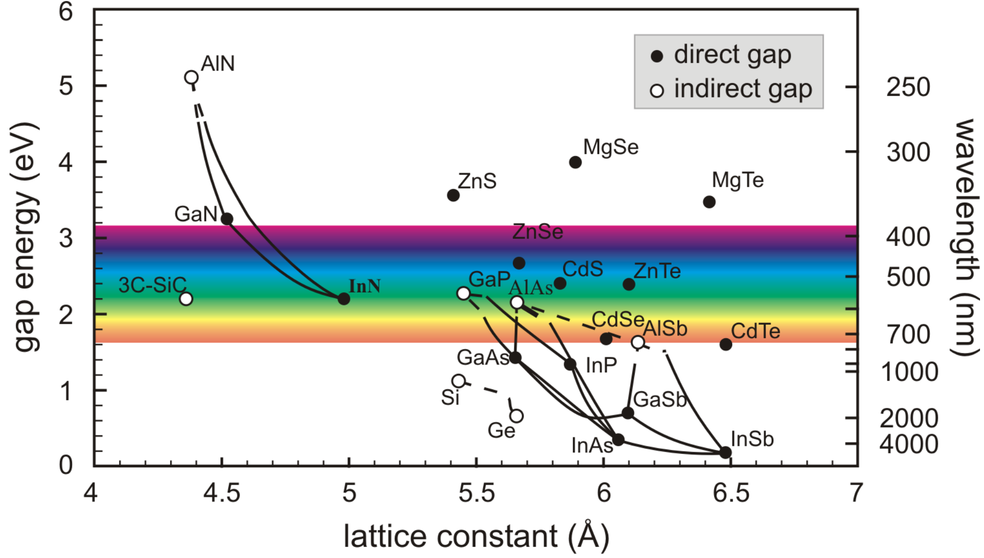

Figure 1.15 – Bandgaps of the most important elemental and binary cubic semiconductors versus their lattice constant at 300°K. The right-hand scale gives the light wavelength λ, corresponding to the band gap energy. Figure taken from [65].

if the deposition of the epilayer take place on a different material, we talk about *heteroepitaxy*.

1.5.1 *Lattice mismatch and elastic energy: relaxed and coherent growth*

In heteroepitaxy, since the lattice constant of the epilayer is different from that of the substrate, strain, originating from the lattice mismatch, can be present. The lattice mismatch strain can be defined as

$$f = \frac{a_s - a_e}{a_e}, \tag{1.36}$$

where a_s is the bulk lattice constant of the substrate and a_e is the bulk lattice constant of the epitaxial layer. We observe that the mismatch may take on either sign, leading to tensile ($f > 0$) and compressive ($f < 0$) strained systems.

In heteroepitaxial systems with low mismatch ($|f| < 1\%$), the initial growth will be strained to match the atomic spacings of the substrate. In this case, the growth is called *pseudomorphic* (or coherent). For a coherent growth, the epilayer is biaxially strained in the plane of the substrate by an amount $\varepsilon_{\|}$, and uniaxially strained in the perpendicular direction by an amount $\varepsilon_{\perp}$. When the

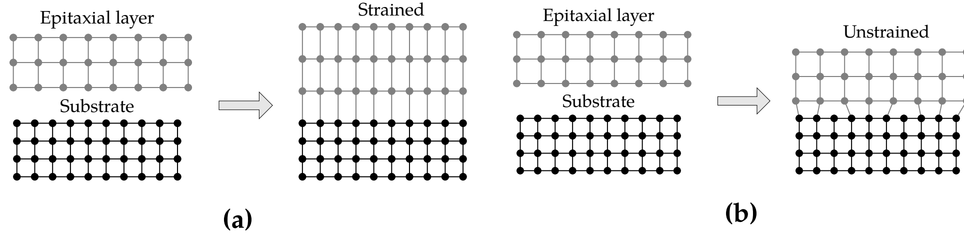

Figure 1.16 – Schematic illustration of (a) strained and (b) relaxed hetero-epitaxial structures.

substrate is thick the in-plane strain is determined from the lattice constant a_s of the substrate and that of the epitaxial layer a_e. Thus

$$\varepsilon_{\parallel} = \frac{a_s - a_e}{a_e} = f. \tag{1.37}$$

Since the pseudomorphic epitaxial layer is free to expand in the perpendicular direction, although no stress is applied along this direction, the result is a *tetragonal distortion* of the lattice. In this case, the perpendicular strain is simply related to $\varepsilon_{\parallel}$ and the Poisson ratio ν as

$$\varepsilon_{\perp} = -\eta \cdot \varepsilon_{\parallel} = -\frac{2\nu}{1-\nu}\varepsilon_{\parallel}. \tag{1.38}$$

Thus, for strained layers of FCC crystals, as Si and Ge, grown along the [001] direction, recalling the results of section 1.2.3, we obtain

$$\nu = \frac{C_{12}}{C_{11} + C_{12}}, \qquad \varepsilon_{xx} = \varepsilon_{yy} = \varepsilon_{\parallel}, \qquad \varepsilon_{zz} = -\frac{2C_{12}}{C_{11}}\varepsilon_{\parallel} \tag{1.39}$$

$$\varepsilon_{xy} = \varepsilon_{yz} = \varepsilon_{zx} = 0.$$

The elastic energy U_{strain} is given by the work of deformation for volume unity and is given by the relation:

$$U_{strain} = \frac{1}{2}(\sigma_{xx}\varepsilon_{xx} + \sigma_{yy}\varepsilon_{yy} + \sigma_{zz}\varepsilon_{zz} + \sigma_{yz}\varepsilon_{yz} + \sigma_{zx}\varepsilon_{zx} + \sigma_{xy}\varepsilon_{xy}) \tag{1.40}$$

Recalling 1.15 and 1.16, is possible to write 1.40 as a function of the elastic constants C_{ij}:

$$U_{strain} = [C_{11} + C_{12} - 2\frac{C_{12}^2}{C_{11}}]\varepsilon_{\parallel}^2, \tag{1.41}$$

which, integrated, gives the density of elastic energy stored for area unity (E_{strain}):

$$E_{strain} = [C_{11} + C_{12} - 2\frac{C_{12}^2}{C_{11}}]\varepsilon_{\parallel}^2 h = A\varepsilon_{\parallel}^2 h, \tag{1.42}$$

where A is the biaxial modulus and h is the thickness of the epilayer. It is possible to rewrite 1.42 as:

$$E_{strain} = 2G\frac{1+\nu}{1-\nu}\varepsilon_{\parallel}^2 h, \tag{1.43}$$

where G is the shear modulus. For an isotropic material, the shear modulus and the Poisson ratio are related to the elastic constants C_{11} and C_{12} by the relations:

$$G = (\frac{C_{11} - C_{12}}{2}) \qquad \nu = (\frac{C_{12}}{C_{11} + C_{12}}). \tag{1.44}$$

In 1.42 it is important to underline how the stored energy increases with the thickness of the deposited epilayer. At a certain layer thickness, called *critical thickness*, it is energetically more favorable to break the perfect order of the crystal lattice and to reduce the accumulated strain energy. At small film thicknesses, some of the strain stored in the epilayer, can be partially accommodated by surface reconstruction [66]. As the strain energy accumulated in the film increases with the film thickness, a higher degree of strain relaxation must be sought. This relaxation can be of two types: elastic relaxation or plastic relaxation. In the first case, the film develops a corrugated surface morphology to partially relieve the strain, though still keeping coherence with the substrate, while extended defects are introduced in the lattice in the case of plastic relaxation.

Elastic relaxation

The interface energy and the lattice mismatch between the epilayer and the substrate have a strong influence on the epitaxial growth modes. As a matter of fact, the stored energy in the epilayer, caused by the stress at the interface, can relax elastically by deformations on lattice planes which evolve in three-dimensional structures called *islands*. The mechanism lowers the elastic energy at the expense of the epilayer surface energy whose increase follows the increase of area.

At thermodynamic equilibrium the Bauer classification[67] identifies three different growth mechanisms if lattice mismatch is present, starting from the surface free energy of the substrate γ_s and of the epilayer γ_e. The deposition of the epilayer can thus occur in three different regimes basing on the value of the mismatch f and of the adhesion coefficient $\xi = (\gamma_s - \gamma_e)/\gamma_s$, which are:

- $\xi > 0$, small f;
  The growth process is called *Frank-Van der Merwe* [68] and it is a layer-by-layer 2D defect-free deposition.

- $\xi < 0$;
  The growth process is called *Volmer-Weber* [69] and it is characterized by

the nucleation of three-dimensional islands in the epilayer.

- $\xi > 0$, high f;
  The growth process is called *Stranski-Krastanov* [70] and the deposition starts with a layer-by-layer regime on top of which the islands growth is estabilished.

Figure 1.17 shows the schematic diagram of three possible growth modes.

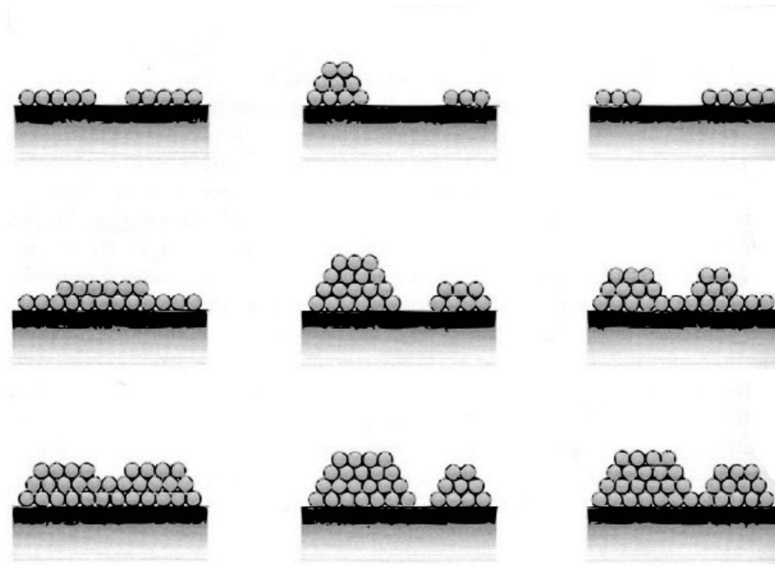

Figure 1.17 – Schematic diagram of the three possible growth modes (from left to right): Frank–van der Merwe, Volmer–Weber and Stranski–Krastanov.

On the other hand, heteroepitaxial growth may occur far from equilibrium, i.e., when the growth is too fast and adatoms have no time to find the thermodynamically most favorable places for incorporation. In such a case, kinetic factors provide an opportunity to tailor the growth mode and morphology in a way to obtain layer-by-layer growth. The most important factors influencing the growth mode and morphology are the surface diffusivity and the growth rate [35]. In the following we will see how the heteroepitaxial deposition of Ge directly on Si is challenging. As a matter of fact, the existence of the large lattice mismatch between Ge and Si, combined with the difference in surface energies, results in a growth process where Ge coalesces in three dimensional islands according to the Stranski–Krastanov mechanism, if growth conditions close to thermodynamic equilibrium are maintained. We will also see how is possible to obtain a layer-by-layer growth by means of a multi temperature

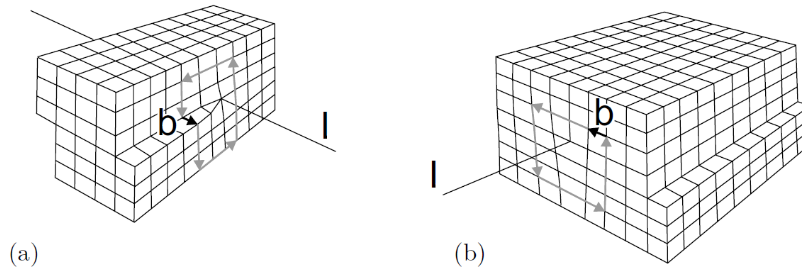

Figure 1.18 – Model of a screw (a) and an edge (b) dislocation. The Burgers vector ***b*** and the dislocation line ***l*** are indicated. Image taken from [46].

technique, where the initial Ge "*seed*" layer is deposited at low temperature to avoid the nucleation of three dimensional islands, attaining a gradual plastic relaxation.

Plastic relaxation

In the case of *relaxed* (or incoherent) growth, the film grows with his own lattice parameter and *misfit dislocation* (absences of rows of atoms at the interface) are generated to relieve some of the mismatch strain. Above the interface the film returns to its original lattice structure.

The type of growth that is effectively realized is that to which it is associated a lower energy of the film. To determine if the growth is relaxed or coherent, we should compare the elastic strain energy that accumulates in a film with the energy necessary for the formation of dislocations. The mechanism of *strain release* is strictly related to the different geometries of dislocations.

Dislocations can be divided in two main types: *screw* and *edge* dislocations (Fig. 1.18). A screw dislocation can be created in a regular crystal lattice by the application of a shear stress that induce the atoms on either side of the shear plane to be displaced by one atomic spacing. An edge dislocation, instead, involves the inclusion of an extra half-plane of atoms in an otherwise perfect crystal. The geometry of a crystal dislocation is specified by its *dislocation line* and its *Burgers vector*. The dislocation line ***l*** runs along the *core* of the dislocation, where the distortion with respect to the perfect lattice is greatest. The *Burgers vector* ***b***, which describes the deformation around the dislocation line, may be determined considering a Burgers circuit. A Burgers circuit is an atom-to-atom path that forms a closed loop in the perfect crystal [see

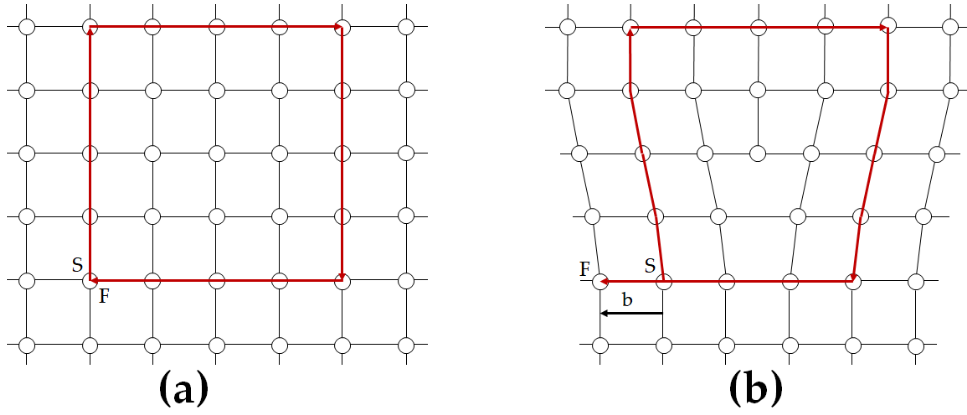

Figure 1.19 – (a) Burgers circuit SF in a perfect crystal. (b) Burgers circuit SF in the presence of the dislocation.

Fig. 1.19(a)]. The failure of the Burgers circuit to close upon itself in the dislocated crystal shows the presence of the dislocation, and the closure failure is the Burgers vector [see Fig. 1.19(b)]. In the case of edge dislocations, the Burgers vector is always perpendicular to the line vector. Therefore, edge dislocations are sometimes referred to as *90° dislocations* [35]. For a screw dislocation, the line vector and Burgers vector are parallel, resulting in the terminology *0° dislocations*. Although pure edge and screw dislocations are encountered in real crystals, dislocations of mixed character are far more common. For example, *60° dislocations* are often observed in diamond and zincblende crystals.

In the case of a cubic lattice, as in Ge, Si, and SiGe alloys, the minimum energy necessary for the formation of a dislocation corresponds to the introduction of 60° dislocations [71]

$$E_D \sim \left(\frac{Gb^2}{8\pi\sqrt{2}a}\right) ln\left(\frac{h}{b}\right), \tag{1.45}$$

where a is the bulk lattice constant of the film, h its thickness, b the length of the Burgers vector, and G the shear modulus as given in 1.44. From the comparison between 1.43 and 1.45, imposing $h = h_c$, we can evaluate, at thermodynamic equilibrium, the critical thickness for a given substrate-epistrate [72]:

$$h_c \sim \left(\frac{1-\nu}{1+\nu}\right)\left(\frac{1}{16\pi\sqrt{2}}\right)\left(\frac{b^2}{a}\right)\left[\left(\frac{1}{f^2}\right) ln\left(\frac{h_c}{b}\right)\right]. \tag{1.46}$$

The behavior of the critical thickness in different $Si_{1-y}Ge_y/Si_{1-x}Ge_x$ heterostructures as a function of the Ge content x is reported in Fig. 1.20. We underline that, for Ge concentrations above 80%, the critical thickness is

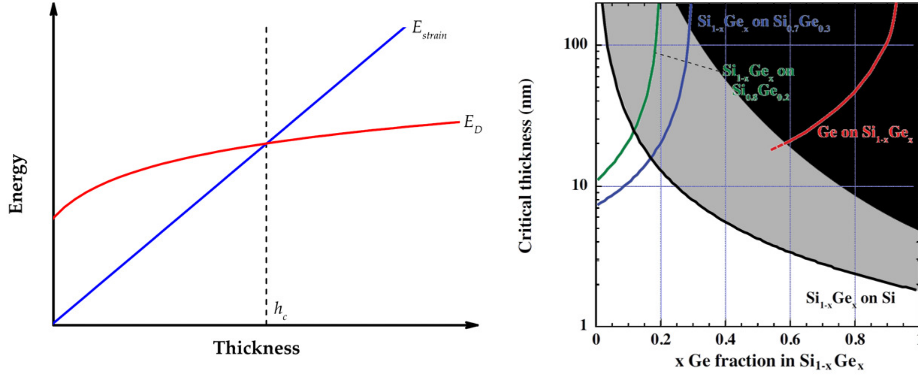

Figure 1.20 – *Left*: Elastic strain energy (E_{strain}) and formation of a dislocation (E_D) as a function of the thickness of the deposited film. For $h < h_c$ the growth will be coherent, for $h > hc$ will be relaxed. *Right*: Critical thickness behavior in different $Si_{1-y}Ge_y/Si_{1-x}Ge_x$ heterostructures as a function of the Ge content x [73]. White, gray, and black regions indicate a stable, metastable, and relaxed with dislocations growth regimes.

limited to a few nanometers. Such low values of critical thickness limit too much the realization of heterostructures suitable for applications, but some countermeasures can be taken. The realization of a system with many layers can be achieved employing the *strain-compensated* structures depicted in Fig. 1.21, in which the stress contributions in each layer compensate with each other and the total elastic stress vanishes. As a matter of fact, interchanging layers with opposite deformation should theoretically results in a null mean strain along the structure, or at least can drastically limit the dislocation generation. The strain-compensated stack of repeated Ge layers with thickness t(Ge) and $Si_{1-x}Ge_x$ layers with thickness t(SiGe), can be treated as a single layer with equivalent concentration x_{eq} given by

$$x_{eq} = \frac{x \cdot t(\text{Ge}) + (1-x) \cdot t(\text{SiGe})}{t(\text{Ge}) + t(\text{SiGe})}. \tag{1.47}$$

It follows that the growth of the strain-compensated stack on top of a $Si_{1-x_{eq}}Ge_{x_{eq}}$ layer will be pseudomorphic.

The presence of dislocations could have serious impact on the entire structure, since they are able to propagate through several layers with detrimental effects on the physical properties of the sample. As a matter of fact, for every misfit dislocation there will always be two *threading dislocations* at the ends of the misfit which must thread to a surface (see right of Fig. 1.21) or form a loop so that the two ends of the dislocation can join. These threads are at 60 degree

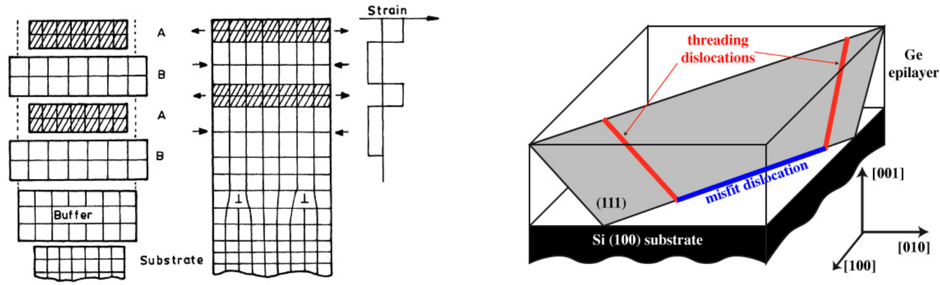

Figure 1.21 – *Left:* Example of a strain-compensated structure. *Right:* Misfit dislocations in Ge extend mostly along the <110> crystallographic directions. Misfit dislocations form segments that are connected to the surface through threading dislocations along (111) lattice planes.

since they glide on the (111) lattice plane. When threading dislocations reach the surface of the epilayer give raise to a crosshatch pattern increasing the surface roughness of the structure. Moreover, dislocations have been found to act as non-radiative recombination centers [74, 75]. Therefore, it is of paramount importance to reduce the defect density of Ge-rich $Si_{1-x}Ge_x$ layers grown on Si substrates. This can be done with the employment of a *virtual substrate* (VS), where a large amount of lattice defects is confined in lower layers. Due to their importance, we shall dedicate a section on the properties of virtual substrates.

1.6 CRYSTAL GROWTH

1.6.1 *Thermodynamics of crystal growth*

Epitaxial crystal growth is a dynamical phase transition, where a stable phase, the epilayer, grows out from a metastable vapor phase [76, 77]. The driving force for the growth is the chemical potential difference of the stable and the metastable phases. The chemical potential of a given phase is the work that has to be done to change the number of particles (atoms or molecules) in the phase by unity. If the chemical potentials of the vapor phase μ_V and growing crystal μ_C are equal, the phases are in equilibrium and no phase transition occurs. The difference

$$\Delta\mu = \mu_V(P,T) - \mu_C(P,T) \tag{1.48}$$

is called *supersaturation*. The condition to be satisfied in order to have crystal growth is $\Delta\mu>0$.

Equation 1.48 can be expressed in terms of the partial pressure P_0 of the nucleating species and the equilibrium vapor pressure P as

$$\Delta\mu = k_B T ln \frac{P_0}{P}. \tag{1.49}$$

Since atomic bonds are partially broken at the surface, creation of a new surface costs energy. The minimum work required to create a unit surface area under a constant volume and temperature is called the surface free energy γ. The change of the Gibbs free energy of the system due to formation of spherical growth nuclei of radius R is given by:

$$\Delta G = -\frac{4\pi R^3}{3}\Delta\mu + 4\pi R^2 \gamma. \tag{1.50}$$

The first term on the right-hand side of Eq. 1.50 is the energy gained when atoms from the vapor phase join the crystal and the second term is the surface free energy of the nuclei. With increasing the nuclei size, ΔG first increases, due to the dominant surface energy term, but then reaches a maximum and finally decreases. The existence of a maximum change in the free energy results in a critical size of the nuclei

$$R^* = \frac{2\gamma}{\Delta\mu}. \tag{1.51}$$

Nuclei smaller than R^* are unstable and decay with a high probability, while those larger than R^* may decrease their free energy by getting more atoms from the ambient phase and therefore should keep growing. The change in free energy evaluated at the critical nucleus size is the height of the energy barrier which should be overcome for the formation of clusters

$$\Delta G^* = \frac{4\pi}{3} R^{*2}\gamma = \frac{16\pi\gamma^3}{3\Delta\mu^2}. \tag{1.52}$$

It follows from Eq. 1.52 that the nucleation barrier decreases rapidly with increasing supersaturation $\Delta\mu$, which in turn is related to reactant partial pressure and temperature, two important growth parameters.
The above considerations are purely macroscopic in the sense that macroscopic thermodynamic quantities have been used for description of the equilibrium between different phases. Moreover, the elementary processes of attachment and detachment of individual building units (atoms or molecules) to and from the growing particles of the new phase have not been taken into account.

1.6.2 *Atomistic model*

In developing an atomistic model for nucleation, it is assumed that atoms arrive at a flat surface with an impingement rate F (atoms per unit area per unit time) connected to the vapour pressure p by

$$F = p\sqrt{\frac{N_A}{2\pi M k_B T}} \tag{1.53}$$

In equation 1.53 N_A is Avogadro's number and M is the molecular weight. The incident flux of atom gives rise to a concentration of adsorbed atom, called *adatoms*, on the surface. The equilibrium concentration of surface adatoms n at temperature T is given by

$$n = n_0 exp\left(-\frac{W_s}{k_B T}\right), \tag{1.54}$$

where n_0 is the total number of surface sites per unit area, and W_s is the binding energy of the atom. Generally, not every particle that strikes the surface will be adsorbed. Introducing the *sticking coefficient* s, the adsorption flux J_a is defined as

$$J_a = sF, \tag{1.55}$$

where F is the incoming flux of atoms. The sticking coefficient is a material-specific property. It depends both on the chemical nature of the adsorbing species and on the local chemistry and structure of the surface. It is also affected by a number of other factors including the surface temperature, the kinetic energy of the impinging particles, and the adsorbant surface coverage [76]. In certain cases, such as chemical vapor deposition, adsorption is accompanied by chemical reactions, which are thermally activated processes characterized by an activation barrier.

The main elementary processes involved in the formation and growth of thin films are illustrated schematically in Fig. 1.24. Atoms arrive from the gaseous phase and become accommodated at the surface adatoms. This creates a population of single adatoms n on the substrate with n_0 sites per unit area. Adatoms migrate over the surface with the diffusion coefficient D until they are lost by one of the following processes. First, they might be desorbed, if the substrate temperature is high enough. Second, adatoms might become captured by existing clusters or at defect sites such as steps. Third, adatoms might combine with another to form a cluster. Each of these

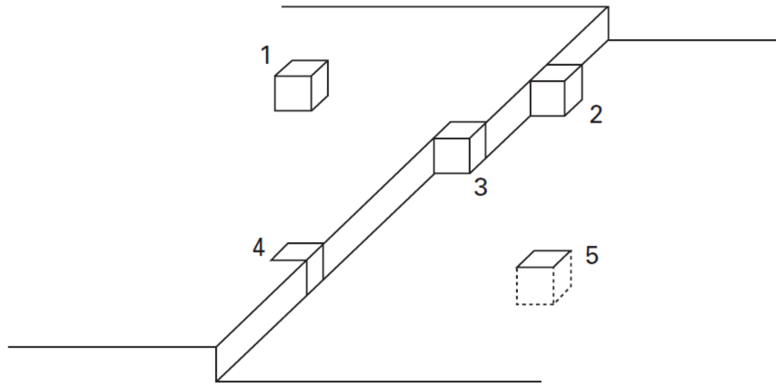

Figure 1.22 – Different types of adsorption positions on the surface: (1) on a terrace; (2) at the step edge; (3) in the kink; (4) in the step edge; (5) in the surface layer. Figure taken from [76].

thermally activated processes will be governed by characteristic times, which themselves will depend on the single-atom concentration and/or coverage and are controlled by activation energies and frequency factors. The time variation of the adatom concentration $n(x, y, t)$ satisfies the continuity equation

$$\frac{\partial n}{\partial t} = D\nabla^2 n + F - \frac{n}{\tau_d} = 0, \tag{1.56}$$

which accounts for the changes of the adatom population due to the surface diffusion, adsorption and desorption. In equation 1.56 we assumed for simplicity that the sticking coefficient s is unity.

Adsorption sites

There are different types of adsorption sites corresponding to different local structures of the surface. On the atomic scale the structure of a crystalline surface may be described in terms of low-index terraces, steps, and kinks. Accordingly, one may distinguish adsorption sites (1) on the terrace, (2) at the step edge, (3) in the kink, and some other positions with a higher coordination, e.g. (4) in the step edge and (5) in the surface layer. These positions are shown schematically in Fig. 1.22.

Among all the different adsorption sites the kinks play a very special role in crystal growth. Attachment of an atom to the kink site or its removal from the kink does not change the number of broken bonds at the surface and, hence, does not change the free surface energy of the crystal. Therefore the kink

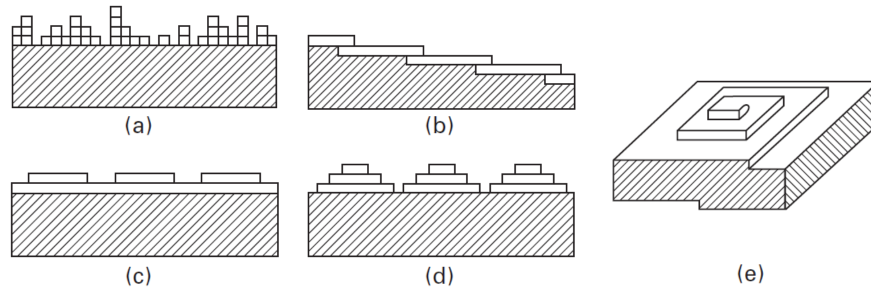

Figure 1.23 – Modes of epitaxial growth: (a) normal growth; (b) step-flow growth; (c) layer-by-layer growth; (d) multilayer growth; (e) spiral growth. Figure taken from [76].

density is one of the major factors that determine the growth kinetics. If the density of kinks is very high they could be found at almost any place on the surface. In this case, the adsorbing particles may directly attach to the kink sites, giving rise to the normal mechanism of growth [Fig. 1.23(a)]. On the contrary, if the surface is atomically smooth, the majority of the adsorption sites are terrace sites and the kinks could be found only at the step edges. In this case, the crystal grows by lateral motion of the steps. Depending on the origin of steps on the surface, one can distinguish four different modes of growth, namely step-flow growth, layer-by-layer growth, multilayer or three-dimensional (3D) island growth, and spiral growth. These growth modes are shown schematically in Fig. 1.23(b–e).

The layer-by-layer growth, desired for high-quality flat crystalline films, starts with the nucleation of 2D islands on the surface. The islands then grow laterally until they coalesce and cover the whole surface. When a layer is completed, the next layer starts to grow and the whole cycle repeats again [Fig. 1.23(c)]. In certain cases the cyclicity of the layer-by-layer growth breaks up and the growth in the upper layers starts before the lower layers are finished. When this happens due to kinetic constraints, the layer-by-layer growth is replaced by multilayer growth, which appears as the growth of characteristic 3D mounds on the surface [Fig. 1.23(d)]. As it has been already mentioned in Sec. 1.5.1, thermodynamic constraints may make the growth of 3D islands energetically preferable, leading to either Volmer–Weber or Stranski–Krastanov growth. Finally, the spiral growth is observed on surfaces with screw dislocations.

1.6.3 *Heterostructures growth techniques*

The two main techniques that allow to obtain abrupt interfaces on the atomic scale, as required in structures made of different layers of few nanometers, are Molecular Beam Epitaxy (MBE) and Chemical Vapor Deposition (CVD). The MBE technique consists in generating a particle beam by heating the solid rough material beyond its melting point, allowing the emitted particles to reach and adhere to the substrate surface while cooling down on the way. The resulting samples grown with this technique are of high quality, although their realization requires a large amount of time. Even if the first epitaxy of $Si_{1-x}Ge_x$ layers was achieved using MBE [78] there is an huge dominance of CVD in production and industrial environments.

The CVD technique consists in a different approach, allowing the deposition starting from a molecular precursor in gaseous form. If the substrate is heated enough, the impinging molecules can be broken by the pyrolysis process (thermal decomposition), allowing the heavy components to remain deposited on the substrate surface while the light components in gaseous form can be pumped away.

The fundamental sequential steps that occur in every CVD process are sketched in Fig. 1.24 and include [79]:

1. Convective and diffusive transport of reactants from the gas inlets to the reaction zone

2. Chemical reactions in the gas phase to produce new reactive species and by-products

3. Transport of the initial reactants and their products to the substrate surface

4. Adsorption (chemical and physical) and diffusion of these species on the substrate surface

5. Heterogeneous reactions catalyzed by the surface leading to film formation

6. Desorption of the volatile by-products of surface reactions

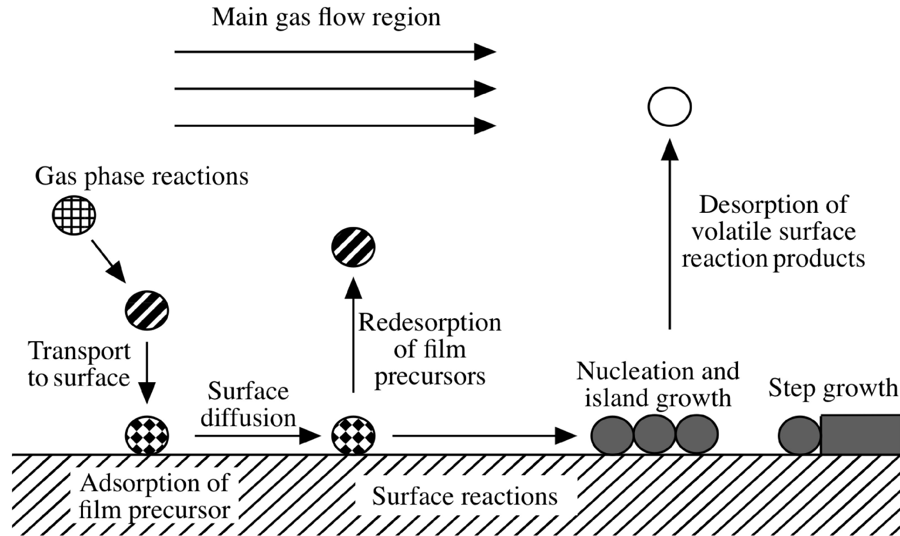

Figure 1.24 – Sequence of gas transport and reaction processes contributing to CVD film growth.

7. Convective and diffusive transport of the reaction by-products away from the reaction zone

The slowest of these steps will determine the growth rate. Typically, the rate limiter is either step 4 or step 5, and these two situations are called *mass transfer limited* and *reaction rate limited*, respectively [35].

Consider the transport of a single reactant to the growing surface. The flux Φ_{gs} of this species to the surface at a particular point is given by

$$\Phi_{gs} = h(N_g - N_0) \tag{1.57}$$

where N_g is the concentration of the reactant in the gas phase, N_0 is the concentration of the reactant at the surface, and h is the gas phase mass transfer coefficient.
The flux Φ_{sf} of the reactant from the surface to the growing film (incorporation) is

$$\Phi_{sf} = kN_0 \tag{1.58}$$

where k is the surface reaction rate constant. Usually, this rate is thermally activated so that

$$k = k_0 exp(-E_a/k_B T) \tag{1.59}$$

where E_a is the activation energy for the process.

Under steady-state conditions, the two fluxes above may be equated $\Phi_{gs}=\Phi_{sf}=\Phi$. Combining these equations, we can determine the growth rate as

$$r = \frac{\Phi}{n} = \frac{N_g}{n}\left(\frac{hk}{h+k}\right) \tag{1.60}$$

where n is the number of atoms per unit volume in the growing crystal (for Si $n = 5\times10^{22}$ cm^{-3}).
At high temperatures $h \ll k$, and

$$r \approx \frac{hN_g}{n}. \tag{1.61}$$

This situation is known as *mass transfer limited* growth (or diffusion-limited growth), and the growth rate is nearly independent of temperature.
At low temperatures $k \ll h$, and

$$r \approx \frac{kN_g}{n}. \tag{1.62}$$

This is referred to as *reaction rate limited* growth. Under these conditions, the growth rate is a strong function of temperature.

The growth rate as a function of temperature for different gaseous precursors of Si is reported in Fig. 1.25.

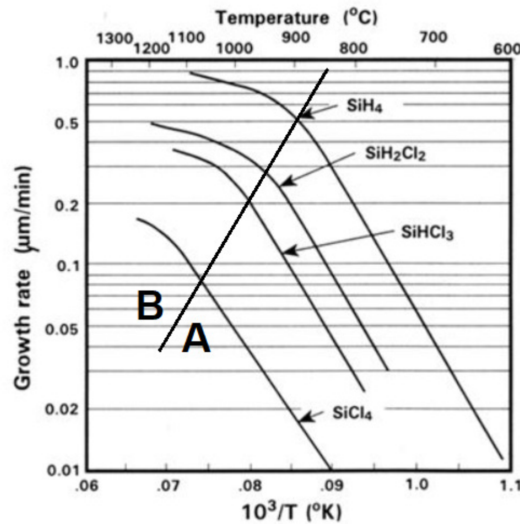

Figure 1.25 – Growth rate as a function of temperature for differents gas precursors of Si. In the region B the deposition is mass transfer limited, while in region A is reaction rate limited

Epitaxial silicon is normally grown in the mass transfer limited regime, at a temperature near the knees of the curves in Fig. 1.25. This temperature region

is selected to be high enough to thermally decompose the selected chemical at a rate commensurate with the surface diffusion rate.

In the SiGe heterostructures deposited in this work, the gaseous precursors that have been used are silane (SiH_4) and germane (GeH_4). The pyrolysis process of these molecules, although including several intermediate stages, can be summarized as follows:

$$SiH_4(g) \; + \; GeH_4(g) \rightarrow Si(s) \; + \; Ge(s) + \; 4H_2(g) \tag{1.63}$$

where (g) and (s) refer to the gaseous and solid phases. This reaction takes place on the substrate surface where reactive sites (e.g. dangling bonds) are present, with a threshold temperature $\simeq$ 500°C for silane and $\simeq$ 300°C for germane.

All the samples investigated in the present work have been grown by CVD. A detailed description of the deposition set-up will be given in Chapter 3 and the growth process will be detailed in Chapter 4.

2

INTER-BAND TRANSITIONS IN QUANTUM WELLS

In this chapter, we introduce the main properties of electronic states in a quantum well. A detailed description goes beyond the purpose of this work and can be easily found in many textbook (we follow the notation used in [36]). This theoretical background will serve as a basis for the calculation of the optical properties we shall characterize by photoluminescence.

2.1 QUANTUM WELLS PROPERTIES

After discussing the possible band alignment of the heterostructures of interest, we now consider the general case of a single quantum well in the conduction band. In order to determine the energies and wavefunctions of the states confined within a QW characterized by a conduction band edge profile $V_0(z)$ like the one depicted in Fig. 2.1, the effective mass approximation and the envelope function approach can be used. This framework is a useful approximation when the potential is slowly varying with respect to the scale of the lattice constant. In the effective mass approximation, it is possible to write the electron wavefunction in the well as [36]:

$$\varphi(\boldsymbol{r}) \simeq \sum_{k \simeq k_0} c_n(k) e^{i\boldsymbol{k}\cdot\boldsymbol{r}} u_{c,k_0}(\boldsymbol{r}) = u_{c,k_0}(\boldsymbol{r})\psi(\boldsymbol{r}), \tag{2.1}$$

where $\boldsymbol{k}_0$ is the crystalline wavevector at the minimum of the conduction band. $\psi(\boldsymbol{r})$ is called *envelope function* and $u_{c,k_0}(\boldsymbol{r})$ is a periodic function of the same form of the Bloch waves. The role of the envelope function is to modulate the Bloch function to give the full wave function $\varphi(\boldsymbol{r})$.
The resolution of the Schrödinger equation depends on the shape of $V_0(z)$.

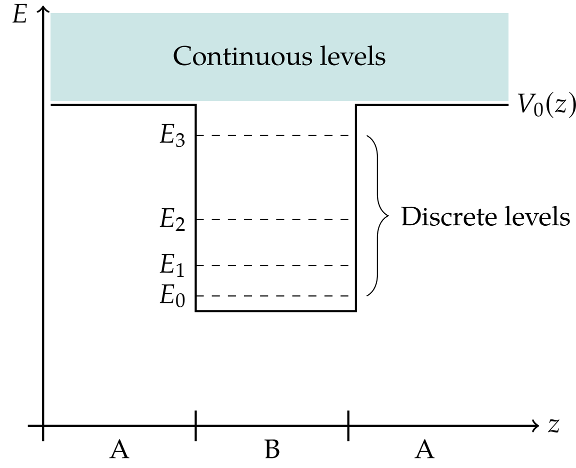

Figure 2.1 – Single QW in material B confined by barriers of material A. The conduction band edge alignment E_c acts as the confining potential $V_0(z)$.

2.1.1 *Infinite potential well*

Let's start considering the infinitely deep quantum well, delimited by two infinite potential barriers at $z = 0$ and $z = d_w$. If null potential is assumed inside the well, the Schrödinger equation to be solved is of this simple form:

$$-\frac{\hbar^2}{2m^*}\frac{d^2}{dz^2}\psi(z) = E\psi(z) \quad \Rightarrow \quad \frac{d^2}{dz^2}\psi(z) = -\frac{2m^*E}{\hbar^2}\psi(z) = -k^2\psi(z) \tag{2.2}$$

and the solutions are plane waves:

$$\psi(z) = Ae^{ikz} + Be^{-ikz}. \tag{2.3}$$

Outside the well, the wavefunctions are zero, because of the infinite potential, thus the solutions $\psi(z)$ inside the well have to satisfy these boundary conditions at $z = 0$ and $z = d_w$. Applying the first one allows to reduce the number of unknown coefficients:

$$\psi(0) = 0 \quad \Rightarrow \quad A + B = 0 \quad \Rightarrow \quad B = -A$$

The eigenfunctions inside the well are then:

$$\psi(z) = A(e^{ikz} - e^{-ikz}) = 2iAsin(kz). \tag{2.4}$$

Applying the boundary conditions at $z = d_w$, instead, we get:

$$\psi(d_w) = 0 \quad \Rightarrow \quad sin(kd_w) = 0 \quad \Rightarrow \quad kd_w = n\pi,$$

with $n \in \mathbb{N}$ starting from 1. The solutions of the Schrödinger equation for an infinite QW can therefore be obtained analytically and they are of the sinusoidal form

$$\psi_n(z) \sim sin\left(\frac{n\pi}{d_w}z\right), \tag{2.5}$$

whose corresponding energies are

$$E_n = \frac{\hbar^2 \pi^2}{2m^* d_w^2} n^2. \tag{2.6}$$

The first important property of a QW is therefore that the level energies are higher when the well is thinner, with a quadratic dependence on d_w. Moreover, the relative distance of the obtained levels increases with the energy (increasing n), and their wavefunctions have even and odd symmetry, alternatively. Since the eigenfunctions with even n have an odd symmetry (and vice versa), the energy levels are usually denoted with the index $l = n - 1$, with corresponding energies

$$E_l = \frac{\hbar^2 \pi^2}{2m^* d_w^2} (l + 1)^2 \tag{2.7}$$

with l starting from 0. In this way, the ground level ψ_0 has an even symmetry, the first excited level ψ_1 has an odd symmetry, and so on. This is the notation that will be used within the present work.
For the purpose of this work, it is important to underline that the ground state energy in a QW is increased by an amount ΔE relative to the unconfined case:

$$\Delta E = \frac{\hbar^2 \pi^2}{2m^* d_w^2}. \tag{2.8}$$

This increase in energy is referred to as the *confinement energy* or *quantum confinement* [43].

2.1.2 *Finite potential well*

When considering the case of a real QW with a finite potential barrier V_0, the penetration of the wavefunction into the barriers has also to be considered. The results obtained in the case of the infinite potential are still valid, but have to be modified as follows:

- the number of confined states is finite, and there is always at least one confined state, independently from how small V_0 is;
- the confinement energies are reduced with respect to the case of the infinite potential.

The electronic states of the samples here investigated have been evaluated by means of a first-neighbor tight-binding Hamiltonian with $sp^3d^5s^*$ orbitals and spin-orbit interaction (see Refs. [80, 81] for details of the model). The

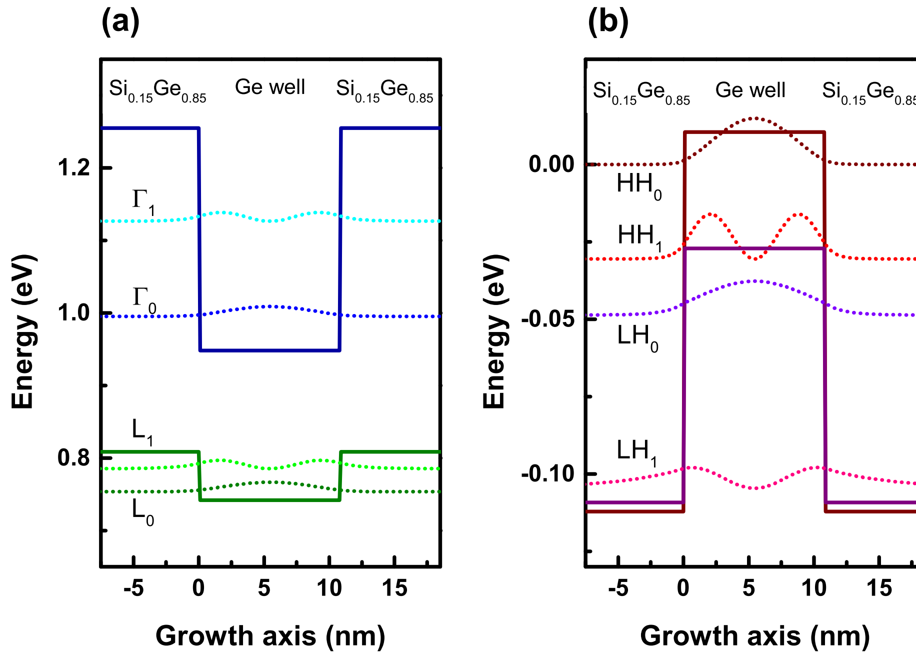

Figure 2.2 – Calculated conduction (a) and valence (b) band edge profiles (continuous lines) and square modulus of the wave functions (dotted lines) for the electron and hole confined states at 80 K of one of the investigated samples.

predictivity of the model for the evaluation of electronic spectra in SiGe multilayer heterostructures is well established[82, 83, 84], and indeed, compatible numerical results have been obtained when calculating the numerical data discussed in this work. The atomistic approach adopted allowed to take into account the geometric details of the whole structure, the chemical composition of the deposited materials and the strain within each layer. Quantum wells and barrier regions have been simulated assuming infinite extension in the QW plane, periodic boundary conditions along the growth direction, and sharp and flat interfaces. Linear interpolation with alloy concentration of the tight-binding parameters (virtual crystal approximation) has been exploited to describe the $Si_{0.15}Ge_{0.85}$ barrier regions. The position of ions in each layer of the QWs have been calculated matching the in-plane lattice constant with the virtual substrate (pseudomorphic growth), while the inter-plane separations along z have been evaluated according to macroscopic elasticity theory. The geometrical and chemical input data to describe the barrier and active materials have been taken from the structural characterization of the samples reported in Chapter 5.

The calculated conduction (a) and valence (b) band edge profiles (continuous lines) and square modulus of the wave functions (dotted lines) for the electron and hole confined states at 80 K of one of the investigated sample are reported in Fig. 2.2. The lowest confined states in the conduction band are found at the L point [green subbands in Fig. 2.2(a)], while confined states at the Γ point have higher energies and are shown in blue. Confined states in the valence band at Γ originate from heavy and light hole bands and are indicated in Fig. 2.2(b) in red and violet, respectively.

2.1.3 *Energy levels of holes*

Up to now, we considered a single quantum well in the conduction band. In the case of a quantum well in the valence band, since heavy hole and light hole have different effective masses, from Eq. 2.6 results that the degeneracy of the two states is lost, even in the absence of uniaxial strain. The quantization, therefore, acts in the opposite direction of tensile strain and in the same direction of compressive strain; i.e. heavy hole states are on top of light hole states. Applying compressive strain, the difference in energy, between heavy-hole and light-hole quantized levels, is thus accentuated, while reduced by tensile strain [85].

2.1.4 *Asymmetric Coupled Quantum Wells*

Two different heterostructure systems will be studied in this work. The first one is called *multi quantum well* (MQW) system and features a periodic repetition of single QWs separated by barriers thick enough to guarantee the wells are isolated from each other and hence not interacting. The second configuration that will be investigated is called *asymmetric coupled quantum well* (ACQW) system, in which every single element of the periodic repetition consists in two QWs with different width separated only by a thin barrier of few atomic layers. The two QWs cannot be therefore considered isolated anymore, because the small thickness of the barrier in the middle allows them to interact with each other. In fact, the tunneling probability through the thin barrier could be very high and the electron wavefunction of each well can extend into the adjacent one. The result is a level mixing that generates global stationary levels with energies different from the original ones associated to

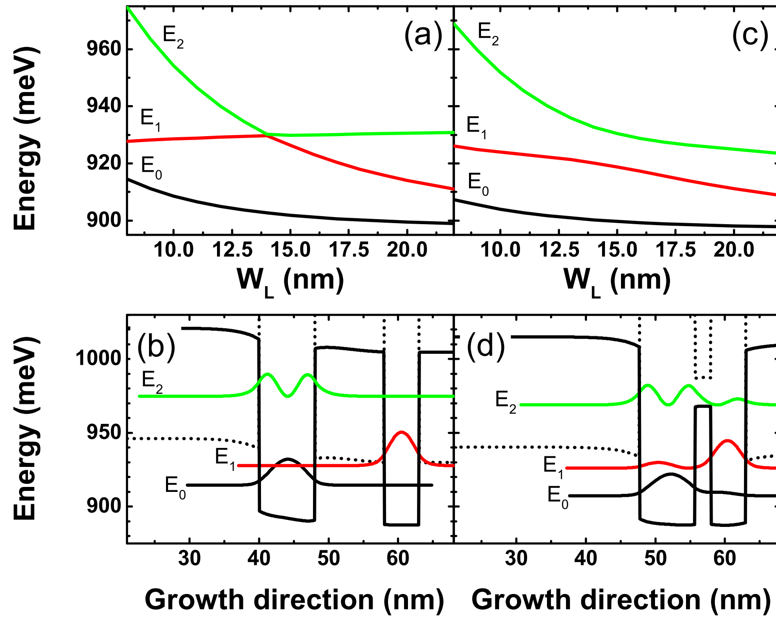

Figure 2.3 – Energy of the fundamental, first-excited, and second-excited electron states (E_0, E_1, and E_2, respectively) calculated for (a) uncoupled (barrier thickness 10 nm) and (c) coupled (barrier thickness 2.3 nm) ACQWs as a function of the thickness of the well. Electron energy and squared wavefunction for uncoupled (b) and coupled (d) ACQWs (solid and dotted black curves represent the L and Δ_2 band profile, respectively).

each single QW. In addition, the generated level wavefunctions lose the defined symmetry they would have in each well if isolated and their overlap becomes a varying parameter set by the specific structural properties. Employing a proper ACQW design, it is therefore possible to tune the optical properties of the system. This characteristic of ACQW systems results in a higher flexibility that can be exploited to finely engineer the optical properties of an eventual device.

As an example, we calculate in Fig. 2.3 the fundamental (E_0), first-excited (E_1), and second-excited (E_2) electron states of asymmetric quantum wells as a function of the well thickness W_L, in the uncoupled (barrier thickness 10 nm) and in the coupled regime (barrier thickness 2.3 nm). Figure 2.3(a) displays the energy of the states in the uncoupled regime as a function of the thickness of the well, while in Fig. 2.3(b) the square of the electron wavefunctions are reported in the case of W_L = 8 nm. Figures 2.3(c)-(d) instead display the energy of the states and the square of the electron wavefunctions calculated for W_L = 8 nm in the coupled configuration. Upon comparing Fig. 2.3(d) with its counterpart in the uncoupled case, i.e. Fig. 2.3(b), it is apparent that the

wavefunctions of E_1 and E_2, although featuring the same main character, now have a non-negligible amplitude in both wells, due to the inter-well coupling resulting from quantum tunneling through the barrier.

2.2 INTER-BAND TRANSITIONS IN SEMICONDUCTORS

In quantum physics, the probability of a transition from one energy eigenstate $|i\rangle$ of a quantum system into other energy eigenstates $|f\rangle$, induced by a weak perturbation, can be derived using Fermi's golden rule:

$$W_{i\to f} = \frac{2\pi}{\hbar} \left|\langle f|H'|i\rangle\right|^2 \rho. \tag{2.9}$$

In Eq. 2.9, ρ is the density of final states and $\langle f|H'|i\rangle$ is the matrix element of the perturbation H' between the final and initial states.
In the presence of an electromagnetic field, the probability per unit time that an electron initially in the state $|i\rangle$ is transferred to the final state $|j\rangle$ with *emission* of one photon of energy $\hbar\omega$ is [34]

$$W_{i\to j} = \frac{2\pi}{\hbar} \left(\frac{eA_0}{m\omega}\right)^2 \left|\langle j|e^{-i\boldsymbol{q}\cdot\boldsymbol{r}}\boldsymbol{e}\cdot\boldsymbol{p}|i\rangle\right|^2 \delta(E_j - E_i + \hbar\omega), \tag{2.10}$$

where A_0 is the amplitude of the vector potential $\boldsymbol{A}$ of the radiation, $\boldsymbol{e}$ its polarization vector, $\boldsymbol{p}$ is the momentum operator, and E_j (E_i) is the energy of the final (initial) state. Since the momentum $\boldsymbol{q}$ carried by the photon is much smaller than the typical momenta of the electrons $\boldsymbol{k}$, we can adopt the *dipole approximation* $e^{-i\boldsymbol{q}\cdot\boldsymbol{r}} \approx 1$, so that in $\boldsymbol{k}$-space the photons can induce only *vertical transitions*.
The rate R at which transition occurs is the probability per unit time for transitions occurring from a filled state to an empty state times the probability that the initial state is filled P_i, and the final state is empty P_j

$$R(\omega) = \sum_{i,j} W_{i\to j} P_i P_j, \tag{2.11}$$

where the sum is over all possible initial and final states.

2.2.1 *Direct band-to-band transitions*

Let us now specify Eq. 2.10 for the case of interband transitions in a semiconductor. Considering as initial state a conduction state $|\psi_{c,\boldsymbol{k}}\rangle$ and the

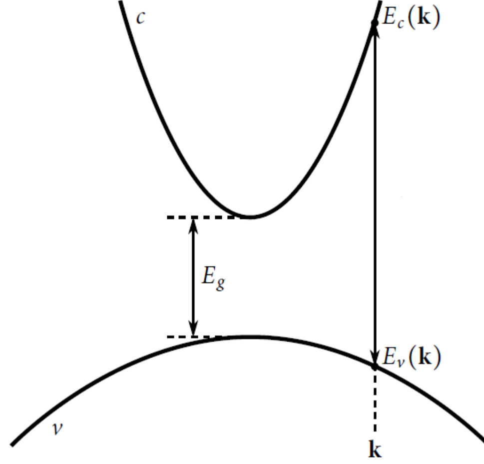

Figure 2.4 – Scheme of a direct interband transition between a pair of parabolic bands, occurring at a wavevector $\boldsymbol{k}$. The gap at Γ is denoted by E_g. Figure taken from [86].

corresponding final state is a valence state $|\psi_{v,\boldsymbol{k}}\rangle$, where the index c (v) labels the different conduction (valence) bands,

$$W_{c\to v} = \frac{2\pi}{\hbar}\left(\frac{eA_0}{m\omega}\right)^2 2\sum_{c,v}\sum_{\boldsymbol{k}}\left|\langle\psi_{v,\boldsymbol{k}}|\boldsymbol{e}\cdot\boldsymbol{p}|\psi_{c,\boldsymbol{k}}\rangle\right|^2 \delta(E_{c,\boldsymbol{k}} - E_{v,\boldsymbol{k}} + \hbar\omega), \quad (2.12)$$

where the factor 2 in front of the sums accounts for the two spin polarizations. We can make a further step converting the sum over all $\boldsymbol{k}$ points in the Brillouin zone (BZ) in an integral:

$$W_{c\to v} = \frac{4\pi}{\hbar}\left(\frac{eA_0}{m\omega}\right)^2 \sum_{c,v}\frac{V}{(2\pi)^3}\int_{BZ} d\boldsymbol{k}|\boldsymbol{e}\cdot\boldsymbol{p}_{c,v}(\boldsymbol{k})|^2\delta(E_{c,\boldsymbol{k}} - E_{v,\boldsymbol{k}} + \hbar\omega), \quad (2.13)$$

where we have defined the momentum matrix element

$$\boldsymbol{p}_{c,v}(\boldsymbol{k}) = \langle\psi_{v,\boldsymbol{k}}|\boldsymbol{p}|\psi_{c,\boldsymbol{k}}\rangle. \quad (2.14)$$

In general, the momentum matrix element $\boldsymbol{p}_{c,v}(\boldsymbol{k})$ is a smooth function of $\boldsymbol{k}$ over the Brillouin zone [34], and its average value can be factorized out of the integral in Eq. 2.13.

We can introduce the *joint density of states*

$$J(E_{c,v}) = \int_{BZ} d\boldsymbol{k}\ \delta(E_{c,\boldsymbol{k}} - E_{v,\boldsymbol{k}} + \hbar\omega), \quad (2.15)$$

that, for parabolic bands, becomes

$$J(E_{c,v}) = \frac{(2m_r^*)^{3/2}}{2\pi^2\hbar^3}\sqrt{\hbar\omega - E_c + E_v}, \quad (2.16)$$

where m_r^* is the reduced effective mass

$$\frac{1}{m_r^*} = \frac{1}{m_c} + \frac{1}{m_v}. \tag{2.17}$$

For the evaluation of the rate of spontaneous emission 2.11, we assume that a given population of electrons and holes is present in the conduction and valence band, respectively, either due to doping or due to an optical pump, such as in photoluminescence experiments. Thus, the rate of spontaneous emission it is proportional to the product of the joint density of states, the population of electrons in the conduction band f_e, the population of holes in the valence band f_h, and the matrix element $\boldsymbol{p}_{c,v}(\boldsymbol{k})$ [87]:

$$R_{sp}(\omega) = \sum_{i,j} W_{i\to j} P_i P_j \propto |\boldsymbol{p}_{c,v}|^2 G(\omega) J(E_{c,v}) f_e f_h. \tag{2.18}$$

In equation 2.18 $G(\omega)$ is the optical density of states of the electromagnetic field defined in such a way that $G(\omega) d\Omega_q d(\hbar\omega)$ is the total number of photons per unit volume contained in the energy interval $d(\hbar\omega)$ and with wavevector $\boldsymbol{q}$ in the solid angle $d\Omega_q$, for a given polarization.

2.2.2 *Indirect band-to-band transitions*

In the previous sections we have considered the interaction of the electrons with the radiation field and we have shown that only vertical transitions may occur. We recall that, in indirect gap semiconductors, such as silicon and germanium, the bottom of the conduction band and the top of the valence band are at different points of the Brillouin zone. Optical transitions between valence and conduction extrema would be forbidden in this case by momentum conservation. However, such transitions are experimentally observed, albeit they are much weaker than the direct transitions.

Transitions between states that are not vertical in the $\boldsymbol{k}$-space are called *indirect transitions*. The possibility of indirect transitions is due to the interaction of electrons with lattice vibrations. Since indirect transitions are forbidden in first-order perturbation theory, due to the momentum selection rule, to evaluate the transition rate we have to adopt the second-order perturbation theory. In this framework, the transition probability per unit time of a process in which the valence electron $\varphi_{v,\boldsymbol{k}v}$ is scattered to the conduction state $\varphi_{c,\boldsymbol{k}c}$

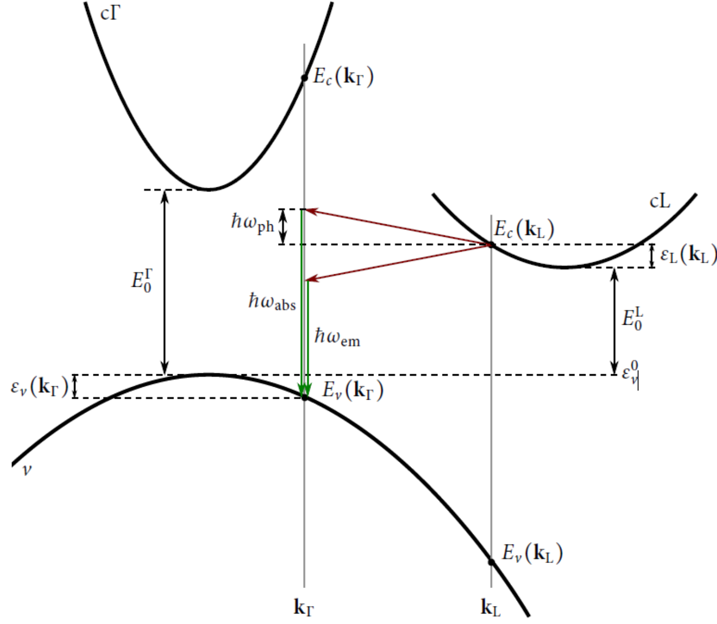

Figure 2.5 – Scheme of an indirect transition occurring between a state in a conduction L valley at $\boldsymbol{k} = \boldsymbol{k}_L$ and energy $E_c(\boldsymbol{k}_L)$, and a valence state (in the band v) at $\boldsymbol{k} = \boldsymbol{k}_\Gamma$ and energy $E_v(\boldsymbol{k}_\Gamma)$. The red arrows represent the emission or absorption of a phonon, while the green arrows represent the emission of a photon. Figure taken from [86].

and a photon of energy $\hbar\omega$ and a phonon of momentum $\boldsymbol{q} = \boldsymbol{k}_c - \boldsymbol{k}_v$ (and energy $\hbar\omega_{\boldsymbol{q}}$) are both absorbed can be obtained as

$$W_{v,\boldsymbol{k}v\to c,\boldsymbol{k}c} = \frac{2\pi}{\hbar}\left(\frac{eA_0}{mc}\right)^2 \left|\frac{\langle\varphi_{c,\boldsymbol{k}c}|V_p(\boldsymbol{q},\boldsymbol{r})|\varphi_{\beta,\boldsymbol{k}v}\rangle n_{\boldsymbol{q}}^{1/2}\langle\varphi_{\beta,\boldsymbol{k}v}|\boldsymbol{e}\cdot\boldsymbol{p}|\varphi_{v,\boldsymbol{k}v}\rangle}{E_\beta(\boldsymbol{k}v) - E_v(\boldsymbol{k}v) - \hbar\omega}\right|^2 \times \delta(E_c(\boldsymbol{k}_c) - E_v(\boldsymbol{k}_v) - \hbar\omega + \hbar\omega_{\boldsymbol{q}}). \quad (2.19)$$

In equation 2.19 $n_{\boldsymbol{q}}$ denotes the phonon occupation number, which in thermal equilibrium is given by the Bose-Einstein expression

$$n_{\boldsymbol{q}} = \frac{1}{e^{\hbar\omega_{\boldsymbol{q}}/k_B T} - 1}. \quad (2.20)$$

Because of $n_{\boldsymbol{q}}$, indirect transitions have a strong temperature dependence.

The calculation of the spontaneous radiative recombination in Ge films, including direct and indirect optical transitions and contributions from all three valence bands, can be found in Ref. [12].

2.3 INTER-BAND TRANSITIONS IN QUANTUM WELLS

Let's consider a transition between a confined conduction state (i) and a confined valence state (j) in a type-I quantum well. The initial and final states can be written as a product of the envelope function and the appropriate Bloch function at Γ [36]

$$|i\rangle = \Omega^{1/2}\psi_c(\boldsymbol{R})u_c(\boldsymbol{R}), \tag{2.21a}$$

$$|j\rangle = \Omega^{1/2}\psi_v(\boldsymbol{R})u_v(\boldsymbol{R}). \tag{2.21b}$$

The matrix element $\langle j|\boldsymbol{e}\cdot\boldsymbol{p}|i\rangle$ thus becomes

$$\langle j|\boldsymbol{e}\cdot\boldsymbol{p}|i\rangle = \Omega\int \psi_v^*(\boldsymbol{R})u_v^*(\boldsymbol{R})(\boldsymbol{e}\cdot\boldsymbol{p})\psi_c(\boldsymbol{R})u_c(\boldsymbol{R})d^3\boldsymbol{R}. \tag{2.22}$$

Since the Bloch functions vary within each unit cell, while the envelope functions are almost constant within each unit cell, we can divide the integral into unit cells and pull the envelope functions out as being constant within each cell, giving

$$\langle j|\boldsymbol{e}\cdot\boldsymbol{p}|i\rangle \approx \Omega\sum_j^{cells}\psi_v^*(\boldsymbol{R})\psi_c(\boldsymbol{R})\int_{cell\ j} u_v^*(\boldsymbol{R})(\boldsymbol{e}\cdot\boldsymbol{p})u_c(\boldsymbol{R})d^3\boldsymbol{R}. \tag{2.23}$$

The integral within each unit cell can be denoted $(\Omega_{cell}/\Omega)\boldsymbol{e}\cdot\boldsymbol{p}_{cv}(0)$, where $\boldsymbol{p}_{cv}(0)$ is the matrix element between the Bloch wave functions at the extrema of the bands. Then

$$\langle j|\boldsymbol{e}\cdot\boldsymbol{p}|i\rangle \approx \boldsymbol{e}\cdot\boldsymbol{p}_{cv}(0)\Omega_{cell}\sum_j^{cells}\psi_v^*(\boldsymbol{R})\psi_c(\boldsymbol{R}). \tag{2.24}$$

Finally, we can turn the sum over cells back into an integral over the whole sample.

$$\langle j|\boldsymbol{e}\cdot\boldsymbol{p}|i\rangle \approx \boldsymbol{e}\cdot\boldsymbol{p}_{cv}(0)\int \psi_v^*(\boldsymbol{R})\psi_c(\boldsymbol{R})d^3\boldsymbol{R}. \tag{2.25}$$

The envelope functions in a quantum well have the separable form of a plane wave in x and y and a bound state along z,

$$\psi_c(\boldsymbol{R}) = A^{-1/2}e^{i(\boldsymbol{k}\cdot\boldsymbol{r})}\phi_{cn}(z) = |cn\boldsymbol{k}\rangle, \tag{2.26a}$$

$$\psi_v(\boldsymbol{R}) = A^{-1/2}e^{i(\boldsymbol{k}'\cdot\boldsymbol{r})}\phi_{vm}(z) = |vm\boldsymbol{k}'\rangle, \tag{2.26b}$$

where c and v indicate the conduction and valence bands, n and m label the bound states, and $\boldsymbol{k}$ and $\boldsymbol{k}'$ are the transverse wave vectors. Thus the matrix element reduces to

$$\langle vm\boldsymbol{k}'|\boldsymbol{e}\cdot\boldsymbol{p}|cn\boldsymbol{k}\rangle \approx \boldsymbol{e}\cdot\boldsymbol{p}_{vm,cn}\delta_{k,k'}\int \phi_{vm}^*(z)\phi_{cn}(z)dz \tag{2.27}$$

$$\equiv \boldsymbol{e}\cdot\boldsymbol{p}_{vm,cn}\delta_{k,k'}\langle vm|cn\rangle \tag{2.28}$$

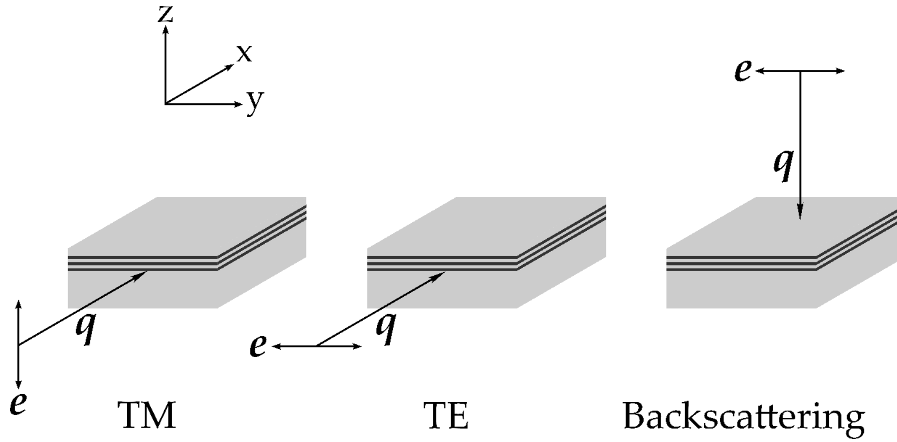

Figure 2.6 – From left to right: propagation parallel and polarization orthogonal to the QW plane (TM mode). Propagation parallel and polarization parallel to the QW plane (TE mode). Propagation orthogonal and polarization parallel to the QW plane (backscattering geometry).

Therefore, the matrix element can be divided in three different parts:

- $\boldsymbol{e} \cdot \boldsymbol{p}_{vm,cn}$, which depends on the nature of the Bloch functions and on the polarization $\boldsymbol{e}$.
- $\delta_{k,k'}$, which imposes vertical transitions, meaning that the transverse wave vector $\boldsymbol{k}$ must not change.
- The matrix element for the envelope functions $\langle vm|cn\rangle$, which is an integral over their product with no dependence on polarization.

INTER-BAND MATRIX ELEMENT Near the band edge and for moderate strain fields, as in the case of the investigated samples, the $c\Gamma$, HH, and LH bulk states close to the Γ point can be roughly described as J-decoupled states with parabolic dispersion [84]. Within this approximation, selection rules for inter-band transitions at Γ involving HH and LH valence states and for different linear polarizations have been calculated [88] and the results are reported in Table 2.1. We note that for a polarization vector in the QW plane (see Fig. 2.6), such as in the backscattering geometry employed in the photoluminescence experiments we shall discuss, the $c\Gamma - HH$ and $c\Gamma - LH$ transitions are both allowed, and the absolute value of the dipole matrix elements for $c\Gamma - HH$ is greater by a factor $\sqrt{3}$ with respect to the $c\Gamma - LH$ transition. Otherwise, for a polarization vector along the growth direction, the strength of the $c\Gamma - LH$ is unchanged while the $c\Gamma - HH$ transition becomes forbidden. This implies that for polarized light propagating parallel to the

QW plane and polarization vectors along the growth direction the $c\Gamma n - HHn$ transitions are expected to be strongly suppressed.

	e_x	e_y	e_z	Transition
Propagation parallel to z	$\frac{\pi}{\sqrt{2}}$	$\frac{\pi}{\sqrt{2}}$	impossible	$c\Gamma n - HHn$
Propagation parallel to x	impossible	$\frac{\pi}{\sqrt{2}}$	forbidden	$c\Gamma n - HHn$
Propagation parallel to y	$\frac{\pi}{\sqrt{2}}$	impossible	forbidden	$c\Gamma n - HHn$
Propagation parallel to z	$\frac{\pi}{\sqrt{6}}$	$\frac{\pi}{\sqrt{6}}$	impossible	$c\Gamma n - LHn$
Propagation parallel to x	impossible	$\frac{\pi}{\sqrt{6}}$	$\frac{2\pi}{\sqrt{6}}$	$c\Gamma n - LHn$
Propagation parallel to y	$\frac{\pi}{\sqrt{6}}$	impossible	$\frac{2\pi}{\sqrt{6}}$	$c\Gamma n - LHn$

Table 2.1 – Selection rules for inter-band transitions at Γ involving HH and LH valence states. The direction z is the growth direction. e_x, e_y, and e_z indicate linear polarization along the x, y, and z directions, respectively [88].

MATRIX ELEMENT OF ENVELOPE FUNCTIONS In the ideal case of an infinitely deep square well in both conduction and valence bands the two sets of envelope functions are identical and the integral becomes

$$\int \phi^*_{vm}(z)\phi_{cn}(z)dz = \int \phi^*_m(z)\phi_n(z)dz = \delta_{m,n}. \tag{2.29}$$

Only inter-band transitions between states with the same subband index n are allowed: $\Delta n = 0$. In the case of a real QW with finite potential barriers, where $\phi_{vm}(z) \neq \phi_{cn}(z)$, transitions with $\Delta n \neq 0$ are also allowed, but very weak. For symmetric QWs, the envelope functions will be symmetric or antisymmetric and their matrix element will vanish unless both have the *same parity*, i.e. transitions with $\Delta n = \pm 2m + 1$, with $m = 0,\ 1,\ 2, \ldots$ are strictly forbidden. There is no restriction on the allowed values of m and n for a well that is asymmetric, either through growth or because it has been distorted by an electric field.

2.4 RECOMBINATION PROCESSES IN SEMICONDUCTORS

A quantum mechanical system that is bound can only take on certain discrete values of energy. Among energy states, the state with the lowest energy is most stable. Therefore, electrons in semiconductors tend to stay in low

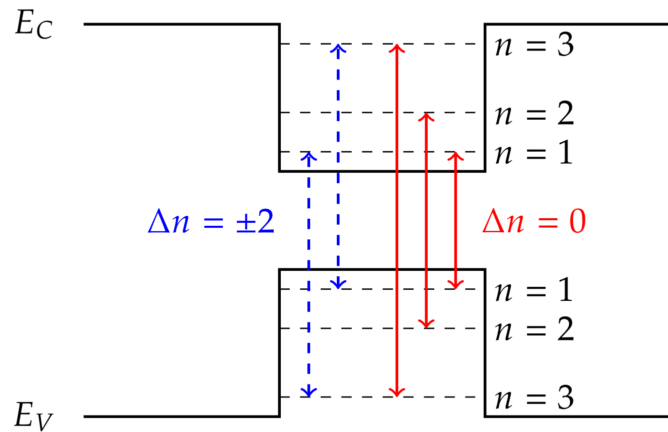

Figure 2.7 – Scheme of inter-band transitions between confined states of a QW. Continuous red lines indicate strong transitions ($\Delta n = 0$), while blue dashed lines indicate weak, but allowed transitions ($\Delta n = 2$).

energy states which are within the valence bands. If they are excited by thermal energy, light, or electron beams, the electrons absorb these energies and transit to high energy states. In the case of a semiconductor, due to this energy exchange, the electron can occupy a state in the conduction band. These transitions of the electrons from low energy states to high energy states are called *excitations*. High energy states, however, are unstable. As a result, to take stable states, the electrons in high energy states transit to low energy states in certain lifetimes. These transitions of the excited electrons from high energy states to low energy states are referred to as *relaxations*. In semiconductors, the transitions of electrons from high energy states to low energy states are designated *recombinations* of the electrons and the holes. The excitation process can be divided in three steps, each with its own lifetime:

- *generation* of electron-hole pairs;
- *thermalization* of pairs towards quasi-thermal-equilibrium distributions;
- *recombination* of electrons and holes.

Recombinations can be subdivided in *radiative recombinations* and *non-radiative recombinations*. Radiative recombinations emit photons, and the energies of the emitted photons correspond to a difference in the energies between the initial and final energy states involved in the transition. On the contrary, in non-radiative recombinations, phonons are emitted to crystal lattices or electrons are trapped in the defects, and the transition energy is transformed into forms other than light. To obtain semiconductor light emitting devices with high efficiency, we have to minimize the non-radiative recombinations.

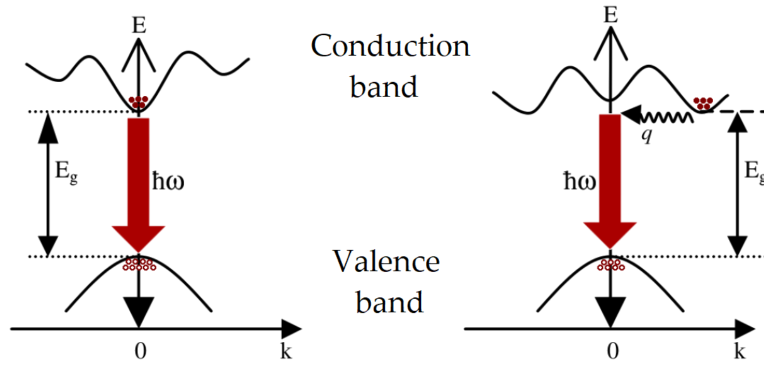

Figure 2.8 – Recombination processes in a direct gap (left) and an indirect gap (right) semiconductor.

2.4.1 *Radiative electron-hole recombination*

The radiative recombination processes for direct and indirect gap semiconductors are shown in Figure 2.8. A radiative transition can be direct or indirect depending on the type of semiconductor. In direct band gap semiconductors, conduction band and valence band extrema occur at the zone center. From conservation of momentum, the wave vector k_1 of the valence band wave function and the wave vector k_2 of the conduction band must differ by the wave vector of the photon. Since the wave vector of the electron is much larger than that of the photon, the k-selection rule is generally written as

$$k_1 = k_2. \tag{2.30}$$

The allowed transitions are, then, between initial and final states of the same wave vector and are called *direct* or *vertical* transitions (since they are vertical in the $E - k$ space). In indirect gap materials, the excited carriers thermalize to the lowest lying states in the respective bands, which minima are not at the same value of k as the valence band. The recombination process now involves a phonon to conserve the momentum. Then, the probability of such transition is extremely low.

Because it takes both an electron *and* a hole for a recombination to occur, the rate of recombination R is proportional to the product of the concentration of electrons and holes [89]:

$$R = Bnp \tag{2.31}$$

where B [cm^3/s] is a parameter that depends on the characteristics of the material, including its composition and defects, temperature and doping. A

Semiconductor	B	τ	
	$cm^3/s \times 10^{-12}$	Intrinsic	10^{17} cm^{-3} majority carriers
Si	0.002	4.6 h	2.5 ms
Ge	0.034	0.61 s	0.15 ms
GaSb	13	0.009 s	0.37 μs
GaP	0.003		3.0 ms
GaAs		2.8 μs	0.04 μs
InAs	21	15 μs	0.24 μs
InSb	40	0.62 μs	0.12 μs
PbS	48	15 μs	0.21 μs
PbTe	52	2.4 μs	0.19 μs
PbSe	40	2.0 μs	0.25 μs

Table 2.2 – Minority carrier radiative lifetime in several semiconductors at room temperature [91, 43, 92]

direct bandgap semiconductor has a much larger B parameter ($\sim 10^{-10}$ cm^3/s) than an indirect bandgap semiconductor ($\sim 10^{-15}$ cm^3/s) [90]. This illustrates why classic III-V laser materials are better light emitters than Ge and Si and why Ge is better than Si (see Table 2.2).

A semiconductor in thermal equilibrium with carrier concentrations n_0 an p_0 has equal rates of generation and recombination. Thus the rate of electron-hole generation is given by:

$$G_0 = Bn_0p_0. \tag{2.32}$$

Now let additional electron-hole pairs be generated at a steady rate R_{ex} (pairs per unit volume per unit time) by means of an external injection mechanism. In this new state the carrier concentrations are $n = n_0 + \Delta n$ and $p = p_0 + \Delta p$ where $\Delta n = \Delta p$ since excess electrons and holes are created and recombine *in pairs* [93]. Due to the external excitation, the rate of recombination R and the rate of generation G_0 are no longer equal

$$R = G_0 + R_{ex} = Bnp. \tag{2.33}$$

Substituting G_0 from 2.32, we can write

$$R_{ex} = R - G_0 = Bnp - Bn_0p_0 = B[(n_0 + \Delta n)(p_0 + \Delta p) - n_0p_0]. \tag{2.34}$$

In the case of a small neutral excitation, we find $\Delta n = \Delta p \ll n_0,\ p_0$, and

$$R_{ex} = \frac{\Delta n}{\tau}, \tag{2.35}$$

where

$$\tau = \frac{1}{B(n_0 + p_0)}. \tag{2.36}$$

The parameter τ can be regarded as the *electron-hole recombination lifetime* of the injected electron-hole pairs and it is a measure of the average time an excess carrier pair spends in the sample before being lost by recombination.

In case of n-type doped semiconductors $n_0 \gg p_0$ and the net recombination rate is governed by the excess-hole density Δp:

$$R_{ex} = B(n_0 \Delta p). \tag{2.37}$$

We can then introduce the *minority carrier lifetime* as

$$\tau_p = \frac{1}{Bn_0}. \tag{2.38}$$

We can observe that the minority carrier lifetime τ_p is thus a function of the doping concentration and decreases with increasing doping. On the other hand, the related radiative recombination rate 2.31 increases with increasing donors concentrations n_0. The effect of doping on the optical properties in Ge shall be discussed in details in following Chapters.
The minority carrier radiative lifetime in several semiconductors at room temperature are reported in Table 2.2.

2.4.2 *Non-radiative transitions*

In addition to radiative recombination, non-radiative recombination also occurs, in which the excess energy is given up in the form of phonons or heat waves. The total recombination rate of the photoexcited population of electron-hole pairs is given by

$$\frac{1}{\tau} = \frac{1}{\tau_{\text{rad}}} + \frac{1}{\tau_{\text{non-rad}}}, \tag{2.39}$$

where $1/\tau_{\text{rad}}$ and $1/\tau_{\text{non-rad}}$ are the radiative and non-radiative recombination rates, respectively.

Non-radiative recombination mechanisms, or transitions, can be classified as either extrinsic or intrinsic. Extrinsic recombination is a decay through an

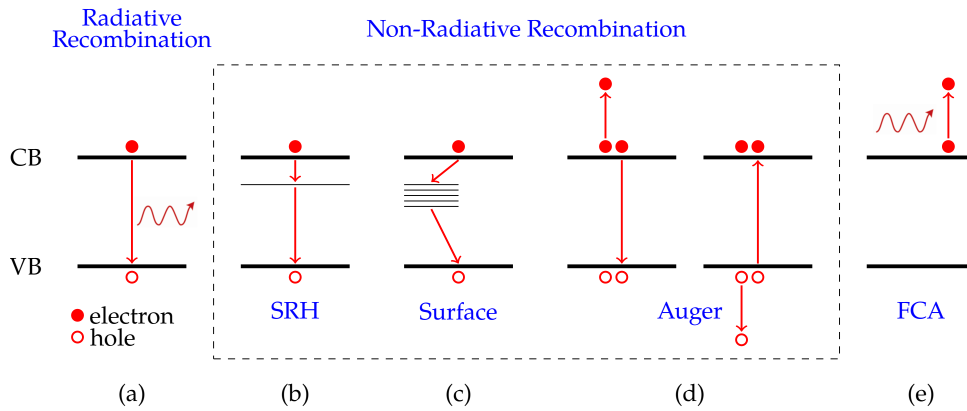

Figure 2.9 – Typical non-radiative recombination mechanisms.

intermediate energy level within the band gap. These recombinations are usually due to surface recombination and defect recombination, or *Schokley-Read-Hall recombination* (SRH). Intrinsic recombination mechanisms are always present, even in an ideal undisturbed crystal without impurities or defects. Typical non-radiative recombination mechanisms are depicted in Figure 2.9

Schokley-Read-Hall recombination

Recombination through defects is a two-step process:

1. An electron (or hole) is trapped by an energy state in the gap, which is introduced through defects in the crystal lattice. These defects can either be unintentionally introduced or deliberately added to the material, for example in doping the material;

2. If a hole (or an electron) moves up to the same energy state before the electron is thermally re-emitted into the conduction band, then it recombines.

Schokley-Read-Hall recombination, also called trap-assisted recombination, is the reason why we stated in Chapter 1 that extended defects, such misfit and threading dislocations, are detrimental for opto-electronic devices.
The rate of recombination through the Shockley-Read-Hall process, R_{SRH}, is given by [94]

$$R_{SRH} = \frac{np - n_i^2}{\tau_p(n + n_1) + \tau_n(p + p_1)}. \tag{2.40}$$

In equation 2.42, the parameter n_1 (p_1) is equivalent to an electron (hole) concentration that would exist in the conduction (valence) band if the trap energy coincided with the Fermi energy [93]. The lifetime for electrons when

the centers are completely empty is given by τ_n, while τ_p is the hole lifetime with all centers occupied by electrons.
Under high level of injection, n and p are equal and much greater than n_i, n_1 or p_1 so that there is a linear relation between carrier concentration and recombination rate

$$R_{SRH} \simeq \frac{n}{\tau_p + \tau_n} = An. \tag{2.41}$$

For the evaluation of the Shockley-Read-Hall rate of recombination, the effect of doping has to be taken into account as [82]

$$R_{SRH}(n_{dop}) = R_{SRH}^{int}(1 + \kappa n_{dop}), \tag{2.42}$$

where R_{SRH}^{int} is the rate of the intrinsic material and $\kappa = 3 \times 10^{-17}$ cm^{-3} (in Ge) a phenomenological proportionality constant. This results in a reduction of the SRH lifetime at room temperature from 30 ns for the intrinsic case to 0.1 ns at a doping level of $\sim 10^{-19}$ cm^{-3} [82, 95]. The reduction of τ_{SRH} at a high density of donors n_{dop} can be explained considering that the introduction of charged dopant ions results in a reduced quality of the epitaxial material.

Up to now we considered semiconductors infinite in extent, while real systems are not infinitely large and therefore surfaces do exist between the semiconductor and an adjacent medium. When a semiconductor is abruptly terminated, the periodicity of the crystal lattice is broken at surface, resulting in allowed electronic energy states within the energy bandgap. Therefore, surface recombination is almost identical to Shockley-Hall-Read recombination, the only difference being that the recombination is due to a two-dimensional density of traps.

Auger recombination

Unlike the non-radiative and radiative recombination processes, which are two-particle processes, the Auger band-to-band recombination is a three-particle process [Fig. 2.9(d)] and it is predominant in highly doped semiconductors. In the case of n-type doping the three particle involved are two electrons and one hole, while p-type semiconductors one electron and two holes are involved [93]. For an n-type semiconductor, an electron and a hole recombine, but rather than emitting the energy as heat or as a photon, the energy is given to a third carrier, an electron in the conduction band. This electron

then thermalizes back down to the conduction band edge. The recombination rates associated is given by

$$R_{Auger} = C_n n(np - n_0^2) + C_p p(np - n_0^2). \tag{2.43}$$

In case of high external excitation, $\Delta n = \Delta p \gg n_0$, Eq. 2.43 becomes

$$R_{Auger} = (C_n + C_p)n^3 = Cn^3. \tag{2.44}$$

References [96] and [97] report the following values for the C_i coefficients in Ge: $C_n = 3 \times 10^{-32}$ cm^6/s and $C_p = 7 \times 10^{-32}$ cm^6/s, respectively.

Free carrier absorption

Free carrier absorption (FCA) occurs when a material absorbs a photon, and a carrier (electron or hole) is excited from an already-excited state to another, unoccupied state in the same band.

2.4.3 *Rate of recombination for excess carrier density*

The rate of recombination, which include both radiative and non-radiative processes, can be expanded in terms of the total amount of excess carrier density Δn in the system;

$$R(\Delta n) = A \cdot \Delta n + B \cdot \Delta n^2 + C \cdot \Delta n^3 = \frac{\Delta n}{\tau}, \tag{2.45}$$

where τ is the lifetime of carriers, A is due to non-radiative recombination, B is due to spontaneous radiative recombination and C accounts for non-radiative Auger recombination. Due to the small value of B, the rate of recombination of excess carrier density is governed by the non-radiative terms SRH and Auger.

2.4.4 *Scaling of photoluminescence intensity as a function of excitation power*

As we will see in the following, photoluminescence experiments are a powerful tool to study the optical properties of a system. We will also see how we can evaluate which is the dominant non-radiative term studying the scaling of the photoluminescence intensity as a function of the excitation power density. As a matter of fact, the detected photoluminescence intensity is proportional to the radiative recombination rate and is thus proportional to the product

of excess electron and hole density $\Delta n \cdot \Delta p \simeq \Delta n^2$. At the same time, the generation rate G is directly proportional to the excitation power density W. Now, in the case that the Shockley-Read-Hall mechanism is dominating, the excess carrier density Δn is linear with the generation rate G and we can conclude that the photoluminescence intensity I varies with the pump power W as $I \propto W^2$. On the other hand, in case that Auger recombinations are dominating $\Delta n \propto W^{1/3}$; it follows that the intensity scales as $I \propto W^{2/3}$.

2.4.5 *Spectral shape of direct gap emission*

The intensity of the emitted light is proportional to the rate of spontaneous emission derived in section 2.2.1 [87]. For band-to-band transitions it is proportional to the product of the joint density of states and the probabilities that the upper state is occupied and the lower state is empty. For a direct transition, the energy of the electron in the conduction band is given by [90]:

$$E_c(k) = E_g + \frac{\hbar^2 k^2}{2m_c}, \tag{2.46}$$

while the energy of the hole in the valence band is given by:

$$E_v(k) = -\frac{\hbar^2 k^2}{2m_v}. \tag{2.47}$$

The energy of the emitted photon is the difference between the energy of the electron and the energy of the hole:

$$\hbar\omega = E_c(k) - E_v(k) = E_g + \frac{\hbar^2 k^2}{2m_r^*}, \tag{2.48}$$

where m_r^* is the reduced effective mass

$$\frac{1}{m_r^*} = \frac{1}{m_c} + \frac{1}{m_v}. \tag{2.49}$$

The joint density of states for parabolic bands is given by:

$$J(E) = \frac{(2m_r^*)^{3/2}}{2\pi^2\hbar^3}\sqrt{\hbar\omega - E_g}, \tag{2.50}$$

while the distribution of carriers is governed by the Boltzmann distribution:

$$F(E) = exp\left(-\frac{E}{k_B T}\right). \tag{2.51}$$

The peak shape for a direct band-to-band transition is proportional to the product of Eqs. 2.50 and 2.51 :

$$I(\hbar\omega) \propto \sqrt{\hbar\omega - E_g} \cdot exp\left(-\frac{\hbar\omega - E_g}{k_B T}\right). \tag{2.52}$$

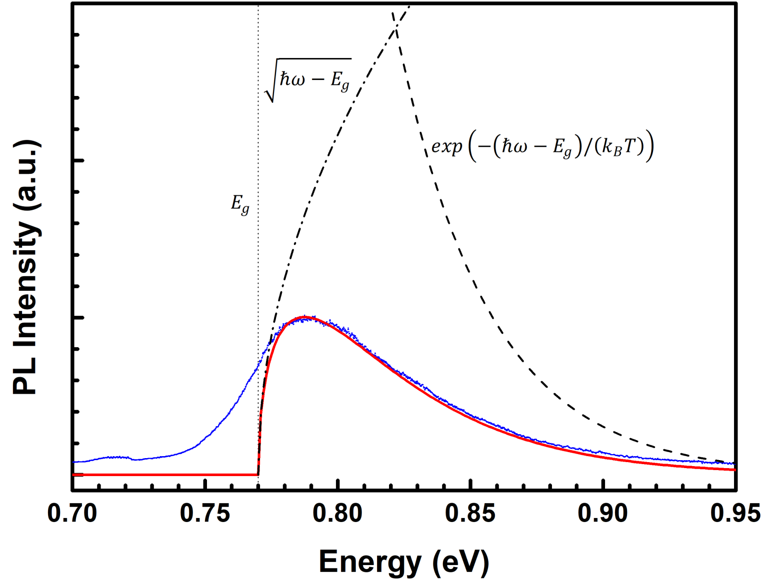

Figure 2.10 – Photoluminescence spectrum due to band to band direct transition in a Ge thin film, measured at RT. The fit of experimental data with Eq. 2.52 and the decomposition into the single factors of the formula are also reported.

Here $I(\hbar\omega)$ denote the intensity of the luminescence due to a direct transition, E_g is the direct bandgap, $\hbar\omega$ is the energy of the emitted photons, k_B is the Boltzmann constant, and T is the temperature of excited carriers, which can significantly differ from the lattice temperature T_L [98]. The photoluminescence spectrum of a Ge thin film, measured at room temperature, is reported in Fig. 2.10. The fit of experimental data with Eq. 2.52 and the decomposition into the single factors of the formula are also reported.
A consequence of Eq. 2.52 is that the PL peak is found at an energy $k_B T/2$ larger than the bandgap.

2.4.6 *Self-absorption*

The shape of the emission spectrum is strongly affected by self-absorption, i.e. part of the light emitted is absorbed by the sample itself before reaching the surface. If a spectrum $L_0(\hbar\omega)$ is emitted at distance d from the surface of reflectance R and the absorption coefficient is $\alpha(\hbar\omega)$, then the spectrum outside the sample is given by [92]

$$L(\hbar\omega) = (1 - R)L_0(\hbar\omega)e^{-\alpha(\hbar\omega)d}. \tag{2.53}$$

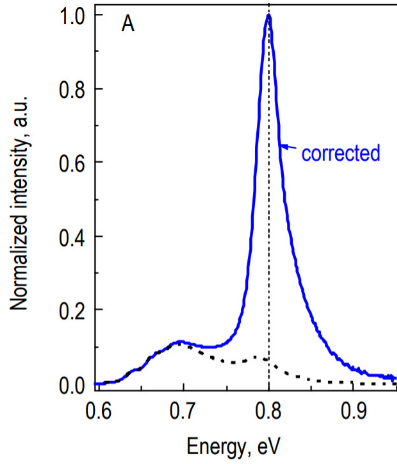

Figure 2.11 – Spectrum of band to band transition of a bulk Ge sample corrected for self-absorption [99].

If the radiative recombination occurs uniformly inside the sample of thickness t, the spectrum radiated externally in one direction is

$$L(\hbar\omega) = (1-R)\frac{L_0(\hbar\omega)}{t}\int_0^t e^{-\alpha(\hbar\omega)x}\,dx = (1-R)L_0(\hbar\omega)\frac{1-e^{-\alpha(\hbar\omega)t}}{\alpha(\hbar\omega)t}. \quad (2.54)$$

Germanium is an indirect gap semiconductor. However, thanks to the reduced energy separation between Γ_c and L_c, it is possible to excite electrons into both valleys, thus obtaining both direct and indirect radiative recombinations. Since self-absorption is different for the two transitions, photoluminescence spectra can be extremely affected. In Figure 2.11 the photoluminescence spectrum of bulk Ge is reported, where the spectrum corrected for self-absorption, using Eq. 2.54, is also reported. We can see that, while in the non-corrected spectrum the intensity of the two transitions is similar, after the correction of the spectrum for self-absorption the intensity of the direct transition exceeds the indirect one about 10 times [99].

2.4.7 *Photoluminescence spectra: resonant and non-resonant excitation conditions*

As we will see in the following, in photoluminescence spectroscopy we measure the energy distribution of emitted photons after optical excitation. The photo-excitation of carriers inside the sample can be achieved using different laser sources and the excitation conditions strongly affect the features of PL spectra. As a matter of fact, the energy of the exciting photons may or may not be *resonant* to optical transitions in the germanium band structure and this can be clearly seen at low lattice temperatures in which thermal excitation plays a minor role.

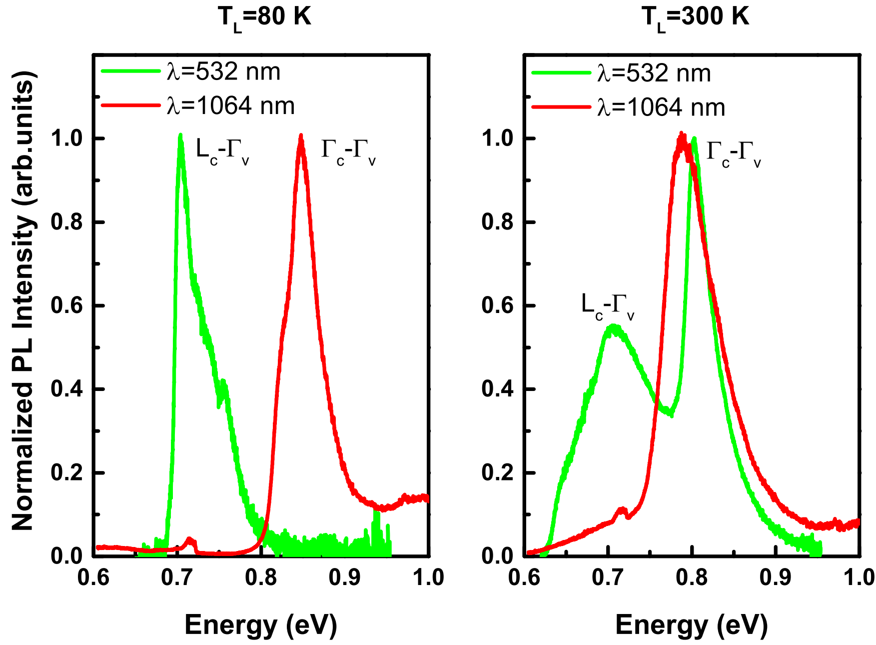

Figure 2.12 – LT (*left*) and RT (*right*) PL spectra of Ge under resonant (red lines) and non-resonant (green lines) excitation conditions.

Fig. 2.12 shows the micro-PL spectra obtained from a Ge bulk crystal acquired at a lattice temperature T_L = 80 K and T_L = 300 K using two different wavelengths (a detailed description of the spectral features will be given in the following Chapters). Whereas at T_L = 300 K the intensity of the direct gap transition $\Gamma_c - \Gamma_v$ ($\sim$ 0.8 eV) is comparable in both cases, at T_L = 80 K it is completely quenched in case of non-resonant excitation (λ=532 nm), and the spectrum is dominated by the indirect gap transition $L_c - \Gamma_v$ ($\sim$ 0.7 eV), but strong in case of excitation wavelength λ=1064 nm. These experimental findings can be interpreted on the basis of the sketch of carrier dynamics of Fig. 2.13, in which the excitation, thermalization and recombination processes under the two excitation conditions are schematically shown.

Let's start considering low temperatures. The term *resonant* is used since the energy of the excitation wavelength λ=1064 nm is E=1.16 eV, which is close to the direct gap energy of 0.80 eV at room temperature or $\sim$ 0.88 eV at 80 K. Therefore electrons are resonantly excited in the Γ_c valley where they can recombine giving rise to the $\Gamma_c - \Gamma_v$ recombination or can be efficiently scattered to L states, and then recombine leading to the indirect $L_c - \Gamma_v$ emission. In the case of non-resonant excitation, electrons are promoted to the continuum states well above the Γ_c valley, from where they can thermalize to the lowest energy state, i.e. the L_c valley. Consequently, only the indirect

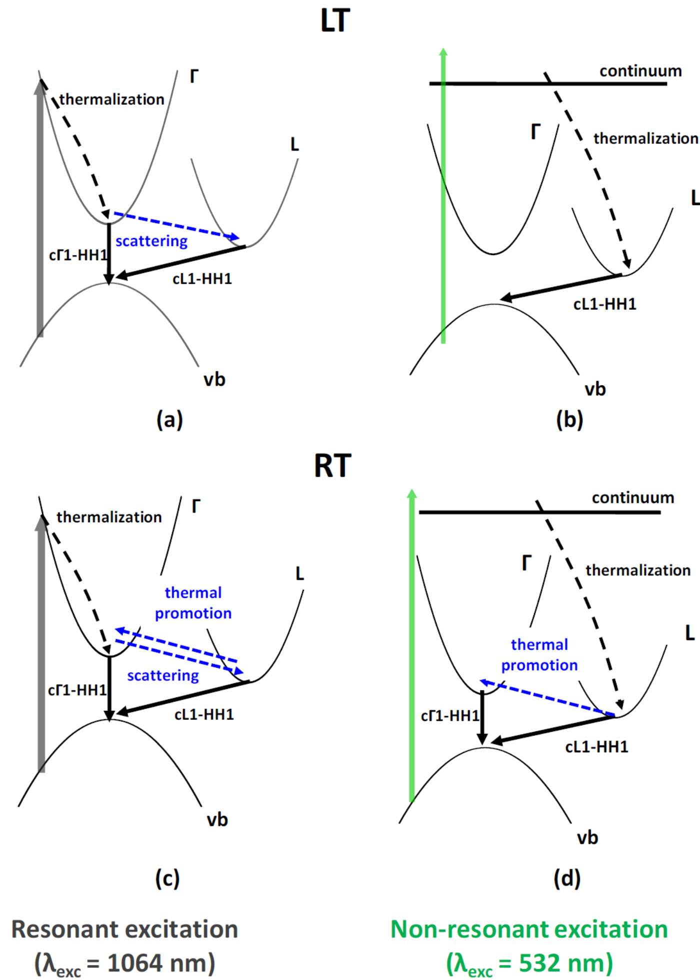

Figure 2.13 – Schematic sketch of carrier dynamics when carriers are excited in resonant [(a), (c)] or non-resonant [(b), (d)] conditions at LT [(a),(b)] and RT [(c), (d)]. Figure taken from [100].

$L_c - \Gamma_v$ recombination can be observed. Increasing temperature, the direct $\Gamma_c - \Gamma_v$ transition is visible in both resonant and non-resonant conditions. This can be explained considering that, when the sample is excited non-resonantly, electrons can be thermally promoted from the L_c valley to Γ_c, leading to the direct $\Gamma_c - \Gamma_v$ transition.

3

EXPERIMENTAL TECHNIQUES

The growth of the samples here investigated took place at the "Laboratory of Mesoscopic Physics and Nanostructures" at "Università degli Studi Roma Tre" by means of ultra-high vacuum (UHV)-CVD. Referring to the components sketched in Fig. 3.1, the set-up consists in one pipe (1) kept at an UHV pressure ($\sim 10^{-10}$ Torr) guaranteed by two ionic pumps, a pressure regime required in order to obtain high quality samples with low contaminations. Several chambers are connected to the tube with the help of suitable valves, allowing the low pressure conditions to be preserved within all the setup components. The only component at higher pressure (10^{-7} Torr) is the N_2-purged load-lock chamber (2), where substrates are loaded into the system.

The substrate is initially prepared in a clean environment under laminal flow equipped with a chemical hood (3) and loaded into the load-lock chamber (2). From there, with the use of magnetic manipulators, the substrate can reach the preparation chamber (4) and, along the tube (1), the UHV-CVD chamber (5) for deposition, or the X-ray photoemission spectroscopy (XPS) chamber (6) for analysis.

Employing the set-up here described, several samples have been grown and their structural properties have been investigated with several techniques.

3.1 CVD GROWTH SET-UP

The CVD chamber for the epitaxial growth is a steel cylinder with low content in carbon and nickel [1 in Fig. 3.2(a)]. The chamber is equipped with external water cooling to limit the contaminant desorption from the internal surface. The UHV pressure is reached with a proper pumping system of

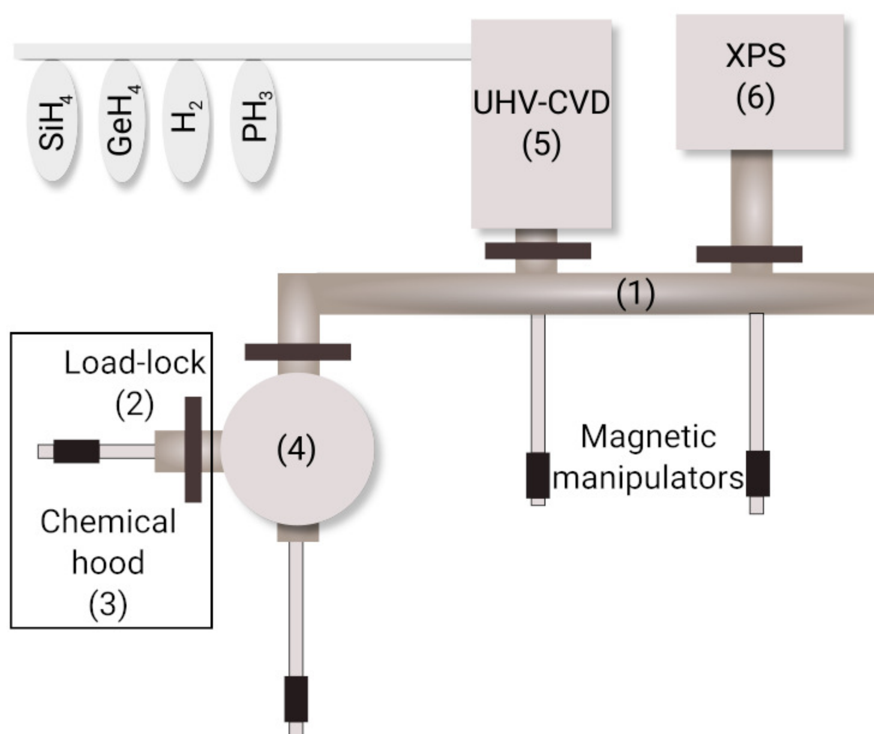

Figure 3.1 – Sketch of the growth set-up: (1) main pipe, (2) load-lock chamber, (3) chemical hood, (4) preparation chamber, (5) UHV-CVD growth chamber, (6) XPS chamber. Magnetic manipulators are used to transport the samples across the system.

turbomolecular and rotary pumps (2). At these pressure values, the molecules impinging the sample surface are few enough to guarantee a clean surface during deposition. As a matter of fact, the number of molecules hitting and sticking to a surface, per unit time and area is proportional to the pressure p, and is given by [79]

$$\Phi = 3.513 \times 10^{22} \frac{p}{\sqrt{mT}}. \tag{3.1}$$

For instance, at a pressure of 10^{-6} Torr the sample surface can be completely covered in about 1 second, while UHV conditions assure a clean surface for several hours. Moreover, the mean distance traveled by molecules between successive collisions, called the mean-free path, at pressure below 10^{-3} Torr is so large that molecules effectively collide only with the wall of the chamber. The presence of a throttle valve (3) in series with the main turbomolecular pump allows to select a reaction pressure in the 10^{-8}-10^{-2} Torr range. The difference of seven order of magnitude between the system base pressure (10^{-10} Torr) and the reaction pressure (10^{-3} Torr) allows to change the gas composition in the CVD chamber in a few seconds. Combined with the low temperature employed during the growth, this results in highly abrupt interfaces between different layers.

The deposition can take place introducing the reacting gases (silane, germane, phosphine, and hydrogen) in the CVD chamber through electro-pneumatic valves and the flux is set by mass flowmeters (5). Each gas has a separate line (4) to the chamber and to the purging system. In order to preserve the gas purity, the gas lines are continuously pumped by a turbomolecular pump. Since the purging system is indipendent from the pumping system of the CVD chamber, the pressure of the reacting gases can be monitored before their introduction in the chamber. Both valves and flowmeters are electronically controlled by a dedicated computer with a Labview graphical interface [Fig.3.2(b)], which is also used for automatic depositions of the heterostructures. The temperature of the substrate required for the gas activation (the pyrolysis process described in section 1.6.3) is reached heating the sample via Joule effect with a power supply [6 in Fig. 3.2(a)] that delivers the set current to the sample through a metal finger (7), connected to an electrical feed-through. As a consequence, it is possible to change the substrate temperature in just a few seconds. A set of windows allows to monitor the substrate temperature and the pressure inside the chamber by different instruments working at different ranges. The

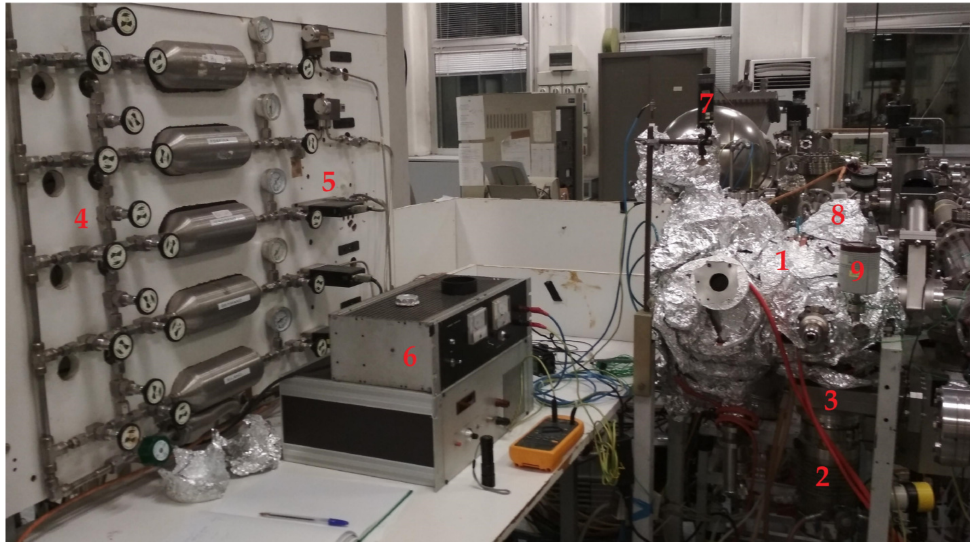

(a)

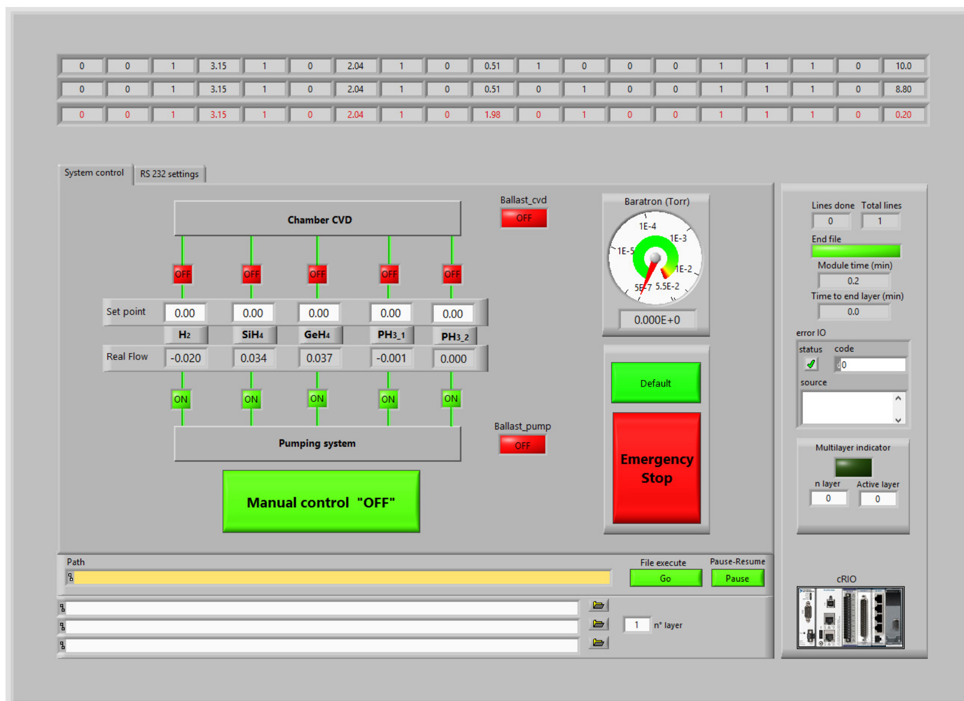

(b)

Figure 3.2 – (a) Photograph of the CVD growth set-up. (b) Labview interface to control gas valves and flowmeters.

Mikron M190 infrared pyrometer allows to monitor the temperature in the 300-1000°C range with a response time of ∼ 50 ms and accuracy between 0.3 and 0.8% of reading. The temperature during the annealing at 1150°C is instead monitored with an Impac IS 140 pyrometer, which works in the 650-1800°C range. The accuracy of this instrument is 0.4% of reading and the response time is less than 1 ms. Before and after the deposition process, the UHV pressure inside the chamber is measured by an ion gauge (8), that has to be switched off when the gaseous precursors are present. In fact, silane and germane can damage the ion gauge because of the hot metal filament it uses to measure the pressure, on which the pyrolysis can occur, resulting in malfunctioning or breaking. During the deposition process the pressure is thus monitored with a capacitive sensor (9), which does not employ a hot filament but can measure pressures only in the range of 10^{-3} Torr.

3.2 STRUCTURAL CHARACTERIZATION

3.2.1 *X-ray photoemission spectroscopy*

The experimental set-up depicted in Fig. 3.1 is equipped with an UHV chamber (6) for X-ray photoemission spectroscopy, used to verify SiGe alloy concentrations and identify eventual contaminants inside the samples and on the substrates surface, directly *in-situ*.

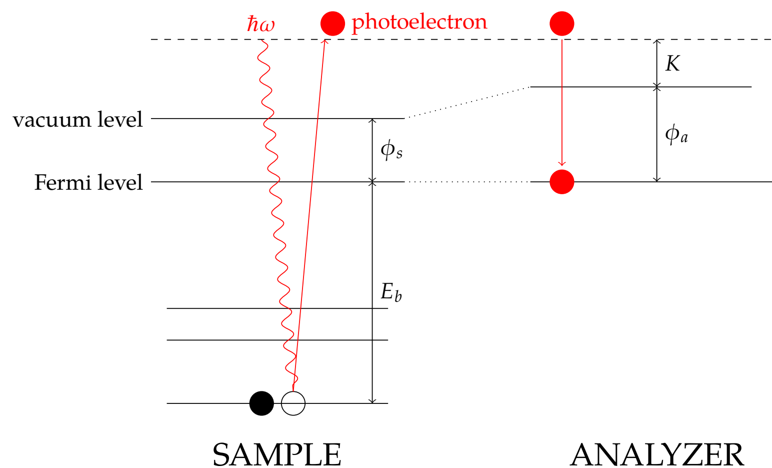

Figure 3.3 – Energy level diagram of XPS. The kinetic energy K of the photoemitted electron, hit by the radiation $\hbar\omega$, is related to the binding energy E_b inside the material.

The operating principle of the XPS technique is based on the photoelectric effect (schematically depicted in Fig. 3.3), according to which a material emits electrons if hit by radiation with a sufficient energy $\hbar\omega$. The kinetic energy K of the photoemitted electrons is given by

$$K = \hbar\omega - E_b - \phi_a, \tag{3.2}$$

where E_b the binding energy related to the initial state before photoemission and ϕ_a the work function of the analyzer, that is the energy separation between the vacuum level and the Fermi level. Knowing ϕ_a and measuring the kinetic energy K of the photoelectrons, using Eq. 3.2 it is therefore possible to retrieve their binding energy E_b, peculiar of each specific element. In the case of the work here presented, the XPS technique has been employed to retrieve the composition of the deposited $Si_{1-x}Ge_x$ alloys to eventually calibrate the growth parameters, as we will see in the following, and to check the contamination level of both samples and substrates, limited to the first surface layers due to the low photoelectrons escape depth inside the material (few Ångström).

In Figure 3.4 is reported a typical XPS spectrum of a SiGe sample in the range 0-600 eV of binding energy (E_b). Several features can be observed, among which we report in the insets three important energy ranges. In the range E_b=20-100 eV the peaks related to photoemission from the Ge 3d and the Si 2p core levels are highlighted, since they are used to retrieve the alloy concentration. As a matter of fact, the number of counts recorded by the analyzer is proportional to the corresponding element abundance, weighted by the cross section of the specific electronic level involved (the atomic sensitivity factors are ASF(Ge^{3d})=0.3 and ASF(Si^{2p})=0.17). Thus, the concentration x of a $Si_{1-x}Ge_x$ layer can be obtained as

$$x = \frac{(I(\mathrm{Ge}^{3d})/0.3)}{[(I(\mathrm{Ge}^{3d})/0.3) + (I(\mathrm{Si}^{2p})/0.17)]}, \tag{3.3}$$

where $I(i)$ is the integrated intensity of the i-peak. Although Eq. 3.3 is valid only in the case of planar films and homogeneous compositions, the Ge concentrations obtained are in good agreement with those measured with XRD, as we will see in the following.

The insets on the right of Fig. 3.4, are a zoom of regions of the spectrum related to the most intense peak of carbon (C^{1s}) and oxygen (O^{1s}), the most common contaminants. The extremely suppressed intensity of the peaks

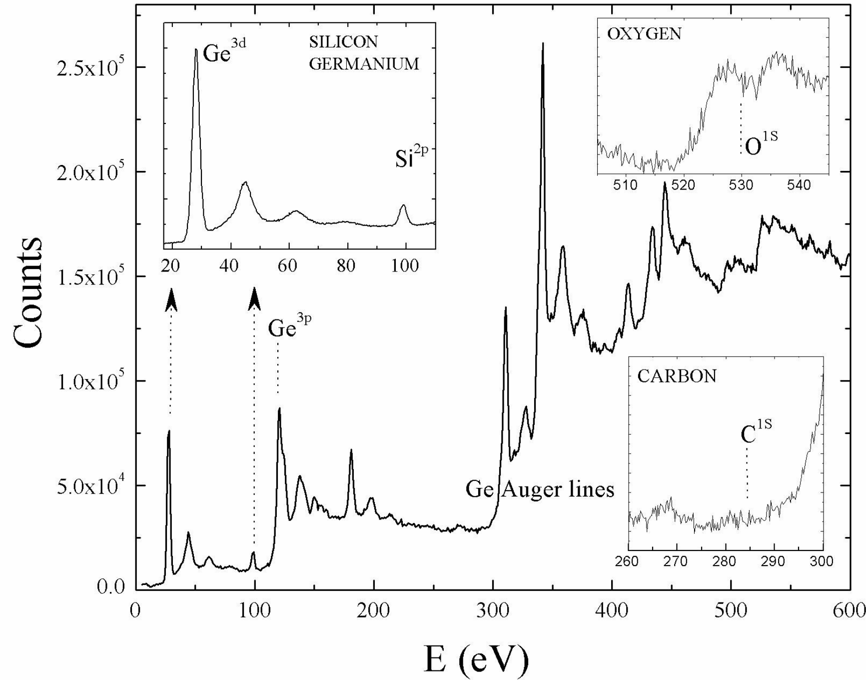

Figure 3.4 – Example of an XPS spectrum acquired to check the desired composition of the SiGe alloy and to verify the presence of eventual contaminants. Insets show the zoom of three important energy ranges in which germanium 3d (Ge^{3d}), silicon 2p (Si^{2p}), oxygen 1s (O^{1s}) and carbon 1s (C^{1s}) peaks are present.

related to carbon and oxygen testifies their low concentration, assuring the high cleaning level and the quality of the sample under investigation.

XPS Set-up

The X-ray photoemission spectroscopy is performed in a commercial Perkin-Elmer UHV-chamber equipped with an X-ray source and an electron analyzer (Fig. 3.5). The source provides a photon beam of 1486.6 eV (Al-K_α line) generated by the radiative electron-hole recombination in the aluminum anode, hit by electrons thermo-emitted from a tungsten cathode. The radiation is sent through a toroidal monochromator to eliminate satellite lines and to reduce its linewidth from $\sim$ 1.1 eV down to a value around 0.3 eV, and it is then directed towards the sample, where the photoelectric effect, described above, takes place. The ejected electrons pass through electrostatic lenses and are then retarded by an amount R before entering the analyzer. The analyzer is an hemispheric cavity whose walls are polarized and acts as a band-pass filter, only transmitting electrons with energy very near to a specific energy (the so called pass-energy). As a matter of fact, varying the applied potential

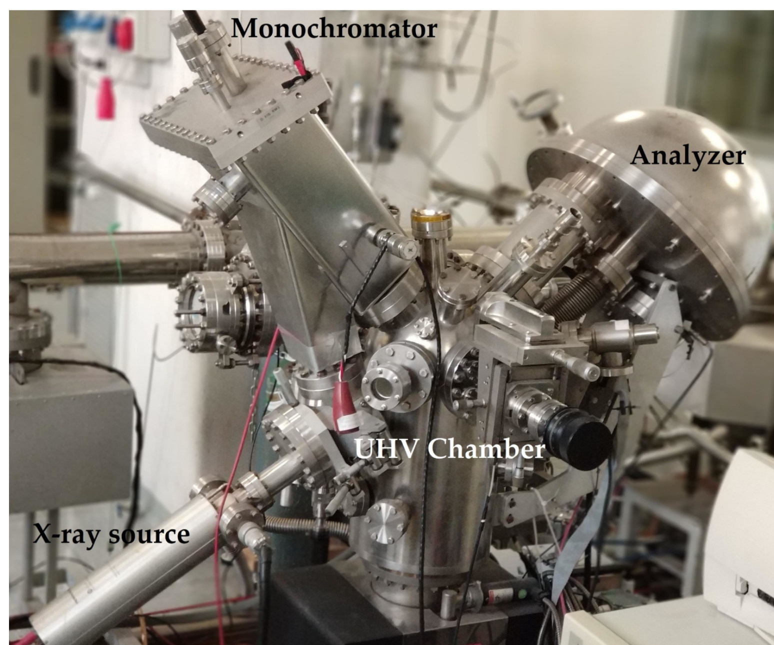

Figure 3.5 – Photograph of the experimental XPS set-up.

it is possible to select only the electrons with the right trajectory, able to get through the cavity without hitting the walls and thus enter a multichannel detector (*channeltron*). In the channeltron, electrons are multiplied in number, emitting several electrons for every incident one in a cascade process which results in an amplification of a factor of 10^6. Therefore, for every electron entering the channeltron an electric signal is generated, associated to the specific electron energy set to exit the hemispheric cavity. The retard R is used to scan the spectrum while the hemispheric cavity is operated at a constant pass-energy. This results in a constant resolution across the entire energy spectrum, whose value is, at the lowest pass-energy, of about 0.35 eV.

3.2.2 *X-ray diffraction*

High resolution X-ray diffraction (HR-XRD) is an unrivaled tool to analyze the crystal structure of heteroepitaxial layers since it is not only possible to determine the lattice parameters, but also to retrieve informations on thickness and crystal quality of epilayers on substrates. In this work, XRD has been employed to retrieve the concentration of the $Si_{1-x}Ge_x$ layers and their relaxation. Moreover, XRD on superlattices allows the determination of layers thickness.

The operating principle of the XRD technique is based on diffraction of X-rays impinging on a crystal surface. Diffraction is a coherent and elastic scattering phenomenon with a momentum transfer between incident and scattered radiation. Considering an X-ray with wavelength λ and wave vector $|k_{in}| = 2\pi/\lambda$, imping on a surface with an angle θ, the scattering vector (momentum transfer) is given by $q = k_{out} - k_{in}$, where k_{out} is the scattered wave vector.

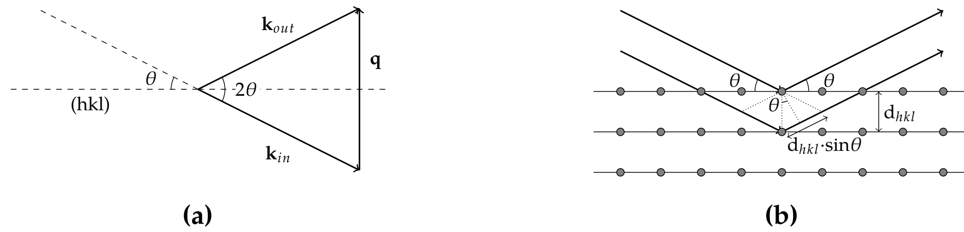

Figure 3.6 – (a) The so-called scattering triangle. (b) Sketch of the Bragg equation.

For parallel planes of atoms, with a space d_{hkl} between the planes, constructive interference occurs only when is satisfied Bragg's law:

$$\lambda = 2d_{hkl} \cdot sin\theta. \tag{3.4}$$

Experimentally, the X-ray wavelength λ is fixed, consequently, a family of planes produce a diffraction peak only at a specific angle θ. The Bragg diffraction from planes parallel or inclined by an angle φ with respect to the crystal surface is defined symmetrical (φ=0) or asymmetrical ($\varphi \neq$0), respectively.

Let ω be the incidence angle with respect to the sample surface of a parallel and monochromatic X-ray beam; three possible scan modes can be performed to measure the intensity profile $I(\omega)$, $I(2\theta)$, $I(\omega - 2\theta)$:

(i) the ω scan when the detector is fixed in 2θ position and ω is changed by rotating the sample on the diffractometer axis (*rocking curve*). The same results can be also obtained rotating jointly source and detector by the same angle;

(ii) the 2θ scan when the sample is fixed and the detector is moved (*detector scan*);

(iii) the $\omega - 2\theta$ scan if the detector is rotated but twice as fast as the sample (for each increment $\Delta\omega$, $\Delta 2\theta = 2\Delta\omega$) [101].

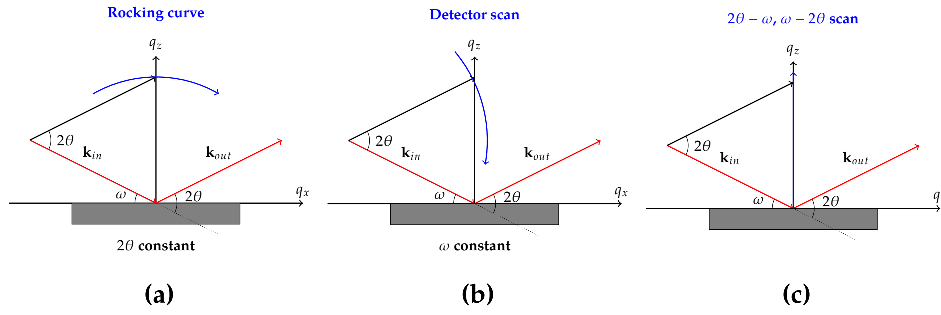

Figure 3.7 – Schematization of the three possible scan modes to perform XRD.

For XRD measurements on silicon and germanium, to infer structural information, the Bragg peaks from symmetric (004) and asymmetric (224) Miller planes are the most commonly used. These planes are illustrated in Fig. 3.8. As can be seen in Fig. 3.8, the Bragg peaks from the (004) planes only carries information about the out-of-plane lattice parameter $a_\perp$, while the peak from the (224) set of planes carries information about both the in-plane and out-of-plane lattice parameters. Due to this, the (004) and (224) peaks are useful because they can be used to determine *both* the in-plane and out-of-plane lattice parameters.

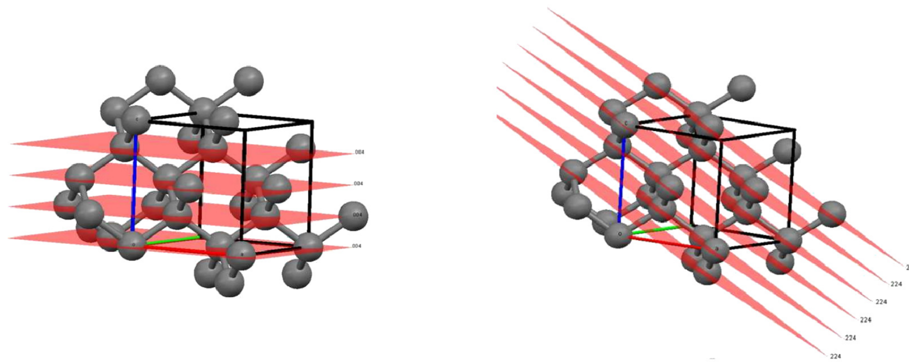

Figure 3.8 – (004) (left) and (224) (right) planes in Si and Ge.

A typical (004) $\omega - 2\theta$ rocking curve scan acquired on an heteroepitaxial Ge layer on a Si (001) substrate is reported in Fig. 3.9 [102]. The two diffraction peaks are related to the Si substrate and the Ge epitaxial layer. The out-of-plane reciprocal lattice parameter can be derived from the diffraction angle as

$$q_z = \frac{2sin(2\theta/2)}{\lambda}, \tag{3.5}$$

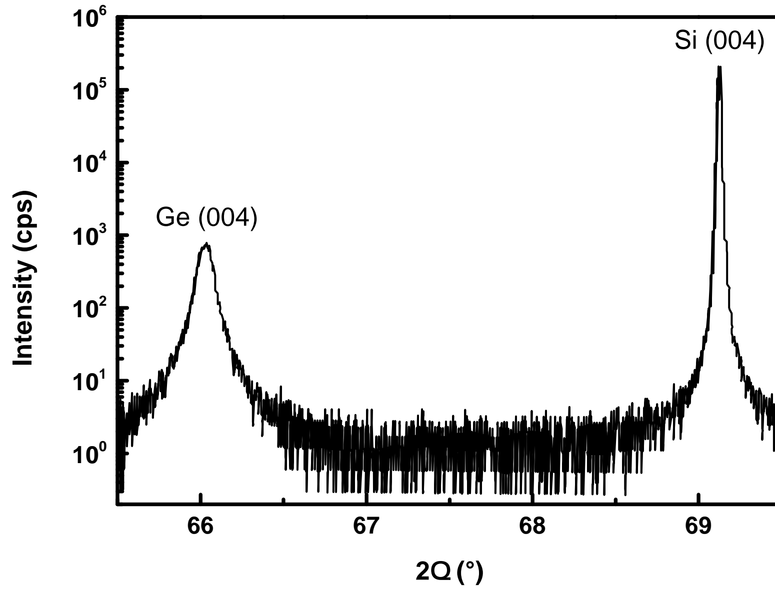

Figure 3.9 – (004) $\omega - 2\theta$ rocking curve scan acquired on heteroepitaxial Ge/Si (001) [102].

and the corresponding lattice parameter is given by

$$a_\perp = 4/q_z. \tag{3.6}$$

Equation 3.6, is valid only in the specific case of (004) rocking curves. In the case of (00l) rocking curves, Eq. 3.6 becomes

$$a_\perp = \sqrt{l^2}/q_z. \tag{3.7}$$

Although the XRD rocking curve is easy and quick to measure, the symmetry scan doesn't provide information about the in-plane lattice constant. Even more important, for alloy crystalline materials, such as SiGe, the lattice parameter is determined by both the component composition and the lattice relaxation. To solve this problems, two-dimensional asymmetric scans of diffraction patterns are very helpful. This method is called XRD reciprocal space mapping (RSM) which is capable of unveiling the relative lattice tilt, the material composition, and an estimate of the residual strain in epitaxial layers compared to the substrate [103]. By selecting an asymmetric reflection, the lattice plane spacing d_{hkl} can be separated into the parallel $d_\parallel$ and perpendicular $d_\perp$ components to the sample surface. A reciprocal space mapping of the scattered intensity, obtained by combining ω and ω-2θ scan modes, enables to separate these contributions. In the 2D RSM, the out-of-plane [00l] direction is plotted as the y-axis and the in-plane [hk0] direction is plotted as

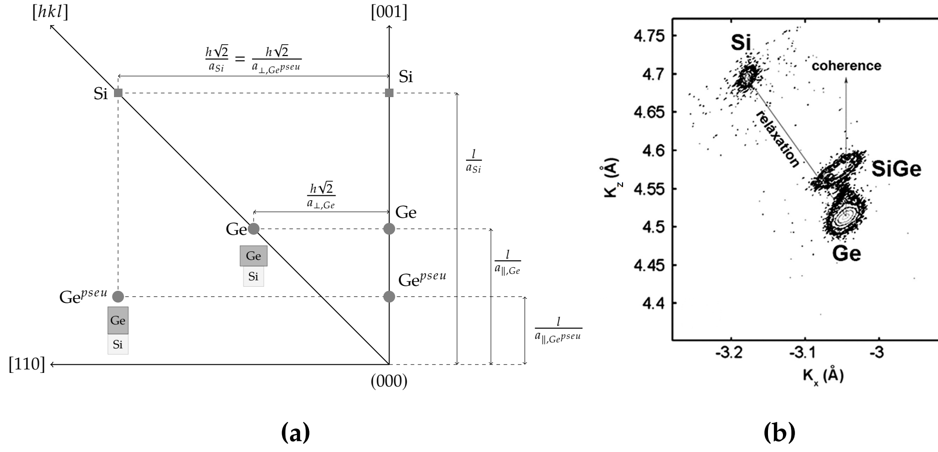

(a) **(b)**

Figure 3.10 – (a) Schematic representation of correlation between distances in reciprocal space and lattice constants in ($a_{\|}$) and perpendicular ($a_{\perp}$) to the [001] direction in the case of pseudomorphic (Ge^{pseu}) and fully relaxed (Ge) Ge layer on Si. (b) Experimental RSM around the Si substrate 224 lattice point in the case of a SiGe layer grown on a Ge/Si VS. Both the relaxation and coherence lines have been reported [105].

the x-axis.

The conversion of a peak intensity position ($\omega,\ \theta$) in reciprocal space coordinates (q_z, q_x) is given by

$$q_x = R[-cos(\omega) + cos(2\omega' - \omega)] \quad (3.8a)$$

$$q_z = R[sin(\omega) + sin(2\omega' - \omega)], \quad (3.8b)$$

where R=$|\boldsymbol{k}_{in}|$=$2\pi/\lambda$, $2\omega'$ corresponds to any arbitrary position of the detector and $2\omega' = 2\theta$ when the Bragg condition is satisfied. A schematic representation of correlation between distances in reciprocal space and lattice parameters in the case of pseudomorphic (Ge^{pseu}) and fully relaxed (Ge) Ge layer on Si, is reported in Fig. 3.10(a) [104]. In the case of asymmetric (224) reflections the lattice parameters are given by

$$a_{\perp} = \sqrt{l^2}/q_z = 4/q_z \quad (3.9a)$$

$$a_{\|} = h\sqrt{2}/q_x = -2\sqrt{2}/q_x \quad (3.9b)$$

where q_x and q_z are the reciprocal lattice parameters calculated according to Eq.s 3.8.

An experimental (224) reciprocal space map acquired on an heteroepitaxial SiGe layer on a Ge/Si virtual substrate is reported in Fig. 3.10(b) [105]. The

relaxation line, going from (000) to the Si substrate 224 lattice point, represents the fully relaxed growth of a cubic crystal ($a_{\perp} = a_{\|}$), i.e. linearly decreasing the Ge content x of relaxed $Si_{1-x}Ge_x$ alloys their diffraction peaks would lie on the relaxation line. The coherence line, instead, reproduces a pseudomorphic growth, i.e. layers having the same in-plane lattice parameter.

XRD Set-up

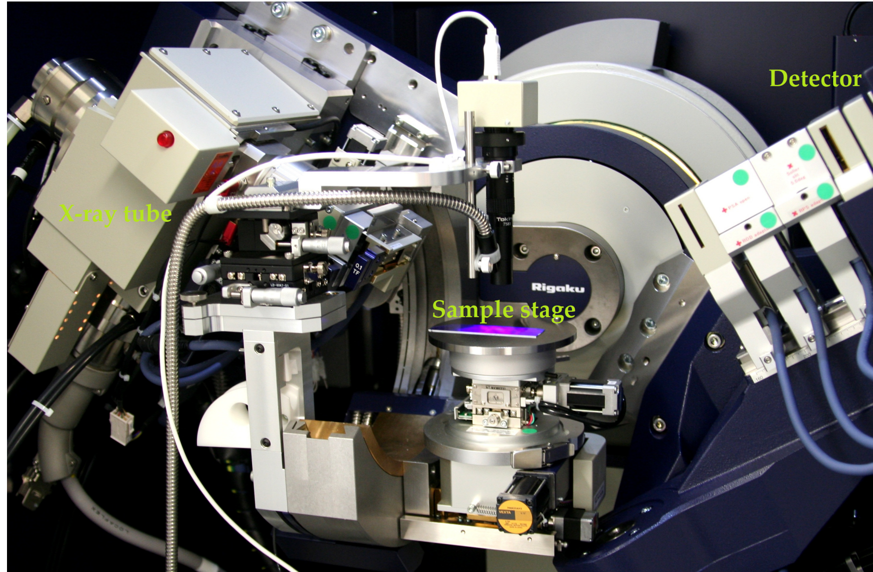

Figure 3.11 – Photograph of the experimental XRD set-up.

A preliminary requirement of X-ray-based techniques for accurate measurements in semiconductor heterostructures is the use of well-collimated monochromatic X-ray sources with small divergence and wavelength dispersion. As a matter of fact, the differentiation of equation 3.4 and the subsequent division of the result by the same equation 3.4 yields the differential Bragg equation

$$\frac{\Delta\lambda}{\lambda} = \frac{\Delta d_{hkl}}{d_{hkl}} + cot\theta \cdot \Delta\theta. \tag{3.10}$$

Equation 3.10 shows that for the accurate determination of the distance d_{hkl} between two adjacent lattice planes it is important to use a highly monochromatic incident beam and very good angular resolution. HR-XRD measurements were carried out at IHP - Leibniz-Institut für innovative Mikroelektronik, Frankfurt (Oder), with a SmartLab diffractometer from Rigaku equipped with a 9 kW rotating anode Cu source (λ = 0.15406 nm), a Ge (400)x2 crystal collimator, and a Ge (220)x2 crystal analyzer. By means of the Ge (400) double-crystal monochromator added in the beam path, whose functional principle is based on the Bragg reflection of the primary beam at

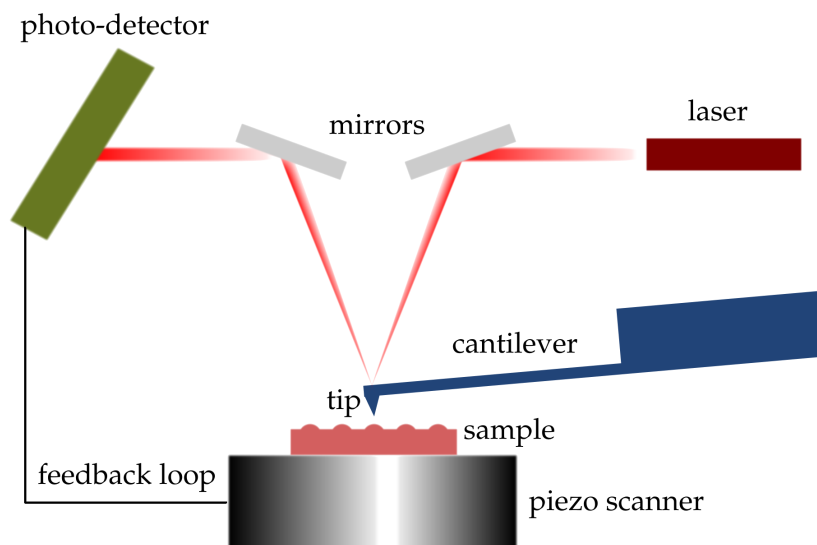

Figure 3.12 – Scheme of AFM.

two germanium crystals with (400) surfaces, the X-ray beam divergence is significantly reduced (up to 5 arc sec). Moreover, the spectral width of the incident Cu K_α X-ray beam can be reduced to $\Delta\lambda/\lambda$ better than a few 10^{-4}, reducing the wavelength distribution of the incident beam nearly to the Cu $K_{\alpha 1}$ line only. The Ge (220)x2 crystal analyzer is used to restrict the 2θ take-off angle and wavelength, allowing precise observations of the diffraction angle.

3.2.3 *Atomic force microscopy*

The atomic force microscopy (AFM) is a scanning probe technique largely used in the characterization of the surface of several kind of samples in different conditions. Here, it has been used to image the surface morphology of the grown structures in order to retrieve the surface roughness and the characteristic dimension of eventual surface defects.

The AFM consists of an elastic cantilever with a sharp tip at its end that is used to scan the sample surface. When the tip is into proximity of a surface, forces between the tip and the sample lead to a deflection of the cantilever according to Hooke's law. Measuring the cantilever deflection, it is possible to evaluate the tip-surface interaction.

The AFM can be divided in three main building blocks: a piezoelectric transducer, a force transducer (force sensor), and a feedback control. While the piezoelectric transducer moves the tip over the sample surface, the force transducer senses the force between the tip and the surface, and the feedback control feeds the signal from the force transducer back in to the piezoelectric, to maintain a fixed force between the tip and the sample. Thus, if the probe registers an increase in force (for instance, while scanning, the tip encounters a particle on the surface), the feedback control causes the piezoelectrics to move the probe away from the surface. In most of the AFM commercially available (included the one employed in this work), the force transducer is based on the detection of the deflection of a laser beam reflected by the back side of a reflective cantilever onto a four-segment position-sensitive photo-detector (PSPD) (see Fig. 3.12). If a probe, mounted on the front side of the cantilever, interacts with the surface the reflected light path will change. The force is then measured by monitoring the change in light detected by the four quadrants of the photo-detector.

The interactive forces measured by AFM can be approximated by a Lennard-Jones potential [Fig. 3.13(a)]:

$$U(r) = U_0 \left[-2 \left(\frac{r_0}{r} \right)^6 + \left(\frac{r_0}{r} \right)^{12} \right], \tag{3.11}$$

where the first term describes the long range attractive Van-der-Waals forces and the second term takes into account the short range repulsion due to the Pauli exclusion principle. The parameter r_0 is the equilibrium distance between atoms, the energy value in the minimum.

Two main operation mode of the AFM can be distinguished, depending on the interaction force to probe. In *contact mode* the feedback system controls the piezoelectric scanner to increase or decrease the tip-sample distance to keep a constant *repulsive* force between the tip and the sample surface. A plot of this upward and downward motion, as a function of the tip x-y position on the sample surface, provides a high-resolution image of the surface topography. High resolution is possible because very small changes in distance [see Fig. 3.13(a)], lead to large changes in force which is the parameter being monitored. However, for some samples such as biological specimens or soft material such as some polymers, contact of the surface with the tip can damage the sample. Another drawback is that the lateral force

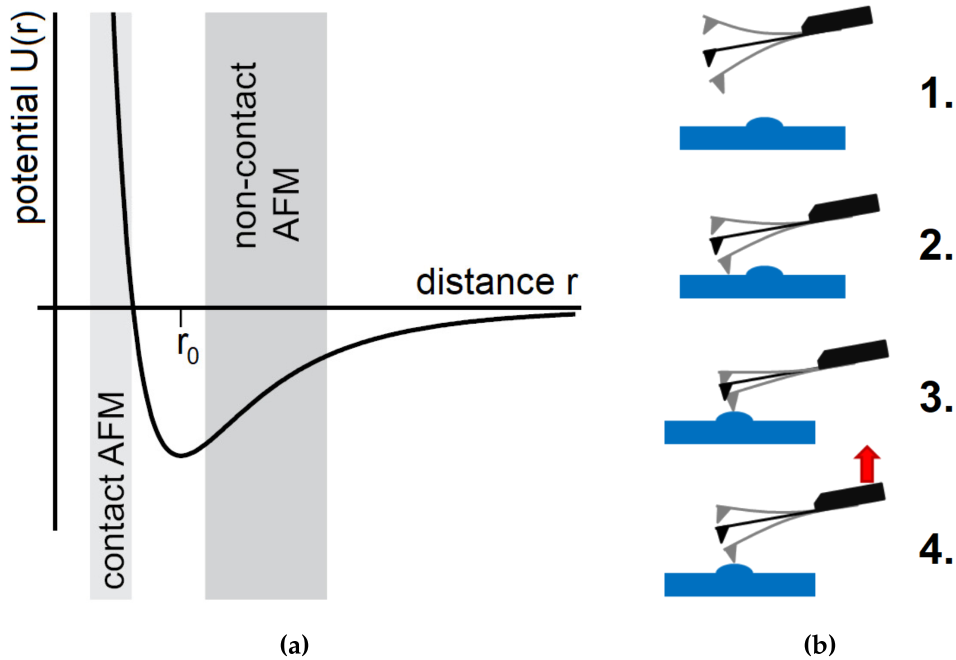

(a)

(b)

Figure 3.13 – (a) Lennard-Jones potential. (b) Operation of tapping mode AFM: 1. Cantilever oscillates in free air: amplitude is larger than setpoint. 2. Tapping on sample: cantilever oscillates at setpoint amplitude. 3. Tip encounter a particle: cantilever oscillation amplitude drops. 4. Feedback increases the tip-surface distance: amplitude returns to setpoint.

exerted on the sample can be quite high. This can result in sample damage or the movement of relatively loosely attached objects. To overcome this problems, an alternative approach is employed referred to as *tapping mode*, which works with longer range forces which are *attractive*. In tapping mode, the vertical resolution is not as high as in contact mode, since changes in the distance r lead to smaller changes in force. However, since the tip touches the surface for a short amount of time, very high lateral resolution can be achieved.

In non-contact AFM mode, the tip of the cantilever does not contact the sample surface. The cantilever is instead oscillated, usually with an additional piezoelectric element, at its resonant frequency. When the oscillating probe approaches the sample surface, the oscillation changes due to the interaction between the probe and the force field from the sample. The effect is a damping of the cantilever oscillation, which leads to a reduction in the frequency and amplitude of the oscillation. The oscillation is monitored by the force transducer and the feeedback loop system adjusts the tip-sample distance to maintain a set cantilever oscillation amplitude. Monitoring the height of

the cantilever above the sample at each (x,y) data point allows to the scanning software to construct a topographic image of the surface [see Fig. 3.13(b)].

The damping of the cantilever oscillation can be understood considering that the cantilever motion can be approximated considering an equation of motion for a 1-dimensional point mass m attached at a spring [106]

$$m\ddot{r} + kr + \frac{m\omega_0}{Q}\dot{r} = F_{ts} + F_0\cos(\omega t), \tag{3.12}$$

where F_0 and ω are the amplitude and the frequency of the driving force, respectively. In the absence of tip-sample interaction (F_{ts}=0) Eq. 3.12 represents the model for the 1-dim force driven harmonic oscillator with damping, whose solution is

$$r = A\cos\big(\omega t - \phi\big) + Be^{-\alpha t}\cos\big(\omega_r t + \beta\big). \tag{3.13}$$

In equation 3.13 ω_r is the resonance angular frequency of the cantilever influenced by the damping effect and ϕ is the phase difference between the driving force and the cantilever motion. The first term of Eq. 3.13 is a steady solution and the second term is a transient one. Neglecting, for the sake of simplicity, the transient term, the solution of Eq. 3.13 shows sinusoidal behavior with an amplitude

$$A(\omega) = \frac{F_0/m}{\sqrt{(\omega_0^2 - \omega^2)^2 + (\omega\omega_0/Q)^2}}. \tag{3.14}$$

Now, in the case of a tip–sample interaction, we can still use Eq. 3.12 with a modified spring constant k_e

$$k_e = k - \Delta F_{ts}, \tag{3.15}$$

which is called the effective spring constant. As a result, the modified resonance frequency is

$$\omega' = \sqrt{\frac{k_e}{m}} = \sqrt{\frac{k - \Delta F_{ts}}{m}}, \tag{3.16}$$

and the amplitude is given by

$$A(\omega') = \frac{F_0/m}{\sqrt{(\omega_0^2 - \omega^2 - \Delta F_{ts}/m)^2 + (\omega\omega_0/Q)^2}}. \tag{3.17}$$

Therefore, the tip-sample interaction results in a resonance frequency ω' and amplitude $A(\omega')$ that are differents from the same parameters without the

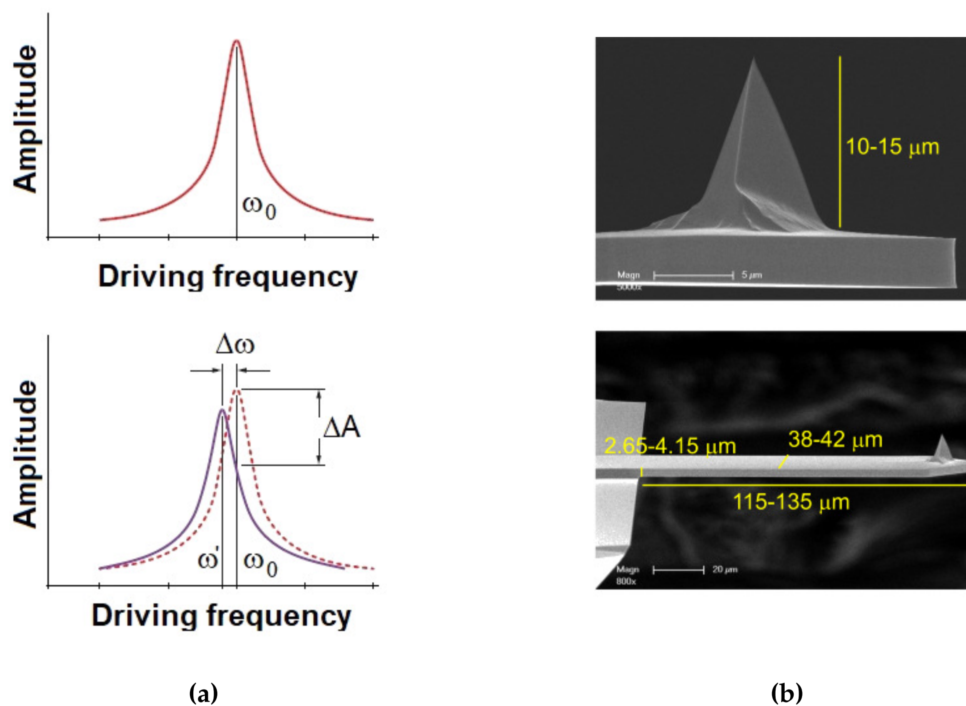

Figure 3.14 – (a) Illustration of the relationship between the frequency shift, the amplitude reduction and the interacting force. (b) Electron micrograph of an AFM tip (top) and cantilever (bottom).

interaction [Fig. 3.14(a)]. It follows that, forcing the cantilever to oscillate at the frequency ω, resonance frequency without interaction, when the tip is close to the surface the system is not resonant anymore, being $\omega \neq \omega'$, and the amplitude drops.

AFM Set-up

The AFM measurements on the investigated samples have been performed in the LIME laboratory (Laboratorio Interdipartimentale Microscopia Elettronica) in Roma Tre with a Bruker Dimension Icon AFM. The system is divided in several specialized components:

- Motorized stage
- Optics and motors
- Scanner
- Probe holder
- Microscope electronics box

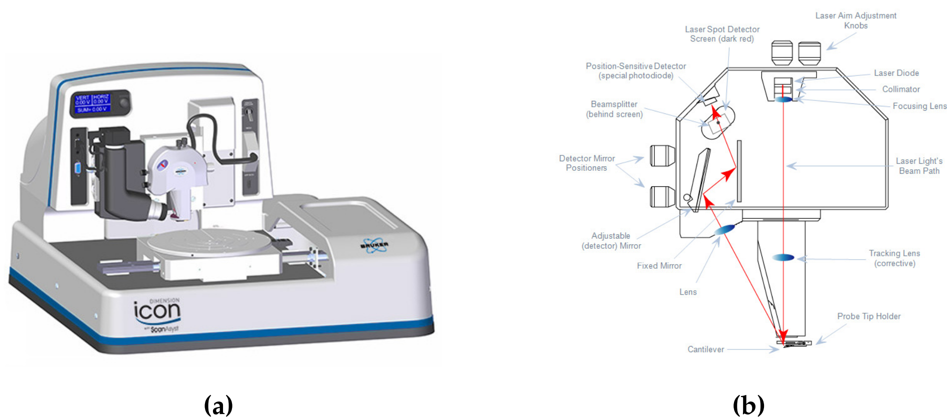

(a) **(b)**

Figure 3.15 – Bruker Dimension Icon AFM and scheme of the scanner.

The xy stage permits micrometer-scale positioning of samples beneath the tip, assuring position repeatability of 2 μm, while the motorized z-stage provides accurate, automatic tip engagement and approach. The rigidity of the z-stage permits low noise and high accuracy imaging, reducing noise levels in the sub-angstroms range for the z-axis, and angstroms in x-y. The optics system assists to locate the cantilever and tip relative to the sample. The system automatically focuses on most samples by adjusting the scanner height. The force transducer of the system is the scanner, which contains the laser source, the beam path, and the photo-detector. The scanner provides accurate imaging of a stationary sample while scanning the integrated detector-probe assembly above the sample. The probe holder contains a piezoelectric stack to oscillate the cantilever for tapping-mode AFM. The same cantilever holder is used for contact AFM, but no voltage is applied to the piezo stack. The microscope electronics box controls the feeedback loop system.
The entire system lies vibration-damping table to isolate the AFM from vertical and horizontal vibrations.

Bruker TESPA-V2 probes have been employed. In this probes, made of Si using MEMS technology, the cantilever has a rectangular shape with an aluminum reflective coating on the backside to increase the laser reflection. The spring constant of the cantilever is strictly related to its geometry, and is given by:

$$k = \frac{Ewt^3}{4L^3}. \tag{3.18}$$

In equation 3.18, E is the Young's modulus, w the width of the cantilever, t its height, and L its length. The spring constant of TESPA-V2 probes is k=37 N/m, while its resonant frequency is ω_0=320 kHz. Tips have a pyramidal

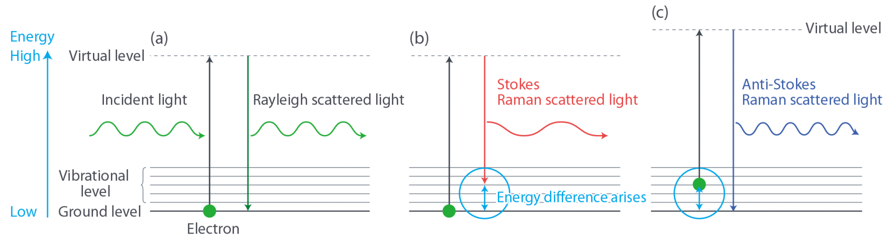

Figure 3.16 – (a) An electron is excited from the ground level and falls to the original ground level. (b) An electron is excited from the ground level and falls to a vibrational level. (c) An electron is excited from a vibrational level and falls to the ground level.

shape, with nominal radius 8 nm and height 12.5 μm. The half-cone angle is 20°.

3.2.4 *Raman spectroscopy*

A standard tool for the investigation of the effects of strain in SiGe heterostructures is Raman spectroscopy, in which the shift of the scattered Raman signal is proportional to the strain in the material [107].

Raman scattering is the inelastic scattering of photons by some excitation of a material [101]. As a matter of fact, when light is scattered by matter, almost all of the scattering is an elastic process (Rayleigh scattering), where electrons are excited to an unstable virtual state and immediately fall to the original ground level (Fig. 3.16). However, a small percentage of the incident light can induce transitions from the ground level to an excited state (Stokes Raman scattering) or from excited states to the ground level (anti-Stokes Raman scattering). Among the many excitations that can interact with photons (plasmons and collective electronic modes, spin flips) in this work we will concentrate on lattice vibrations, i.e. phonons.

The Raman scattering efficiency, I, depends on the polarization vector of the incident (e_i) and scattered (e_s) light, and is given by [108]

$$I = C \sum_j |e_i \cdot R_j \cdot e_s|^2, \tag{3.19}$$

where C is a constant and R_j is the Raman tensor of the j-phonon. The Raman tensor is a second rank tensor that can be used to calculate selection rules regarding which vibrations can be probed with incident light

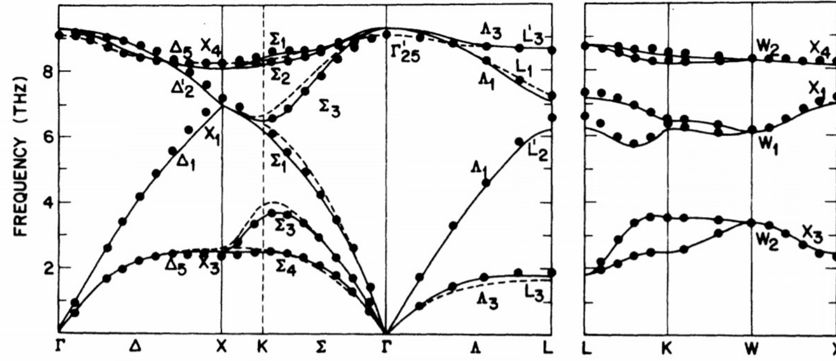

Figure 3.17 – Dispersion curves for acoustic and optical phonons in germanium [109].

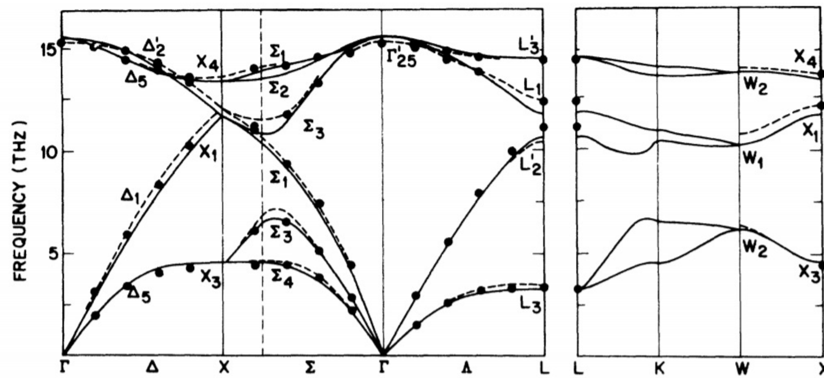

Figure 3.18 – Dispersion curves for acoustic and optical phonons in silicon [109].

with a certain polarization. The experimental geometry employed allows to simplify the problem. As a matter of fact, in the specific configuration of backscattering geometry from the (001) sample surface, only scattering by longitudinal optical (LO) phonons leads to a non-zero scattering intensity I.

Usually, Raman spectra are reported as intensity of scattered light versus wavenumber (called Raman shift). For instance, a Raman peak at 547.14 nm, obtained by a 532 nm excitation wavelength, can be converted into a wavenumber as

$$\text{Raman shift} = \left(\frac{1}{532\ \text{nm}} - \frac{1}{547.14\ \text{nm}}\right) = 520\ \text{cm}^{-1}. \tag{3.20}$$

This notation is used because the Raman shift is linearly related with energy and makes the form of the Raman spectrum independent of the excitation wavelength.

GERMANIUM PHONON DISPERSION The dispersion curve of phonons of a cubic lattice, such as Si and Ge, is characterized by six branches, three optical

phonon modes and three acoustical ones. At $\boldsymbol{k}$=0 the optical and acoustic branches are degenerate. The frequency of the acoustical branches equals zero in Γ, whereas the frequency of optical phonons at 300 K is $\nu_{LTO}(\Gamma_{25'})$=9.02×10^{12} Hz for Ge, and $\nu_{LTO}(\Gamma_{25'})$=15.53×10^{12} Hz for Si [110]. The dispersion curve of phonons in Ge and Si, along several lines of high symmetry, are reported in Fig. 3.17 and Fig. 3.18, respectively.

The triply degenerate optical vibration modes at $\boldsymbol{k} = 0$ are Raman active. However, the presence of a static electric field or a static strain is responsible of lowering the crystal symmetry lifting the degeneracy. This is the reason why Raman spectroscopy represents an effective method to obtain information about strain configuration in crystals. The possible approaches to link strain distribution and Raman shifts are mainly based on group theory or first order perturbation theory. While the former is purely qualitative and does not give an insight into the mechanism responsible for Raman shift, the latter can describe how the microscopic parameters of the crystal, such as the atomic force constants, the electronic polarizability and the atomic displacements, can enter the frequency shift. In this second framework, the quasi-harmonic approach of Ganesan *et al.* is collocated[111]. By means of a first order perturbation theory, the vibration frequencies are evaluated as an effect of a generalized force (i.e. strain field) on the atoms of a crystal which execute harmonic vibrations among equilibrium positions (shifted from the ones in absence of the generalized force). The effect of stress on the Raman modes for the three optical phonon modes is given by:

$$\omega^2 \hat{\boldsymbol{e}}_j = \sum_k K_{jk} \hat{\boldsymbol{e}}_k \tag{3.21}$$

with $j, k = x, y, z$, $\hat{\boldsymbol{e}}_j$ are the eigenvectors in cubic coordinates, ω is the Raman mode frequency in presence of strain and K_{jk} are the elements of the force constant tensor. At first order perturbation theory, whose validity is confirmed by the fact that $\varepsilon_{lm} << 1$, we can write that

$$K_{ij} = \omega_0^2 \delta_{ij} + \sum_{lm} \varepsilon_{lm} K^{(\varepsilon)}_{lmjk} \tag{3.22}$$

where ω_0 is the Raman frequency of the unstrained crystal, δ_{jk} the Kronecker delta and ε_{lm} the element of the strain tensor. The zincblend structure of Ge, with its 48 symmetry operations related to the cubic lattice symmetry [112], has only three independent components and non zero elements up to the 81

of a four matrix tensor. They are called phonon deformation potentials and show the following relations:

$$
\begin{aligned}
K^{(\varepsilon)}_{xxxx} &= K^{(\varepsilon)}_{yyyy} = K^{(\varepsilon)}_{zzzz} = p \\
K^{(\varepsilon)}_{xxyy} &= K^{(\varepsilon)}_{xxzz} = K^{(\varepsilon)}_{yyzz} = q \\
K^{(\varepsilon)}_{xyxy} &= K^{(\varepsilon)}_{xzxz} = K^{(\varepsilon)}_{yzyz} = r.
\end{aligned}
\tag{3.23}
$$

Combining eq. 3.21 and eq. 3.23, we can obtain

$$
\begin{vmatrix}
p\varepsilon_{xx} + q(\varepsilon_{yy} + \varepsilon_{zz}) - \lambda_i & 2r\varepsilon_{xy} & 2r\varepsilon_{xz} \\
2r\varepsilon_{xy} & q\varepsilon_{xx} + p(\varepsilon_{yy} + \varepsilon_{zz}) - \lambda_i & 2r\varepsilon_{yz} \\
2r\varepsilon_{xz} & 2r\varepsilon_{xz} & q(\varepsilon_{xx} + \varepsilon_{yy}) + p\varepsilon_{zz} - \lambda_i
\end{vmatrix} = 0.
\tag{3.24}
$$

The expected Raman shifts $\Delta\omega = \omega_i - \omega_0$ are obtained by numerically calculating the eigenvalues $\lambda_i = \omega_i^2 - \omega_0^2$ of the secular matrix. In the case of backscattering geometry, the relative Raman shift $\Delta\omega = \omega_i - \omega_0$ is given by the element (3,3) of matrix 3.24:

$$
\Delta\omega = \omega_i - \omega_0 = q(\varepsilon_{xx} + \varepsilon_{yy}) + p\varepsilon_{zz},
\tag{3.25}
$$

where z correspond to the [001] direction.

RAMAN SPECTRA OF SI, GE AND $SI_{1-x}GE_x$ In $Si_{1-x}Ge_x$ alloys, three Raman modes are present: the Ge-Ge, the Si-Ge and the Si-Si nearest neighbor vibrations [114]. The appearance and frequency of these three optical phonon bands are mainly affected by two parameters: the Ge content of the alloy and strain.

Figure 3.19 reports the Raman spectra of pure Ge, pure Si, and $Si_{1-x}Ge_x$ for different concentrations x, as calculated in [113]. The inset show the Raman spectra of pure Ge, that exhibits a single band around 300 cm^{-1}, and that of pure Si, with a single band around 520 cm^{-1}. These two bands are attributed to the Ge-Ge and Si-Si optical phonons, respectively. Upon alloying with Si, the Ge-Ge mode of Ge rich SiGe, shifts to lower wavenumbers and decreases in intensity. At the same time, a double-peak band around $\sim$ 400 cm^{-1} occurs. This band is attributed to the Ge-Si vibrational modes. The shift of the Si-Si and Ge-Ge mode frequency, in unstrained $Si_{1-x}Ge_x$ heterostructures, linearly depends on the Ge molar fraction, and is given by [114]:

$$
\omega^{Ge-Ge}(x, \varepsilon) = 280.3 + 19.4 \cdot x,
\tag{3.26a}
$$

$$
\omega^{Si-Si}(x, \varepsilon) = 520.7 - 66.9 \cdot x.
\tag{3.26b}
$$

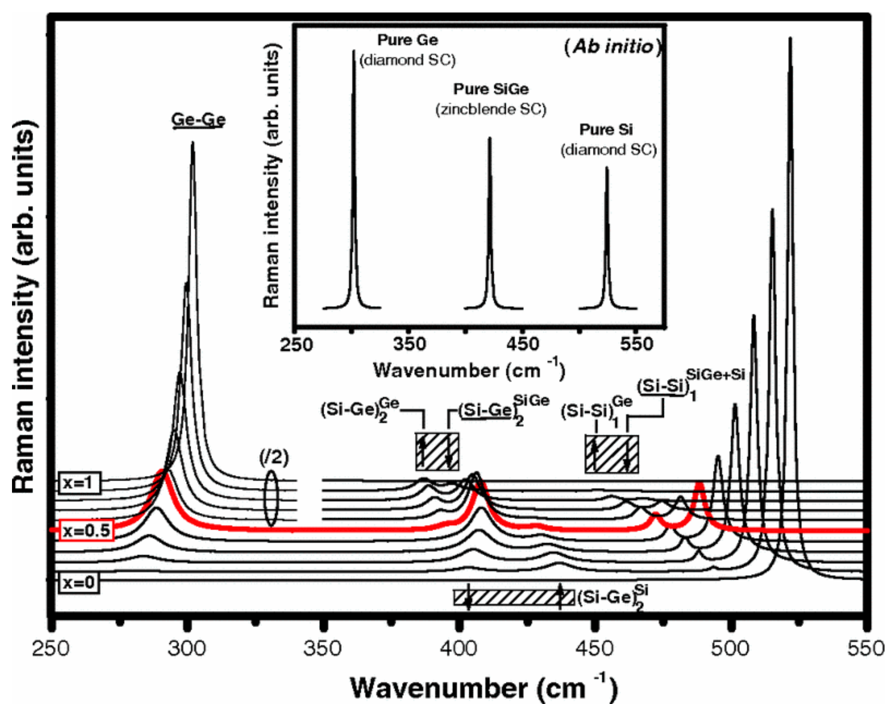

Figure 3.19 – Calculated optical active modes in $Si_{1-x}Ge_x$ visible in Raman spectra. The spectra for $Si_{1-x}Ge_x$ alloys with different concentrations x are reported. The evolution of the single peak intensities as a function of x is hence visible. The inset shows the three vibrational modes Ge-Ge, Si-Ge, and Si-Si for pure Ge, pure Si, and $Si_{50}Ge_{50}$ with the Si and Ge atoms distributed in a zincblende lattice [113].

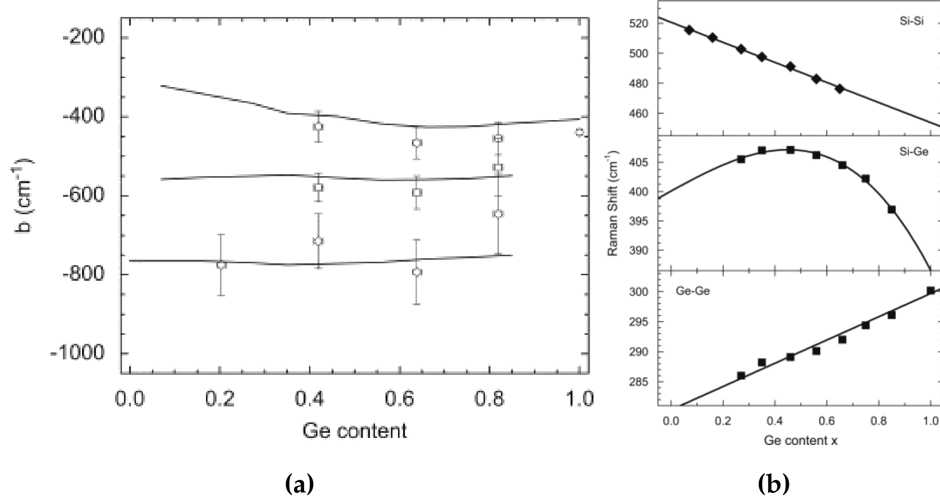

Figure 3.20 – (a) Experimental strain shift coefficients and (b) Peak positions of the Raman modes Ge-Ge, Si-Ge, and Si-Si (top down) of $Si_{1-x}Ge_x$ as a function of the Ge molar fraction x [115].

The Raman shift of the Si-Ge mode, on the contrary, shows a cubic dependence on x

$$\omega^{Si-Ge}(x,\varepsilon) = 400.1 + 24.5 \cdot x - 4.5 \cdot x^2 - 33.5 \cdot x^3. \tag{3.27}$$

However, in a $Si_{1-x}Ge_x/Si$ heterostructure the composition effect, that determines the three mode peak positions, is superimposed on the effect of the biaxial strain. The strain-induced shift of all the alloy modes is a linear function of the biaxial in-plane strain [115]:

$$\Delta\omega = \omega_i - \omega_0^i = q(\varepsilon_{xx} + \varepsilon_{yy}) + p\varepsilon_{zz} = b^i \cdot \varepsilon. \tag{3.28}$$

In Equation 3.28, b^i is the so called *phonon strain shift coefficient*, ε is the biaxial strain and ω_0^i and ω_i are the ith mode Raman frequencies of the relaxed and strained alloy, respectively. The three phonon strain-shift coefficients are nearly constant throughout the entire composition range of $Si_{1-x}Ge_x$ alloys [Fig. 3.20(a)] [107].

Combining Eqs. 3.26 and 3.27 with Eq. 3.28, the position of the peaks of the Ge-Ge, Si-Ge and Si-Si modes in $Si_{1-x}Ge_x/Si$ heterostructures, as a function of the biaxial in-plane strain ε and the Ge concentration x is reported in Fig. 3.20(b), and is given by [115]:

$$\omega^{Ge-Ge}(x,\varepsilon) = 280.3 + 19.4 \cdot x - 450 \cdot \varepsilon, \tag{3.29a}$$

$$\omega^{Si-Ge}(x,\varepsilon) = 400.1 + 24.5 \cdot x - 4.5 \cdot x^2 - 33.5 \cdot x^3 - 570 \cdot \varepsilon, \tag{3.29b}$$

$$\omega^{Si-Si}(x,\varepsilon) = 520.7 - 66.9 \cdot x - 730 \cdot \varepsilon. \tag{3.29c}$$

Raman Set-up

Micro-(μ-)Raman measurements were carried out at IHP using a Renishaw inVia microscope in backscattering geometry with 633 nm helium−neon red laser, 1800 lines/mm grating, and 50× objective with numerical aperture of 0.75, which results in a laser spot size of ≃520 nm in diameter and a Ge penetration depth of ≃32 nm.

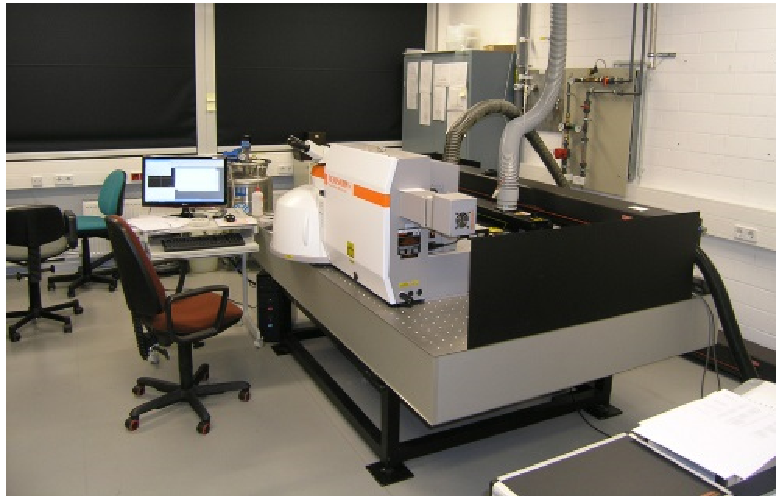

Figure 3.21 – Photograph of the Raman set-up.

3.3 OPTICAL CHARACTERIZATION

The inter-band transition study presented in this thesis mainly focuses on two different aspects: how to increase the radiative efficiency of Ge and how to tune the emission wavelength to reach 1550 nm. Both the aspects have been investigated using photoluminescence spectroscopy.

3.3.1 *Photoluminescence Spectroscopy*

In photoluminescence spectroscopy we measure the energy distribution of emitted photons after optical excitation. As already discussed in Chapter 2, by means of an excitation mechanism, an electron is excited from the valence band to the conduction band of a semiconductor. In PL spectroscopy the excitation mechanism is given by a laser beam impinging on the sample. If the photon energy is less than the bandgap energy, the photons are not absorbed and the light is transmitted through the material. Therefore, the semiconductor appears to be transparent. On the contrary, if photons have an

energy higher than the bandgap energy of the semiconductor, the excitation of electrons from the valence band into the conduction band, takes place.

3.3.2 *Photoluminescence Set-up*

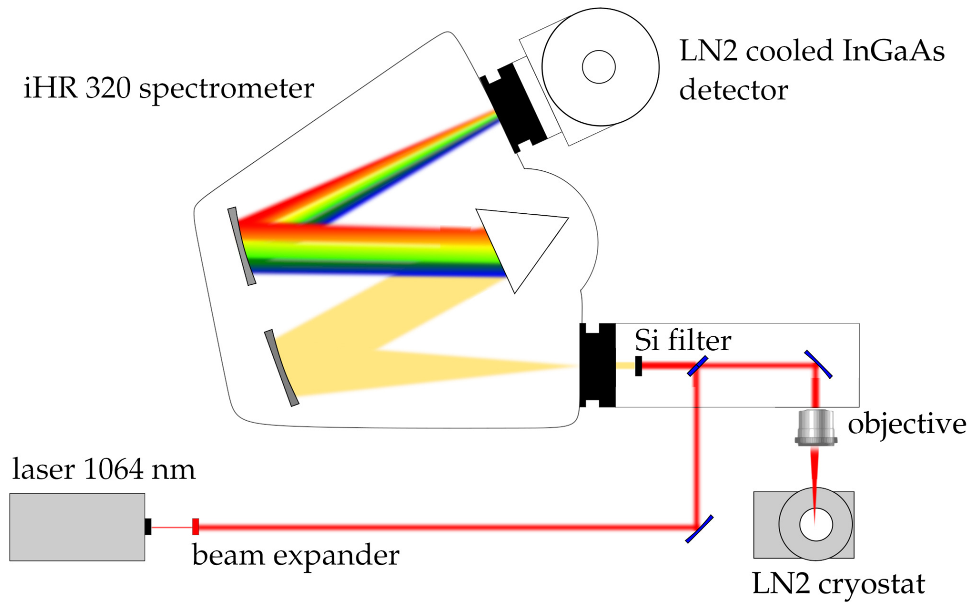

Figure 3.22 – PL set-up

The spectra reported in this work have been collected by means of a μ-PL set-up at IHP. The experimental set-up is sketched in Fig. 3.22 and consists of four main parts:

- an excitation light source;
- an objective to focus the beam on the sample;
- a cryostat to make temperature-dependent measurements;
- a detection system to disperse and analyze the photons emitted from the sample.

The light source is a Nd:Yag solid-state laser, emitting continuous-wave at a wavelength of 1064 nm and photons are focused on the sample with a 50x objective having a numerical aperture of 0.65. The spot of the laser beam at the surface is about 1.7 μm in diameter. The measurements have been performed in a back-scattering geometry, that is, the radiation emitted from the sample is collected by the same objective. A beam-splitter divides excitation and collection paths.

A LINKAM nitrogen cryostat is used to cool down the samples from room temperature 300 K to liquid nitrogen temperature 77 K within a ±5 K accuracy. A telescope system is used to collect the photoluminescence signal into the scalable width (0-2 mm) entrance slit of a grating monochromator. The grating of the monochromator can be 300, 600 or 900 lines/mm. A Si filter placed between the telescope system and the slit of the monochromator is used to filter out the laser light which is much stronger than the fluorescence signal and hides it. The emitted beam is dispersed by an iHR 320 Horiba Jobin-Yvon spectrometer and measured with an extended InGaAS detector array cooled with liquid nitrogen to reduce the effects of dark current.

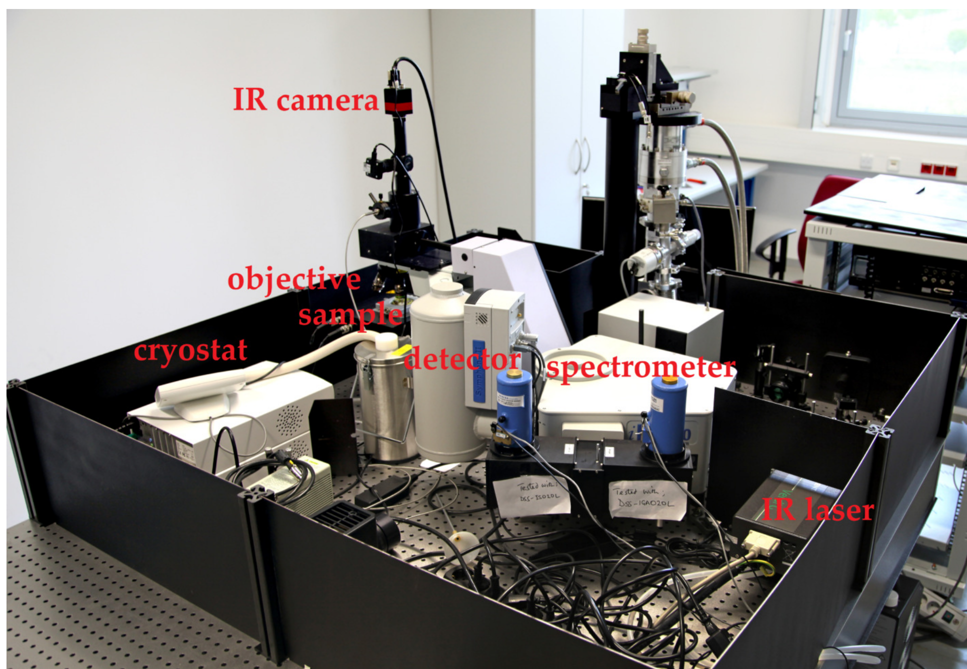

Figure 3.23 – Photograph of the PL set-up.

In all the measurements, the spectra obtained were corrected for the instrument response, obtained using a black-body calibration lamp. The spectral responsivity of the entire PL set-up at the photo-detector [reported in Fig. 3.24(a)] is updated every 6 months. At the begin of every set of measurements, we acquired the PL spectrum of a Ge/Si (001) reference sample, paying attention that the intensity and the spectral shape were each time the same. Any variation is the result of a misalignment of the excitation path and/or the collection path, which need to be adjusted. The pump power densities, reported in power-dependent PL measurements, have been measured on the sample surface by means of a Thorlabs laser power-meter. The intensity of

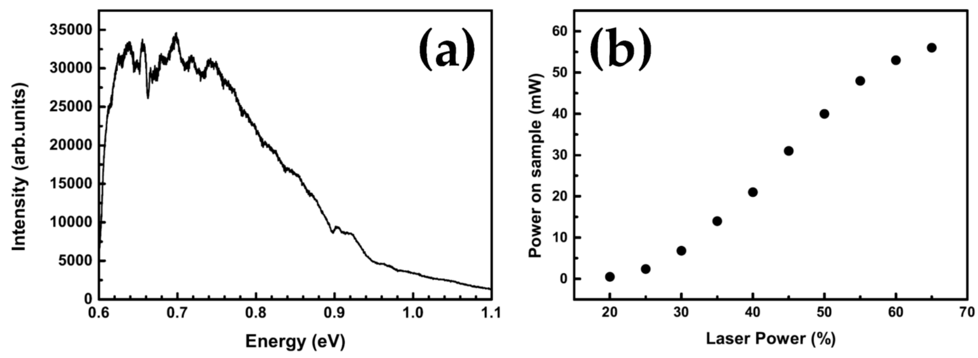

Figure 3.24 – (a) Spectral responsivity of the entire PL set-up at the photo-detector. (b) Pump power density on the sample as a function of the laser power.

the laser beam energy output is periodically determined and the calibration for the measurements reported in this work in shown in Fig. 3.24(b).

4

GROWTH AND CHARACTERIZATION OF VIRTUAL SUBSTRATES

As we discussed in section 1.2, the bandgap of Ge can be modified by design and we can investigate its electronic structures by means of PL. While in the next Chapter we shall investigate the optical properties of Ge/SiGe QWs and how they are affected by quantum effects (such as thickness of the QWs, coupling between the wells), doping and strain, here we discuss the structural and optical properties of the virtual substrate on which they are deposited. As a matter of fact, employing many substrate layers with different concentrations may results in complicated PL spectra. This is true in particular if a long-wave pump is used for homogeneous excitation and the number of QWs is limited to few repetitions, since both the MQW region and the under-lying layers are simultaneously excited. Indeed in this case a one-to-one identification of all the individual spectral components is not trivial, especially if complementary techniques, such as optical absorption, are not employed. Aiming at an unequivocal identification of the origin of the peaks in the PL spectra, we now discuss how the several layers of the VS have been deposited, and their PL features will be investigated in detail.

The high lattice mismatch between the Si substrate and the Ge-rich SiGe heterostructures is released by misfit dislocations. Dislocations nucleate at surface sites and glide to the interface resulting, for each misfit segment, in two threading segments that connect the interface with the surface. While misfit dislocations release the epitaxial strain, threading dislocations do not contribute to relaxation. Hence, larger strain to be relaxed requires denser misfit dislocation arrays. When the density of misfit on the same heterointerface is high, they start to interact with each other, hindering their motion. Propagation of a dislocation will occur until (a) it reaches a wafer edge; (b) sufficient strain has been relieved by the misfit that further expansion is

energetically unfavorable; (c) it meets another threading dislocation mutually annihilating; or (d) it is unable to pass another orthogonally placed dislocation becoming pinned [116].
To reduce the threading dislocation density, SiGe *virtual substrates* are commonly employed. Moreover, from the interplay between the Ge content x and the relaxation of the SiGe VS, it is possible to deposit a buffer with a proper lattice constant and, thus, to controll the strain of the heterostructures, i.e. realizing strain-compensated structures described in section 1.5.1.

Virtual substrates are usually realized following two main techniques. The first approach introduced, called *linear graded* virtual substrate, consists in linearly grading the Ge content in the buffer layer from pure Si to the final $Si_{1-x}Ge_x$ composition x [117]. The composition grading allows to gradually distribute the total lattice mismatch among many layers, so that misfit dislocations are gradually nucleated along the whole thickness of the graded layer, reducing the threading dislocations density (TDD) in the final layer, since the TDD is experimentally seen to increase with lattice mismatch [118]. While linear graded virtual substrates are commonly used for low ($x<0.5$) Ge content, for final composition in the high Ge content range the thickness to be deposited is so large (~10–20 μm) that the growth of high quality materials is both impractical and very difficult to achieve with standard deposition techniques, such as CVD and MBE. Moreover, dislocations tend to be piled up on the same (111) atomic glide planes [119], resulting in small surface steps. It follows that the resulting thick-VS exhibits large surface undulations, known as *crosshatch*, which must be removed via an ex-situ chemical mechanical polishing [120].

To overcome these limitations, a different approach has been proposed [121, 119]. This technique, called *terrace grading*, has shown the possibility to generate smoother interfaces, enhancing relaxation and lowering TDD values by releasing pinned dislocations. The idea of *forward* grading was proposed by Capewell *et al.*[119] and consists of alternating linear graded regions followed by constant composition layers (terraces). In *reverse* grading[121, 105] the alloy content is graded *down* from a relatively high quality, relaxed pure Ge layer to the required final composition instead of grading *up* from the Si wafer, thus reducing the thickness of the VS. Another advantage of this technique, is that the buffers relax under tensile strain, while linear graded buffers relax

under compressive strain, resulting in smoother epilayers, since the surface roughness depends on the sign of strain [122].

Technique	Total thickness (μm)	Grading thickness (nm)	GR (% μm^{-1})	x_f (%)	TDD (cm^{-2})	Ref.
RTG	3.9	1844	12.6	76.5	2.1×10^6	[121]
RLG	4.3	1885	11.4	78.4	3.3×10^6	[123]
RLG	2.4	347	61	78.4	4.5×10^6	[123]
LG	12	10	10000	100	$1-5 \times 10^7$	[124]
LG with CMP	12	10000	10	100	2×10^6	[124]
LG with CMP	12	10000	9	88.5	1×10^5	[125]
LG	5.5	3400	25	85	$< 1 \times 10^6$	[126]
LG	11.5	10500	8	84.5	1.3×10^5	[127]
RTG	2	1000	70	75	7.8×10^7	[128]
RTG	2.5	450	42	81	$\sim 1 \times 10^8$	Present work

Table 4.1 – Comparison of literature data for different virtual substrates realized with different techniques: linear grading (LG), linear grading with chemical mechanical polishing (CMP), and reverse terrace grading (RTG). The grading rate (GR) is defined as $(x_f - 1)/\text{grading thickness}$.

The growth of reverse graded VSs starts with the deposition of an initial Ge layer directly on the Si substrate. However, the large mismatch between Ge and Si, combined with the difference in surface energies, results in a growth process where Ge coalesces in three dimensional islands according to the Stranski–Krastanov mechanism, if growth conditions close to thermodynamic equilibrium are maintained [129]. The growth of planar Ge layers on Si has been achieved using a double temperature deposition technique [130, 131, 132] where an initial "*seed*" Ge layer is deposited at low temperature, in order to keep the system out of thermodynamic equilibrium. However, too low temperatures prevent the germane pyrolysis and thus the growth itself. Figure 4.1 displays the results of the pioneering work of Cunningham *et al.* who reported the deposition of heteroepitaxial Ge films with a smooth surface topology on (001) single-crystal silicon. Figure 4.1 reports the cross-sectional micrographs of films grown in the temperature range 275-560°C. At or below 300°C the pyrolysis does not take place and a null Ge thickness is present, while between 300 and 350°C the films are smooth, indicating a 2D growth. Above 375°C the 3D islands formation starts and the surface appears corrugated. This islanding is extremely apparent at 430 °C. The allowed temperature interval for an epitaxial deposition of Ge on Si substrates is therefore 300°C-375°C. At this low temperature, the Ge layer is highly defected. However, upon

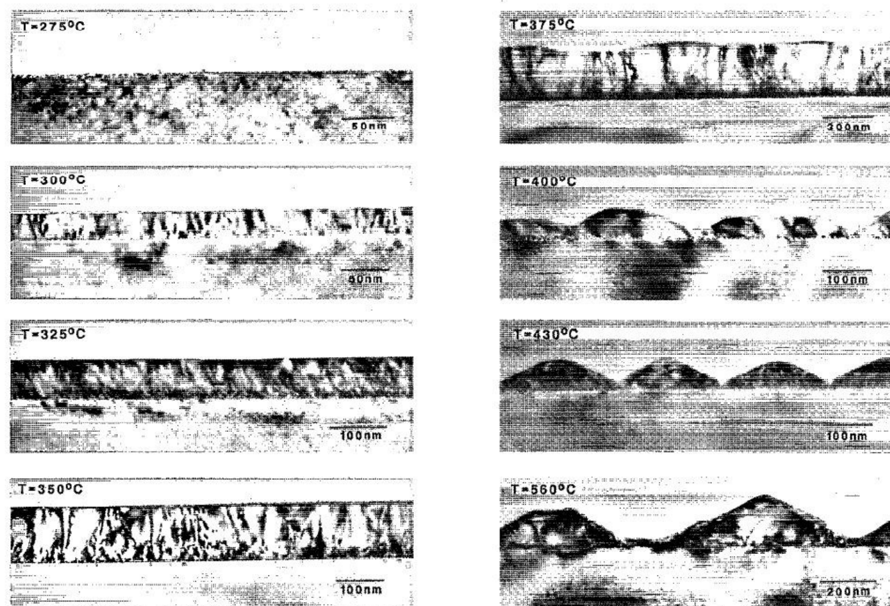

Figure 4.1 – Transmission electron microscopy images of Ge layers on Si substrate at different growth temperatures [135].

increasing the amount of the deposited Ge, the lattice strain is plastically relaxed, allowing a consecutive epitaxial deposition at higher temperature, characterized by a higher growth speed, relaxation and crystalline quality. Typical values of TDD in Ge heteroepitaxial layers are $\sim 10^9$ cm^2 that can be reduced to $\sim 10^7$ cm^2 [118, 133, 134] thanks to thermal treatments that enhance gliding of the threading arms of misfit dislocations and mutual annihilation or elimination at wafer edges.

4.1 SUBSTRATE PREPARATION

The realization of high quality samples starts from a correct Si substrate preparation. On the opposite, a contaminated substrate generates defects propagating through the whole structure, which leads to a poor final result, even if accurate procedures and perfect growth steps are performed afterwards.

The substrates are cut, in a clean environment with a professional semi-automatic scriber, from an highly quality n-doped ($\simeq 10^{15}$ cm^{-3}) Si (001) wafer in a 18×9 mm^2 rectangular shape with sides aligned along the $\langle 011 \rangle$ directions. Doping is necessary in order to allow the current propagation needed

to heat the substrate.

The Si substrate preparation is an important factor in producing good epitaxial crystal quality and can be summarized in the following steps:

- Chemical and mechanical cleaning performed in the chemical hood (3) to remove physisorbed contaminants;

- Thermal cleaning at $\sim$ 500°C in the preparation chamber to remove chemisorbed and physisorbed contaminants;

- Annealing in H_2 at 1150°C in the CVD chamber to remove native silicon oxide;

- Deposition of a Si buffer layer in the CVD chamber to reconstruct a planar Si surface.

The cleaning process of the substrates starts inside the chemical hood with an ultrasonic bath in isopropyl alcohol (2-propanol $CH_3CH(OH)CH_3$) for an overall duration of 20 minutes. This step assures the desorption of organic contaminants present on the substrate surface. To remove any traces of alcohol left on the surface, the substrate undergoes to a continuous-flow rinse in de-ionized water. Then, the substrate is dried under an ultra-high purity nitrogen jet, in order to remove any water residue without contaminating the clean surface. After the cleaning, the substrate is mounted on a sample holder consisting of a conductive part in tantalum and Inconel (an austenitic nickel-chromium-based alloy), and an insulating part in quartz and Macor (a glass-ceramic). The substrate is fixed to the holder by means of molybdenum contacts and steel screws. The choice of such materials is forced by the high temperatures the system has to endure during the annealing and deposition processes, which could induce thermal stress and deformation in the substrate if the proper materials are not employed. The sample holder is sketched in Fig. 4.2.

Once the substrate is fixed on the holder, it is inserted in the load-lock and in the preparation chamber afterwards. While the substrate is in the preparation chamber [(4) in Fig. 3.1], it is heated above 400°C for 12 hours. This step is especially effective in removing water molecules from the Si substrates. Finally, the substrate is brought to the CVD chamber where it is heated

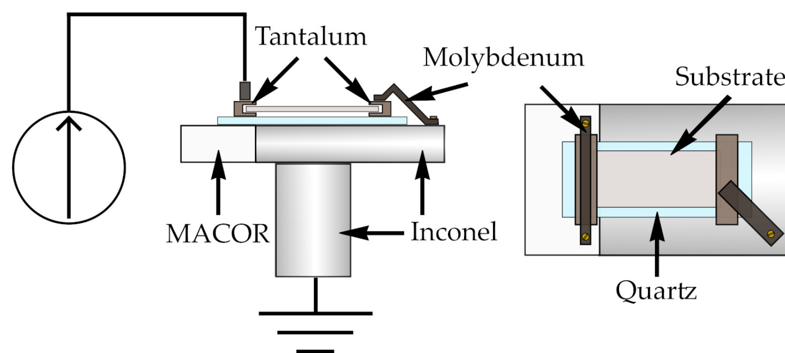

Figure 4.2 – Sample holder in side and top view.

up to 1150°C in H_2 atmosphere for 10 minutes. This procedure removes the non-stoichiometric native oxide and leaves an exposed Si surface clean but irregular and corrugated, requiring a reconstruction layer before the heterostructure deposition. To this aim, a Si layer is grown at 850°C via CVD of silane, allowing to restore a planar Si surface with high crystalline quality.

The effectiveness of the substrate preparation procedure is demonstrated in Fig. 4.3, where the XPS spectra of a Si substrate "as-loaded" (no treatments), after the ex-situ cleaning, and after the in-situ annealing at 1150°C are reported. In the insets the C^{1s} and O^{1s} peaks are highlighted. From the intensity of the peaks we can estimate that $\sim$ 7% of the as-loaded silicon surface is covered by carbon and $\sim$ 30% by oxygen. The chemical cleaning results in a reduction of the carbon coverage to $\sim$ 2% while it not effective in the removal of oxygen, since still $\sim$ 30% of the surface is covered by O. After the annealing the surface coverage of carbon and oxygen are reduced to $<$ 0.5% and $<$ 0.7%, respectively.

4.2 GE VIRTUAL SUBSTRATE

After the Si substrate preparation, the deposition process can take place starting with the growth of a Ge seed layer, which covers the Si substrate and collects most of the defects induced by the high lattice mismatch. The deposition takes place for one hour at the substrate temperature of 350°C (LT step) and pressure of 4 mTorr. It is important to recall that special attention has to be payed to the deposition temperature, since too high values force the growth not to be planar but with islands, and too low values prevent the germane pyrolysis. Once most of the lattice mismatch is plastically released,

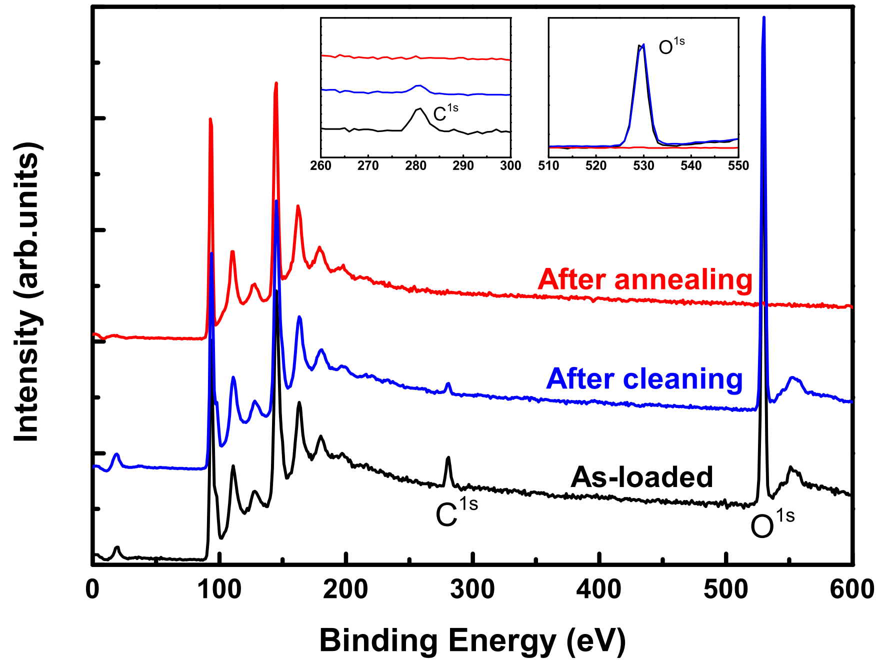

Figure 4.3 – XPS spectra of a Si substrate "as-loaded" (no treatments), after the ex-situ cleaning, and after the in-situ annealing at 1150°C. The suppression of the C^{1s} and O^{1s} peaks verifies the effectiveness of the substrate preparation procedure. In all the spectra the intensity of the Si^{2p} peak (at ~ 100 eV) has been normalized to unity. In the insets the C^{1s} and O^{1s} peaks are highlighted.

and an epitaxial planar deposition is established, it is possible to increase the temperature to 600°C (HT) for 5 minutes. The surface morphology at the end of this step, as investigated by AFM, is displayed in Fig. 4.4(a). Thanks to the low temperature employed during the deposition a planar 2D growth is established and the surface is characterized by multi-layer terraces, resulting in a root-mean-square (RMS) roughness of ~ 3 nm. In order to further increase the growth rate (thus reducing the time needed to complete the deposition) and improve the crystal quality, the subsequent process step comprises a deposition at 700°C (VHT) for 30 minutes. The increase of temperature results in a smaller average width of the multi-atomic terraces than those at the end of the previous step [see Fig. 4.4(b)]. To reduce the threading dislocation density, the sample undergoes to an annealing process at 800°C (UHT) for 20 minutes in a p~ 0.1 mTorr germane atmosphere. Although this step interrupts the deposition, being the growth rate negligible at p~ 0.1 mTorr, it results in a smoothing of the surface, as can be observed in Fig. 4.4(c). In the figure, several pits can be noticed, with a depth of few-tenth-nm and density of ~ $10^7 cm^{-2}$. In order to fill the surface pits, the last step of the

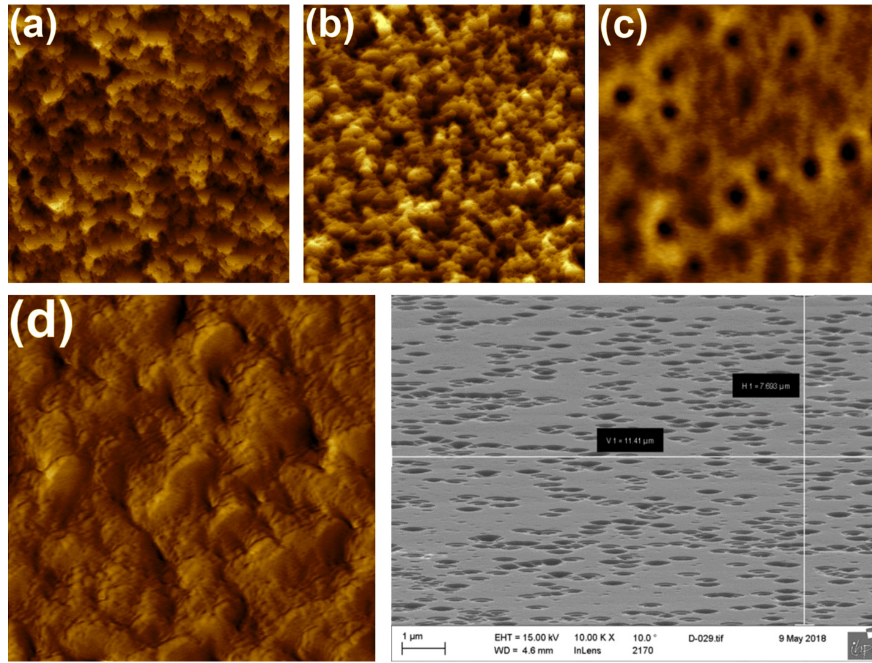

Figure 4.4 – 15×15 μm^2 AFM images of a Ge virtual substrate at different growth stages: (a) after the HT step; (b) after the VHT step; (c) after the UHT step; (d) at the end of the deposition. Images side are aligned along the $\langle 011 \rangle$ directions. In the right-bottom corner is shown the etch-pit count on the surface of the complete Ge VS.

deposition process consists in the growth of a thick Ge layer for 45 minutes at a temperature of 500°C and pressure of 1.20 mTorr. This step allows to recover a smooth surface [see Fig. 4.4(d)] with a RMS roughness of $\sim$ 1.5 nm. The threading dislocation density at the end of this step, obtained by etch-pit counting (Fig. 4.4), is about $2 \times 10^7 \text{cm}^{-2}$ on the surface.

The deposition process, including all the several steps, results in a Ge buffer layer $\sim$ 700 nm-thick with a high relaxation level and low defect density.

The annealing process at 800°C (UHT step) results in three main effects: *i)* reducing the TDD density, *ii)* smoothing the surface (as we can observe in Fig. 4.4), and *iii)* inducing a thermal lattice strain. As a matter of fact, as we discussed in section 1.1, the lattice parameter a is a function of the lattice temperature and the change with T is expressed by means of the coefficient of thermal expansion α. The origin of the lattice strain is the mismatch of Ge and Si CTE [136]; while the out-of-plane lattice parameter of Ge, $a_{\perp}$(Ge), is free to expand perpendicularly to the sample surface, the in-plane $a_{\parallel}$(Ge) is forced to expand following the thicker Si substrate, which has a CTE smaller than the

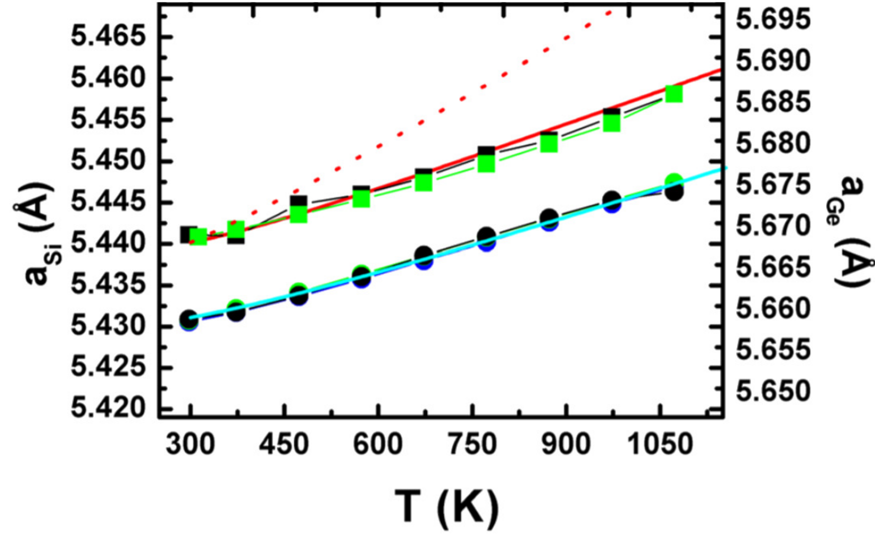

Figure 4.5 – In-plane measured (dot) and calculated (cyan line) $a_{\|}$(Si) as a function of T. On the right axis is reported $a_{\|}$(Ge) (squares) together with its expansion from the measured value at RT as calculated using the Si (red line) or the Ge (dotted line) CTE values. Figure taken from [136].

value of Ge. This effect can be clearly observed in Fig. 4.5, where the in-plane lattice parameters of Si and Ge are reported as a function of temperature. Since $a_{\|}$(Ge) is not free to expand, its variation during the cooling process from a high temperature, T_H, down to a lower temperature, T_L, is parallel to the variation of $a_{\|}$(Si). The resulting in-plane strain $\varepsilon_{\|}$ is given by:

$$\varepsilon_{\|}(T_L, T_H) \simeq \int_{T_L}^{T_H} (\alpha_{\text{Ge}}(T') - \alpha_{\text{Si}}(T'))dT', \tag{4.1}$$

and can be measured by means of XRD. As a matter of fact, as we discussed in the previous Chapter, asymmetric $(4\bar{2}\bar{2})$ reflections allows to retrieve both $a_{\perp}$ and $a_{\|}$ and, hence, the strain values. For instance, the in-plane lattice strain $\varepsilon_{\|}$ of the Ge VS can be calculated considering that

$$a_{\|}(\text{Ge}) = a_0(\text{Ge})(1 + \varepsilon_{\|}), \tag{4.2}$$

where a_0(Ge) is the bulk lattice parameter of Ge. From Eq. 4.2, we get that the Ge VS is tensile strained with $\varepsilon_{\|}$=0.17%.

4.2.1 *Optical Properties of the Ge Virtual Substrate*

In Fig. 4.6 (a), we report the PL spectra acquired on the 700 nm thick Ge/Si(001) VS, at a constant pump power density, estimated to be 3.7×10^5 W·cm^{-2}, and varying the lattice temperature from 80 K to 330 K, in ∼ 30 K steps. The

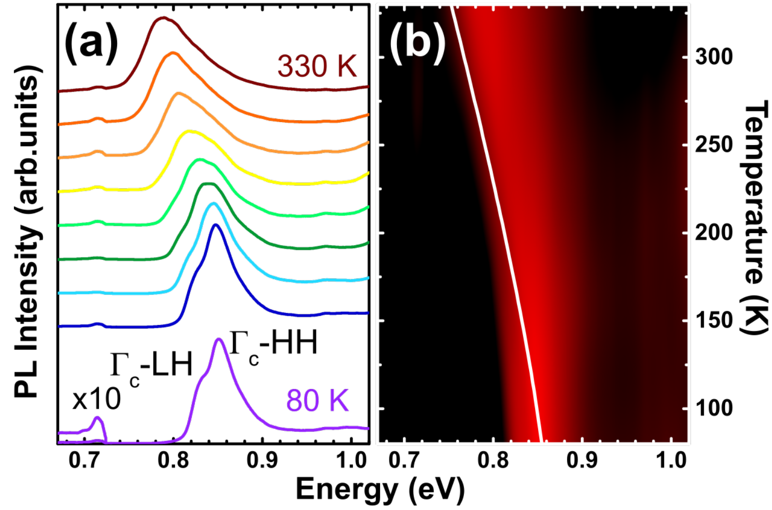

Figure 4.6 – (a): PL spectra acquired on the Ge VS. Lattice temperatures range from 80 K to 330 K in ~ 30 K steps. The signal related to the indirect L_c-LH transition at 80 K has been enhanced by a factor 10. (b): Contour plot of the PL spectra as a function of T with integrated intensity at each temperature normalized to unity. Continuous line is the result of the fitting of experimental data with Varshni equation.

spectra show a broad peak at ≃ 0.85 eV at 80 K, that redshifts to ≃ 0.80 eV at RT. We attribute this feature to the Γ_c-HH direct band-to-band recombination. The experimental Γ_c-HH transition energies, evaluated from the PL peaks by means of the procedure introduced in section 2.4.5, have been fitted with the T-dependence of the direct gap, following Varshni equation (section 1.1):

$$E(T) = E(0) - \frac{\alpha T^2}{T+\beta} = 0.868 - \frac{5.82\times 10^{-4} T^2}{T+296}, \quad (4.3)$$

where the parameters α and β are those of bulk Ge [137] (reported in Table 1.3) and $E(T)$ is in eV. The behavior of the peaks as a function of temperature can be clearly observed in the contour plot of the PL spectra, reported in Fig. 4.6 (b), where the fitting of the Γ_c-HH transitions is also reported as a continuous white line. Increasing the temperature, the PL peak broadens and visually redshifts, due to temperature-induced shrinking of the gap.

On the low-energy side of the peaks acquired at low temperatures, we can see a shoulder related to the Γ_c-LH direct recombination (see Fig. 4.7). As a matter of fact, for moderate in-plane strain the LH-HH splitting δ is linearly dependent on the biaxial tensile strain $\varepsilon_{\parallel}$ as $\delta = (6700 \pm 50)$ meV $\times\, \varepsilon_{\parallel}$ [138].

From Eq. (4.1), it is clear that, decreasing the temperature T_L, the in-plane strain $\varepsilon_{\parallel}$ increases, leading to a larger LH-HH splitting δ. Assuming $T_H \simeq$ 875 K[136] and $T_L \simeq$ 80 K, $\varepsilon_{\parallel}$ is estimated to be $\simeq$ 0.25 % at 80 K. The corresponding LH-HH splitting is $\simeq$ 17 meV, compatible with the peak separation in the PL spectra. At 300 K, the biaxial tensile strain $\varepsilon_{\parallel}$ calculated with Eq. (4.1) is reduced to $\varepsilon_{\parallel}$= 0.17, perfectly matching the value obtained by XRD measurements. The corresponding LH-HH splitting δ is $\simeq$ 11 meV. Due to the reduced separation as well as the increased electron thermal energy, associated to a larger density of states for the HH band, the peak related to the direct Γ_c-LH can not be clearly resolved. Indeed, the relative PL intensity of the two features, in the temperature range investigated, can be explained considering that, although the Γ_c-LH transition is energetically favored, the final density of states for the Γ_c-HH recombination and the associated dipole in the out-of-plane direction are larger than the corresponding quantities for the Γ_c-LH transition [84].

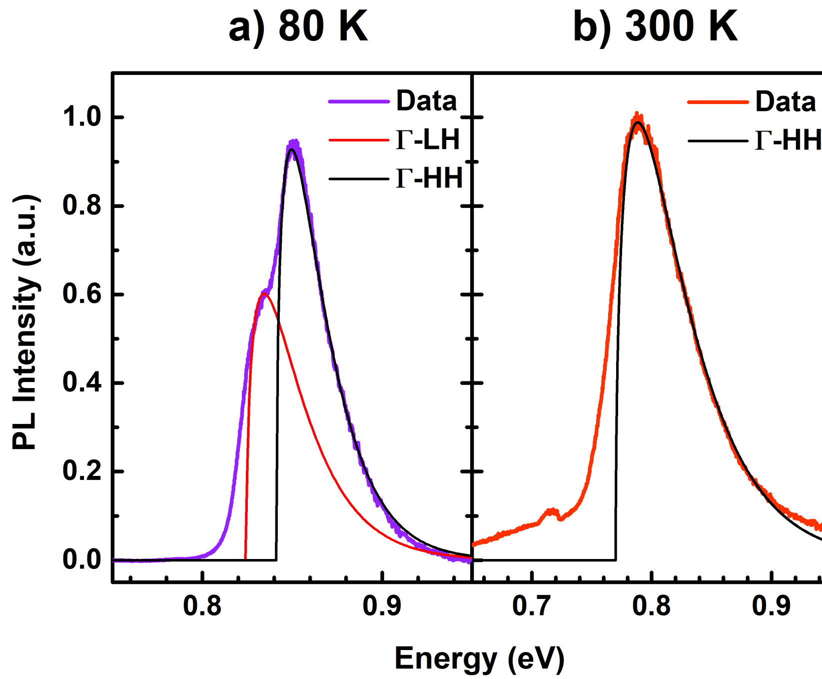

Figure 4.7 – PL spectra at 80 K (left) and 300 K (right). The spectral shape of direct transitions, as given in Eq. 4.4, is also reported.

For comparison, we also report in Fig. 4.7 the spectral shape of the direct gap recombination derived in section 2.4.5:

$$I(\hbar\omega) = \sqrt{(\hbar\omega - E_g)} \cdot \exp\left(-(\hbar\omega - E_g)/k_B T\right). \tag{4.4}$$

In Equation (4.4), E_g is the direct gap energy, k_B is the Boltzmann constant, and T is the temperature of excited carriers, which is found to be higher than the lattice temperature T_L, due to pump-induced electron heating effects. The discrepancy between the fitting curve and experimental data in the high-energy tail can be explained considering the non-parabolicity of the valence band at high electron momentum.

Finally, it is interesting to underline that the signal related to the indirect $L_c - \Gamma_v$ transition is extremely low at all the investigated temperatures [the small signal at $\sim$ 0.71 eV in Fig. 4.12(a), related to the L_c-LH transition, has been enhanced by a factor 10], and PL spectra are dominated by direct recombinations. The rationale is that, since we are dealing with epitaxial thin films, the optical path of the emitted light is small, and then the direct gap emission is not as much reabsorbed as in bulk Ge [99] (see for a comparison section 2.4.6). Moreover, in the whole investigated temperature range, excess electrons have sufficient thermal energy to populate the Γ_c valley, where the recombination rate is much higher [139]. The dominance of the direct gap recombination in Ge films has been also reported in Ref. [140] where the small signal of the indirect gap transitions has been related to strong non-radiative recombinations at the film-substrate interface.

4.3 SIGE VIRTUAL SUBSTRATE

Starting from the relaxed Ge layer it is possible to proceed with the *reverse graded* (RG) layer deposition at 500°C, consisting of a stack of SiGe layers with increasing Si concentration, realized by injecting both germane and silane in the CVD chamber (co-deposition). Two different "strategies" are employed, depending on the desired final concentration to achieve. The first strategy, adopted when the final concentration x is in the 80-90% range, consists in the deposition of four $Si_{1-x}Ge_x$ layers with Ge concentration decreasing, i.e., from x=1 to x=0.81, with a $\sim$ 5% difference between each adjacent layer. This is achieved keeping the flux of germane constant and increasing the silane concentration in the chamber at each step. The same procedure applies to any final Ge concentration needed, e.g. 85% or 90%. The proper precursor flows needed to achieve the desired concentration are estimated before the deposition and then checked experimentally with XPS and/or XRD. Giving

the deposition conditions reported in Table 4.2, each layer results in a thickness of ~ 150 nm.

$\Phi(GeH_4)$ (sccm)	$\Phi(SiH_4)$ (sccm)	Δt (min)	p (mTorr)	x
2.1	0.6	10	4	~0.95
2.1	1.1	10	4	~0.91
2.1	1.6	10	4	~0.86
2.1	2.1	10	4	~0.81

Table 4.2 – Example of step graded $Si_{1-x}Ge_x$ layers deposition conditions: precursors injected flows $\Phi(GeH_4)$ and $\Phi(SiH_4)$ (1 sccm=$1.64\cdot10^{-2}cm^3/s$), deposition time Δt, pressure p and Ge layer concentration x.

In order to achieve the final crystal quality and relaxation, a 1.2 μm-thick SiGe layer with the same Ge concentration of the last step graded layer (e.g. $Si_{0.19}Ge_{0.81}$ as above) is grown at 500°C with a pressure of 1.20 mTorr.

Figure 4.8 shows the Energy-Dispersive X-ray spectroscopy (EDX) composition profile with the corresponding Scanning Transmission Electron Microscopy (STEM) image in BF mode for the $Si_{0.19}Ge_{0.81}$ buffer layer down to the Si substrate. No inter-diffusion or segregation is observed within the sensitivity of the technique. In the bottom part of the TEM image, we notice the presence of extended defects, such as threading and misfit dislocations, due to the plastic relaxation of the heteroepitaxial strain [105, 141]. The threading dislocation density on the surface, obtained by etch-pit counting (not shown here), is about $1\times10^8cm^{-2}$. The lattice tilt, arising from the network of dislocations, leads to a formation of a cross-hatch pattern at the surface [142, 143], as shown in the AFM image reported in Fig 4.8(b). The root-mean-square surface roughness is about 2.5 nm within a 25 × 25 μm^2 image.

For Ge concentrations x above 90%, a different approach is employed. As a matter of fact, this strategy is used when the strain-compensated structures introduced in 1.5.1 are required and the precise control of the in-plane lattice parameter of the VS is necessary. For the sake of simplicity, we here describe the strategy in the specific case of a desired final concentration x = 95%, but it is valid for any concentration above 90%. In this case, on top of the relaxed 700 nm-thick Ge buffer, the Ge concentration is initially decreased to ~95%

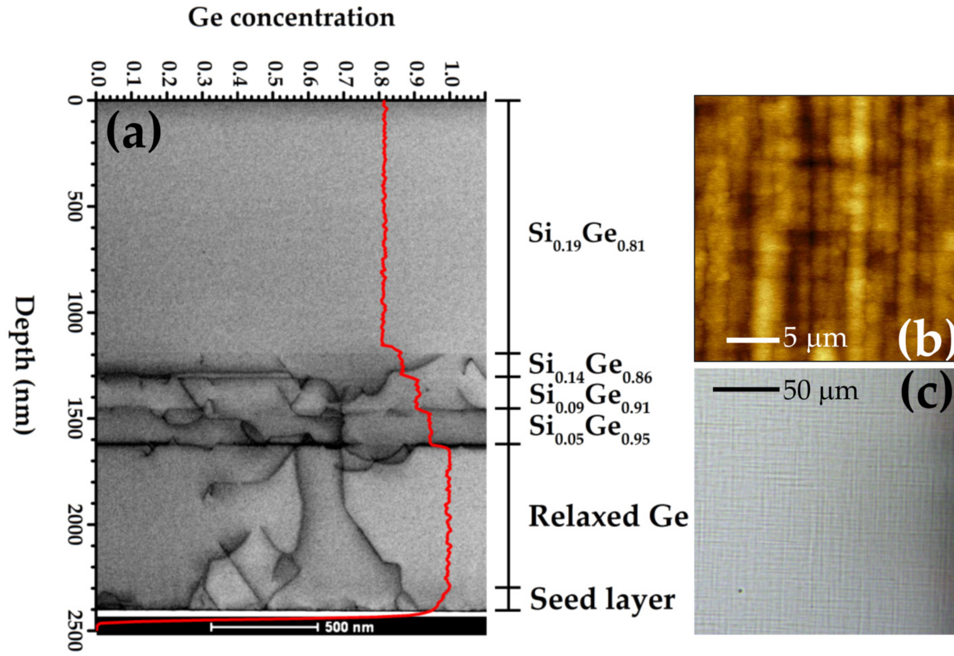

Figure 4.8 – (a) EDX composition profile of the RG-VS (terrace compositions are nominal) of a $Si_{0.19}Ge_{0.81}$ VS superimposed on the corresponding STEM. (b) 25×25 μm^2 surface morphology of the buffer measured with AFM. The height range is 21 nm. Image sides are aligned along the $\langle 011 \rangle$ directions. (c) Optical microscope image of the buffer.

and then to ~90%, as in the case of low-x buffers. On top of the last step of the reverse grading is deposited a 1.2 μm-thick $Si_{0.09}Ge_{0.90}$ buffer. Finally, a 500 nm-thick $Si_{0.05}Ge_{0.95}$ layer is deposited. The rationale of this strategy is that, due to thermal strain, the direct deposition of a $Si_{0.05}Ge_{0.95}$ layer would feature an in-plane lattice parameter *equivalent* to that of a $Si_{1-y}Ge_y$ alloy, with $y > 0.95$. Therefore, the goal of the $Si_{0.09}Ge_{0.90}$ buffer is to balance the tensile thermal strain with the compressive strain originated by the coherent growth, and the lattice of the $Si_{0.05}Ge_{0.95}$ layer is thus cubic. (004) XRD rocking curve and RSM of asymmetric $(4\bar{2}\bar{2})$ reflections of a $Si_{0.05}Ge_{0.95}$ VS are reported in Fig. 4.9. Starting from the angular position of the peaks, using Bragg's law, it is easy to extract the in-plane $a_{\|}$ and out-of-plane $a_{\perp}$ lattice parameters. Moreover, knowing the relationship linking $a_{\|}$ and $a_{\perp}$ to the bulk, unstrained lattice parameter a_0

$$a_0 = \left(\frac{1-\nu}{1+\nu}\right) a_{\perp} + \left(\frac{2\nu}{1+\nu}\right) a_{\|}, \tag{4.5}$$

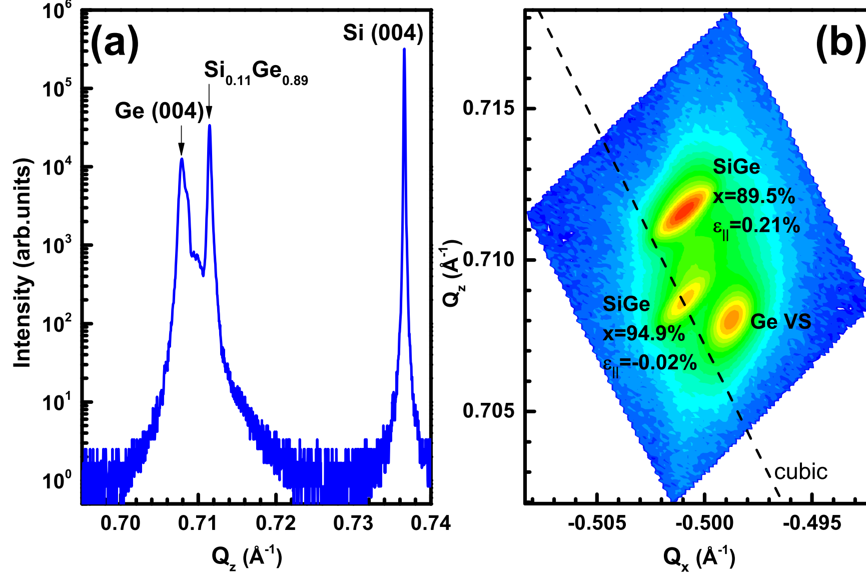

Figure 4.9 – (a) (004) XRD rocking curve and (b) reciprocal space maps of asymmetric $(4\bar{2}\bar{2})$ reflections of a $Si_{0.05}Ge_{0.95}$ VS.

where ν=0.273 is the elastic modulus of Ge [144], it is possible to verify the Ge composition x of the layers. Indeed, the bulk lattice parameter of $Si_{1-x}Ge_x$ alloys is given by Dismukes equation[145]:

$$a_0(x) = 5.431 + 0.2 \cdot x + 0.027 \cdot x^2. \quad (4.6)$$

From the measured value of a_0=5.631 (5.645) Å, the Ge content x is equal to 0.89 (0.95). Since the $Si_{0.11}Ge_{0.89}$ buffer is strained, due to thermal strain, its in-plane lattice parameter is equivalent to the lattice parameter of a $Si_{1-y}Ge_y$ relaxed bulk alloy, with $y > 0.89$. The *equivalent concentration* y can be calculated recalling the bulk lattice parameter of $Si_{1-x}Ge_x$ alloys given by Eq. 4.6, obtaining that the in-plane lattice parameter $a_{\|}$ of the $Si_{0.11}Ge_{0.89}$ layer is equivalent to the lattice parameter of a $Si_{0.06}Ge_{0.94}$ relaxed alloy. The in-plane lattice strain $\varepsilon_{\|}$ of the $Si_{0.05}Ge_{0.95}$ layer can be calculated considering that, owing to the coherent growth, the in-plane lattice parameter of the $Si_{0.05}Ge_{0.95}$ layer and the in-plane lattice parameter of the VS are the same $a_{\|}(Si_{0.05}Ge_{0.95})$ = $a_{\|}(Si_{0.06}Ge_{0.94})$. Then, the in-plane lattice strain $\varepsilon_{\|}$ can be calculated as

$$\varepsilon_{\|} = \frac{a_{\|}(Si_{0.06}Ge_{0.94}) - a_{\|}(Si_{0.05}Ge_{0.95})}{a_{\|}(Si_{0.05}Ge_{0.95})} = -0.02\%. \quad (4.7)$$

It follows that the $Si_{0.05}Ge_{0.95}$ layer is slightly compressively strained. The condition of coherent growth can be demonstrated with the help of Fig. 4.9(b). As a matter of fact, we observe that the peak related to the $Si_{0.05}Ge_{0.95}$ layer is vertically aligned to that of the $Si_{0.11}Ge_{0.89}$ buffer. Moreover, the $Si_{0.05}Ge_{0.95}$

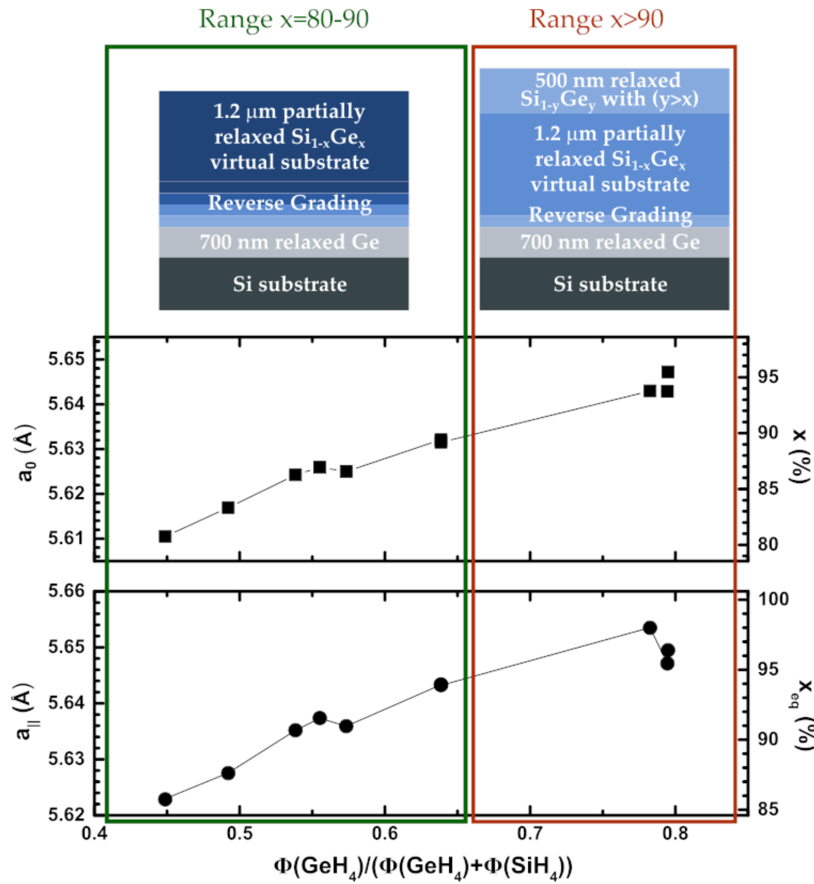

Figure 4.10 – Lattice parameter (and the corresponding concentration x) of the $Si_{1-x}Ge_x$ buffer, as measured by XRD, as a function of the injected fluxes of GeH_4 and SiH_4.

peak lies on the line of the growth of cubic relaxed SiGe alloys, indicating that indeed thermal and epitaxial strain are balanced.

The lattice parameter (and the corresponding concentrations x) of the final $Si_{1-x}Ge_x$ buffer, as measured by XRD, as a function of the injected fluxes of GeH_4 and SiH_4 is reported in Fig. 4.10. The two different strategies employed for the growth of the SiGe VS are also reported.

4.3.1 *Optical Properties of the SiGe Virtual Substrate*

In Fig. 4.12 (a), we report the PL spectra acquired on a $Si_{0.19}Ge_{0.81}$ VS, at a constant pump power density, estimated to be 3.7×10^5 W·cm^{-2}, and varying the lattice temperature from 80 K to 330 K, in ~ 30 K steps. The behavior of the PL spectra acquired on the VS sample is similar to that observed in the Ge sample [Fig. 4.6(a)] but, in this case, the high-energy side of the

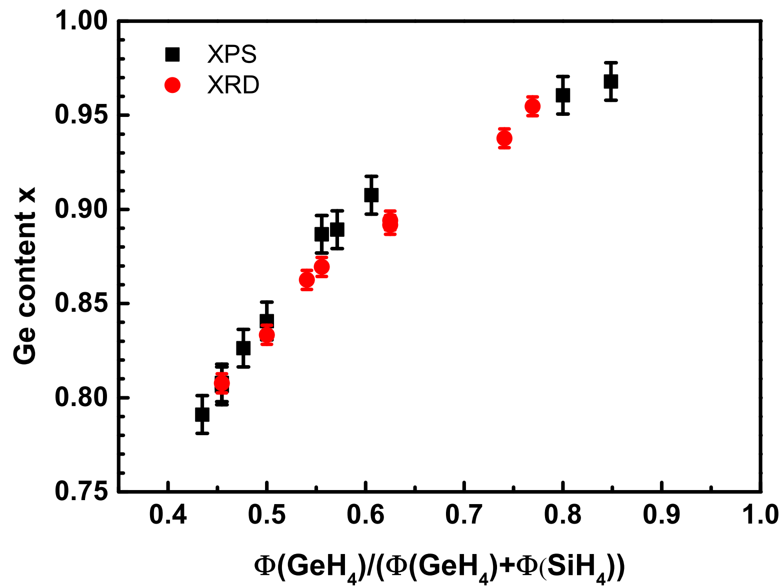

Figure 4.11 – Ge content x in different $Si_{1-x}Ge_x$ samples, measured by XPS and XRD, as a function of the injected fluxes of GeH_4 and SiH_4.

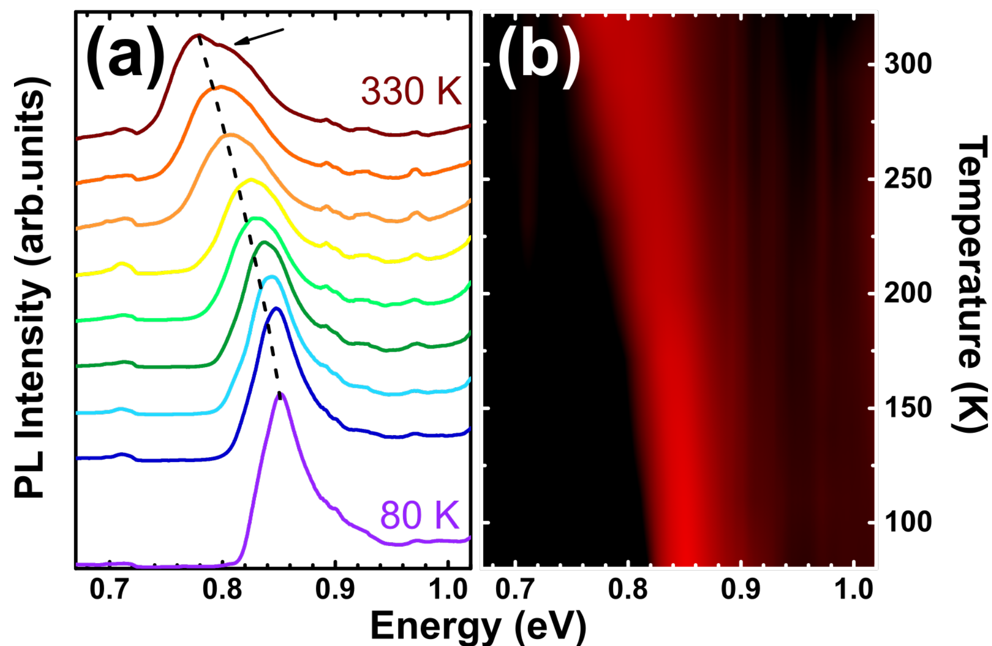

Figure 4.12 – (a): PL spectra acquired on the VS. Lattice temperatures range from 80 K to 330 K in ~ 30 K steps. (b): Contour plot of the PL spectra as a function of T with integrated intensity at each temperature normalized to unity. Dashed line is the result of the fitting of Ge experimental data with Varshni equation.

peaks is broader [see arrow in Fig. 4.12(a)]. Indeed, the fitting of the Γ_c-HH transitions in Ge with the Varshni equation (dashed line) reported in Fig. 4.12(a) clearly evidences the presence of an high-energy shoulder. Since the direct gap energy of a SiGe alloy is an increasing function of its Si content, as we discussed in section 1.3 (see Fig. 1.12), we can attribute this feature to the fact that we are also probing the direct recombination across the VS layers. In particular, our numerical results indicate that, at the pump-energy used, the 95% step of the RG-VS also contributes to the PL signal, while the other SiGe layers, richer in Si, remain almost transparent to the excitation (note that, as a consequence, reabsorption effects involving photons emitted from the inner Ge and $Si_{0.05}Ge_{0.95}$ layers can be also neglected in our samples).

5

GROWTH AND CHARACTERIZATION OF GE/SIGE QUANTUM WELLS

Once a good-quality virtual substrate has been grown and its structural and optical properties have been investigated in details, it is possible to deposit the heterostructures, consisting in alternating a sequence of Ge and SiGe layers for a certain amount of time. The growth starts with a $Si_{0.19}Ge_{0.81}$ layer as connection with the virtual substrate and continues with the periodic QW heterostructure finally covered with a 30 nm-thick SiGe layer for protection. At the end of every layer a $\sim$ 20 seconds vacuum-purge has been inserted in order to expel every gas residue from the previous step. As a matter of fact, the residential gas time in the chamber is $\sim$ 1 s and the purging ensures to perform every step of the deposition in a clean and uncontaminated environment. The optimal deposition-condition has been thoroughly investigated in Refs. [146, 147], and has been determined to be p = 1.20 mTorr and T = 500°C. The growth rate, necessary to convert the targeted layer-thickness in time of deposition, has been evaluated with the help of a calibration sample featuring a stack of QWs and barriers with different thicknesses.

The TEM-EDX image of the calibration sample is reported in Fig. 5.1(a). In the false-color image the content of silicon and germanium is depicted in red and blue tones, respectively. With the sensitivity of the technique we are able to clearly distinguish the ~5% composition-variation of the $Si_{1-x}Ge_x$ layer indicated by the white arrow in Fig. 5.1(a). The thickness of the several layers has been measured by means of TEM-EDX and Time-of-Flight Secondary Ion Mass Spectrometry (ToF-SIMS) and the results obtained are in good agreement [see Fig. 5.1(b)].

The rate of growth have been evaluated interpolating the thicknesses of the calibration sample, measured by TEM and SIMS, as a function of the deposi-

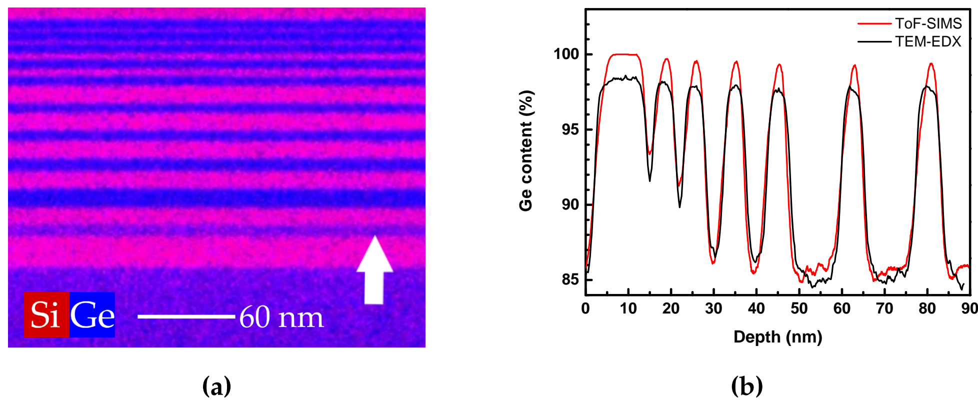

Figure 5.1 – (a) False color TEM-EDX image of the calibration sample. The content of silicon and germanium is depicted in a red and blue tone, respectively. (b) Ge-content depth-profile as measured by TEM-EDX and ToF-SIMS.

tion time [Fig. 5.2(a) and 5.2(b)], obtaining ~ 6.5 nm/min for the QWs and ~ 4.5 nm/min for the barriers. Since the rate of growth is strongly dependent on the temperature T, and pressure p during the deposition, we performed all the growths under the same conditions of p = 1.20 mTorr and T = 500°C.

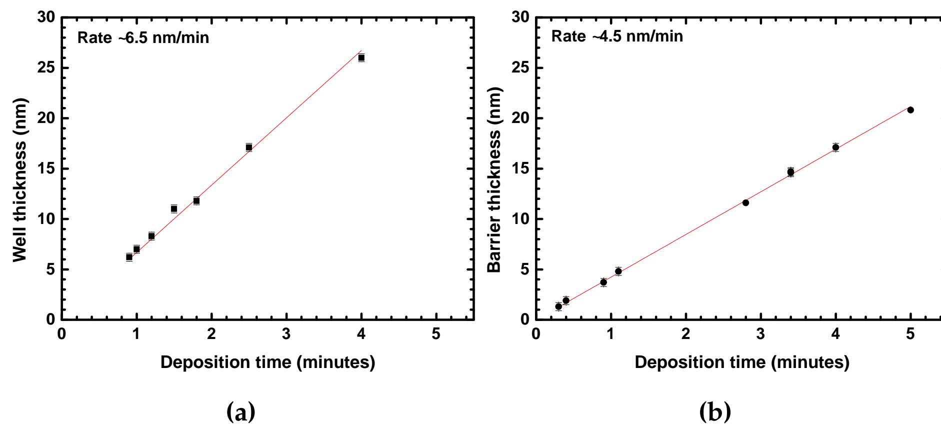

Figure 5.2 – (a) Ge wells, and (b) $Si_{0.15}Ge_{0.85}$ barriers thickness as a function of the deposition time. All the samples have been grown at 500°C and 1.20 mTorr.

To unambiguously disentangle the effect of strain, doping, and quantum tunneling between the barriers, we firstly discuss the optical properties of symmetric quantum wells. The study of the structural and optical properties of this simple structure allows to calibrate the theoretical modeling introduced in Chapter 2. The investigation of the optical properties of the VS discussed in Chapter 4 will be of paramount importance for make a one-to-one identification of all the spectral features. We will find that the main limitations

that hinder the employment of Ge/SiGe QWs as an active material in a Si-based light emitter are the emission wavelength in the E-band and a strong quenching of the PL signal at increasing temperature.
As profoundly analyzed in 1.2.3, the redshift of the emitted light can be achieved by means of tensile strain. To induce tensile strain in the Ge lattice an external SiN stressor has been deposited on one of the investigated sample. The mechanism of strain-transfer will be discussed in details with the help of finite element method (FEM) simulations and μ-Raman spectroscopy. As a result of the tensile strain induced in the QWs, a redshift of the light emission will be demonstrated.
To enhance the optical properties of bulk Ge doping is commonly employed. Thus, we will investigate how heavy n-type doping affects the PL of Ge symmetric QWs. We will find that heavy doping can be detrimental to the optical properties of the QWs if a threshold dopant concentration is exceeded. Finally, the possibility of relaxing the selection rules for inter-band transition in QWs, introduced in Chapter 2, will be demonstrated studying the optical properties of asymmetric quantum wells.

5.1 symmetric quantum wells

In this section we report the structural and optical properties of the symmetric multi-quantum wells. A detailed investigation of this simple structure, consisting in the periodic repetition of symmetric elements of single QWs separated by thick barriers to prevent any coupling between them, is of paramount importance. As a matter of fact, these samples will be a benchmark for evaluating the modification of the optical properties induced by external stress, doping and coupling between adjacent quantum wells.
The nominal parameters of the samples here investigated are reported in Table 5.1.

5.1.1 *Structural Properties of Symmetric QWs*

The structural characterization have been performed in order to retrieve the properties of the samples needed for the calculation of their electronic states, as reported in Chapter 2, and to assess therefore the quality of the model system.

Sample	Periods	d_w [nm]	d_b [nm]
S10-2	2	10	17
S10-5	5	10	17
S10-10	10	10	17
S17-2	2	17	15
S17-5	5	17	15
S25-2	2	25	15
S25-5	5	25	15

Table 5.1 – Nominal parameters of the samples here investigated. Samples are labeled as S *thickness of QW-number of periods*.

The geometrical parameters of the quantum wells, i.e. thickness of wells and barriers, have been measured by means of scanning transmission electron microscopy and energy-dispersive X-ray spectroscopy. As we discussed in section 3.2.2, the composition of the several $Si_{1-x}Ge_x$ layers and their strain can be investigated by X-ray diffraction and Raman spectroscopy. XRD has been also employed to retrieve the superlattice periodicity of the samples. The good agreement between the values obtained with different techniques allowed to unambiguously define the input parameters of the numerical calculations. Last but not least, the structural characterization has confirmed the good quality of the samples and a high-degree of reproducibility in the deposition process.

TEM

For the Ge/SiGe QW stack, homogeneous periodicity and smooth barrier-well interfaces are observed (see Fig. 5.3). From the STEM images, the thickness of Ge wells and SiGe barriers has be determined and their values are reported in Table 5.2. In Figure 5.3 is also reported the EDX composition profile of Si and Ge superimposed on the corresponding STEM image for the QWs region of sample S10-10. No segregation is observed within the sensitivity of the technique. A quantitative analysis of the EDX composition profile indicates the presence of SiGe intermixing at the interfaces resulting in a broadening of the well/barrier profile over a length-scale of $\sim$ 0.8 nm, well-matching the results obtained by Bashir *et al.* on nominally identical Ge/SiGe MQWs [148].

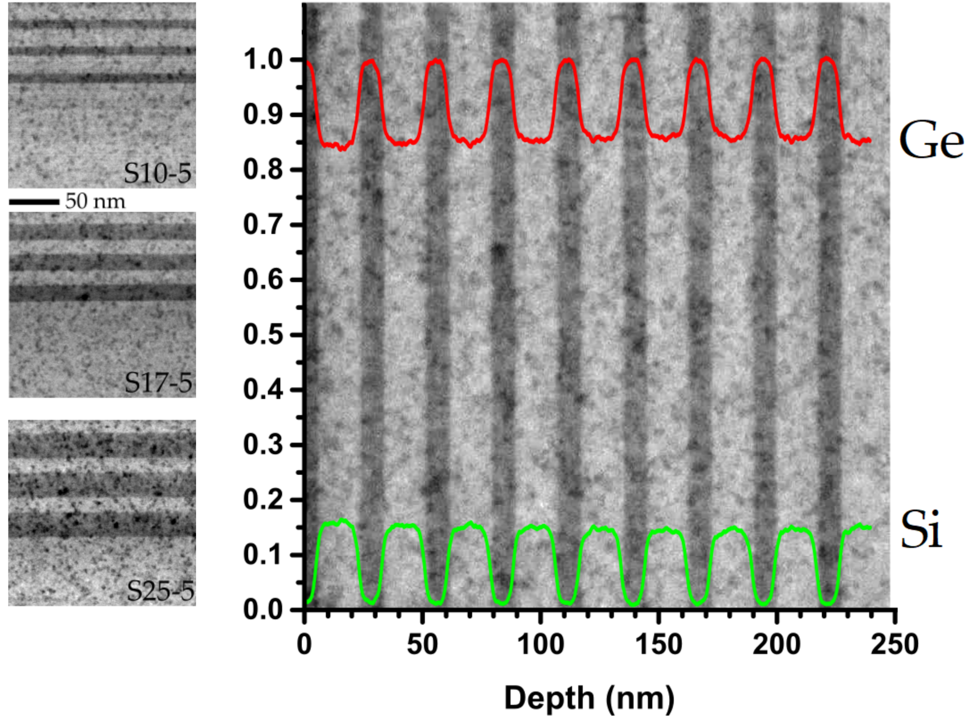

Figure 5.3 – *Left:* STEM images of the QWs region of samples S10-5, S17-5, and S25-5. *Right:* EDX composition profile superimposed to the corresponding STEM image of the QWs region of sample S10-10.

It is interesting to underline that in the STEM images reported in Fig. 5.3 the number of quantum wells that can be observed is different from the values reported in Table 5.1. As a matter of fact, for TEM analysis the sample needs to be cut in ultra-thin lamellas using a focused ion beam (FIB) and, unfortunately, during the lamella preparation the first layers of the samples have been damaged.

Sample	Periods	t_w+t_b STEM (XRD)	$\varepsilon_{\parallel}$(Ge)	$\varepsilon_{\parallel}$(SiGe)
S10-2	2	(26.3) nm	-0.5%	0.1 %
S10-10	10	10.5+17.2=27.7 (27.5) nm	-0.6%	0.1 %
S10-5	5	10.9+17.1=28.0 (28.1) nm	-0.6%	0.1 %
S17-5	5	17.1+14.7=31.8 (31.5) nm	-0.5%	0.1 %
S25-5	5	25.9+14.6=40.5 (41.1) nm	-0.6%	0.1 %

Table 5.2 – Material parameters of the samples here investigated as determined by TEM and XRD.

XRD

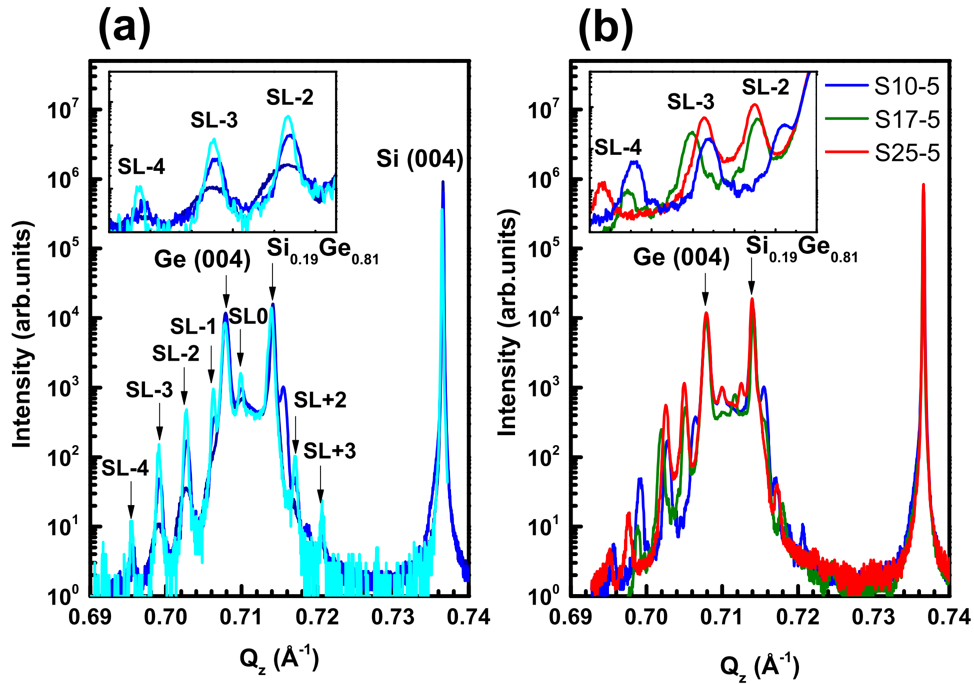

Figure 5.4 – (a) XRD rocking curve of samples S10-2 (dark blue), S10-5 (blue), and S10-10 (light blue). The nominal thickness of the QWs is the same. In the inset, a detail of SL peaks is reported. (b) XRD rocking curve of samples S10-5 (blue), S17-5 (green), and S25-5 (red). In the inset, the different periodicity of the SL-peaks is clearly observed.

To determine the strain and the actual composition of the SiGe layers, the samples were characterized by XRD rocking curves and XRD reciprocal space maps (RSM).

In Fig. 5.4(a) we report a (004) rocking curve of samples S10-2, S10-5, and S10-10 around the (004) Ge and (004) Si Bragg peaks. The only difference between the samples is the number of QWs, the thickness of wells (t_w) and barriers (t_b) being nominally the same. As introduced in section 3.2.2, the out-of-plane scattering vector Q_z can be derived from the diffraction angle with the help of Eq. 3.5

$$Q_z = 4\pi sin(2\Theta/2)/\lambda.$$

Three main peaks are observed at scattering vectors Q_z ~0.708, ~0.714, and ~0.736, which are related to diffraction peaks from the Ge, SiGe and Si layers, respectively. Multiple orders of superlattice (SL) satellites are observed for all the samples, indicating high crystal quality and sharp interfaces between Ge

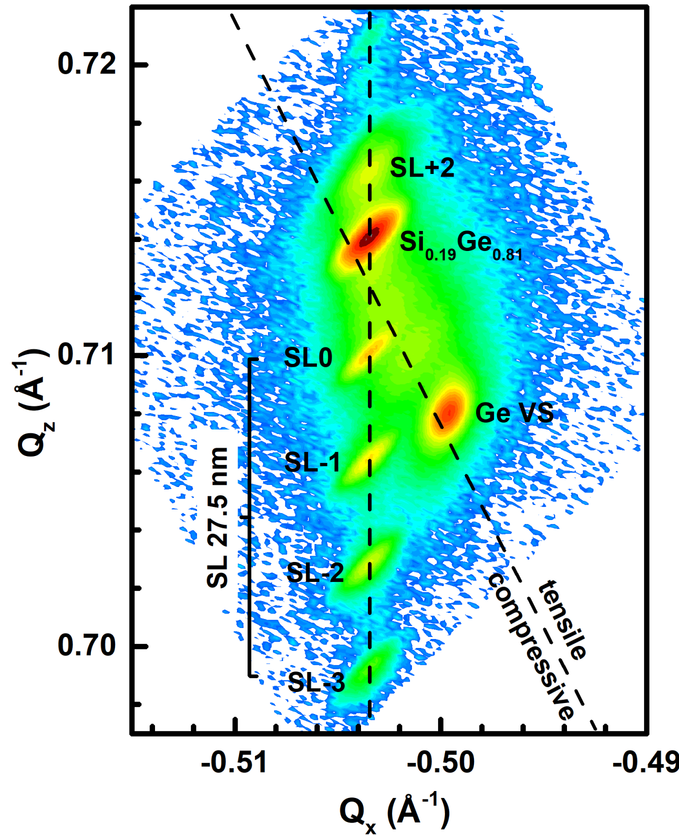

Figure 5.5 – Reciprocal space maps of asymmetric ($4\bar{2}\bar{2}$) reflections of sample S10-10.

wells and SiGe barriers, as also demonstrated by TEM images. The spacing between the superlattice fringes (Kiessig fringes) is inversely proportional to the periodicity of the Ge wells [143], and the spatial periodicity of the grown heterostructures obtained (27.5 nm for sample S10-10) is in good agreement with the analysis of TEM images (27.7 nm for sample S10-10). For all the samples the peak positions are the same, indicating a good repeatability in the thickness of the QWs. As expected, increasing the number of periods the intensity of the SL peaks increases. XRD rocking curve measurements have been carried out on all the samples [Fig. 5.4 (b)], and the spatial periodicity obtained is reported in Table 5.1.

The HR-XRD reciprocal space map around asymmetric ($4\bar{2}\bar{2}$) reflections of sample S10-10 is shown in Fig. 5.5. The spots corresponding to the Ge VS and the $Si_{0.19}Ge_{0.81}$ buffer layer are slightly shifted from the relaxation line (i.e., the line of fully relaxed growth of SiGe alloys, going from Si to Ge, represented by the dashed diagonal line), indicating that the layers are over-relaxed, due to the difference between the coefficient of thermal expansion in Ge and Si. The SiGe buffer layer exhibits a chemical composition $x = 0.81$ and a tensile strain

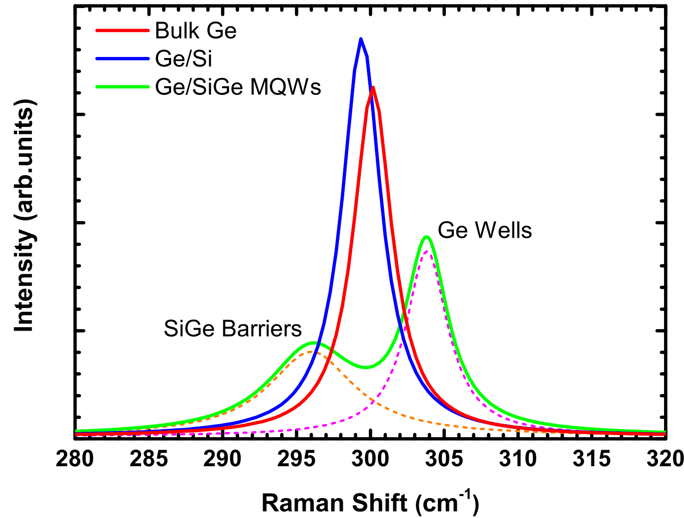

Figure 5.6 – Comparison between the Raman spectra of a reference bulk Ge (001) substrate, a Ge/Si (001) epitaxial thin film, and sample S10-5.

of $\varepsilon_{\|} = 0.22\%$. Since the $Si_{0.19}Ge_{0.81}$ layer is tensile strained, the MQWs are not strain-compensated. Nevertheless, Figure 5.5 indicates that the peaks related to the MQWs are vertically aligned to the peak of the $Si_{0.19}Ge_{0.81}$ buffer layer (dashed vertical line) and thus exhibit the maximum of the epitaxial strain. It follows that, although the strain is not symmetrized, the entire MQW stack is coherent with the in-plane lattice parameter of the under-lying VS, thanks to the small number of periods. Owing to the coherent growth it is possibile to estimate the strain conditions of Ge wells and SiGe barriers. As a matter of fact, the in-plane lattice parameter of the wells will be $a_{\|}(\mathrm{Ge})=a_{\|}(\mathrm{Si}_{0.14}\mathrm{Ge}_{0.86})$ and the lattice distortion can be calculated considering that

$$a_{\|}(\mathrm{Ge}) = a_0(\mathrm{Ge})(1 + \varepsilon_{\|}). \tag{5.1}$$

With the help of 5.1 and considering that the entire $Ge/Si_{1-x}Ge_x$ stack is coherent with the in-plane lattice parameter of the VS, we get that the Ge wells are tetragonally distorted with $\varepsilon_{\|}$= -0.6, while the $Si_{0.15}Ge_{0.85}$ barrier lattice is slightly tensile strained, being $\varepsilon_{\|}$= 0.1 (see Table 5.2).

Raman

Although measured by XRD, composition and strain of the active region of the samples have been also investigated by means of Raman spectroscopy. Indeed, in the following we shall investigate the local strain in structures featuring size of a few micro-meters. Due to the complete penetration of the

sample by the X-rays, a large volume is investigated and local variations of strain can not be discriminated. Therefore, the μ-Raman set-up described in section 3.2.4 has been employed.

The Raman spectrum of sample S10-5 is reported in Fig. 5.6 together with that of a bulk Ge (001) reference and a Ge/Si (001) virtual substrate. For bulk and epitaxial Ge, a peak is observed at 300 cm^{-1}, which is related to the Ge-Ge LO mode. The QWs spectrum clearly shows two features below and above 300 cm^{-1} associated to the Ge-Ge vibration mode excited in the SiGe barriers and in the Ge wells, respectively.

As discussed in section 3.2.4, the knowledge of the vibrational frequencies as obtained by Raman spectroscopy enables the simultaneous determination of the composition x and the biaxial strain $\varepsilon_{\|}$. This can be done recalling Eq. 3.29

$$\omega^{Ge-Ge}(x, \varepsilon_{\|}) = 280.3 + 19.4 \cdot x - 450 \cdot \varepsilon_{\|}.$$

For Ge wells, x=1 and, using Eq. (3.29), the strain $\varepsilon_{\|}$ is determined to be -0.6±0.1% for sample S10-5, indicating that the Ge layers are compressively strained, as estimated by XRD. Correspondingly, the in-plane lattice parameter of the Ge layers is $a_{\|}(Ge) = a_0(Ge)(1 + \varepsilon_{\|}) = 5.624$ Å, in perfect agreement with the value measured for the $Si_{0.19}Ge_{0.81}$ buffer layer by means of XRD, confirming the coherent growth of the MQWs stack and the appropriate choice of the strain shift coefficient. For SiGe barriers, the in-plane lattice constant can be expressed as

$$a_{\|}(\text{SiGe}) = a_0(\text{SiGe})(1 + \varepsilon_{\|}(\text{SiGe})), \tag{5.2}$$

where $\varepsilon_{\|}$(SiGe) is the in-plane strain of the $Si_{1-x}Ge_x$ layers, and a_0(SiGe) is the bulk lattice constant of $Si_{1-x}Ge_x$ alloys given by Eq. 4.6. Because of the pseudomorphic growth conditions of the Ge/$Si_{1-x}Ge_x$ QW stack, as confirmed by XRD, $a_{\|}$(SiGe)=$a_{\|}$(Ge). From Eq. (3.29) the frequency shift of the Ge-Ge vibration mode in the barrier region is given by

$$\Delta\omega(x, \varepsilon_{\|}) = 19.4(x - 1) - 450 \cdot \Delta\varepsilon_{\|}, \tag{5.3}$$

where $\Delta\varepsilon_{\|}$=$\varepsilon_{\|}$(SiGe)-$\varepsilon_{\|}$(Ge). Given the frequency shift $\Delta\omega$ and using Eq. (5.2), the Ge composition in the $Si_{1-x}Ge_x$ barrier is determined to be x=0.85 with an in-plane strain of $\varepsilon_{\|}$(SiGe)=0.3±0.1% for sample S10-5.

The good agreement between the values of strain measured by Raman and XRD allows to validate the phonon strain shift coefficients introduced in section 3.2.4. We stress that this will be of paramount importance for evaluating the strain of the heterostructures after the deposition of the external SiN stressor since μ-Raman is the only technique exploitable for local strain measurements on micro-structures.

5.1.2 *Optical Properties of Symmetric QWs*

Once that the origin of the PL features related to the virtual substrate has been established, temperature-dependent PL measurements have been carried out under the same conditions on sample S10-10. Since the photon energy is larger than the direct gap of Ge, but smaller than the direct gap of the $Si_{0.15}Ge_{0.85}$ barriers, the *quasi-resonant* excitation of carriers involves holes and electronic states confined in the Ge QWs. Therefore, as we discussed in section 2.4.7 the spectra are expected to be dominated by direct recombinations.

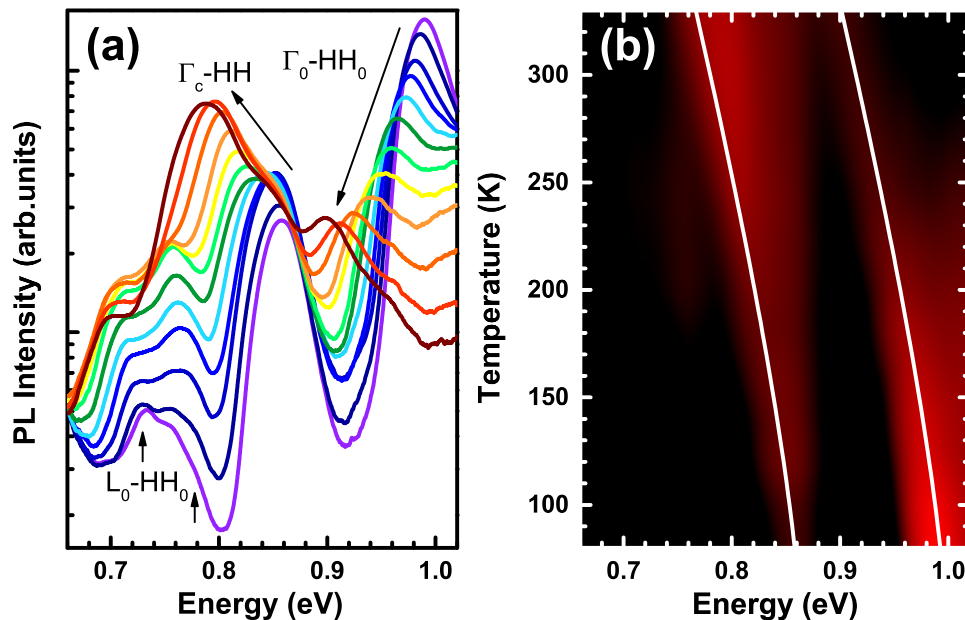

Figure 5.7 – (a) PL spectra acquired on sample S10-10. Lattice temperatures range from 80 K (violet) to 330 K (maroon) in ~ 30 K steps. (b) Contour plot of the PL spectra on sample S10-10 at different lattice temperatures. The integrated intensity at each temperature has been normalized to unity. The results of the fitting of experimental transitions in the Ge layer and the Ge QWs with Varshni equation are also reported as continuous lines.

PL spectra are shown in Fig. 5.7. At first glance, a clear difference between sample S10-10 and the two benchmark samples is observed (see Fig. 5.8), consisting in the intense feature at high energy ranging from $\simeq$ 1 eV at 80 K to $\simeq$ 0.9 eV at 330 K. Supported by our numerical model, we relate this feature to a direct transition inside the Ge well between the first confined states in the conduction and valence bands (Γ_0-HH$_0$). As for the direct recombination in Ge, increasing the temperature, the Γ_0-HH$_0$ transition is redshifted. At the same time, its intensity is quenched. On the low-energy side, a structure related to the indirect transition L_0-HH$_0$ is also observed. Since this structure consists of two features separated by $\sim$ 56 meV (arrows in Fig. 5.7), we attribute them to transitions accompanied by emission and/or absorption of a longitudinal acoustic phonon, being E_{LA}= 28 meV [99]. To support this attribution, we note that, increasing the temperature, the relative intensity of the peak related to phonon absorption is enhanced. The experimental and calculated energies of indirect and direct recombination energies are in excellent agreement as shown in Table 5.3 for selected temperatures.

Temperature (K)	Γ_0-HH$_0$ (eV)		L_0-HH$_0$ (eV)		
	Exp.	Theory	Exp. (ph.em.)	Exp. (ph.abs.)	Theory
80	0.990 ± 0.002	0.995	0.733 ± 0.002	0.779 ± 0.002	0.753
140	0.977 ± 0.002	0.980	0.716 ± 0.002	0.765 ± 0.002	0.738
200	0.958 ± 0.002	0.959	0.708 ± 0.002	0.758 ± 0.002	0.719
300	0.913 ± 0.002	0.916		0.706 ± 0.002	0.682

Table 5.3 – Experimental and calculated Γ_0-HH$_0$ and L_0-HH$_0$ transition energies at selected temperatures.

In between the direct and indirect transitions in the QWs, the direct transition (Γ_c-HH) due to the under-lying VS is also observed. To better evidence the behavior, as a function of temperature, of the ratio of the intensity of the PL feature related to the direct transition in the Ge well to the direct transition in the VS, we report in Fig. 5.7(b) a contour plot of the spectral intensity where the integrated intensity of each spectrum has been normalized to unity. From Fig. 5.7(b) it is clear that the intensity of the Γ_0-HH$_0$ peak is quenched at increasing the temperature, while the intensity of the Γ_c-HH peak is boosted, the ratio between the two features going from $\simeq$ 4.39 at 80 K to $\simeq$ 0.07 at RT. Despite the T-dependent non-radiative recombination dynamics in the substrate and in the QW layers is largely undetermined, the observed

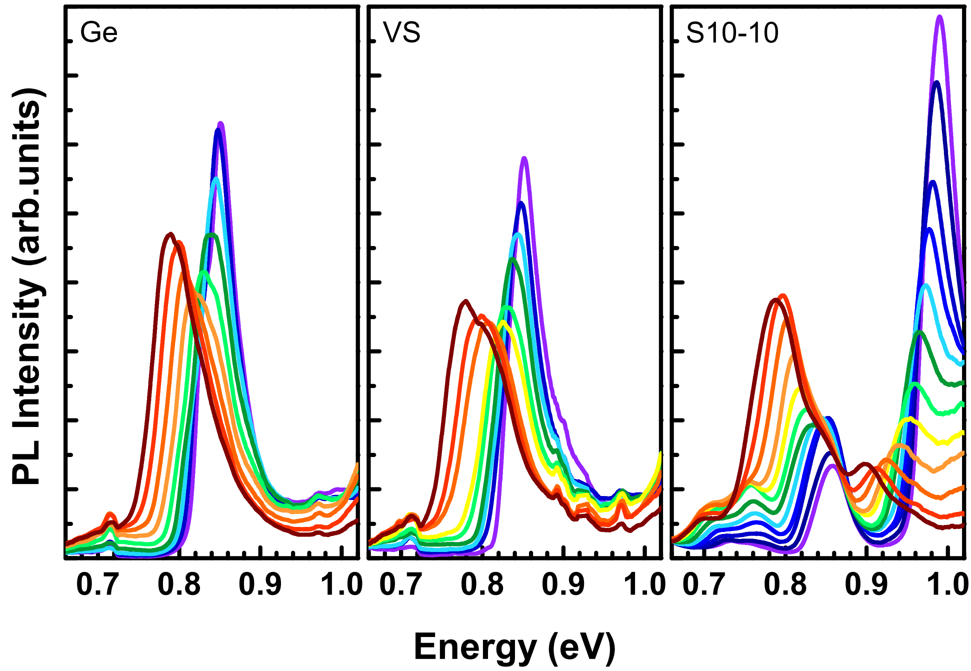

Figure 5.8 – Comparison between the temperature-dependent PL spectra acquired on samples Ge, VS, and S10-10.

behavior of the intensity ratio may suggest that the spatial distribution of the excess carrier density becomes more concentrated in the substrate region at increasing temperature.

To quantitatively characterize the direct band transition in the Ge wells of sample S10-10, we have calculated the corresponding electronic states and band structure relying on the theoretical framework introduced in section 2.1.2 [see Fig. 5.9(a)]. The experimental and theoretical energies for the Γ_0-HH_0 transition as a function of the temperature are reported in Fig. 5.9(b) as filled and empty circles, respectively. Experimental data have been fitted following Varshni equation with the same values for α and β used in Eq. (4.3), but setting a larger $E(0)$ to account for the confinement energy. The result of this fitting procedure is reported in Fig. 5.9 as a continuous line. The experimental, calculated, and fitted energies are in good agreement, confirming that this PL feature originates from direct transitions in the Ge QWs involving the fundamental HH_0 and Γ_0 confined states.

To definitively confirm that the observed high-energy peak is related to the Γ_0-HH_0 transition in the QW, we report in Fig. 5.10(a) the PL spectra acquired at 80 K on samples S10-2, S10-5, and S10-10 which have equal nominal thick-

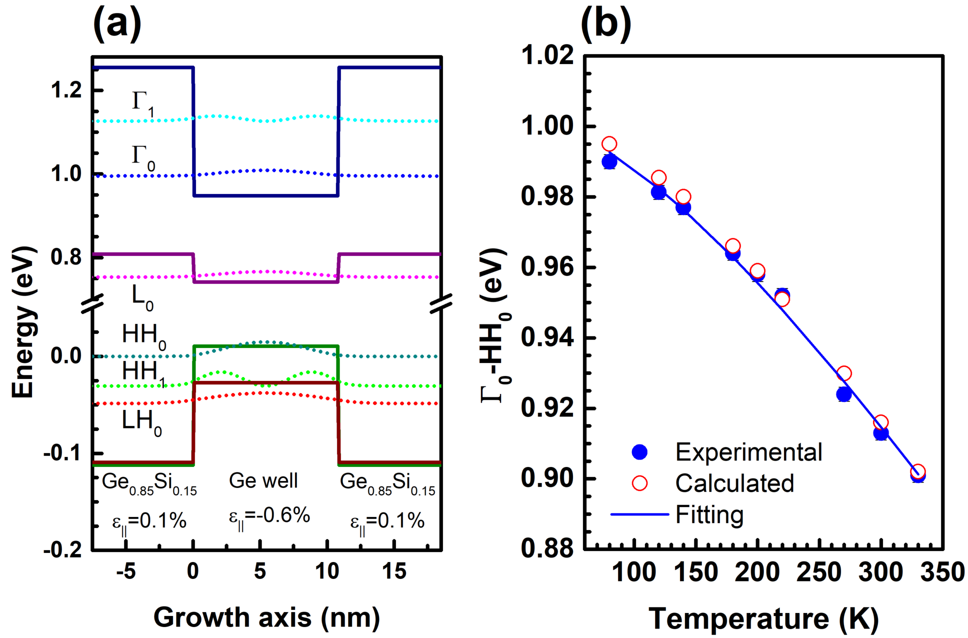

Figure 5.9 – (a) Conduction- and valence-band edge profiles (continuous lines) and square modulus of the wave functions (dotted lines) for the electron and hole confined states of sample S10-10 at 80 K. (b) Experimental (filled circles) and calculated (empty circles) energy of the Γ_0-HH_0 transition in sample S10-10 as a function of the lattice temperature. The fitting of the experimental data with Varshni equation is reported with a continuous line.

ness but different number of periods. Spectra have been normalized so that the intensity of the peak related to the direct transition in the VS is equal to unity. As for the XRD rocking curve, the position of the QW peak is the same for all the samples, indicating good repeatability and the absence of thickness fluctuations, while the intensity of the PL signal is approximately proportional to the number of QW periods, as can be seen in the inset of Fig. 5.10(a). This observation is compatible with a scenario where the MQWs are uniformly excited and the ratio of the excess carrier density in a single QW to that in the substrate does not vary significantly with the number of periods. The reproducibility of the deposition process and the repeatability of the optical properties of samples featuring the same QWs-thickness but different number of periods ensure to obtain light emission even if the thickness of the active region is limited by external constraints, as we will see in the following.

In the right panel of Fig. 5.10 we show the integrated intensity of the PL spectra as a function of $\beta = 1/k_B T$. The integrated intensity, collected from

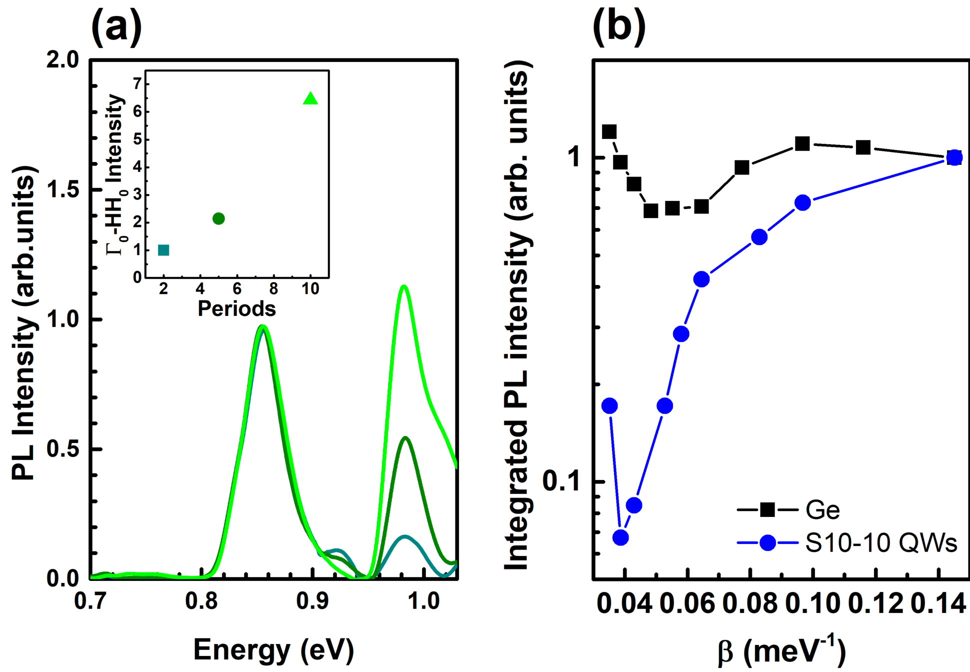

Figure 5.10 – (a) PL spectra acquired at 80 K on samples S10-2 (dark green), S10-5 (green), and S10-10 (light green). In the inset: Integrated PL intensity of the QWs peaks as a function of the number of periods. (b) Integrated PL intensity as a function of $\beta = 1/k_B T$. Squares and circles represent Ge and sample S10-10, respectively.

the Ge sample is displayed as squares, while circles represent the intensity of the QWs feature in sample S10-10. For both samples, data in Fig. 5.10 have been normalized to unity at 80 K.

The two curves show a non-monotonic trend with a single minimum at β equal to 0.048 and 0.039 for the Ge and QW sample, respectively. This behavior can be attributed to the interplay between the thermal boost of the PL intensity induced by the increase of the electron population in the Γ valley and by thermal emission of carriers from dislocations [149], which determines the negative slope in the high-temperature regime [32, 139], and the quenching of the PL dominating in the low-T regime, caused by non-radiative processes whose rate increase with T [150, 151, 152]. In the case of the QW sample, the thermal promotion of electrons from L_0 to Γ_0 is hindered by the larger energy difference occurring between the direct and indirect gap, which in the QW system is associated to the lighter confinement mass of Γ electrons with respect to the L ones (see 2.1.1). Therefore in the high T regime, the increase with T of the non-radiative recombination rate plays in this case a major role in suppressing the PL signal. Moreover, also the T-driven migration of

excess carriers toward the substrate region observed increasing T [see Fig. 5.7(b)] contributeS to the quenching of the $\Gamma_0 - HH_0$ signal. As a result, the integrated PL signal for the QW sample shown in Fig. 5.10 as a function of β spans a broader range and the minimum is shifted to a lower value with respect to the Ge case.

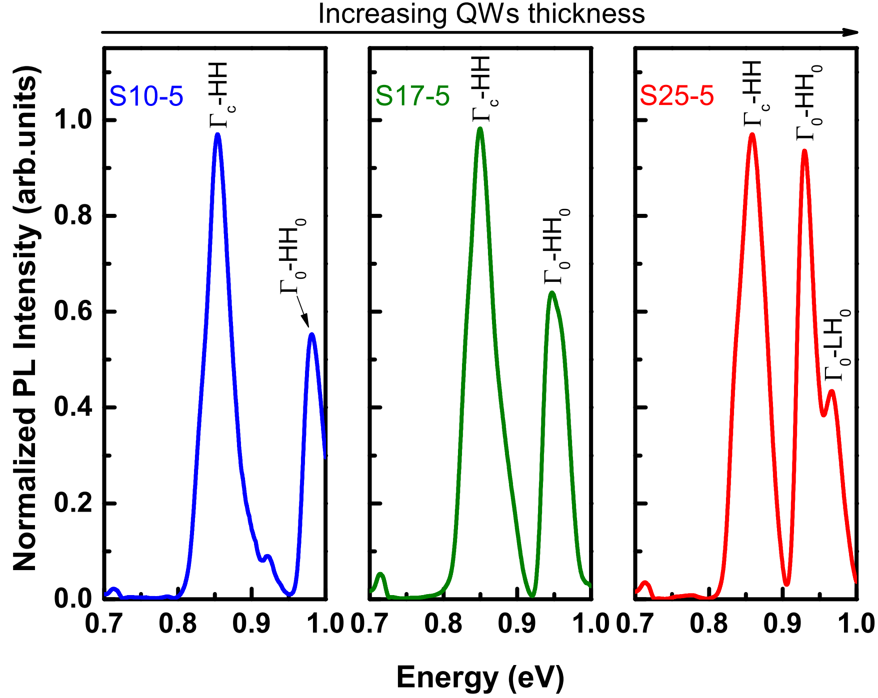

Figure 5.11 – PL spectra acquired at 80 K on samples S10-5 (blue), S17-5 (green), and S25-5 (red) The redshift of Γ_0-HH$_0$ with increasing thickness is clearly observed.

To clarify the effect of quantum confinement, we also performed temperature-dependent PL measurements on QWs with different thickness (spectra at 80 K reported in Fig. 5.11), whose value has been measured by XRD and TEM (see Table 5.1). Interestingly, in the larger-well sample (S25-5), a spectral feature at $\sim$ 39 meV above the Γ_0-HH$_0$ one is also distinguishable. Since our model predicts an excess energy of 40 meV for the Γ_0-LH$_0$ recombination, we can safely attribute this additional peak to radiative recombinations across the direct gap, involving the light-hole fundamental state.

The experimental and calculated Γ_0-HH$_0$ transition energies at 80 K and RT are reported as a function of the QW thickness in Fig. 5.12 as filled and empty symbols, respectively. Their values are larger than the one associated to the direct recombination in the Ge sample ($\simeq$ 0.85 eV at 80 K and $\simeq$ 0.80 eV at RT), due to the concomitant effect of quantum confinement and compressive

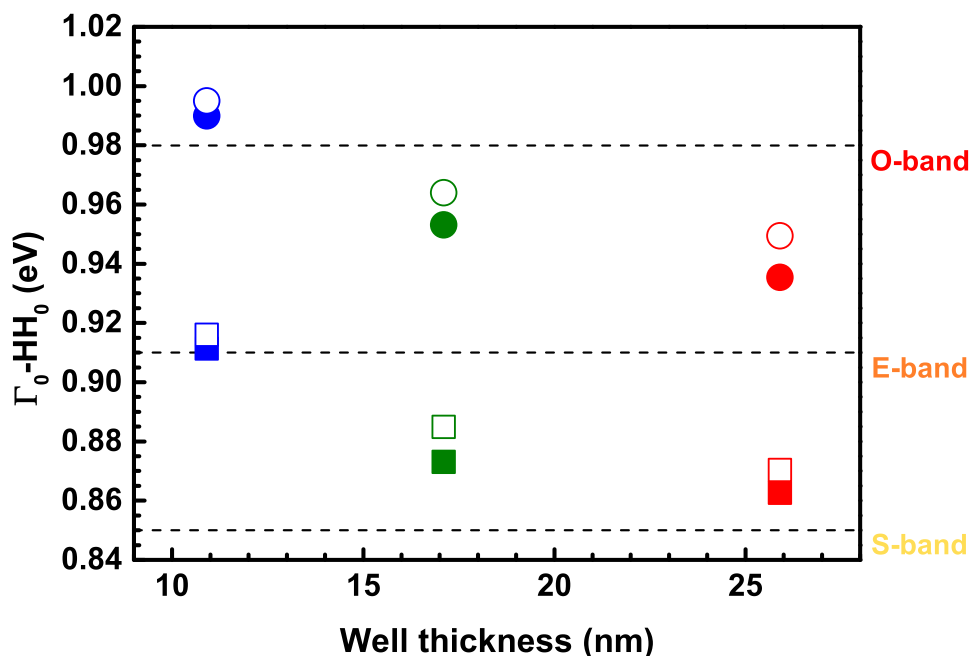

Figure 5.12 – Experimental (filled symbols) and calculated (empty symbols) energy of the Γ_0-HH_0 transition, as a function of the QWs thickness, at 80 K (circles) and 300 K (squares).

strain. Moreover, as expected, a redshift of the PL peak with the increase of the well thickness is clearly observed.
As discussed in the introduction of this work, the effect of quantum confinement is to blueshift the emission wavelength of Ge from the commercially important C-band (0.79-0.81 eV) to the E-band (at RT).

Finally, we conclude discussing PL data collected at different pump-power densities. In Fig. 5.13(a), we show PL spectra measured from the Ge sample at 80 K in the 5.6×10^4 and 5.6×10^5 W·cm^{-2} range. Note that the peak position is not redshifted at high-power density, pointing to the absence of significative pump-induced lattice heating. The LH-HH splitting is clearly observed in each curve and, increasing the pump power density, the relative intensity of the Γ_c-HH recombination increases with respect to the Γ_c-LH one, due to the larger density of hole states.

PL spectra, as a function of the laser pump power density, measured on sample S25-5, with t_w = 25.9 nm, are reported in Fig. 5.13(b). Again, increasing the power density, the energies of the Γ_c-HH and Γ_c-LH recombinations in the Ge layer are not affected, while the peak related to the Γ_0-HH_0 transition slightly

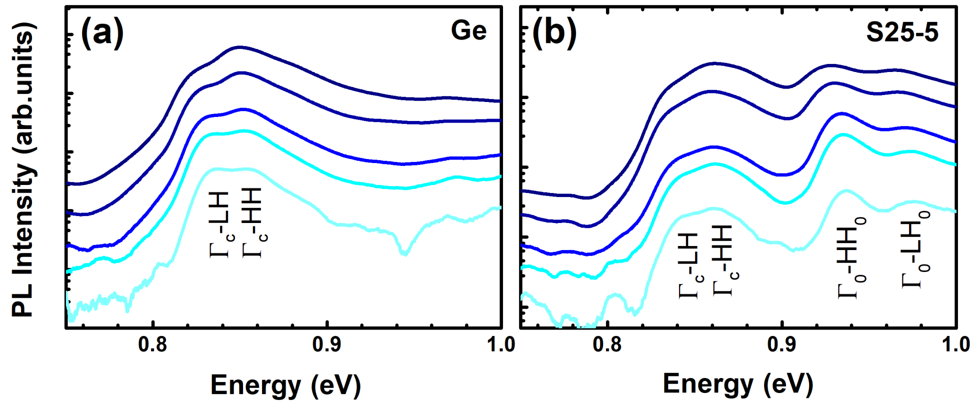

Figure 5.13 – PL spectra measured from the Ge (a) and S25-5 (b) sample at 80 K with different pump power density, ranging in the 5.6×10^4-5.6×10^5 W·cm^{-2} interval.

redshifts at excitation densities > 1.9 $\times 10^5$ W·cm^{-2}.

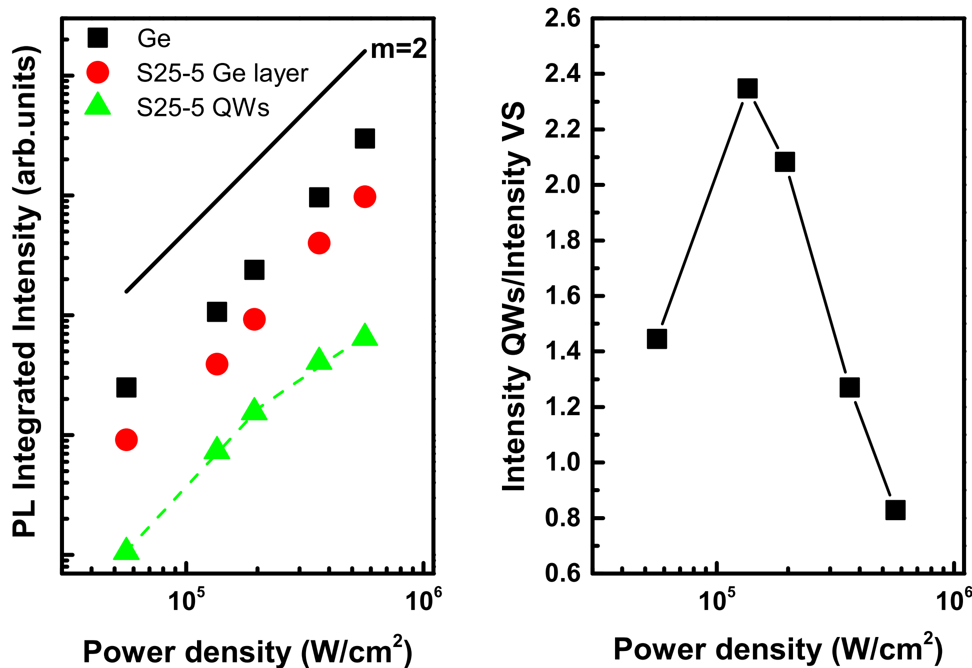

Figure 5.14 – *Left*: Integrated PL intensity for the Ge sample (square), and for the Ge (circle) and QW (triangle) features of the S25-5 sample, as a function of the pump power density. *Right*: Ratio of the integrated PL intensity of the QWs signal to the VS signal of sample S25-5, as a function of the pump power density.

Figure 5.14(a) shows the integrated PL intensity at 80 K as a function of the excitation power density. As a matter of fact, in section 2.4.4 we introduced how we can evaluate which is the dominant non-radiative term studying

the scaling of the photoluminescence intensity as a function of the excitation power density. Data of the Ge sample and the component related to the Ge layer in S25-5 follow a power-law dependence $I \propto W^m$. The fit-power exponents m found are close to the theoretical value of m= 2 (black line), expected when the dominant non-radiative mechanism is related to SRH recombination [139]. On the other hand, the integrated intensity of the QWs feature shows a scaling exponent m= 2 for excitation densities up to 1.9 $\times 10^5$ W$\cdot$cm^{-2} but, increasing further the excitation, the intensity tends to level off to a value of $m \simeq 1.3$ indicating the contribution of Auger recombination mechanism. To underline the quenching of the QW feature increasing the pump power density, we report in Fig. 5.14(b) the ratio of the integrated intensity of the QW signal of sample S25-5 to that related to the VS.

5.2 STRAINED QUANTUM WELLS

In section 5.1.2 we demonstrated that the energy of the $\Gamma_0 - HH_0$ transition at RT is in the 0.86-0.92 eV range for QWs thickness between 10 and 26 nm. It follows that depositing QWs with a specific thickness we obtain light emission between ~ 1350 and ~ 1445 nm. Therefore there is a significant demand to shift the emission wavelength into the C-band (1530-1565 nm) for potential application. As we discussed in 1.2.3, this can be achieved by means of tensile strain.

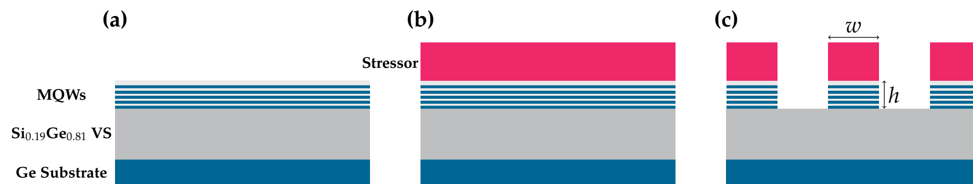

Figure 5.15 – (a) Unstressed QWs. (b) Deposition of the external stressor. (c) Geometry description of the microstructures under investigation for clear definition of height (h) and width (w).

Tensile strain has been induced in the Ge quantum wells by means of an external stressor made of a CMOS compatible insulating layer. Several advantages led to the choice of using silicon nitride, among which, ease of fabrication, surface optical access, and its compatibility with a CMOS processing environment. In addition, the nitride layer can act as a passivation layer and reduce surface recombination. The realization of tensile strained Ge quantum wells can be divided in three steps (sketched in Fig. 5.15):

(a) Growth of unstressed Ge quantum wells.

(b) Deposition of compressively strained SiN via PE-CVD.

(c) Definition of the microstructures by means of electron-beam lithography.

The compressive stress accumulated in the stressor layer during its deposition is relaxed through the fabrication of the structures by means of electron-beam lithography. The micro-fabrication process allows for a lateral expansion of the stressor that, as in a loaded spring, releases its strain energy and induces a tensile strain field in the underlying Ge quantum wells (see Fig. 5.16) [52]. Clearly, the geometrical parameters of the microstructures will determine how the elastic energy, and hence the strain, will be redistributed in the stacks.

Two types of microstructures have been investigated featuring strain relaxation into one or two dimensions. As a matter of fact, as can be observed in Fig. 5.16, the stress originating from the SiN layer is released at free surfaces along the edges of the structures. It follows that in the *microstripes* (see Fig. 5.2.1) tensile strain can be relaxed only along the strip width direction x, and the strain field in not purely biaxial. In the *pillars*, instead, x and y directions are equivalent and then the strain field is purely biaxial since the Ge layers are free to expand in two dimensions.

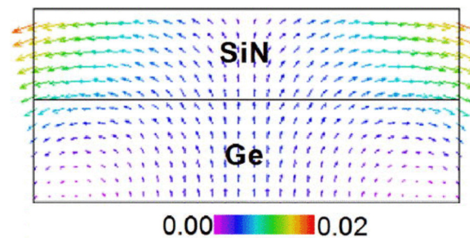

Figure 5.16 – Displacement field of a micro-stripe. Taken from Ref. [52].

5.2.1 *Strain Analysis of Strained QWs*

The facilities of Scuola Superiore Sant'Anna were able to investigate and define a SiH_4-NH_3-N_2 mixture for the deposition of a SiN stressor on top of Ge microstructures using plasma enhanced chemical vapor deposition (PECVD), obtaining a compressive stress of $\sigma_{in} = -1.8$ GPa. This value has represented the starting point for the geometry optimization of the microstructures under investigation. The SiN stressor was deposited with

PECVD technique exploring the parameters space of Si_3N_4 and NH_3 mixture in combination with proper evaluation of CVD pressure and deposition time. One of the main issues of the strain optimization of SiN on silicon, germanium and SiGe is represented by the adherence of the stressor. The innovative approach has been given by the deposition of a thin layer of SiO_2 (10-20 nm) before the CVD deposition. This method is not only able to guarantee a higher quality of the stressor layer and to reduce the presence of surface defects, but is also not influencing the SiN_3 refractive index and, as a consequence, its response to light radiation, as we will see in the following. The micropillars and microstripes were fabricated with standard UV-lithographic tecniques applying a duty cycle of the same size of the structure width. A following etching process in SiN layer and underlying Ge has been developed to reach the simulation optimization of 350 nm thick Ge substrate.

FEM SIMULATIONS The strain relaxation of the microstructures was modeled using COMSOL Multiphysics, a 3D finite element tool. The SiN layer, defined as elastically isotropic, at the initial pressure of $\sigma_{in} = -1.8$ GPa has been considered as initial condition. Germanium microstripes and micropillars were fixed and their boundaries allowing the rest of the structures to deform freely, in combination with an orthotropic model defined by means of elastic stiffness of Ge (values reported in Table 1.4) and considering the presence of thermal strain of $\varepsilon_{therm} = 2.5 \cdot 10^{-3}$ as initial conditions. The first investigation of the strain-optimized microstructures reached two relevant conclusions in terms of the the design of the Ge microstructures. First of all, the thickness of the SiN stressor needs to be higher than 200 nm in order to allow the presence of a strain field distribution along the entire microstructure, as shown in Fig. 5.17, where the maps of the biaxial strain in Ge micropillars of the same geometry and different SiN thickness are reported.

However, the technological constraints for CVD depositions limited the stressor thickness to a maximum height of 400 nm that was selected as design parameter for mechanical simulations and further fabrication of the device. Secondly, the compressive regions existing at the lateral edges of the microstructures [153], originated by the outward bending of the stripe sidewalls, are the reason why biaxial strain in pillars and uniaxial strain in microstripes are not a monotonic function of the microstructure width but present a

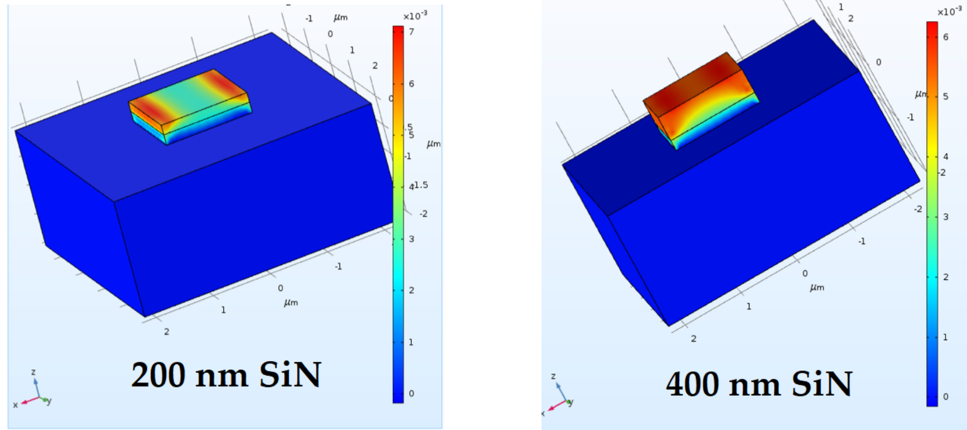

Figure 5.17 – Map of the biaxial strain in Ge micropillar of the same geometry with a SiN 200 nm thick and 400 nm thick. The thickness of the SiN stressor needs to be higher than 200 nm in order to allow a distribution of the strain fields along the entire structure.

maximum than can vary with the structure height, as shown in Figure 5.18.

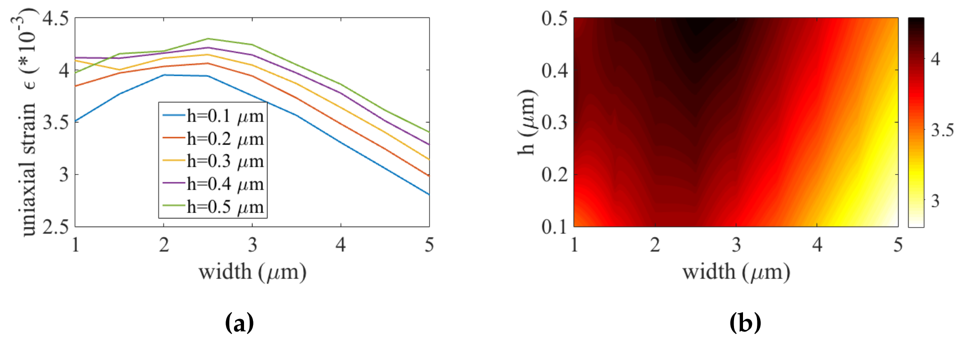

Figure 5.18 – (a) Behavior of the uniaxial strain as a function of the structure width. (b) Contour-plot of the biaxial strain as a function of the geometric parameters.

Knowing these features of the mechanical deformations, the height of the Ge microstructures has been set to 350 nm and the width of the microstripes and micropillars to 1.5 μm, 3 μm, 5 μm. The relative cross sections are shown in Fig 5.19.

Following the geometry optimization, the microstructures have been fabricated on sample S10-5. We have chosen to investigate this sample since its well width is thin enough to do not observe the $\Gamma_0 - LH_0$ recombination within the spectral range measurable with our experimental set-up. Therefore, we do not expect to observe any PL feature related to direct $\Gamma_0 - LH_0$ recombination.

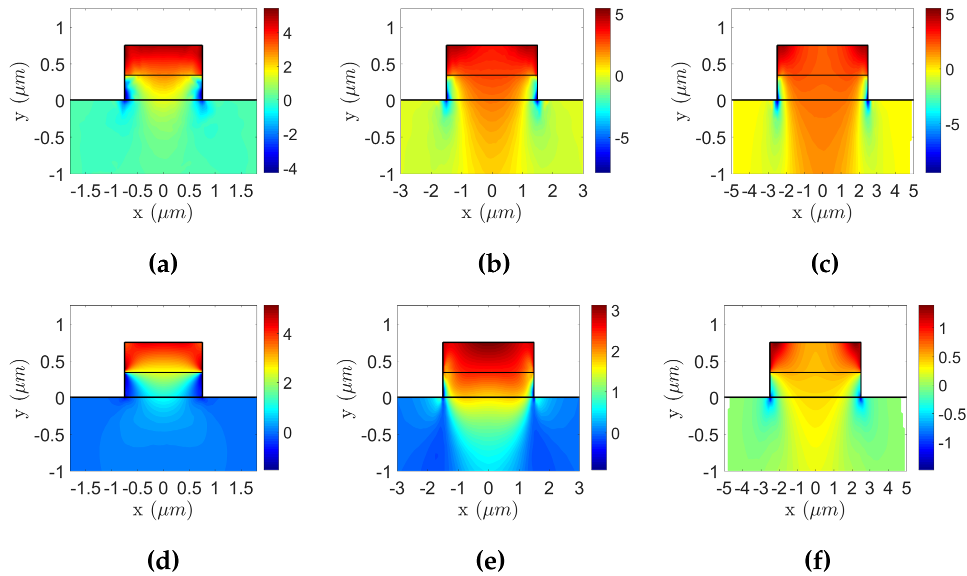

Figure 5.19 – Equivalent strain profile for microstripes of cross section 1.5 μm, 3 μm, 5 μm, respectively (a), (b) and (c) and for pillars with cross section 1.5 μm, 3 μm, 5 μm (d), (e), (f).

In Figure 5.2.1 we present a Scanning Electron Microscopy (SEM) image of the wafer surface showing microstructures of the two types here investigated.

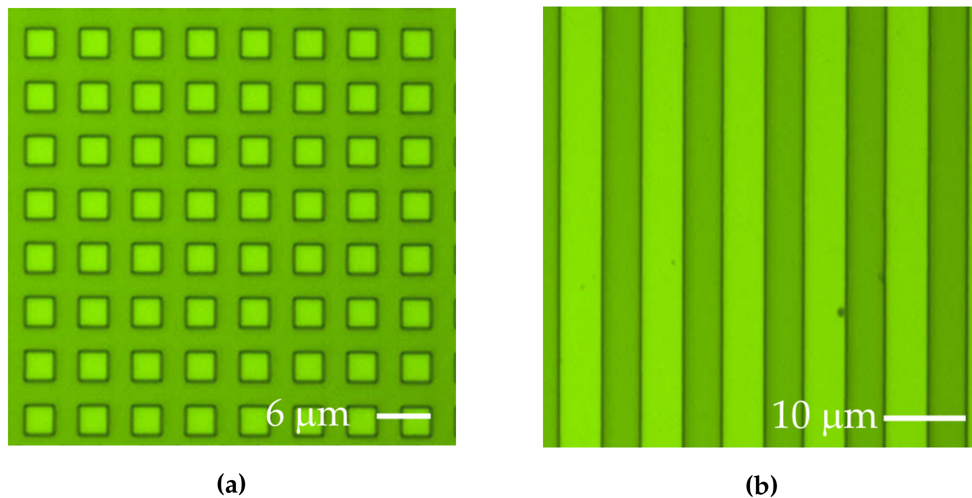

Figure 5.20 – SEM images of the fabricated microstructures; (a) 3 μm micropillars, (b) 5 μm microstripes.

COMPARISON BETWEEN RAMAN EXPERIMENTS AND FEM SIMULATIONS: AN EFFECTIVE TOOL The strain values of the microstructures have been investigated by means of Raman. Moreover, high-resolution Raman measurements allowed to validate the results obtained by FEM simulations. As a matter of fact, Raman maps can be reconstructed from the strain components obtained

by simulations if the p and q parameters introduced in section 3.2.4 are known.

The comparison between experimental and theoretical Raman is shown in Fig. 5.21. The accuracy in the determination of the Raman shift was between 0.2 and 0.4 cm^{-1}. Having selected an ω_0 frequency of 302 cm^{-1}, the values obtained for the fit parameters are $p = -1.78\omega_0^2$, $q = -2.82\omega_0^2$, in good agreement with Ref. [154].

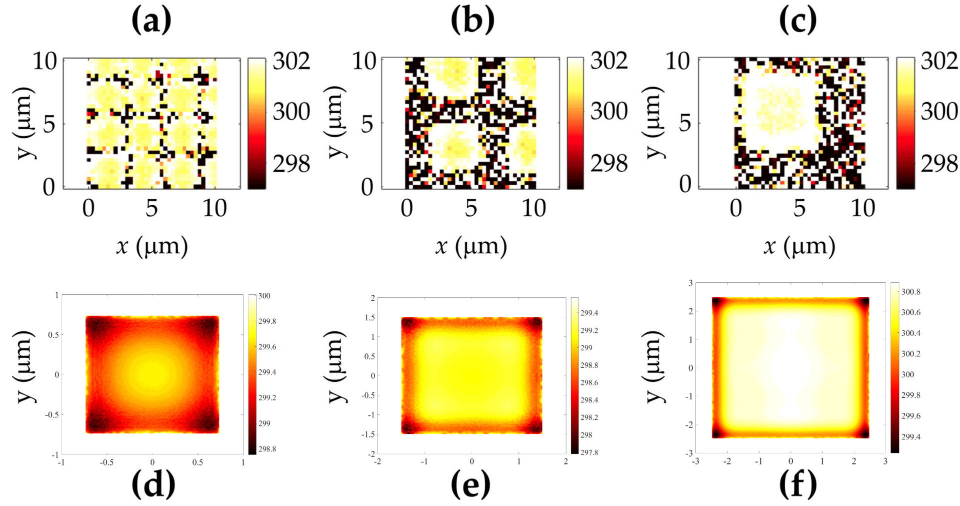

Figure 5.21 – Comparison between experimental Raman map for pillar of side 1.5 μm, 3 μm, 5 μm, respectively (a), (b) and (c) and reconstruction of Raman map starting from FEM simulations for the same structure of the pillar [1.5 μm, 3 μm, 5 μm, respectively (d), (e), (f)].

The parameters obtained from the micropillars gave also the possibility to compare the Raman strain map of a microstripe obtaining the perfect agreement shown in Figure 5.22.

Room temperature uniaxial and biaxial strain measured by Raman at the center of the different structures are reported in Fig. 5.23 together with the results of FEM simulations.

As in 5.1.1, the in-plane biaxial strain ε_b was calculated using the relationship

$$\frac{\omega^{Ge-Ge} - 300.3}{-450} = \varepsilon_b.$$

Strain values between $-0.4 \pm 0.1\%$ and $-0.2 \pm 0.1\%$ were obtained. Uniaxial strain ε_x instead was calculated using

$$\frac{\omega^{Ge-Ge} - 300.3}{-225} = \varepsilon_x.$$

The corresponding strain values are between $-1.0 \pm 0.2\%$ and $-0.8 \pm 0.2\%$.

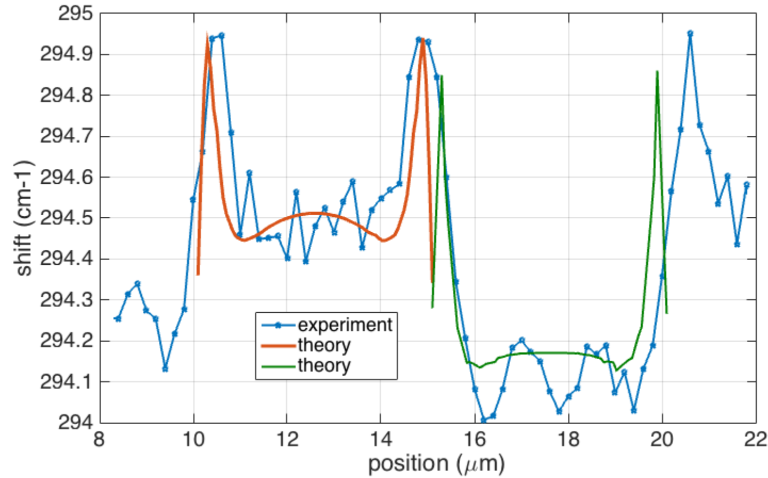

Figure 5.22 – Comparison between experimental Raman and theoretical Raman for a 5 μm width microstripe.

5.2.2 *Optical Properties of Strained QWs*

As discussed in section 5.1.2, PL spectra of Ge QWs are strongly quenched at increasing temperature, therefore we investigated the optical properties of the microstructures at 80 K. PL spectra acquired on the different structures are reported in Fig. 5.24 together with that of an unpatterned region. The intensity of the VS direct recombination has been normalized to unity in all the spectra. Firstly, we observe that in the case of 1.5 μm-wide structures the signal related to transitions in the QWs consists in one intense peak that we attribute to the direct $\Gamma_0 - HH_0$ recombination. The peaks are slightly shifted to lower energy with respect to the transition energy in the unpatterned region (vertical dashed line in Fig. 5.24) due to the effect of the tensile strain induced by the stressor. Increasing the width of the structures the QWs peak is divided in two features; one at higher energy than the unstressed QWs and one at lower energy. We remind that the feature at higher energy can not be related to the $\Gamma_0 - LH_0$ transition since its energy is not in the spectral range measurable with our experimental set-up. We attribute this feature to the direct recombination in the 95% step of the VS. As a matter of fact, our model predicts a direct gap of 1.01 eV at 80 K. To realize the microstructures, the region in between two adjacent stripes/pillars has been etched for 350 nm (see Fig. 5.15), removing the QWs region. It follows that the light emitted in the radiative $\Gamma_c - \Gamma_v$ recombination in the VS is much less absorbed in the top region of the sample since the volume of the absorbing material (the QWs) is reduced with respect to the unstressed QWs. This explains why after the

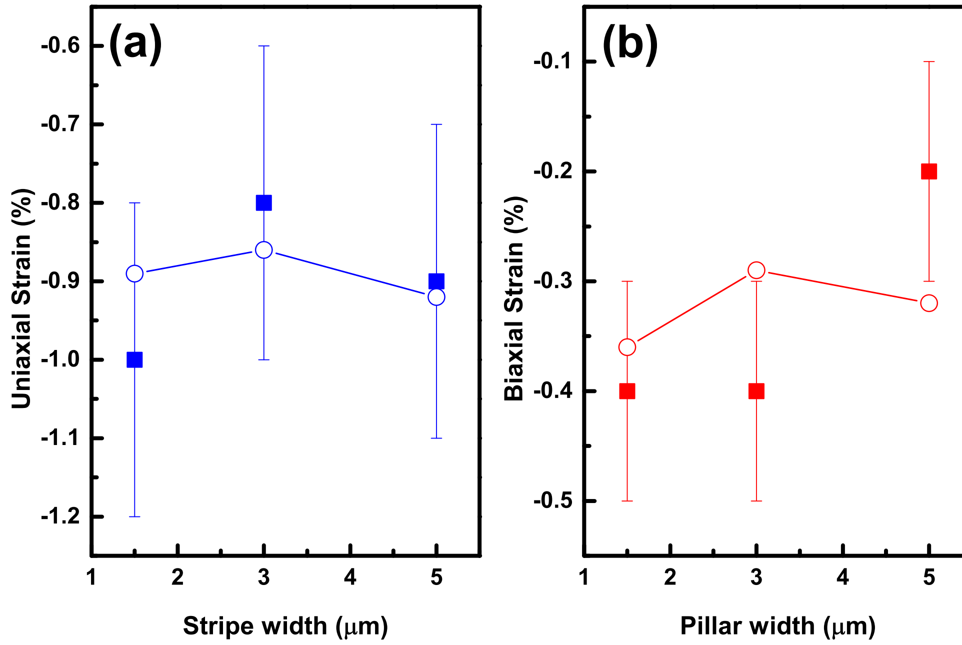

Figure 5.23 – (a) Uniaxial and (b) biaxial strain as a function of the width of the structures measured by Raman at 300 K on stripes and pillars, respectively. Empty circles are the results of FEM simulations.

definition of the microstructure the spectral feature of the VS can be observed even at low temperature.

To confirm that the doublet at high energy was not related to inhomogeneous vertical strain distributions, we calculated the three strain components ε_{xx}, ε_{yy}, and ε_{zz} at 80 K as a function of the depth inside the sample ($d = 0$ is the interface between the SiN stressor and the SiGe cap layer) for all the structures. The results of FEM simulations for the 1.5 μm structures are reported in Fig. 5.25. We observe that in the case of pillars, where strain is biaxial, the in-plane strain components ε_{xx} and ε_{yy} are equal, while in the case of stripes, where strain is uniaxial, the strain component perpendicular to the length of the stripe, ε_{xx}, is higher than the longitudinal one, ε_{yy}. The effect of strain is to reduce the compressive strain of the Ge lattice, due to the sum of thermal (tensile) and epitaxial (compressive) strains.

From Fig. 5.25 it is evident that for the application of external stressors to MQWs systems the thickness of the active region should be limited to a few hundreds of nm. As a matter of fact, in Fig. 5.25 we note that the induction of uniaxial and biaxial tensile strain is maximum close to the interface between the stressor and the QWs and decreases going down in the sample. It follows

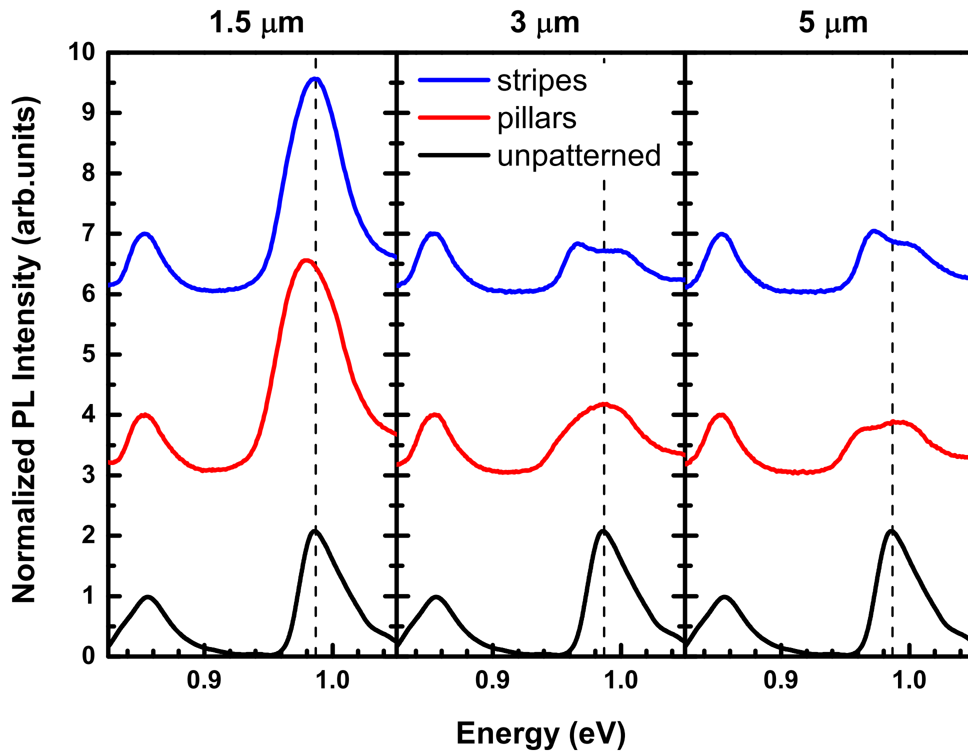

Figure 5.24 – PL spectra at 80 K acquired on the unpatterned region, pillars, and stripes of width (from left to right) 1.5 μm, 3 μm, and 5 μm.

that the strain values of the five QWs are different and, therefore, the energy of the emitted radiation is different. The modification of the $\Gamma_0 - HH_0$ transition can be extimated with the help of Eq. 1.30 using the hydrostatic deformation potentials, obtaining $\Delta E \sim 2$ meV for each couple of adjacent QWs. Thus, the energy difference between the first (closest to the surface) and the last QW is ~ 10 meV, less than the energy separation between the two components of the doublet observed in 3 and 5 μm-wide structures.

For similar structures, Virgilio *et al.* [150] observed that PL spectra were modulated by intensity oscillations attributed to Fabry-Perot (FP) fringes related to the lateral modes of the microstrip cavities (i.e. the ones along the strip width direction x). T-dependent PL spectra of the microstructures investigated in Ref. [150] are reported in Fig. 5.26. A quantitative analysis of their wavelength periodicity and the absence of fringes in the low-energy side of the peaks reported in Fig. 5.24, allowed us to exclude that the observed doublet were related to Fabry-Perot fringes.

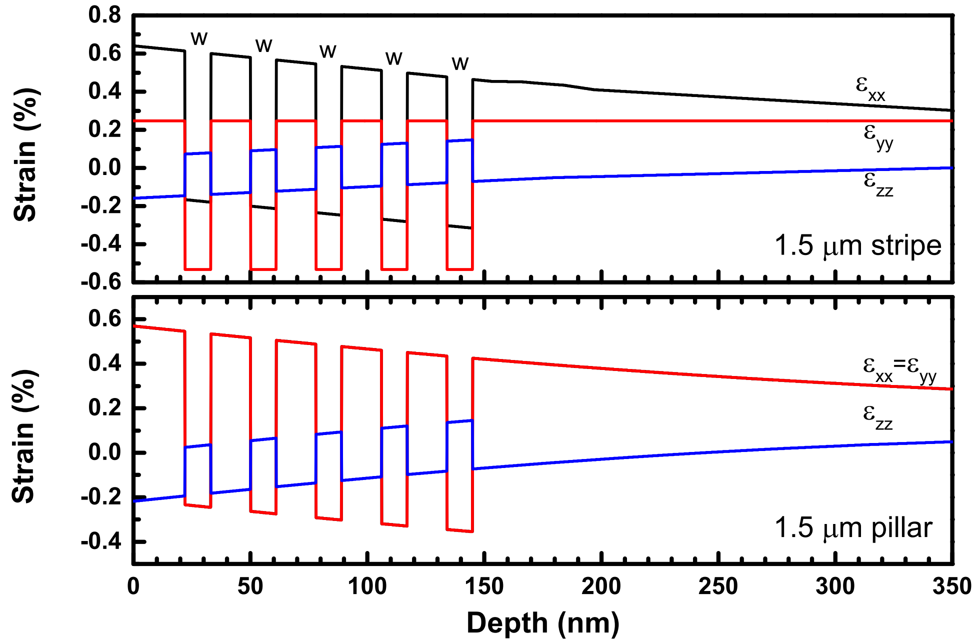

Figure 5.25 – FEM strain components ε_{xx}, ε_{yy}, and ε_{zz} as a function of the depth inside the sample for 1.5 μm stripe and pillar. w denotes QW regions.

The considerations discussed above suggests that the high-energy shoulder is actually related to radiative recombinations across the direct gap of the 95% step of the RG-VS.

Once that the origin of the spectral features has been clarified, we investigate the effect of strain on the energy of the $\Gamma_0 - HH_0$ transition. We report in Fig. 5.27 the redshift of the transition-energy as a function of the width of the structures. In the case of stripes [Fig. 5.27(a)], the redshift follows the trend of measured and theoretical uniaxial strain, i.e., increasing the applied strain the energy of the $\Gamma_0 - HH_0$ transition shifts to lower energy, as expected. In the case of pillars [Fig. 5.27(b)], instead, the redshift follows the trend of theoretical biaxial strain but not the measured one. In both the cases the maximum redshift is reached for 3 μm-wide structures confirming that in this kind of systems strain is not a monotonic function of the width.
The maximum shift of the $\Gamma_0 - HH_0$ recombination is obtained for pillars of width 3 μm and corresponds to $\sim$ 33 meV. It follows that, fabricating the same structure on a sample featuring thicker QWs, such as S25-5, may result in a RT emission wavelength in the S-band.

The definition of the microstructures may also affect the non-radiative dynamics. As a matter of fact, the fabrication of pillars and stripes results in

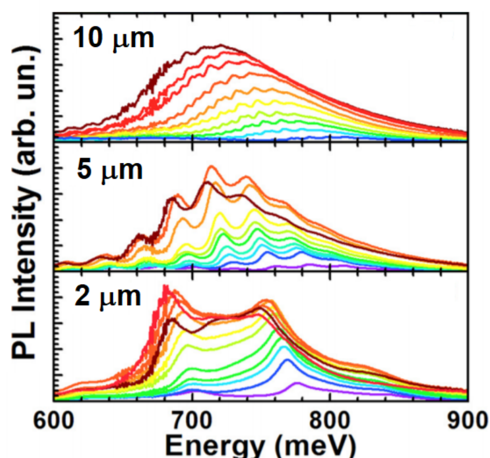

Figure 5.26 – PL spectra acquired from Ge microstrip samples featuring different sizes, as indicated in the left top corner of each panel. Lattice temperatures range from 100 K (violet curves) to 430 K (dark red) in 30 K-steps [150].

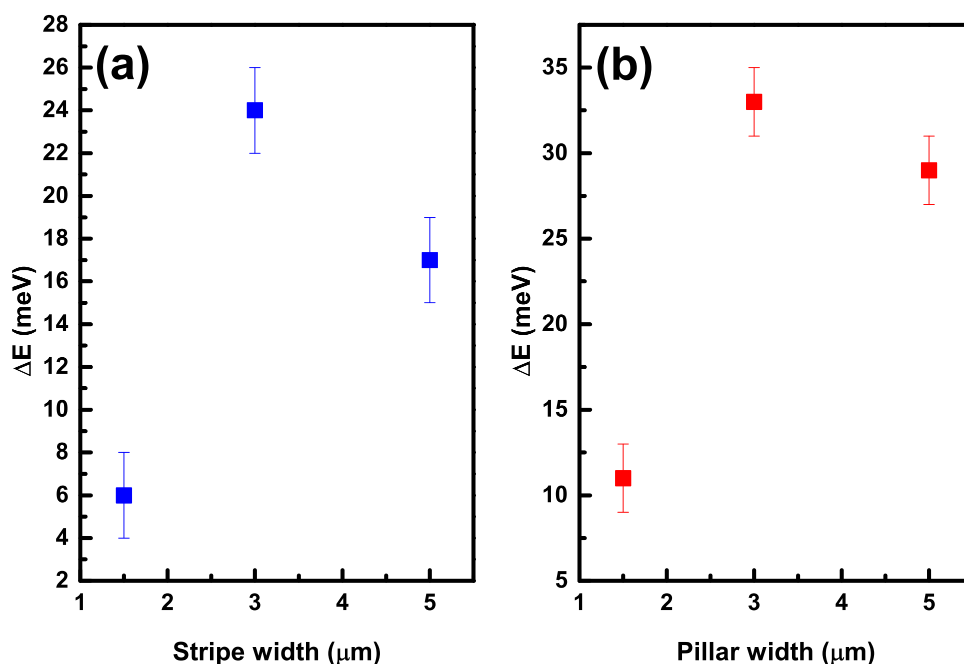

Figure 5.27 – Redshift of the $\Gamma_0 - HH_0$ recombination as a function of the width of the structures measured by PL at 80 K on stripes and pillars, respectively.

the introduction of the lateral surfaces of the structures. Therefore defects are introduced and SRH non-radiative recombinations may increase. On the other hand, the deposition of the SiN layer results in the increase of the absorptance of the system, as can be see in Fig. 5.28. It follows that the power density absorbed by the sample is enhanced together with the excess carrier density Δn. Since the rate of Auger recombinations goes as

Δn^3, the non-radiative dynamics may be dominated by Auger recombinations.

To evaluate which is the dominant non-radiative term we now discuss the scaling of the photoluminescence intensity as a function of the excitation power density.

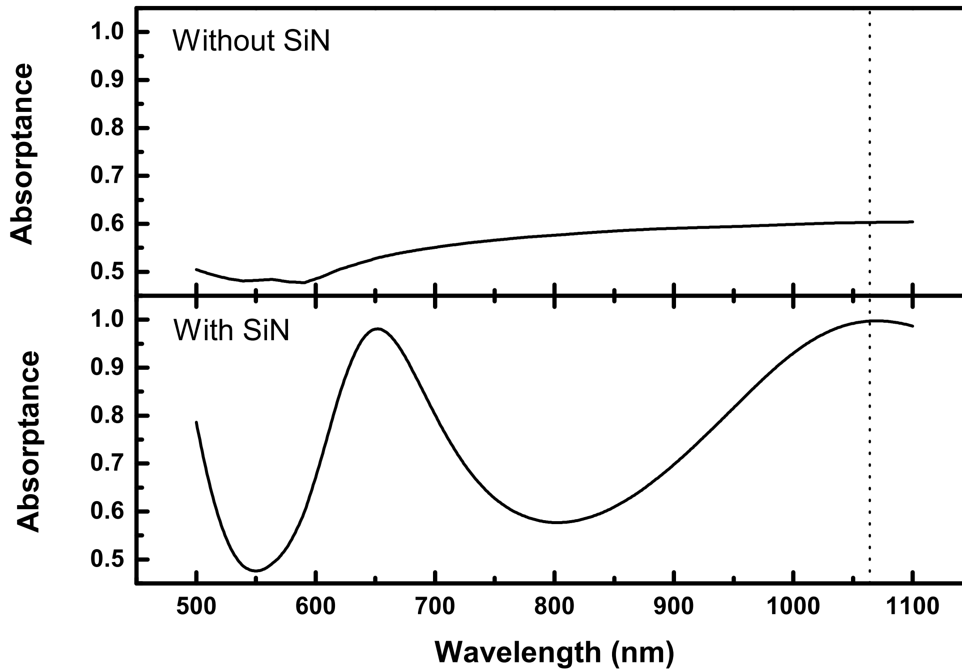

Figure 5.28 – Absorptance as a function of the wavelength without (top) and with (bottom) the SiN stressor[155].

Figure 5.29 shows the integrated PL intensity at 80 K as a function of the excitation power density. Data of the VS feature of the unpatterned region, 1.5 μm pillars and 1.5 μm stripes are reported in Fig. 5.29(a) as black, red, and blue squares, respectively. The integrated PL intensity of all the investigated regions follows a power-law dependence $I \propto W^m$ with $m \simeq 2$. It follows that the dominant non-radiative mechanism is related to SRH recombination. We recall that, before the deposition of the external stressor, we observed that the integrated intensity of the QWs feature shows a scaling exponent m= 2 for excitation densities up to 1.9 $\times 10^5$ W$\cdot$cm^{-2} but, increasing further the excitation, the intensity tends to level off to a value of $m \simeq 1.3$ indicating the contribution of Auger recombination mechanism. This can be also observed after the deposition of the SiN stressor in the unpatterned regions [see Fig. 5.29(b)]. On the other hand, the integrated PL intensity of the microstructures follows a power-law dependence with $m \simeq 0.7$ constant in all the power

range investigated, indicating that Auger recombination is the dominant non-radiative mechanism even at low excitation densities.

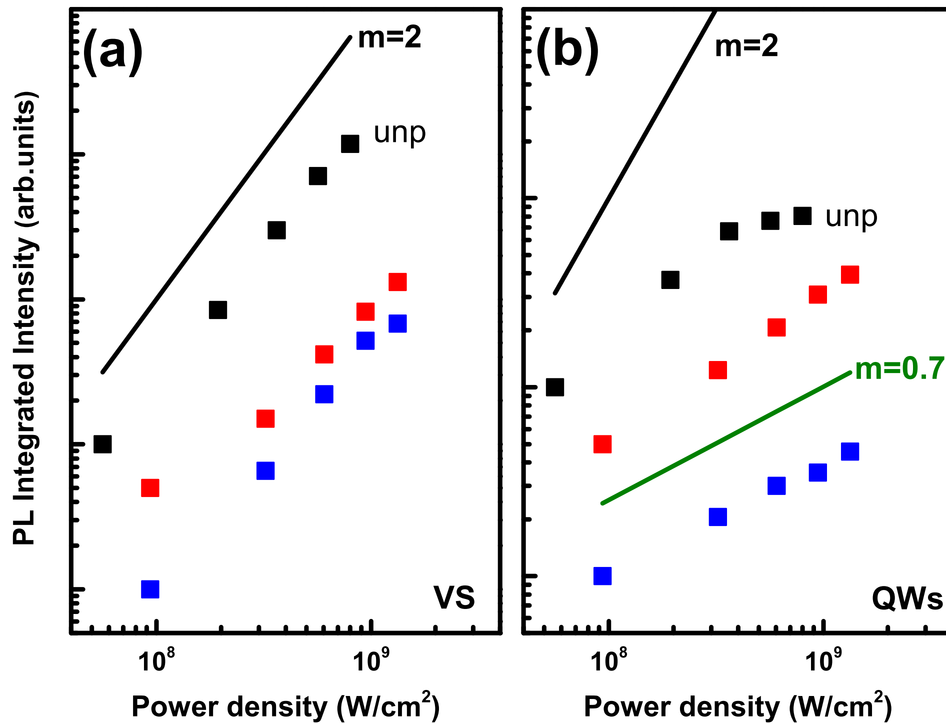

Figure 5.29 – Integrated PL intensity for (a) the VS and (b) QW features as a function of the pump power density. Data related to the unpatterned region, 1.5 μm pillars and 1.5 μm stripes are reported as black, red, and blue squares, respectively.

In summary, we have demonstrated a CMOS-compatible approach to tune the emission wavelength of Ge MQWs. Unfortunately, while in 1.5 μm structures the ratio of the QWs feature to the VS peak is $\sim 6-7$, in wider pillars and stripes the integrated intensity of the two features is comparable. Therefore, it highly desirable to boost the intensity of the $\Gamma_0 - HH_0$ transition.

5.3 DOPING

It is well known that the electrical and optical properties of pure semiconductors can be substantially altered by adding a small controlled amounts of specially chosen impurities, or dopants. The effect of n-type doping is to introduce energy levels close to the conduction band edge. In the case of high dopant concentrations, the energy levels are not discrete but form a continuous band merged with the conduction band. In this case the semicon-

ductor is said to be degenerate. In degenerate Ge, the Fermi level is shifted toward higher energies, thus reducing the Γ-L energy barrier and enhancing the Γ_c carrier density with a consequent increase in the photon emission rate. On the other hand, a high density of donors can lead to a quenching of the radiative emission, due to the concomitant effect of a reduced quality of the material, induced by the increased density of point defects, and the enhancement of the non-radiative recombination rate through the Auger mechanism. Recently, Barget *et al.*[82], investigating the influence of donors on the light emission efficiency of heavily doped Ge/Si layers, found that, owing to the competitive mechanism discussed above, the PL signal is not a monotonically increasing function of the donor concentration, but shows a maximum at a doping concentration of $\sim 3 \times 10^{19}$ cm^{-3}. The integrated PL intensity at room temperature, for their optimal doping concentration, was enhanced by a factor 7 with respect to the undoped sample. Following their results, we decided to investigate the optical properties of heavily doped Ge QWs.

n-type doping of the structures has been performed via phosphine (PH_3) co-deposition in the quantum well region. To calibrate the concentration of dopants, we deposited a calibration sample featuring several n-doped Ge layers, increasing at each step the amount of phospine introduced in the CVD-chamber. The phosphorus concentration-profile, as measured by SIMS, is reported in Fig. 5.30. The desired dopant concentration has been interpolated from data reported in the bottom panel of Fig. 5.30, where the P-concentration measured by SIMS is reported as a function of the partial pressure of phosphine.

Following the results of Barget *et al.*, we firstly deposited two samples replica of S10-10 (10 periods of 10 nm-wide Ge wells embedded between 17 nm-thick $Si_{0.15}Ge_{0.85}$ barriers) where the quantum well region was co-doped by phosphine resulting in a phosphorous concentration $\sim 3 \times 10^{19}$ cm^{-3} as measured by SIMS. While in sample S10-10-D1 the whole 10 nm of the quantum wells were doped, in sample S10-10-D2 a different approach has been employed, doping a 2 nm-wide region in the center of the QWs. On the contrary to what found in Ref. [82], the intensity of the PL signal related to the QWs was not boosted but completely quenched. To elucidate the origin of this detrimental behavior, we deposited three samples with different dopant

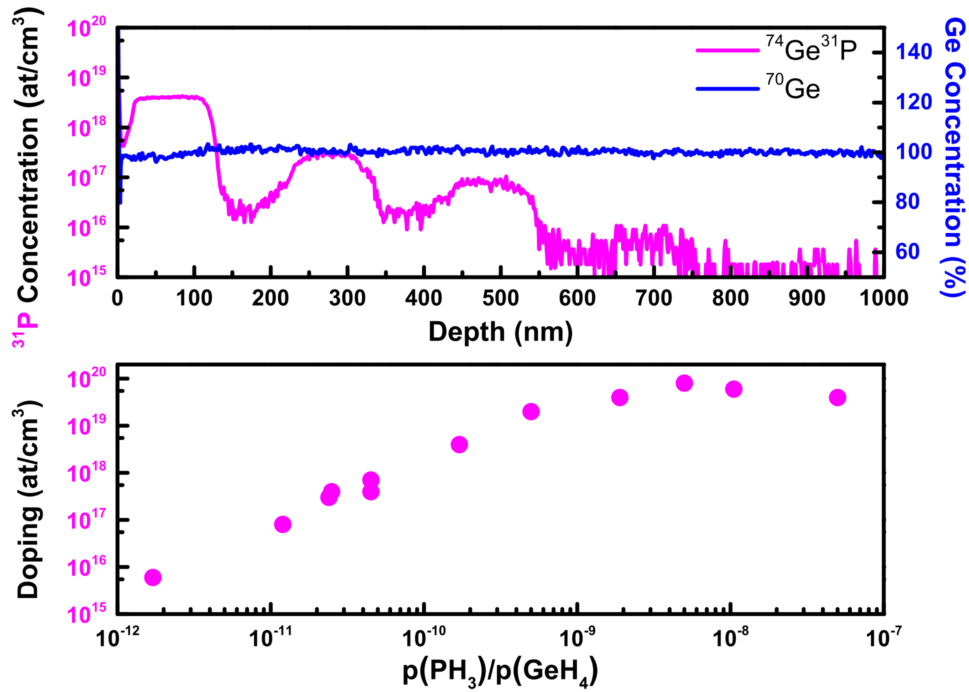

Figure 5.30 – *Top*: Phosphorus concentration-profile, as measured by SIMS. *Bottom*: Dopant concentration as a function of the partial pressure of phosphine.

concentration, S23-D1, S23-D2, and S23-D3, and we investigated their optical properties by means of PL.

Sample	Periods	Doping [cm^{-3}]	d_w [nm]	d_b [nm]	$d_w + d_b$ nominal (XRD) [nm]
S25-5	5	0	26	15	41 (41.1)
S23-D1	10	$\sim 4 \times 10^{17}$	6+**10**+7	18	41 (44.2)
S23-D2	10	$\sim 3 \times 10^{18}$	6+**10**+7	18	41 (51.4)
S23-D3	10	$\sim 4 \times 10^{17}$	3+**5**+6+**5**+4	18	41 (43.2)
S10-10	10	0	10	17	27 (27.5)
S10-10-D1	10	$\sim 3 \times 10^{19}$	**10**	17	27 (37.4)
S10-10-D2	10	$\sim 3 \times 10^{19}$	4+**2**+4	17	27 (35.4)

Table 5.4 – Parameters of the doped samples here investigated. The thickness of the doped region is reported in bold.

5.3.1 *Structural Properties of Doped QWs*

We started the analysis of doped samples investigating their structural properties. We report in Figure 5.31 the rocking curve of samples S10-10, S10-10-D1 and S10-10-D2, featuring the same nominal thickness of the QWs but different dopant concentration. While the position of the peaks related to the Ge, and

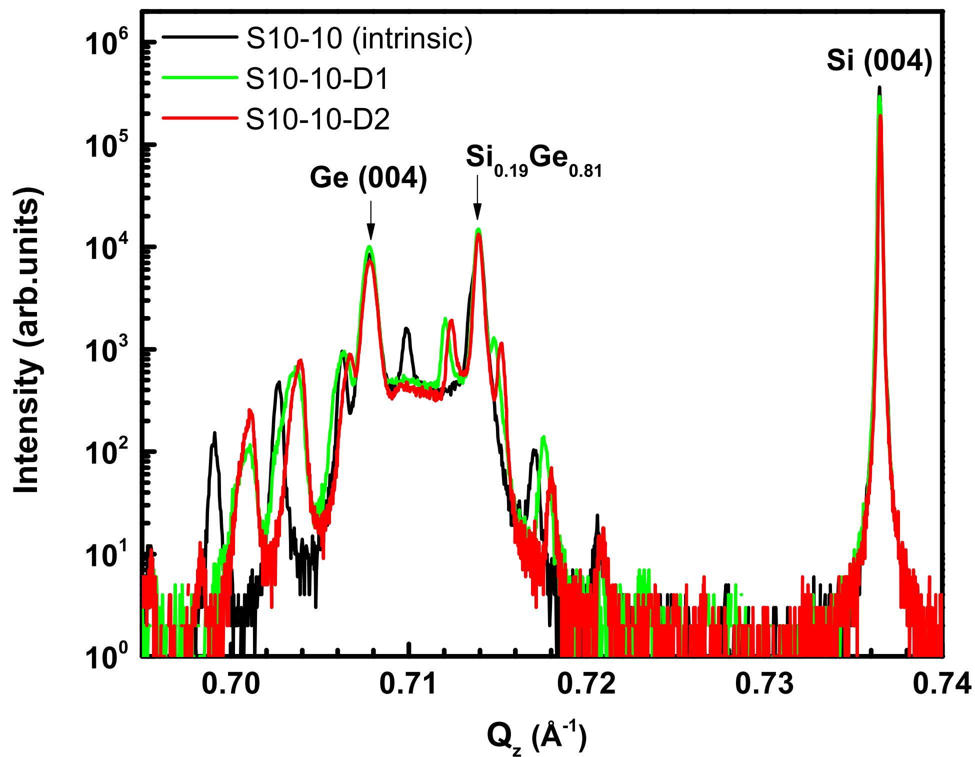

Figure 5.31 – XRD rocking curve of samples S10-10, S10-10-D1 and S10-10-D2. The nominal thickness of the QWs is the same.

$Si_{0.19}Ge_{0.81}$ layers are not shifted, indicating once again the good reproducibility in the deposition process, the periodicity of the SL fringes is different. Since the spacing between the fringes is related to the period of the superlattice, we obtain that doping an intrinsic sample results in thicker QWs, e.g. co-doping the 10 nm of the QW of sample S10-10 with $\sim 3 \times 10^{19}$ cm^{-3} phosphorus atoms (S10-10-D1) results in a difference in the superlattice periodicity of $\sim$ 10 nm. This result is completely unexpected since phosphorous-doping is assumed to influence the growth rate of SiGe alloys but in the opposite direction. As a matter of fact, it is expected a reduction of the deposition rate due to surface adsorption of PH_3, which results in a lower density of free surface sites [156]. It is also assumed that both the SiH_4 and GeH_4 molecules can not react effectively on the P or PH_x adsorbed sites.

To further investigate this trend, we studied different samples with different dopant concentrations and a different VS. In Figure 5.32(a) the RSM of sample S23-D1 is shown, where a Ge concentration x = 0.83 and an in-plane strain $\varepsilon_{\|}$ = 0.19% were measured for the VS. Figure 5.32(b), instead, reports the rocking curve of sample S3-D1 and S23-D2, which features the same nominal

superlattice period of 41 nm. Again the position of the peaks related to the Ge and $Si_{0.17}Ge_{0.83}$ VS are not shifted, while the superlattice fringes display a different periodicity. We performed XRD rocking curves on all the samples and the measured periodicity of the SL is reported in Table 5.4. From the results we can see how the superlattice periodicity is affected by doping, i.e., doped samples are thicker than intrinsic one. Moreover, the difference between nominal and measured thickness increases with dopants concentrations.

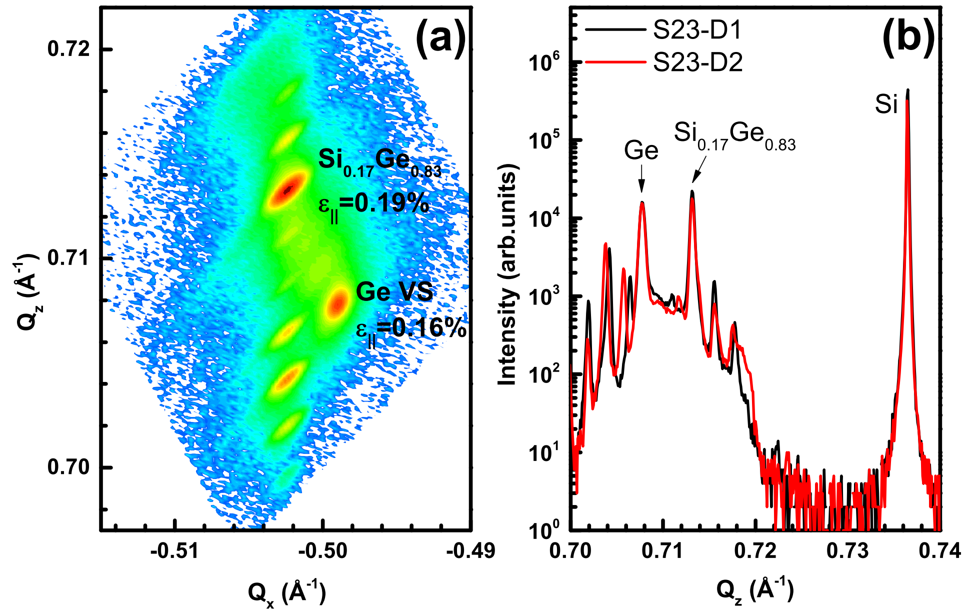

Figure 5.32 – (a): Reciprocal space maps of asymmetric ($4\bar{2}\bar{2}$) reflections of sample S23-D1. (b) XRD rocking curve of samples S3-D1 and S23-D2. The nominal thickness of the QWs is the same.

5.3.2 *Optical Properties of Doped QWs*

PL spectra acquired at 80 K on sample S10-10, S10-10-D1, and S10-10-D2, are reported in Fig. 5.33. Spectra are normalized so that the intensity of the $\Gamma_c - HH$ feature of the VS is equal to unity. The strong feature of the $\Gamma_0 - HH_0$ recombination in the intrinsic sample S10-10 is completely quenched in the other samples. Although the goal of doping was to enhance the electron population in Γ and, thus, to boost the intensity of the direct recombination, it results in the complete flattening of the QW signal and in the appearance of a feature at $\simeq 0.74$ eV. Supported by our numerical calculations, that predict an indirect $L_c - LH$ bandgap of 716 meV for 0.17% strained Ge films, we related

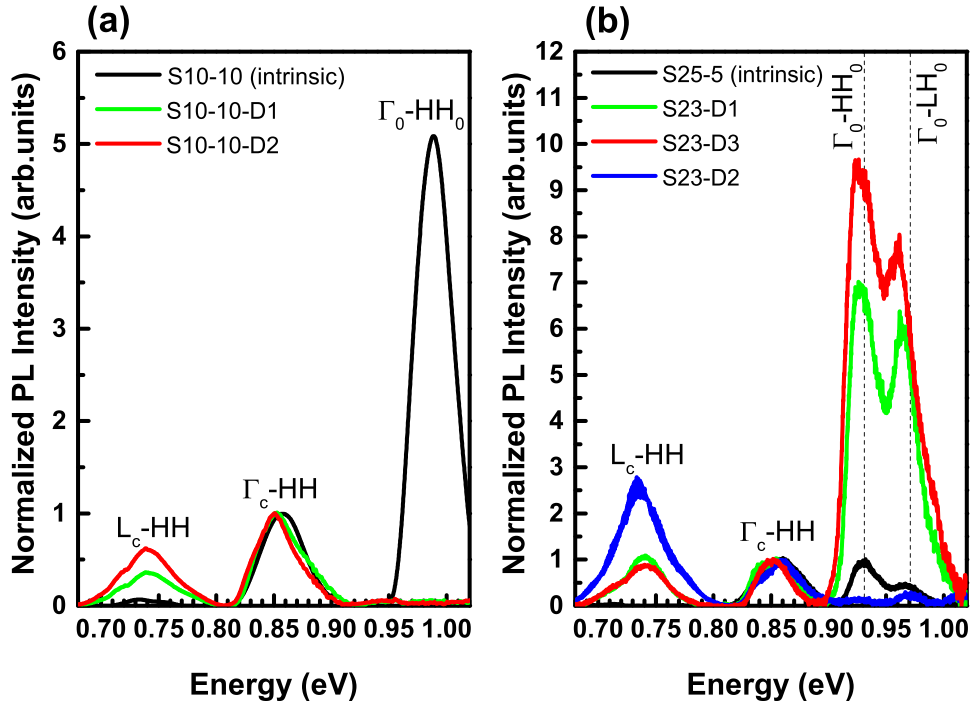

Figure 5.33 – PL spectra acquired at 80 on (a) thin and (b) thick doped Ge wells.

this feature to the indirect $L_c - HH$ recombination in the Ge VS. Moreover, on the low-energy side of the $L_c - HH$ signal, we can see a shoulder related to the $L_c - LH$ recombination at $\simeq 0.72$ eV, validating once again the proposed modelling.

The enhancement of the indirect band-to-band recombination in doped samples has been observed also in Refs. [82, 95] and it has been explained as follows; while in intrinsic Ge films the electron momentum required in an indirect recombination is provided only via electron-phonon interaction, in doped samples it can be also provided by means of Coulomb scattering with charged impurities or electron-electron scattering. Therefore, we conclude that the band at lower energy in the doped samples is related to second order $L_c - HH$ and $L_c - LH$ recombinations where the missing momentum is provided by $L_c - \Gamma_c$ Coulomb elastic scattering.

As already stated in Chapter 2, the Shockley-Read-Hall rate of recombination is proportional to the concentraction of donors n_{dop}, therefore reducing doping should results in longer τ_{SRH}. PL spectra, acquired at 80 K on 23 nm-thick QWs, are reported in Fig. 5.33(b). While the nominal thickness of wells and barriers is the same, doping is different. In the case of sample S23-D2, where

the dopants concentration is higher, we do not observe the direct $\Gamma_0 - HH_0$ recombination while the signal related to the indirect transition is intense. In samples S23-D1 and S23-D3, where doping is reduced to $\sim 4 \times 10^{17}$ cm^{-3}, the strong enhancement of the $\Gamma_0 - HH_0$ feature can be clearly observed. As a matter of fact, the intensity of the quantum well signal is enhanced by a factor ~ 10 with respect to the feature related to the direct recombination in the intrinsic sample S25-5 (although the intrinsic sample features 5 periods of QWs instead of 10). Moreover, we can observe the redshift of the $\Gamma_0 - HH_0$ and $\Gamma_0 - LH_0$ recombinations in doped samples respect to the intrinsic sample [dashed lines in Fig. 5.33(b)]. The shift of peak positions is related to the concomitant effect of strain, associated to the different concentration of the VS, and the increase in the QWs thickness discussed in the structural characterization.

In summary, we found that the PL intensity is not a monotonically increasing function of the donor density, in agreement with Ref. [82]. The maximum of the PL signal was found for a dopant concentration of $\sim 4 \times 10^{17}$ cm^{-3}, well below the $\sim 3 \times 10^{19}$ cm^{-3} found by Barget *et al.*

5.4 ASYMMETRIC QUANTUM WELLS

Four strain-compensated Ge/$Si_{0.2}Ge_{0.8}$ multi-asymmetric quantum wells samples consisting of a wide and a narrow Ge well separated by a tunneling barrier with thickness w_L, w_t, and b_t, respectively, were grown. This stack, embedded between thick $Si_{0.2}Ge_{0.8}$ barrier layers (b_L) which avoid coupling between the adjacent modules, has been periodically repeated 20 times. A 10 nm-wide region at the center of the wide well was co-doped by phosphine resulting in an active phosphorous donor density of $\sim 1 \times 10^{17}$ cm^{-3}.

Sample	b_L [nm]	w_L [nm]	b_t [nm]	w_t [nm]	dSL_{nom} [nm]	dSL_{XRD} [nm]	Doping [cm^{-3}]
S1	20	12	2.5	5	39.5	39.5	0
S2	20	0.6+**10**+1.4	2.5	5	39.5	41.6	$\sim 7 \times 10^{17}$
S3	20	2.5+**6**+3.5	2.5	5	39.5	40.6	$\sim 1 \times 10^{17}$
S4	20	1+**10**+1	3.5	5	40.5	43.0	$\sim 5 \times 10^{17}$

Table 5.5 – Parameters of the AQWs samples here investigated. The thickness of the doped region is reported in bold.

5.4.1 *Structural Properties of Asymmetric QWs*

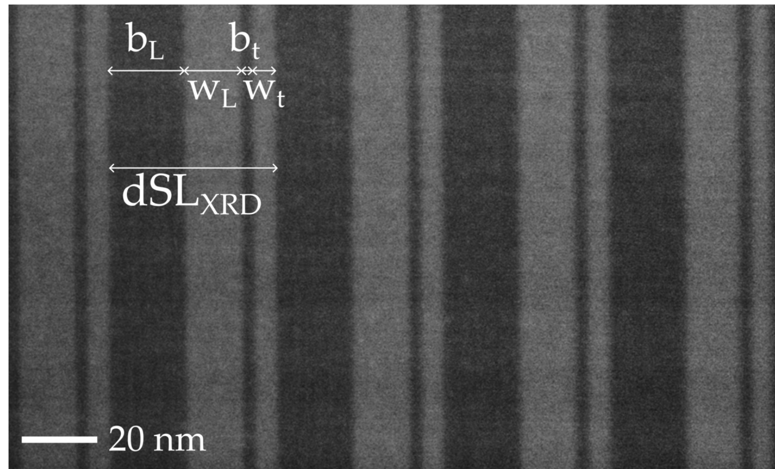

Figure 5.34 – STEM image of sample S3

In Figure 5.34, we report the STEM of one of the investigated samples, where we can observe abrupt interfaces and thickness reproducibility (within 2%) of the growth in each of the AQW modules. The quality of the heterostructures can be also appreciated in the RSM around the $(4\bar{2}\bar{2})$ reflections acquired on sample S1 [Fig. 5.35(a)]. From the RSM we observe that the entire structure is lattice-matched to the SiGe VS, which exhibits a Ge content x = 86% and a slightly residual strain of $\varepsilon_{\parallel}$ = 0.19%, that is related to the difference in the CTE between the Si substrate and the VS. The measured in-plane lattice parameter $a_{\parallel}$ = 5.6373 Åcorresponds to that of a cubic SiGe layer with an equivalent composition x_{eq} ∼ 0.92. The equivalent composition x_{eq} was targeted to fulfill the condition of strain-symmetrization, necessary to avoid the strain relaxation that may occur, since the repetition of QWs has been increased with respect to the cases discussed up to now. As in the case of symmetric doped QWs, doping results in a reduced SL periodicity, as can be observed in Fig. 5.35(b) where the XRD rocking curve of samples S1 and S2 are reported.

The interface roughness between the several layers of the heterostructures has been measured by Atom Probe Tomography (APT) at the Department of Engineering Physics, École Polytechnique de Montréal. APT is the only technique offering extensive capabilities for both 3D imaging and chemical composition measurements at the atomic scale (around 0.1 – 0.3 nm resolution in depth and 0.3 – 0.5 nm laterally). In this technique the sample is prepared in the form of a very sharp tip by means of a dual-channel FIB [Fig. 5.36(a)].

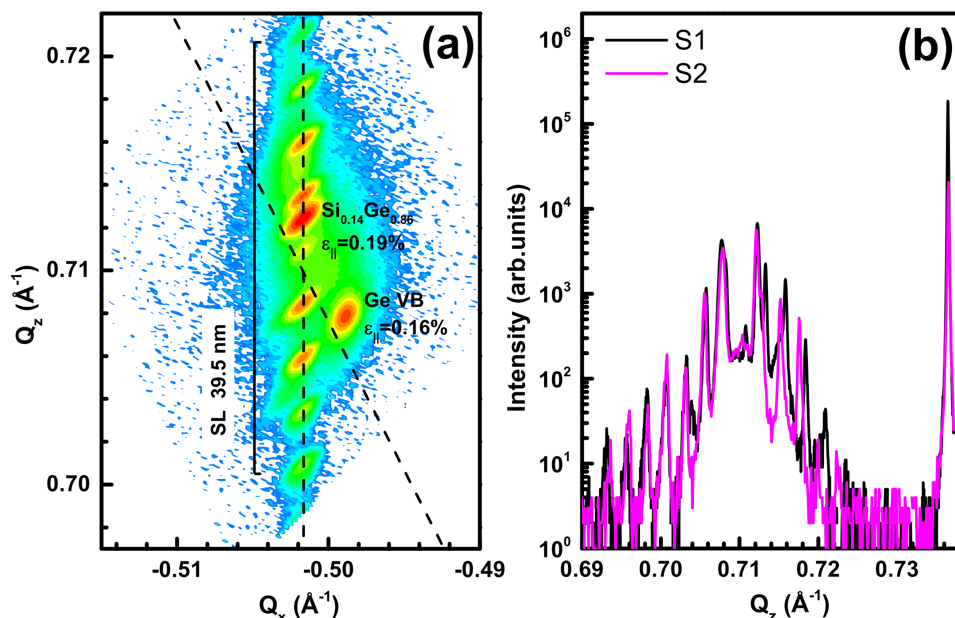

Figure 5.35 – (a): Reciprocal space maps of asymmetric ($4\bar{2}\bar{2}$) reflections of sample S1. (b) XRD rocking curve of samples S1 and S2. The nominal thickness of the QWs is the same.

With the help of high DC voltage and laser or HV pulsing, one or more atoms are evaporated from the surface and projected onto a position-sensitive detector. The detector allows to simultaneously measure the time of flight of the ions (so their mass over charge ratio) and the position of the ion impact on the detector (allowing to reconstruct the original position of the atoms on the tip). Combining the two informations and repeating the sequence, the atoms are progressively removed from the tip, and a 3D image of the material can be reconstructed at the atomic scale.

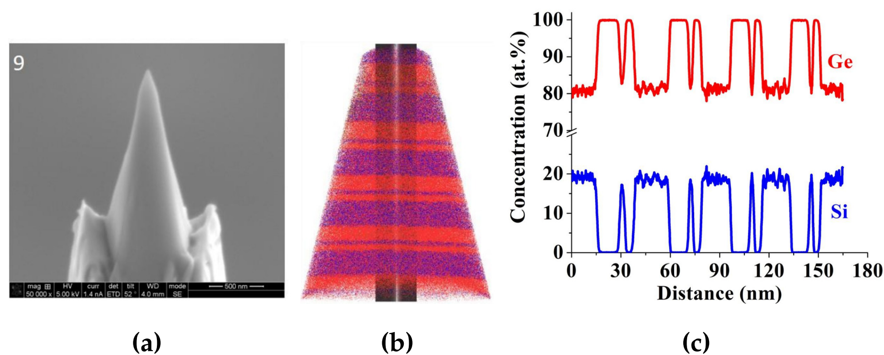

Figure 5.36 – (a) Electron micrograph of the APT tip. (b) 3D atom-by-atom reconstruction of the tip. (c) 1D concentration profile of Si and Ge along the long axis of the tip.

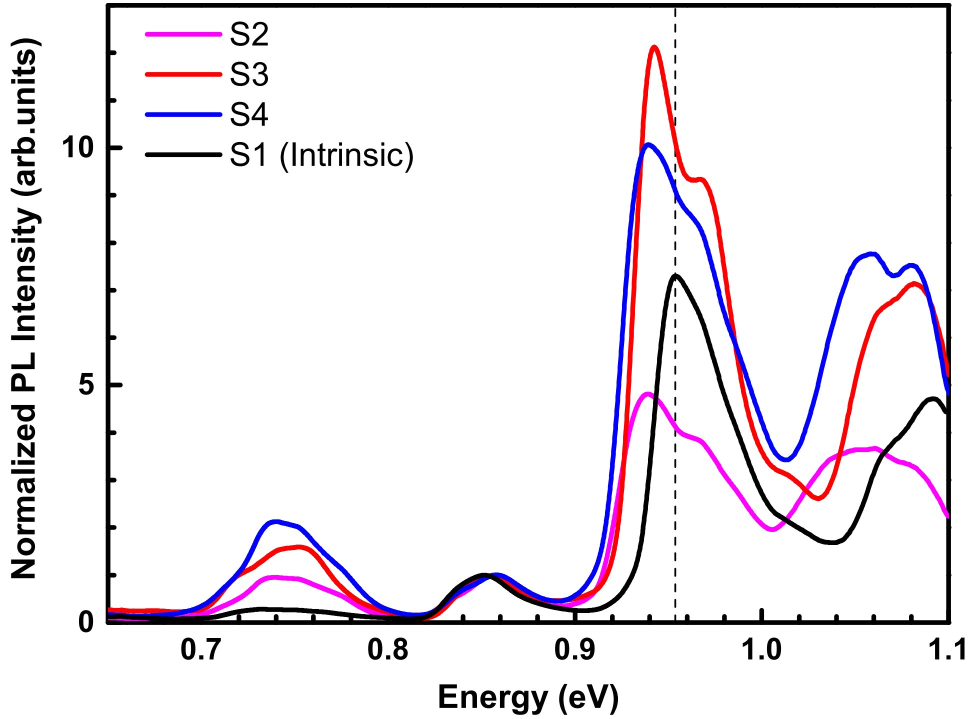

Figure 5.37 – PL spectra acquired at 80 K on the asymmetric QWs samples.

The interface RMS roughness has been measured at the center of the tip along a cylinder of 30 nm diameter, obtaining a value of 0.17±0.10 nm, with a correlation length of 6.88±0.11 nm for sample S2.

5.4.2 *Optical Properties of Asymmetric QWs*

To investigate the optical properties of the AQWs, we recall (section 2.1.4) that if the barrier b_t is thin enough, the two quantum wells are in a coupled regime and the wavefunctions of the excited states have a non-negligible amplitude in both wells (see Fig. 2.3). Therefore, the matrix element of envelope functions, defined by Eq. 2.29, between the fundamental state and the first excited level is non-zero and the transition is thus allowed.

The PL spectra, acquired at 80 K, of the four samples investigated are reported in Fig. 5.37. Spectra have been normalized so that the intensity of the $\Gamma_c - HH$ transition in the VS is equal to unity. The intense features between 0.9 and 1 eV have been attributed to direct recombinations in the QWs and the energy of the $\Gamma_0 - HH_0$ transition in the intrinsic sample is displayed as dashed line. We can clearly see the redshift of the $\Gamma_0 - HH_0$ transition increasing doping. As discussed in section 5.3.2, doping also affects the PL intensity of the QWs

feature. As a matter of fact, doping with a P-concentration of $\sim 1 \times 10^{17}$ cm^{-3}, the intensity of the $\Gamma_0 - HH_0$ transition is enhanced by a factor ~ 1.75 with respect to the intrinsic sample. Increasing further the concentration of dopants the PL intensity is quenched. In agreement with 5.3.2, the optimal dopant concentration is found to be in the $1 - 4 \times 10^{17}$ cm^{-3} range.

A clear difference can be observed from the comparison between the PL spectra of symmetric QWs reported in Fig. 5.10 and the spectra acquired on asymmetric QWs, consisting in a shoulder at ~ 25 meV above the $\Gamma_0 - HH_0$ peak. To quantitatively characterize the inter-band transitions in the Ge wells of sample S2, we have calculated the corresponding electronic states and band structure relying on the theoretical framework introduced in section 2.1.2 [see Fig. 5.38]. Supported by our numerical model, we relate the high-energy shoulder to a direct transition inside the wide Ge well between the fundamental state in the conduction band and the first excited state in the valence band, here denoted as Γ_0-HH_2. As discussed in section 2.1.4, in the case of isolated QWs with infinite barriers, the transition between the fundamental state in the conduction band and the first excited state in the valence band features a matrix element between wavefunctions having opposite parity and is therefore null. Due to the presence of the thin barrier, instead, the wavefunction of the HH_2 state has a non-negligible amplitude in both wells and its overlap with the wavefunction of the Γ_0 state is non-null. It follows that the transition becomes allowed.

With the help of the numerical model, we attribute the broad bands at $\sim 0.7 - 0.8$ eV and $\sim 1.0 - 1.1$ eV to a convolution of different indirect and direct recombinations, respectively. A good agreement is found for the experimental and calculated energies of direct and indirect transitions in sample S2, reported in Table 5.6 and Fig. 5.39 as filled (experimental) and empty (calculated) circles. The constant redshift of ~ 27 meV between the experimental and calculated energies is related to the increase of the QWs thickness due to doping, as already discussed.

We conclude this section noticing that also in sample S4, where the central barrier is thicker (b_t = 3.5 nm), the two wells are still in a coupled regime and the $\Gamma_0 - HH_2$ transition is observed.

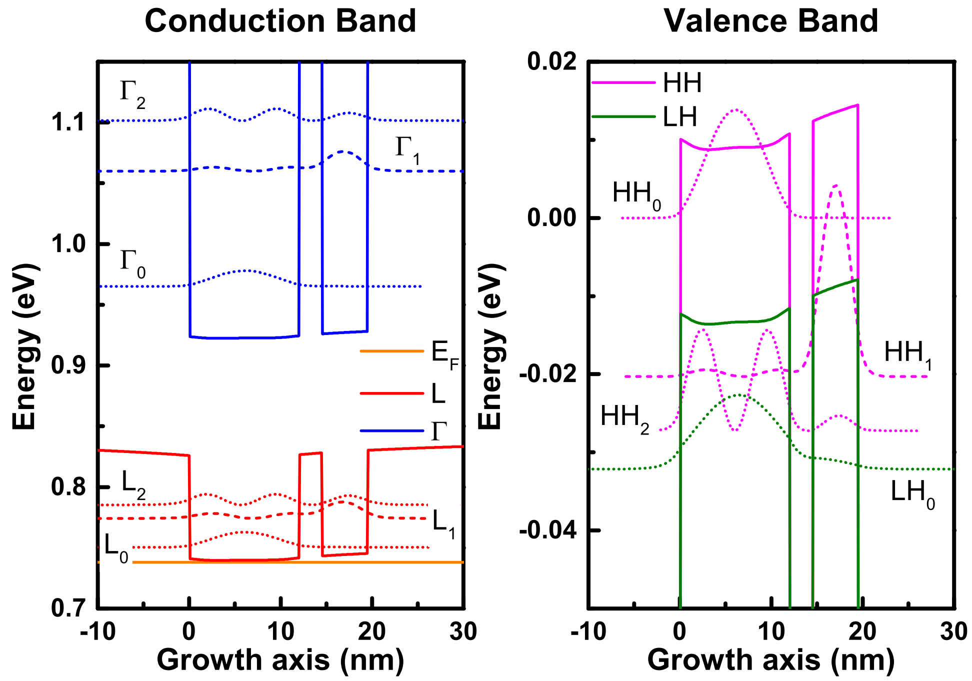

Figure 5.38 – Conduction- and valence-band edge profiles (continuous lines) of sample S2 at 80 K. The square modulus of the wave functions for the electron and hole confined states of the wide (narrow) Ge well are reported as dotted (dashed) lines.

Transition	Energy (eV)	
	Exp.	Theory
L_0-HH_0	0.721 ± 0.002	0.750
L_0-HH_2	0.748 ± 0.002	0.777
L_2-HH_2	0.783 ± 0.002	0.812
Γ_0-HH_0	0.936 ± 0.002	0.965
Γ_0-HH_2	0.963 ± 0.002	0.992
Γ_1-HH_0	1.031 ± 0.002	1.060
Γ_1-HH_1	1.051 ± 0.002	1.080

Table 5.6 – Experimental and calculated transition energies in sample S2.

The relaxation of the selection rules for inter-band transitions in QWs here demonstrated introduces a new parameter, in addition to the thickness of the QWs (as discussed in 5.1.2) and the magnitude of induced strain (as discussed in 5.2.2), to tune the emission wavelength by design. Moreover, the possibility to obtain two radiative transitions, whose separation in energy can be controlled, may enables the realization of light emitters of different "colors" integrated on the same chip (wavelength division multiplexing).

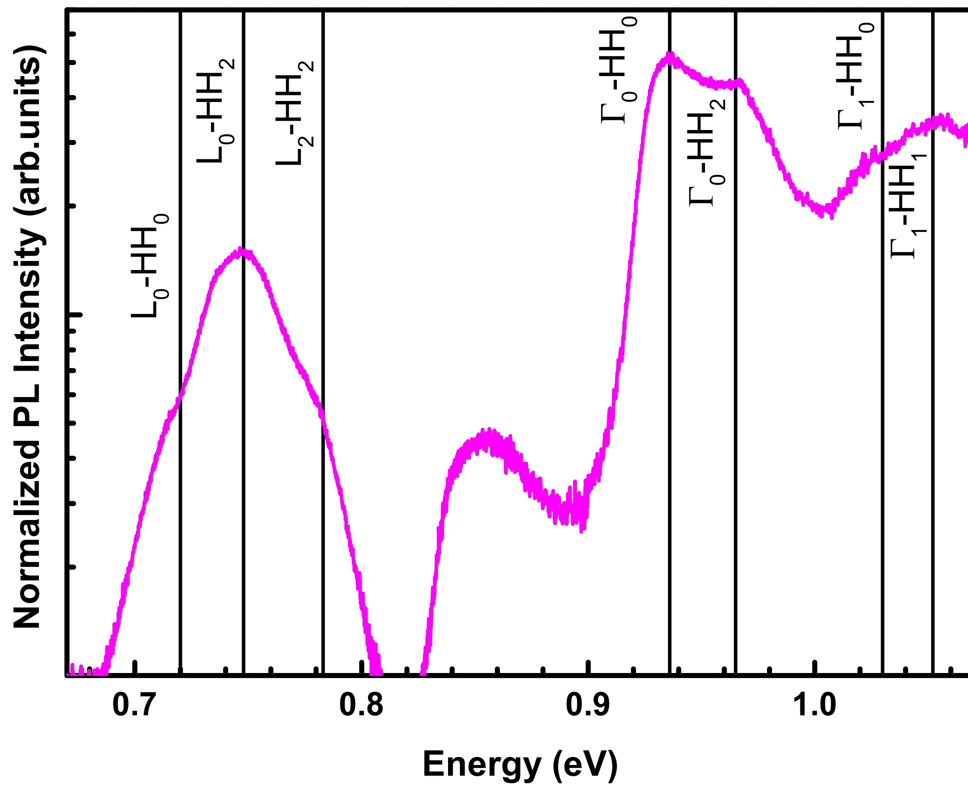

Figure 5.39 – Experimental and calculated energies of direct and indirect transitions in sample S2.

SUMMARY AND CONCLUSIONS

The overall goal of this thesis was to investigate how the photoluminescence properties of Ge/SiGe heterostructures can be tuned leveraging on quantum confinement, doping, and strain. Particular attention has been payed to structures suitable to achieve radiative emission from transitions that fall in the commercially important C-band (1530-1565 nm) of telecommunications.

The samples here investigated have been grown by means of ultra-high vacuum chemical vapor deposition on Si(100) substrates to satisfy the important requirement of compatibility with the standard Si-based microelectronics CMOS platform for the large scale production. The issues and the challenges beyond the deposition of Ge-rich SiGe heterostructures on Si substrate have been discussed in details. To minimize defects arising from the lattice mismatch between Si and Ge we employed reverse graded SiGe virtual substrates, where the mismatch is gradually distributed among the several layers they are made of. The structural and optical properties of the virtual substrates have been profoundly investigated to isolate the properties of the heterostructures from those of the substrate.

On top of the thick SiGe virtual substrates we have deposited different Ge wells confined between SiGe barriers with different thickness and/or number of periods. Two different kinds of QW structures have been investigated. The first one is a multi quantum well structure which consists in the periodic repetition of symmetric elements of single QWs separated by thick barriers to prevent any coupling between them. The structural characterization of this structure have been performed in order to retrieve the properties of the samples needed for the calculation of their electronic states. The good agreement between the observed and simulated data, allowed us to unambiguously interpret the emission spectra.

The main results obtained from the characterization of the samples can be summarized as follows:

- The integrated PL intensity is quenched increasing temperature.
- The $\Gamma_0 - HH_0$ transition energies are larger than the one associated to the direct recombination in the Ge due to the concomitant effect of quantum confinement and epitaxial strain (compressive). Moreover, as expected, a redshift of the PL peak with the increase of the well thickness is observed.

Since the effect of quantum confinement is to blueshift the emission wavelength of Ge from the commercially important C-band (0.79-0.81 eV) to the E-band (at RT) there is a significant demand to shift the emission wavelength into the C-band for potential application. This can be achieved by means of tensile strain.

Tensile strain has been induced in the Ge quantum wells by means of an external SiN stressor. Microstructures of different size and shape have been fabricated, allowing the Ge layers to freely expand into one, or two dimensions, resulting in different strain distribution profiles along the structure. The strain relaxation of the microstructures was modeled using COMSOL Multiphysics, a 3D finite element tool, and probed by μ-Raman spectroscopy. Strain values between $-0.4 \pm 0.1\%$ and $-0.2 \pm 0.1\%$ were obtained for the pillars and between $-1.0 \pm 0.2\%$ and $-0.8 \pm 0.2\%$ for the stripes. The strain in the QWs, before the deposition of the external stressor, was measured by XRD and Raman and is given by the sum of thermal (tensile) and epitaxial (compressive) strains. The values measured by Raman and XRD are in good agreement and correspond to $-0.6 \pm 0.1\%$.
In both pillars and stripes the maximum redshift is reached for 3 μm-wide structures confirming that in this kind of systems strain is not a monotonic function of the width. The maximum shift of the $\Gamma_0 - HH_0$ recombination is obtained for pillars of width 3 μm and corresponds to $\sim$ 33 meV. It follows that, fabricating the same structure on a sample featuring thicker QWs, such as S25-5, may result in a RT emission wavelength in the S-band.

To enhance the optical properties of bulk Ge doping is commonly employed. With the aim of boosting the PL signal of direct recombinations in the QWs, we deposited and investigated heavily n-doped Ge QWs. We found that the PL signal is not a monotonically increasing function of the donor concentration, but shows a maximum at a dopant concentration in the $1 - 4 \times 10^{17}$ cm^{-3} range.

Increasing further the amount of dopants the PL intensity of the $\Gamma_0 - HH_0$ transition is completely quenched due to the reduced crystal quality that results in an increase of SRH non-radiative recombinations.

The last configuration that has been investigated is called asymmetric coupled quantum well system, in which every single element of the periodic repetition consists in two QWs with different width separated only by a thin barrier of few atomic layers. Due to the small thickness of the barrier in the middle, the tunneling probability through the thin barrier could be very high and the electron wavefunction of each well can extend into the adjacent one. The result is a level mixing that generates global stationary levels with energies different from the original ones associated to each single QW. The breaking of the $m \neq n$ selection rule has been demonstrated with the observation of the $\Gamma_0 - HH_2$ recombination in the PL spectra.

In summary, we have analyzed, through microphotoluminescence measurements and theoretical calculations, the optical properties of Ge MQWs surrounded by Ge-rich SiGe barriers, grown on reverse-graded SiGe virtual substrates by means of ultrahigh-vacuum chemical vapor deposition. In view of the exploitation of Ge/SiGe MQWs as optical emitters, these results are crucial to unambiguously understand the photoluminescence spectra of samples with few periods of QWs grown on reverse graded virtual substrates. The high quality of the samples has been confirmed by high-resolution transmission electron microscopy, as well as x-ray diffraction and atomic force microscopy. The structural analysis demonstrates that strain-symmetrization is not a mandatory requirement for few multi-layer repetitions. The good agreement between experimental data and theoretically predicted transition energies, validates the proposed modeling and allows us to distinguish the spectral features originating in the excited portion of the substrate from those associated to the QWs. Moreover, the investigation of the symmetric QWs allowed to define the main limitations that hinder the employment of Ge/SiGe QWs as an active material in a Si-based light emitter. The deposition of the external SiN stressor effectively results in a redshift of the emitted light and a CMOS-compatible approach to tune the emission wavelength of Ge MQWs has been demonstrated. A boost of the PL intensity was observed in n-doped QWs for donor concentrations in the $1-4 \times 10^{17}$ cm^{-3} range. A further increase in the donor density worsens the optical emission. Finally,

the relaxation of the selection rules for inter-band transitions in QWs has been demonstrated in asymmetric coupled quantum wells, introducing a new parameter to tune the emission wavelength by design. Moreover, the possibility to obtain two radiative transitions, whose separation in energy can be controlled, may enables the realization of light emitters of different "colors" integrated on the same chip.

In conclusion, the present work of thesis presents a comprehensive study on Ge/SiGe quantum wells that provides a useful step towards the understanding of the optical properties of group-IV quantum wells for opto-electronic applications and their exploitation in the realization of engineered structures featuring properties suitable for the future implementation in a silicon-based lasing structure for light emission in the C-band of telecommunications.

LIST OF PUBLICATIONS

JOURNAL PAPERS

- C. Ciano, M. Virgilio, M. Montanari, L. Persichetti, L. Di Gaspare, M. Ortolani, L. Baldassarre, M. H. Zoellner, O. Skibitzki, G. Scalari, J. Faist, D. J. Paul, M. Scuderi, G. Nicotra, T. Grange, S. Birner, G. Capellini, and M. De Seta, "Control of electron state coupling in asymmetric Ge/GeSi quantum wells", Phys. Rev. Applied **11**, 014003 (2019)

- M. Montanari, M. Virgilio, C. L. Manganelli, P. Zaumseil, M. H. Zoellner, Y. Hou, M. A. Schubert, L. Persichetti, L. Di Gaspare, M. De Seta, E. Vitiello, E. Bonera, F. Pezzoli, and G. Capellini, "Photoluminescence study of inter-band transitions in few, pseudomorphic and strain-unbalanced Ge/GeSi multiple quantum wells", *Phys. Rev. B* **98**, 195310 (2018)

- C. L. Manganelli, M. Virgilio, O. Skibitzki, M. Salvalaglio, P. Zaumseil, Y. Yamamoto, M. Montanari, W. M. Klesse, and G. Capellini, "Unveiling the temperature dependence of strain-shift coefficients in epitaxial Ge/Si(001)", IN PREPARATION

- N. Taoka, G. Capellini, V. Schlykowa, M. Montanari, P. Zaumseil, O. Nakatsuka, S. Zaima, and T. Schroeder, "Electrical and optical properties improvement of GeSn layers formed at high temperature under well-controlled Sn migration", *Mater. Sci. Semicond. Process* **57**, 48-53 (2017)

CONFERENCES

- M. Montanari, M. Virgilio, C. L. Manganelli, P. Zaumseil, M. H. Zoellner, Y. Hou, M. A. Schubert, L. Persichetti, L. Di Gaspare, M. De Seta, E. Vitiello, E. Bonera, F. Pezzoli, and G. Capellini, "Photoluminescence study of inter-band transitions in Ge-rich Ge/SiGe multiple quantum wells", E-MRS 2018 Fall Meeting, September 16-20, Warsaw - Poland

- M. Montanari, C. Ciano, L. Di Gaspare, L. Persichetti, M. Virgilio, M. Ortolani, L. Baldassarre, G. Capellini, M. Zoellner, O. Skibitzki, A. Pashkin, M. Helm, G. Scalari, D. Stark, J. Faist, K. Rew, D.J. Paul , T.

Grange, S. Birner, and M. De Seta, "Towards a THz quantum cascade laser based on silicon heterostructures", E-MRS 2018 Fall Meeting, September 16-20, Warsaw - Poland

- M. Montanari, C. Ciano, L. Di Gaspare, L. Persichetti, M. Virgilio, M. Ortolani, L. Baldassarre, G. Capellini, M. Zoellner, O. Skibitzki, M. Helm, G. Scalari, D. Stark, J. Faist, K. Rew, D. J. Paul, T. Grange, S. Birner, and M. De Seta, "Optical properties of n-doped Ge/SiGe quantum wells in the THz range", ISTDM, May 27-31 2018, Potsdam - Germany

LIST OF ABBREVIATIONS

2D:	two-Dimensional
3D:	three-Dimensional
ACQW:	Asymmetric Coupled Quantum Wells
AFM:	Atomic Force Microscope
APT:	Atom Probe Tomography
BZ:	Brillouin Zone
CTE:	Coefficient Thermal Expansion
CVD:	Chemical Vapor Deposition
EDX:	Energy Dispersive X-ray spectroscopy
FP:	Fabry-Pérot
FEM:	Finite Element Method
FIB:	Focused Ion Beam
HH:	Heavy Hole
LH:	Light Hole
LO:	Longitudinal Optical
MBE:	Molecular Beam Epitaxy
MQW:	Multiple Quantum Wells
PE-CVD:	Plasma-Enhanced Chemical Vapor Deposition
PL:	Photoluminescence
RG-VS:	Reverse Graded Virtual Substrate
RSM:	Root Mean Square
RT:	Room Temperature
SEM:	Scanning Electron Microscope
SL:	Superlattice
SRH:	Shockley-Read-Hall
STEM:	Scanning Transmission Electron Microscope
TDD:	Threading Dislocation Density
ToF-SIMS:	Time-of-Flight Secondary Ion Mass Spectrometry
UHV:	Ultra-High Vacuum
VS:	Virtual Substrate
XPS:	X-ray Photoelectron Spectroscopy
XRD:	X-Ray Diffraction

LIST OF FIGURES

Figure 1 The virtuous circle of the semiconductor industry. . . v
Figure 2 Plot of CPU transistor counts against dates of introduction. Data from [2]. vi
Figure 3 Optical from submarine to on-chip. Adapted from [9]. vii
Figure 4 Configuration of an optical circuit. vii
Figure 5 Optical fiber transmission windows. ix
Figure 6 Gap modification xi
Figure 1.1 FCC lattice and its Brillouin zone 2
Figure 1.2 Many-valley structure of Si and Ge 2
Figure 1.3 Band diagram of Si and Ge 3
Figure 1.4 Valence band of Si and Ge 4
Figure 1.5 Possible band alignments in heterostructures 8
Figure 1.6 Stress components 10
Figure 1.7 Effects of strain on a doubly degenerate band 13
Figure 1.8 Band-edge energies in Ge as a function of the in-plane biaxial strain 15
Figure 1.9 Band-edge energies in Ge as a function of strain along different crystallographic directions 17
Figure 1.10 Relative offset of the Γ and L conduction band minima realized in Ge by uniaxial and biaxial tensile strain . . 17
Figure 1.11 Liquidus–solidus curve of the $Si_{1-x}Ge_x$ system 18
Figure 1.12 SiGe band gap extension as a function of the Ge content 19
Figure 1.13 Band alignment properties of SiGe heterostructures . 20
Figure 1.14 Type I band alignment in a $Ge/Si_{0.2}Ge_{0.8}$ quantum well 21
Figure 1.15 Bandgaps of the most important elemental and binary cubic semiconductors versus their lattice constant . . 22
Figure 1.16 Illustration of hetero-epitaxial structures 23
Figure 1.17 Schematic diagram of the three possible growth modes 25
Figure 1.18 Model of a screw and an edge dislocation 26
Figure 1.19 Burgers circuit 27

Figure 1.20 Elastic strain energy and formation of a dislocation as a function of the thickness of the deposited film and critical thickness as a function of the Ge content . . . 28
Figure 1.21 Example of a strain-compensated structure and misfit dislocations in Ge/Si 29
Figure 1.22 Different types of adsorption positions on the surface 32
Figure 1.23 Modes of epitaxial growth 33
Figure 1.24 CVD steps 35
Figure 1.25 Growth rate as a function of temperature for silane . . 36
Figure 2.1 Single QW in conduction band 40
Figure 2.2 Calculated conduction and valence band edge profiles in a $Ge/Si_{0.15}Ge_{0.85}$ QW 42
Figure 2.3 Electron energy of ACQWs in the uncoupled and coupled regime 44
Figure 2.4 Scheme of a direct interband transition 46
Figure 2.5 Scheme of an indirect interband transition 48
Figure 2.6 TM mode, TM mode and backscattering geometry . . 50
Figure 2.7 Scheme of inter-band transitions between confined states of a QW 52
Figure 2.8 Radiative recombination processes in semiconductors 53
Figure 2.9 Typical non-radiative recombination mechanisms . . 56
Figure 2.10 PL peak shape 60
Figure 2.11 Spectrum of band to band transition of a bulk Ge sample corrected for self-absorption 61
Figure 2.12 Sketch of resonant and non-resonant excitations . . . 62
Figure 2.13 Sketch of resonant and non-resonant excitations . . . 63
Figure 3.1 Sketch of the growth set-up 66
Figure 3.2 (a) Photograph of the CVD growth set-up. (b) Labview interface to control gas valves and flowmeters. 68
Figure 3.3 Energy level diagram of XPS 69
Figure 3.4 Example of an XPS spectrum 71
Figure 3.5 Photograph of the experimental XPS set-up 72
Figure 3.6 (a) The so-called scattering triangle. (b) Sketch of the Bragg equation. 73
Figure 3.7 Schematization of the three possible scan modes to perform XRD 74
Figure 3.8 (004) (left) and (224) (right) planes in Si and Ge. 74

Figure 3.9 (004) $\omega - 2\theta$ rocking curve scan acquired on heteroepitaxial Ge/Si (001) [102]. 75
Figure 3.10 (a) Schematic representation of correlation between distances in reciprocal space and lattice constants in ($a_{\|}$) and perpendicular ($a_{\perp}$) to the [001] direction in the case of pseudomorphic (Ge^{pseu}) and fully relaxed (Ge) Ge layer on Si. (b) Experimental RSM around the Si substrate 224 lattice point in the case of a SiGe layer grown on a Ge/Si VS. Both the relaxation and coherence lines have been reported [105]. 76
Figure 3.11 Photograph of the experimental XRD set-up 77
Figure 3.12 Scheme of AFM 78
Figure 3.13 Lennard-Jones potential and operation of tapping mode AFM 80
Figure 3.14 (a) Illustration of the relationship between the frequency shift, the amplitude reduction and the interacting force. (b) Electron micrograph of an AFM tip (top) and cantilever (bottom). 82
Figure 3.15 Bruker Dimension Icon AFM and scheme of the scanner 83
Figure 3.16 Schematization of Raman scattering 84
Figure 3.17 Ge dispersion curves for acoustic and optical phonons 85
Figure 3.18 Si dispersion curves for acoustic and optical phonons 85
Figure 3.19 Raman spectra for $Si_{1-x}Ge_x$ alloys with different concentrations x 88
Figure 3.20 Strain shift coefficeints and frequencies of $Si_{1-x}Ge_x$ modes as a function of the Ge molar fraction x 89
Figure 3.21 Photograph of the Raman set-up 90
Figure 3.22 PL set-up 91
Figure 3.23 Photograph of the PL set-up 92
Figure 3.24 PL instrument response and pump power density on the sample 93
Figure 4.1 TEM images of Ge layers on Si substrate at different growth temperatures 98
Figure 4.2 Sample holder in side and top view 100
Figure 4.3 XPS spectra before and after the substrate preparation 101
Figure 4.4 AFM images of a Ge virtual substrate at different growth stages 102

Figure 4.5 Ge and Si lattice parameters as a function of T 103

Figure 4.6 PL spectra acquired on Ge 104

Figure 4.7 PL spectra acquired on the Ge VS at 80 K and 300 K . 105

Figure 4.8 EDX composition profile, TEM, AFM and optical microscope images of the RG-VS 108

Figure 4.9 Rocking curve and RSM of a $Si_{0.05}Ge_{0.95}$ VS 109

Figure 4.10 Lattice parameter of the $Si_{1-x}Ge_x$ buffer as a function of the injected fluxes of GeH_4 and SiH_4 110

Figure 4.11 Ge content, as measured by XPS and XRD as a function of the injected gases 111

Figure 4.12 PL spectra acquired on the VS 111

Figure 5.1 TEM-EDX and ToF-SIMS of the calibration sample . . 114

Figure 5.2 Ge wells and $Si_{0.15}Ge_{0.85}$ barriers thickness as a function of the deposition time 114

Figure 5.3 *Left:* STEM images of the QWs region of samples S10-5, S17-5, and S25-5. *Right:* EDX composition profile superimposed to the corresponding STEM image of the QWs region of sample S10-10. 117

Figure 5.4 (a) XRD rocking curve of samples S10-2 (dark blue), S10-5 (blue), and S10-10 (light blue). The nominal thickness of the QWs is the same. In the inset, a detail of SL peaks is reported. (b) XRD rocking curve of samples S10-5 (blue), S17-5 (green), and S25-5 (red). In the inset, the different periodicity of the SL-peaks is clearly observed. 118

Figure 5.5 Reciprocal space maps of asymmetric $(4\bar{2}\bar{2})$ reflections of sample S10-10. 119

Figure 5.6 Comparison between the Raman spectra of a reference bulk Ge (001) substrate, a Ge/Si (001) epitaxial thin film, and sample S10-5. 120

Figure 5.7 (a) PL spectra acquired on sample S10-10. Lattice temperatures range from 80 K (violet) to 330 K (maroon) in ~ 30 K steps. (b) Contour plot of the PL spectra on sample S10-10 at different lattice temperatures. The integrated intensity at each temperature has been normalized to unity. The results of the fitting of experimental transitions in the Ge layer and the Ge QWs with Varshni equation are also reported as continuous lines. 122

Figure 5.8 T-dependent PL spectra acquired on samples Ge, VS, and S10-10 124

Figure 5.9 (a) Conduction- and valence-band edge profiles (continuous lines) and square modulus of the wave functions (dotted lines) for the electron and hole confined states of sample S10-10 at 80 K. (b) Experimental (filled circles) and calculated (empty circles) energy of the Γ_0-HH_0 transition in sample S10-10 as a function of the lattice temperature. The fitting of the experimental data with Varshni equation is reported with a continuous line. 125

Figure 5.10 (a) PL spectra acquired at 80 K on samples S10-2 (dark green), S10-5 (green), and S10-10 (light green). In the inset: Integrated PL intensity of the QWs peaks as a function of the number of periods. (b) Integrated PL intensity as a function of $\beta = 1/k_B T$. Squares and circles represent Ge and sample S10-10, respectively. . 126

Figure 5.11 PL spectra acquired at 80 K on samples S10-5 (blue), S17-5 (green), and S25-5 (red) The redshift of Γ_0-HH_0 with increasing thickness is clearly observed. 127

Figure 5.12 Experimental (filled symbols) and calculated (empty symbols) energy of the Γ_0-HH_0 transition, as a function of the QWs thickness, at 80 K (circles) and 300 K (squares). 128

Figure 5.13 PL spectra measured from the Ge (a) and S25-5 (b) sample at 80 K with different pump power density, ranging in the 5.6×10^4-5.6×10^5 W$\cdot$cm^{-2} interval. . . . 129

Figure 5.14 *Left*: Integrated PL intensity for the Ge sample (square), and for the Ge (circle) and QW (triangle) features of the S25-5 sample, as a function of the pump power density. *Right*: Ratio of the integrated PL intensity of the QWs signal to the VS signal of sample S25-5, as a function of the pump power density. 129

Figure 5.15 (a) Unstressed QWs. (b) Deposition of the external stressor. (c) Geometry description of the microstructures under investigation for clear definition of height (h) and width (w). 130

Figure 5.16 Displacement field of a micro-stripe. Taken from Ref. [52]. 131

Figure 5.17 Map of the biaxial strain in Ge micropillar of the same geometry with a SiN 200 nm thick and 400 nm thick. The thickness of the SiN stressor needs to be higher than 200 nm in order to allow a distribution of the strain fields along the entire structure. 133

Figure 5.18 (a) Behavior of the uniaxial strain as a function of the structure width. (b) Contour-plot of the biaxial strain as a function of the geometric parameters. 133

Figure 5.19 Equivalent strain profile for microstripes of cross section 1.5 μm, 3 μm, 5 μm, respectively (a), (b) and (c) and for pillars with cross section 1.5 μm, 3 μm, 5 μm (d), (e), (f). 134

Figure 5.20 SEM images of the fabricated structures 134

Figure 5.21 Comparison between experimental Raman map for pillar of side 1.5 μm, 3 μm, 5 μm, respectively (a), (b) and (c) and reconstruction of Raman map starting from FEM simulations for the same structure of the pillar [1.5 μm, 3 μm, 5 μm, respectively (d), (e), (f)]. . 135

Figure 5.22 Comparison between experimental Raman and theoretical Raman for a 5 μm width microstripe. 136

Figure 5.23 (a) Uniaxial and (b) biaxial strain as a function of the width of the structures measured by Raman at 300 K on stripes and pillars, respectively. Empty circles are the results of FEM simulations. 137

Figure 5.24 PL spectra at 80 K acquired on the unpatterned region, pillars, and stripes of width (from left to right) 1.5 μm, 3 μm, and 5 μm. 138
Figure 5.25 FEM strain components ε_{xx}, ε_{yy}, and ε_{zz} as a function of the depth inside the sample for 1.5 μm stripe and pillar. w denotes QW regions. 139
Figure 5.26 PL spectra acquired from Ge microstrip samples featuring different sizes, as indicated in the left top corner of each panel. Lattice temperatures range from 100 K (violet curves) to 430 K (dark red) in 30 K-steps [150]. 140
Figure 5.27 Redshift of the $\Gamma_0 - HH_0$ recombination as a function of the width of the structures measured by PL at 80 K on stripes and pillars, respectively. 140
Figure 5.28 Absorptance as a function of the wavelength without (top) and with (bottom) the SiN stressor[155]. 141
Figure 5.29 Integrated PL intensity for (a) the VS and (b) QW features as a function of the pump power density. Data related to the unpatterned region, 1.5 μm pillars and 1.5 μm stripes are reported as black, red, and blue squares, respectively. 142
Figure 5.30 *Top*: Phosphorus concentration-profile, as measured by SIMS. *Bottom*: Dopant concentration as a function of the partial pressure of phosphine. 144
Figure 5.31 XRD rocking curve of samples S10-10, S10-10-D1 and S10-10-D2 145
Figure 5.32 (a): Reciprocal space maps of asymmetric $(4\bar{2}\bar{2})$ reflections of sample S23-D1. (b) XRD rocking curve of samples S3-D1 and S23-D2. The nominal thickness of the QWs is the same. 146
Figure 5.33 PL spectra acquired at 80 on (a) thin and (b) thick doped Ge wells. 147
Figure 5.34 STEM image of sample S3 149
Figure 5.35 (a): Reciprocal space maps of asymmetric $(4\bar{2}\bar{2})$ reflections of sample S1. (b) XRD rocking curve of samples S1 and S2. The nominal thickness of the QWs is the same. 150

Figure 5.36 (a) Electron micrograph of the APT tip. (b) 3D atom-by-atom reconstruction of the tip. (c) 1D concentration profile of Si and Ge along the long axis of the tip. . . . 150
Figure 5.37 PL spectra acquired at 80 K on the asymmetric QWs samples. 151
Figure 5.38 Conduction- and valence-band edge profiles (continuous lines) of sample S2 at 80 K. The square modulus of the wave functions for the electron and hole confined states of the wide (narrow) Ge well are reported as dotted (dashed) lines. 153
Figure 5.39 Experimental and calculated energies of direct and indirect transitions in sample S2. 154

LIST OF TABLES

Table 1.1 Lattice constants and thermal expansion coefficients for Si and Ge . . . 3
Table 1.2 Band minima and maxima and the effective masses for Si and Ge . . . 5
Table 1.3 E_0, α and β Varshni's parameters of bulk Si and Ge . . 5
Table 1.4 Stiffness constants of Si and Ge . . . 11
Table 1.5 Deformation potentials for the L and Γ conduction edges 16
Table 2.1 Selection rules for inter-band transitions at Γ involving HH and LH valence states . . . 51
Table 2.2 Minority carrier radiative lifetime in several semiconductors at room temperature [91, 43, 92] . . . 54
Table 4.1 Comparison of literature data for different virtual substrates . . . 97
Table 4.2 Example of a reverse graded deposition . . . 107
Table 5.1 Nominal parameters of the samples here investigated. Samples are labeled as S *thickness of QW-number of periods*.116
Table 5.2 Material parameters of the samples here investigated as determined by TEM and XRD. . . . 117
Table 5.3 Experimental and calculated Γ_0-HH_0 and L_0-HH_0 transition energies at selected temperatures. . . . 123
Table 5.4 Parameters of the doped samples here investigated. The thickness of the doped region is reported in bold. 144
Table 5.5 Parameters of the AQWs samples here investigated. The thickness of the doped region is reported in bold. 148
Table 5.6 Experimental and calculated transition energies in sample S2. . . . 153

BIBLIOGRAPHY

[1] W. Arden, M. Brillouet, P. Cogez, M. Graef, B. Huizing, and R. Mahnkopf. "More-than-Moore, White Paper."

[2] Wikipedia contributors. "Transistor count - Wikipedia, The Free Encyclopedia."

[3] D. A. B. Miller. "Optical interconnects to electronic chips." *Appl. Opt.* **49** (25), F59 (2010).

[4] M. J. Deen and P. K. Basu. *Silicon Photonics: Fundamentals and Devices*. John Wiley & Sons (2012). ISBN 978-0-470-51750-5.

[5] C. Gunn. "CMOS Photonics for High-Speed Interconnects." *IEEE Micro* **26** (2), 58 (2006).

[6] Semiconductor Industry Association. "International Technology Roadmap for Semiconductors (ITRS)."

[7] D. Miller. "Miller, D.: Device requirements for optical interconnects to silicon chips. Proc. IEEE 97, 1166-1185." **97**, 1166 (2009).

[8] C. A. Mack. "Fifty Years of Moore's Law." *IEEE Transactions on Semiconductor Manufacturing* **24** (2), 202 (2011).

[9] J. Wang and Y. Long. "On-chip silicon photonic signaling and processing: a review." *Science Bulletin* **63** (19), 1267 (2018).

[10] G. T. Reed and A. P. Knights. *Silicon Photonics: An Introduction*. John Wiley & Sons (2004). ISBN 978-0-470-87034-1.

[11] R. Soref. "Mid-infrared photonics in silicon and germanium." *Nature Photonics* **4**, 495 (2010).

[12] M. Virgilio, C. L. Manganelli, G. Grosso, G. Pizzi, and G. Capellini. "Radiative recombination and optical gain spectra in biaxially strained n-type germanium." *Phys. Rev. B* **87**, 235313 (2013).

[13] J. Liu, X. Sun, R. Camacho-Aguilera, L. C. Kimerling, and J. Michel. "Ge-on-Si laser operating at room temperature." *Opt. Lett.* **35** (5), 679 (2010).

[14] R. E. Camacho-Aguilera, Y. Cai, N. Patel, J. T. Bessette, M. Romagnoli, L. C. Kimerling, and J. Michel. "An electrically pumped germanium laser." *Opt. Express* **20** (10), 11316 (2012).

[15] R. Koerner, M. Oehme, M. Gollhofer, M. Schmid, K. Kostecki, S. Bechler, D. Widmann, E. Kasper, and J. Schulze. "Electrically pumped lasing from Ge Fabry-Perot resonators on Si." *Opt. Express* **23** (11), 14815 (2015).

[16] M. Bonfanti, E. Grilli, M. Guzzi, M. Virgilio, G. Grosso, D. Chrastina, G. Isella, H. von Känel, and A. Neels. "Optical transitions in Ge/SiGe multiple quantum wells with Ge-rich barriers." *Phys. Rev. B* **78**, 041407 (2008).

[17] M. D. Seta, G. Capellini, M. Ortolani, M. Virgilio, G. Grosso, G. Nicotra, and P. Zaumseil. "Narrow intersubband transitions in n-type Ge/SiGe multi-quantum wells: control of the terahertz absorption energy trough the temperature dependent depolarization shift." *Nanotechnology* **23** (46), 465708 (2012).

[18] Y. H. Kuo, Y. K. Lee, Y. Ge, S. Ren, J. E. Roth, T. I. Kamins, D. A. B. Miller, and J. S. Harris. "Strong quantum confined Stark effect in germanium quantum-well structures on silicon." *Nature* **437** (7063), 1334 (2005).

[19] D. J. Paul. "8-band **k.p** modeling of the quantum confined Stark effect in Ge quantum wells on Si substrates." *Phys. Rev. B* **77**, 155323 (2008).

[20] R. K. Schaevitz, J. E. Roth, S. Ren, O. Fidaner, and D. A. B. Miller. "Material Properties of Si-Ge/Ge Quantum Wells." *IEEE Journal of Selected Topics in Quantum Electronics* **14** (4), 1082 (2008).

[21] D. Marris-Morini, P. Chaisakul, M.-S. Rouifed, J. Frigerio, D. Chrastina, G. Isella, S. Edmond, X. Le Roux, J.-R. Coudevylle, and L. Vivien. "Towards low energy consumption integrated photonic circuits based on Ge/SiGe quantum wells." *Nanophotonics* **2**, 279 (2013).

[22] P. Chaisakul, D. Marris-Morini, G. Isella, D. Chrastina, M. Rouifed, J. Frigerio, and L. Vivien. "Ge quantum well optoelectronic devices for light modulation, detection, and emission." *Solid-State Electronics* **83**, 92

(2013). Selected Papers from the 6th International SiGe Technology and Device Meeting (ISTDM 2012).

[23] L. Lever, Y. Hu, M. Myronov, X. Liu, N. Owens, F. Y. Gardes, I. P. Marko, S. J. Sweeney, Z. Ikonić, D. R. Leadley, G. T. Reed, and R. W. Kelsall. "Modulation of the absorption coefficient at 1.3μm in Ge/SiGe multiple quantum well heterostructures on silicon." *Opt. Lett.* **36** (21), 4158 (2011).

[24] O. Fidaner, A. K. Okyay, J. E. Roth, R. K. Schaevitz, Y. H. Kuo, K. C. Saraswat, J. S. Harris, and D. A. B. Miller. "Ge-SiGe Quantum-Well Waveguide Photodetectors on Silicon for the Near-Infrared." *IEEE Photonics Technology Letters* **19** (20), 1631 (2007).

[25] E. Onaran, M. C. Onbasli, A. Yesilyurt, H. Y. Yu, A. M. Nayfeh, and A. K. Okyay. "Silicon-Germanium multi-quantum well photodetectors in the near infrared." *Opt. Express* **20** (7), 7608 (2012).

[26] G.-E. Chang, S.-W. Chen, and H. H. Cheng. "Tensile-strained Ge/SiGe quantum-well photodetectors on silicon substrates with extended infrared response." *Opt. Express* **24** (16), 17562 (2016).

[27] C. Lange, G. Isella, D. Chrastina, F. Pezzoli, N. S. Köster, R. Woscholski, and S. Chatterjee. "Spin band-gap renormalization and hole spin dynamics in Ge/SiGe quantum wells." *Phys. Rev. B* **85**, 241303 (2012).

[28] A. Giorgioni, F. Pezzoli, E. Gatti, S. Cecchi, C. Kazuo Inoki, C. Deneke, E. Grilli, G. Isella, and M. Guzzi. "Optical tailoring of carrier spin polarization in Ge/SiGe multiple quantum wells." *Applied Physics Letters* **102** (1), 012408 (2013).

[29] A. Giorgioni, S. Paleari, S. Cecchi, E. Vitiello, E. Grilli, G. Isella, W. Jantsch, M. Fanciulli, and F. Pezzoli. "Strong confinement-induced engineering of the g factor and lifetime of conduction electron spins in Ge quantum wells." *Nature Communications* **7**, 13886 (2016).

[30] S. De Cesari, E. Vitiello, A. Giorgioni, and F. Pezzoli. "Progress towards Spin-Based Light Emission in Group IV Semiconductors." *Electronics* **6** (1), 19 (2017).

[31] P. Chaisakul, D. Marris-Morini, G. Isella, D. Chrastina, N. Izard, X. Le Roux, S. Edmond, J.-R. Coudevylle, and L. Vivien. "Room

temperature direct gap electroluminescence from Ge/$Si_{0.15}Ge_{0.85}$ multiple quantum well waveguide." *Applied Physics Letters* **99** (14), 141106 (2011).

[32] E. Gatti, E. Grilli, M. Guzzi, D. Chrastina, G. Isella, and H. von Känel. "Room temperature photoluminescence of Ge multiple quantum wells with Ge-rich barriers." *Applied Physics Letters* **98** (3), 031106 (2011).

[33] "Electronic band structures of silicongermanium (SiGe) alloys." In Y. Shiraki and N. Usami (Editors) "Silicon-Germanium (SiGe) Nanostructures," , Woodhead Publishing Series in Electronic and Optical Materials, 26 – 42. Woodhead Publishing (2011). ISBN 978-1-84569-689-4.

[34] G. Grosso and G. P. Parravicini. *Solid State Physics*, . Academic Press (2014). ISBN 978-0-12-304460-0.

[35] J. E. Ayers. *Heteroepitaxy of Semiconductors: Theory, Growth, and Characterization*. CRC Press (2007). ISBN 9781420006643.

[36] J. H. Davies. *The Physics of Low-Dimensional Semiconductors*, . Cambridge University Press (1998). ISBN 9780511819070.

[37] Y. Varshni. "Temperature dependence of the energy gap in semiconductors." *Physica* **34** (1), 149 (1967).

[38] J. Singh. *Electronic and Optoelectronic Properties of Semiconductor Structures*, . Cambridge University Press (2003).

[39] V. R. D'Costa, Y.-Y. Fang, J. Tolle, J. Kouvetakis, and J. Menéndez. "Tunable Optical Gap at a Fixed Lattice Constant in Group-IV Semiconductor Alloys." *Phys. Rev. Lett.* **102**, 107403 (2009).

[40] N. Lothar. "Zur Elektronentheorie der Metalle. I." *Annalen der Physik* **401** (5), 607.

[41] A. R. Denton and N. W. Ashcroft. "Vegard's law." *Phys. Rev. A* **43**, 3161 (1991).

[42] C. G. Van de Walle and R. M. Martin. "Theoretical calculations of heterojunction discontinuities in the Si/Ge system." *Phys. Rev. B* **34**, 5621 (1986).

[43] P. Y. Yu and M. Cardona. *Fundamentals of Semiconductors*, . Springer, Berlin, Heidelberg (2010).

[44] C. Kittel. *Introduction to Solid State Physics*. John Whiley and sons (2004). ISBN 978-0-471-41526-8.

[45] O. Madelung. *Group IV Elements and III-V Compounds*, . Springer-Verlag Berlin Heidelberg (1991). ISBN 978-3-540-53150-0.

[46] M. Grundmann. *The Physics of Semiconductors*, . Springer, 2 edition (2010). ISBN 978-3-642-13884-3.

[47] J.-M. Jancu and P. Voisin. "Tetragonal and trigonal deformations in zinc-blende semiconductors: A tight-binding point of view." *Phys. Rev. B* **76**, 115202 (2007).

[48] J. Bardeen and W. Shockley. "Deformation Potentials and Mobilities in Non-Polar Crystals." *Phys. Rev.* **80**, 72 (1950).

[49] F. H. Pollak and M. Cardona. "Piezo-Electroreflectance in Ge, GaAs, and Si." *Phys. Rev.* **172**, 816 (1968).

[50] R. Geiger, T. Zabel, and H. Sigg. "Group IV Direct Band Gap Photonics: Methods, Challenges, and Opportunities." *Frontiers in Materials* **2**, 52 (2015).

[51] L. Liu, M. Zhang, L. Hu, Z. Di, and S.-J. Zhao. "Effect of tensile strain on the electronic structure of Ge: A first-principles calculation." *Journal of Applied Physics* **116** (11), 113105 (2014).

[52] G. Capellini, G. Kozlowski, Y. Yamamoto, M. Lisker, C. Wenger, G. Niu, P. Zaumseil, B. Tillack, A. Ghrib, M. de Kersauson, M. El Kurdi, P. Boucaud, and T. Schroeder. "Strain analysis in SiN/Ge microstructures obtained via Si-complementary metal oxide semiconductor compatible approach." *Journal of Applied Physics* **113** (1), 013513 (2013).

[53] D. Nam, D. S. Sukhdeo, J.-H. Kang, J. Petykiewicz, J. H. Lee, W. S. Jung, J. Vuckovic, M. L. Brongersma, and K. C. Saraswat. "Strain-Induced Pseudoheterostructure Nanowires Confining Carriers at Room Temperature with Nanoscale-Tunable Band Profiles." *Nano Letters* **13** (7), 3118 (2013). PMID: 23758608.

[54] D. S. Sukhdeo, D. Nam, J.-H. Kang, M. L. Brongersma, and K. C. Saraswat. "Direct bandgap germanium-on-silicon inferred from 5.7% <100> uniaxial tensile strain." *Photon. Res.* **2** (3), A8 (2014).

[55] M. J. Süess, R. Geiger, R. A. Minamisawa, G. Schiefler, J. Frigerio, D. Chrastina, G. Isella, R. Spolenak, J. Faist, and H. Sigg. "Analysis of enhanced light emission from highly strained germanium microbridges." *Nature Photonics* (7), 466 (2013).

[56] R. Geiger, M. J. Süess, C. Bonzon, R. Spolenak, J. Faist, and H. Sigg. "Strained Ge microbridges to obtain a direct bandgap laser." In "2014 7th International Silicon-Germanium Technology and Device Meeting (ISTDM)," 7–8 (2014).

[57] M. Prost, M. E. Kurdi, A. Ghrib, S. Sauvage, X. Checoury, N. Zerounian, F. Aniel, G. Beaudoin, I. Sagnes, F. Boeuf, and P. Boucaud. "Tensile-strained germanium microdisk electroluminescence." *Opt. Express* **23** (5), 6722 (2015).

[58] A. Ghrib, M. El Kurdi, M. Prost, S. Sauvage, X. Checoury, G. Beaudoin, M. Chaigneau, R. Ossikovski, I. Sagnes, and P. Boucaud. "All-Around SiN Stressor for High and Homogeneous Tensile Strain in Germanium Microdisk Cavities." *Advanced Optical Materials* **3** (3), 353.

[59] F. Schäffler. "High-mobility Si and Ge structures." *Semiconductor Science and Technology* **12** (12), 1515 (1997).

[60] E. Kasper and H.-J. Herzog. "Structural properties of silicon-germanium (SiGe) nanostructures." In Y. Shiraki and N. Usami (Editors) "Silicon-Germanium (SiGe) Nanostructures," , Woodhead Publishing Series in Electronic and Optical Materials, 3 – 25. Woodhead Publishing (2011). ISBN 978-1-84569-689-4.

[61] M. M. Rieger and P. Vogl. "Electronic-band parameters in strained $Si_{1-x}Ge_x$ alloys on $Si_{1-y}Ge_y$ substrates." *Phys. Rev. B* **48**, 14276 (1993).

[62] R. Braunstein, A. R. Moore, and F. Herman. "Intrinsic Optical Absorption in Germanium-Silicon Alloys." *Phys. Rev.* **109**, 695 (1958).

[63] J. Weber and M. I. Alonso. "Near-band-gap photoluminescence of Si-Ge alloys." *Phys. Rev. B* **40**, 5683 (1989).

[64] M. Virgilio and G. Grosso. "Type-I alignment and direct fundamental gap in SiGe based heterostructures." *Journal of Physics: Condensed Matter* **18** (3), 1021 (2006).

[65] P. D. H. L. a. Professor Dr. Harald Ibach. *Solid-State Physics: An Introduction to Principles of Materials Science*, . Advanced Texts in Physics. Springer Berlin Heidelberg (2003). ISBN 978-3-540-43870-0,978-3-662-05342-3.

[66] M. Suemitsu and S. Filimonov. "Understanding crystal growth mechanisms in silicon-germanium (SiGe) nanostructures." In Y. Shiraki and N. Usami (Editors) "Silicon-Germanium (SiGe) Nanostructures," , Woodhead Publishing Series in Electronic and Optical Materials, 45 – 71. Woodhead Publishing (2011). ISBN 978-1-84569-689-4.

[67] E. Bauer. "Phänomenologische Theorie der Kristallabscheidung an Oberflächen. I." *Zeitschrift fur Kristallographie* **110**, 372 (1958).

[68] F. C. Frank and J. H. van der Merwe. "One-dimensional dislocations. I. Static theory." **198** (1053), 205 (1949).

[69] M. Volmer and A. Weber. *Zeitschrift fur Physikalische Chemie* 277 (1926).

[70] I. Stranski and L. Krastanov. *Sitzungsber. Akad. Wiss. Wien, 146* 797–810 (1938).

[71] R. People and J. C. Bean. "Calculation of critical layer thickness versus lattice mismatch for Ge_xSi_{1-x}/Si strained-layer heterostructures." *Applied Physics Letters* **47** (3), 322 (1985).

[72] J. Matthews and A. Blakeslee. "Defects in epitaxial multilayers: III. Preparation of almost perfect multilayers." *Journal of Crystal Growth* **32** (2), 265 .

[73] D. Paul. "The progress towards terahertz quantum cascade lasers on silicon substrates." *Laser & Photonics Reviews* **4** (5), 610.

[74] L. M. Giovane, H.-C. Luan, A. M. Agarwal, and L. C. Kimerling. "Correlation between leakage current density and threading dislocation density in SiGe p-i-n diodes grown on relaxed graded buffer layers." *Applied Physics Letters* **78** (4), 541 (2001).

[75] J. G. Fiorenza, G. Braithwaite, C. W. Leitz, M. T. Currie, J. Yap, F. Singaporewala, V. K. Yang, T. A. Langdo, J. Carlin, M. Somerville, A. Lochtefeld, H. Badawi, and M. T. Bulsara. "Film thickness constraints for manufacturable strained silicon CMOS." *Semiconductor Science and Technology* **19** (1), L4 (2004).

[76] M. Suemitsu and S. Filimonov. "Understanding crystal growth mechanisms in silicongermanium (SiGe) nanostructures." In Y. Shiraki and N. Usami (Editors) "SiliconGermanium (SiGe) Nanostructures," , Woodhead Publishing Series in Electronic and Optical Materials, 45 – 71. Woodhead Publishing (2011). ISBN 978-1-84569-689-4.

[77] I. V. Markov. *Crystal Growth for Beginners*, . WORLD SCIENTIFIC, 2nd edition (2003).

[78] E. Kasper, H. J. Herzog, and H. Kibbel. "A one-dimensional SiGe superlattice grown by UHV epitaxy." *Applied physics* **8** (3), 199 (1975).

[79] M. Ohring. *Materials Science of Thin Films*, . Academic Press (2002). ISBN 978-0-12-524975-1.

[80] G. Pizzi, M. Virgilio, and G. Grosso. "Tight-binding calculation of optical gain in tensile strained [001]-Ge/SiGe quantum wells." *Nanotechnology* **21** (5), 055202 (2010).

[81] M. Virgilio and G. Grosso. "Quantum-confined Stark effect in Ge/SiGe quantum wells: A tight-binding description." *Phys. Rev. B* **77**, 165315 (2008).

[82] M. R. Barget, M. Virgilio, G. Capellini, Y. Yamamoto, and T. Schroeder. "The impact of donors on recombination mechanisms in heavily doped Ge/Si layers." *Journal of Applied Physics* **121** (24), 245701 (2017).

[83] Y. Busby, M. De Seta, G. Capellini, F. Evangelisti, M. Ortolani, M. Virgilio, G. Grosso, G. Pizzi, P. Calvani, S. Lupi, M. Nardone, G. Nicotra, and C. Spinella. "Near- and far-infrared absorption and electronic structure of Ge-SiGe multiple quantum wells." *Phys. Rev. B* **82**, 205317 (2010).

[84] M. Virgilio, M. Bonfanti, D. Chrastina, A. Neels, G. Isella, E. Grilli, M. Guzzi, G. Grosso, H. Sigg, and H. von Känel. "Polarization-dependent absorption in Ge/SiGe multiple quantum wells: Theory and experiment." *Phys. Rev. B* **79**, 075323 (2009).

[85] B. Nag. "Physics of Quantum Well Devices." In "Solid-State Science and Technology Library," volume 7. Springer (2002).

[86] G. Pizzi. *Band Structure Engineering of Ge-rich SiGe Nanostructures for Photonics Applications*. Ph.D. thesis, Scuola Normale Superiore di Pisa.

[87] H. Bebb and E. Williams. "Photoluminescence: Theory." volume 8 of *Semiconductors and Semimetals*, chapter 4, 181 – 320. Elsevier (1972).

[88] G. Bastard. *Wave mechanics applied to semiconductor heterostructures 1992*, (1992). ISBN 2868830927,9782868830920.

[89] B. E. A. Saleh and M. C. Teich. *Fundamentals of Photonics*. John Wiley and sons, 2 edition (2007). ISBN 978-0-471-35832-9.

[90] S. Sze and K. K. Ng. *Physics and Properties of Semiconductors-A Review*, , chapter 1, 5–75. Wiley-Blackwell (2006). ISBN 9780470068328.

[91] R. Hall. "Recombination processes in semiconductors." *Proceedings of the IEE Part B Electronic and Communication Engineering* **106** (1959).

[92] P. Jacques I. Pankove. *Optical Processes in Semiconductors*, . Dover Books on Physics. Dover Publications, 2 edition (2010). ISBN 0486602753,9780486602752.

[93] D. Neamen. *Semiconductor Physics And Devices*. McGraw-Hill, Inc., New York, NY, USA, 4 edition (2011). ISBN 0072321075, 9780072321074.

[94] R. N. Hall. "Electron-Hole Recombination in Germanium." *Phys. Rev.* **87**, 387 (1952).

[95] S. A. Srinivasan, C. Porret, M. Pantouvaki, Y. Shimura, P. Geiregat, R. Loo, J. Van Campenhout, and D. Van Thourhout. "Carrier scattering induced linewidth broadening in in situ P-doped Ge layers on Si." *Applied Physics Letters* **113** (16), 161101 (2018).

[96] S. Marchetti, M. Martinelli, R. Simili, M. Giorgi, and R. Fantoni. "Measurement of Ge Electrical Parameters by Analysing its Optical Dynamics." *Physica Scripta* **64** (5), 509 (2001).

[97] R. Conradt and J. Aengenheister. "Minority carrier lifetime in highly doped Ge." *Solid State Communications* **10** (3), 321 (1972).

[98] J. A. Van Vechten and M. Wautelet. "Variation of semiconductor band gaps with lattice temperature and with carrier temperature when these are not equal." *Phys. Rev. B* **23**, 5543 (1981).

[99] T. Arguirov, M. Kittler, and N. V. Abrosimov. "Room temperature luminescence from Germanium." *Journal of Physics: Conference Series* **281** (1), 012021 (2011).

[100] E. Gatti. *Recombination processes and carrier dynamics in Ge/SiGe multiple quantum wells*. Ph.D. thesis, Universitá degli studi di Milano-Bicocca.

[101] C. Lamberti. *Characterization of Semiconductor Heterostructures and Nanostructures*. Elsevier Science (2008). ISBN 9780444530998.

[102] G. Capellini, M. De Seta, P. Zaumseil, G. Kozlowski, and T. Schroeder. "High temperature x ray diffraction measurements on Ge/Si(001) heterostructures: A study on the residual tensile strain." *Journal of Applied Physics* **111** (7), 073518 (2012).

[103] J. A. Olsen, E. L. Hu, S. R. Lee, I. J. Fritz, A. J. Howard, B. E. Hammons, and J. Y. Tsao. "X-ray reciprocal-space mapping of strain relaxation and tilting in linearly graded InAlAs buffers." *Journal of Applied Physics* **79** (7), 3578 (1996).

[104] G. Bauer, J. Li, and E. Koppensteiner. "X-ray reciprocal space mapping of SiSi$_{1-x}$Ge$_x$ heterostructures." *Journal of Crystal Growth* **157** (1), 61 (1995).

[105] G. Capellini, M. De Seta, Y. Busby, M. Pea, F. Evangelisti, G. Nicotra, C. Spinella, M. Nardone, and C. Ferrari. "Strain relaxation in high Ge content SiGe layers deposited on Si." *Journal of Applied Physics* **107** (6), 063504 (2010).

[106] Y. Seo and W. Jhe. "Atomic force microscopy and spectroscopy." *Reports on Progress in Physics* **71** (1), 016101 (2008).

[107] F. Pezzoli, E. Bonera, E. Grilli, M. Guzzi, S. Sanguinetti, D. Chrastina, G. Isella, H. von Känel, E. Wintersberger, J. Stangl, and G. Bauer. "Phonon strain shift coefficients in Si$_{1-x}$Ge$_x$ alloys." *Journal of Applied Physics* **103** (9), 093521 (2008).

[108] I. D. Wolf. "Micro-Raman spectroscopy to study local mechanical stress in silicon integrated circuits." *Semiconductor Science and Technology* **11** (2), 139 (1996).

[109] W. Weber. "Adiabatic bond charge model for the phonons in diamond, Si, Ge, and $\alpha-$Sn." *Phys. Rev. B* **15**, 4789 (1977).

[110] O. Madelung, U. Rössler, and M. Schulz (Editors). *Germanium (Ge), phonon dispersion, phonon frequencies*. Springer Berlin Heidelberg (2002).

[111] S. Ganesan, A. Maradudin, and J. Oitmaa. "A lattice theory of morphic effects in crystals of the diamond structure." *Annals of Physics* **56** (2), 556 (1970).

[112] C. L. Manganelli, P. Pintus, and C. Bonati. "Modeling of strain-induced Pockels effect in Silicon." *Opt. Express* **23** (22), 28649 (2015).

[113] O. Pagés, J. Souhabi, V. J. B. Torres, A. V. Postnikov, and K. C. Rustagi. "Re-examination of the SiGe Raman spectra: Percolation/one-dimensional-cluster scheme and ab initio calculations." *Phys. Rev. B* **86**, 045201 (2012).

[114] F. Pezzoli, E. Grilli, M. Guzzi, S. Sanguinetti, D. Chrastina, G. Isella, H. von Känel, E. Wintersberger, J. Stangl, and G. Bauer. "Strain-induced shift of phonon modes in $Si_{1-x}Ge_x$ alloys." *Materials Science in Semiconductor Processing* **9**, 541 (2006).

[115] F. Pezzoli, E. Bonera, E. Grilli, M. Guzzi, S. Sanguinetti, D. Chrastina, G. Isella, H. von Känel, E. Wintersberger, J. Stangl, and G. Bauer. "Raman spectroscopy determination of composition and strain in $Si_{1-x}Ge_x$/Si heterostructures." *Materials Science in Semiconductor Processing* **11** (5), 279 (2008).

[116] F. Montalenti, F. Rovaris, R. Bergamaschini, L. Miglio, M. Salvalaglio, G. Isella, F. Isa, and H. von Känel. "Dislocation-Free SiGe/Si Heterostructures." *Crystals* **8** (6) (2018).

[117] E. A. Fitzgerald, Y.-H. Xie, M. L. Green, D. Brasen, A. R. Kortan, J. Michel, Y.-J. Mii, and B. E. Weir. "Totally relaxed Ge_xSi_{1-x} layers with low threading dislocation densities grown on Si substrates." *Applied Physics Letters* **59** (7), 811 (1991).

[118] Y. B. Bolkhovityanov, O. P. Pchelyakov, L. V. Sokolov, and S. I. Chikichev. "Artificial GeSi substrates for heteroepitaxy: Achievements and problems." *Semiconductors* **37** (5), 493 (2003).

[119] A. D. Capewell, T. J. Grasby, T. E. Whall, and E. H. C. Parker. "Terrace grading of SiGe for high-quality virtual substrates." *Applied Physics Letters* **81** (25), 4775 (2002).

[120] K. Sawano, S. Koh, Y. Shiraki, Y. Hirose, T. Hattori, and K. Nakagawa. "Mobility enhancement in strained Si modulation-doped structures by chemical mechanical polishing." *Applied Physics Letters* **82** (3), 412 (2003).

[121] V. Shah, A. Dobbie, M. Myronov, and D. Leadley. "Reverse graded strain relaxed SiGe buffers for CMOS and optoelectronic integration." *Thin Solid Films* **520** (8), 3227 (2012).

[122] Y. H. Xie, G. H. Gilmer, C. Roland, P. J. Silverman, S. K. Buratto, J. Y. Cheng, E. A. Fitzgerald, A. R. Kortan, S. Schuppler, M. A. Marcus, and P. H. Citrin. "Semiconductor Surface Roughness: Dependence on Sign and Magnitude of Bulk Strain." *Phys. Rev. Lett.* **73**, 3006 (1994).

[123] V. A. Shah, A. Dobbie, M. Myronov, and D. R. Leadley. "Reverse graded SiGe/Ge/Si buffers for high-composition virtual substrates." *Journal of Applied Physics* **107** (6), 064304 (2010).

[124] M. T. Currie, S. B. Samavedam, T. A. Langdo, C. W. Leitz, and E. A. Fitzgerald. "Controlling threading dislocation densities in Ge on Si using graded SiGe layers and chemical-mechanical polishing." *Applied Physics Letters* **72** (14), 1718 (1998).

[125] Y. Bogumilowicz, J. Hartmann, C. D. Nardo, P. Holliger, A.-M. Papon, G. Rolland, and T. Billon. "High-temperature growth of very high germanium content SiGe virtual substrates." *Journal of Crystal Growth* **290** (2), 523 (2006).

[126] "Smooth and high quality epitaxial strained Ge grown on SiGe strain relaxed buffers with 70-85% Ge." *Journal of Crystal Growth* **324** (1), 15 (2011).

[127] J. M. Hartmann, L. Sanchez, W. V. D. Daele, A. Abbadie, L. Baud, R. Truche, E. Augendre, L. Clavelier, N. Cherkashin, M. Hytch, and S. Cristoloveanu. "Fabrication, structural and electrical properties

of compressively strained Ge-on-insulator substrates." *Semiconductor Science and Technology* **25** (7), 075010 (2010).

[128] S. Cecchi, E. Gatti, D. Chrastina, J. Frigerio, E. Müller Gubler, D. J. Paul, M. Guzzi, and G. Isella. "Thin SiGe virtual substrates for Ge heterostructures integration on silicon." *Journal of Applied Physics* **115** (9), 093502 (2014).

[129] J. Stangl, V. Holý, and G. Bauer. "Structural properties of self-organized semiconductor nanostructures." *Rev. Mod. Phys.* **76**, 725 (2004).

[130] L. Colace, G. Masini, F. Galluzzi, G. Assanto, G. Capellini, L. Di Gaspare, and F. Evangelisti. "Ge/Si (001) Photodetector for Near Infrared Light." In "Light Emission from Silicon," volume 54 of *Solid State Phenomena*, 55–58. Trans Tech Publications (1997).

[131] L. Colace, G. Masini, F. Galluzzi, G. Assanto, G. Capellini, L. Di Gaspare, E. Palange, and F. Evangelisti. "Metal-semiconductor-metal near-infrared light detector based on epitaxial Ge/Si." *Applied Physics Letters* **72** (24), 3175 (1998).

[132] J. Hartmann, A. Papon, V. Destefanis, and T. Billon. "Reduced pressure chemical vapor deposition of Ge thick layers on Si(001), Si(011) and Si(111)." *Journal of Crystal Growth* **310** (24), 5287 (2008).

[133] H.-C. Luan, D. R. Lim, K. K. Lee, K. M. Chen, J. G. Sandland, K. Wada, and L. C. Kimerling. "High-quality Ge epilayers on Si with low threading-dislocation densities." *Applied Physics Letters* **75** (19), 2909 (1999).

[134] J. M. Hartmann, A. Abbadie, A. M. Papon, P. Holliger, G. Rolland, T. Billon, J. M. Fedeli, M. Rouviere, L. Vivien, and S. Laval. "Reduced pressure-chemical vapor deposition of Ge thick layers on Si(001) for 1.3-1.55 μm photodetection." *Journal of Applied Physics* **95** (10), 5905 (2004).

[135] B. Cunningham, J. O. Chu, and S. Akbar. "Heteroepitaxial growth of Ge on (100) Si by ultrahigh vacuum, chemical vapor deposition." *Applied Physics Letters* **59** (27), 3574 (1991).

[136] G. Capellini, M. De Seta, P. Zaumseil, G. Kozlowski, and T. Schroeder. "High temperature x ray diffraction measurements on Ge/Si(001) het-

erostructures: A study on the residual tensile strain." *Journal of Applied Physics* **111** (7), 073518 (2012).

[137] L. E. Vorobyev. "Volume 1: Si, Ge, C (Diamond), GaAs, GaP, GaSb, InAs, InP, InSb." In M. E. Levinshtein, S. L. Rumyantsev, and M. Shur (Editors) "Handbook Series on Semiconductor Parameters," volume 1, chapter 2, 33–57. World Scientific, London (1996).

[138] L. Carroll, F. Imbert, H. Sigg, M. Süess, E. Müller, M. Virgilio, G. Pizzi, P. Rossbach, D. Chrastina, and G. Isella. "Quantum-confined direct-gap transitions in tensile-strained Ge/SiGe multiple quantum wells." *Applied Physics Letters* **99** (3), 031907 (2011).

[139] M. Virgilio, T. Schroeder, Y. Yamamoto, and G. Capellini. "Radiative and non-radiative recombinations in tensile strained Ge microstrips: Photoluminescence experiments and modeling." *Journal of Applied Physics* **118** (23), 233110 (2015).

[140] G. Grzybowski, R. Roucka, J. Mathews, L. Jiang, R. T. Beeler, J. Kouvetakis, and J. Menéndez. "Direct versus indirect optical recombination in Ge films grown on Si substrates." *Phys. Rev. B* **84**, 205307 (2011).

[141] E. Fitzgerald and S. Samavedam. "Line, point and surface defect morphology of graded, relaxed GeSi alloys on Si substrates." *Thin Solid Films* **294** (1), 3 (1997).

[142] M. H. Zoellner, M.-I. Richard, G. A. Chahine, P. Zaumseil, C. Reich, G. Capellini, F. Montalenti, A. Marzegalli, Y.-H. Xie, T. U. Schülli, M. Häberlen, P. Storck, and T. Schroeder. "Imaging Structure and Composition Homogeneity of 300 mm SiGe Virtual Substrates for Advanced CMOS Applications by Scanning X-ray Diffraction Microscopy." *ACS Applied Materials & Interfaces* **7** (17), 9031 (2015).

[143] M.-I. Richard, M. H. Zoellner, G. A. Chahine, P. Zaumseil, G. Capellini, M. Häberlen, P. Storck, T. U. Schülli, and T. Schroeder. "Structural Mapping of Functional Ge Layers Grown on Graded SiGe Buffers for sub-10 nm CMOS Applications Using Advanced X-ray Nanodiffraction." *ACS Applied Materials & Interfaces* **7** (48), 26696 (2015).

[144] J. J. Wortman and R. A. Evans. "Young's Modulus, Shear Modulus, and Poisson's Ratio in Silicon and Germanium." *Journal of Applied Physics* **36** (1), 153 (1965).

[145] M. M. Rieger and P. Vogl. "Electronic-band parameters in strained $Si_{1-x}Ge_x$ alloys on $Si_{1-y}Ge_y$ substrates." *Phys. Rev. B* **48**, 14276 (1993).

[146] M. De Seta, G. Capellini, Y. Busby, F. Evangelisti, M. Ortolani, M. Virgilio, G. Grosso, G. Pizzi, A. Nucara, and S. Lupi. "Conduction band intersubband transitions in Ge/SiGe quantum wells." *Applied Physics Letters* **95** (5), 051918 (2009).

[147] Y. Busby, M. De Seta, G. Capellini, F. Evangelisti, M. Ortolani, M. Virgilio, G. Grosso, G. Pizzi, P. Calvani, S. Lupi, M. Nardone, G. Nicotra, and C. Spinella. "Near- and far-infrared absorption and electronic structure of Ge-SiGe multiple quantum wells." *Phys. Rev. B* **82**, 205317 (2010).

[148] A. Bashir, K. Gallacher, R. W. Millar, D. J. Paul, A. Ballabio, J. Frigerio, G. Isella, D. Kriegner, M. Ortolani, J. Barthel, and I. MacLaren. "Interfacial sharpness and intermixing in a Ge-SiGe multiple quantum well structure." *Journal of Applied Physics* **123** (3), 035703 (2018).

[149] F. Pezzoli, A. Giorgioni, K. Gallacher, F. Isa, P. Biagioni, R. W. Millar, E. Gatti, E. Grilli, E. Bonera, G. Isella, D. J. Paul, and L. Miglio. "Disentangling nonradiative recombination processes in Ge micro-crystals on Si substrates." *Applied Physics Letters* **108** (26), 262103 (2016).

[150] M. Virgilio, C. L. Manganelli, G. Grosso, T. Schroeder, and G. Capellini. "Photoluminescence, recombination rate, and gain spectra in optically excited n-type and tensile strained germanium layers." *Journal of Applied Physics* **114** (24), 243102 (2013).

[151] F. Pezzoli, F. Isa, G. Isella, C. V. Falub, T. Kreiliger, M. Salvalaglio, R. Bergamaschini, E. Grilli, M. Guzzi, H. von Känel, and L. Miglio. "Ge Crystals on Si Show Their Light." *Phys. Rev. Applied* **1**, 044005 (2014).

[152] F. Pezzoli, A. Giorgioni, D. Patchett, and M. Myronov. "Temperature-Dependent Photoluminescence Characteristics of GeSn Epitaxial Layers." *ACS Photonics* **3** (11), 2004 (2016).

[153] G. Capellini, C. Reich, S. Guha, Y. Yamamoto, M. Lisker, M. Virgilio, A. Ghrib, M. E. Kurdi, P. Boucaud, B. Tillack, and T. Schroeder. "Tensile Ge microstructures for lasing fabricated by means of a silicon complementary metal-oxide-semiconductor process." *Opt. Express* **22** (1), 399 (2014).

[154] F. Cerdeira, A. Pinczuk, J. C. Bean, B. Batlogg, and B. A. Wilson. "Raman scattering from Ge_xSi_{1-x}/Si strained-layer superlattices." *Applied Physics Letters* **45** (10), 1138 (1984).

[155] Filmetrics. "Reflectance Calculator."

[156] J. Murota. *[Semiconductors and Semimetals] Silicon Epitaxy Volume 72 || Chapter 4 Epitaxial growth techniques: Low-temperature epitaxy*, (2001). ISBN 9780127521817.